

Transformation optics: a tool to reveal and make use of symmetries in plasmonics

Matthias Kraft

Department of Physics
Imperial College London

This dissertation is submitted for the degree of
Doctor of Philosophy

2016

Declaration of Originality

I hereby declare that except where specific reference is made to the work of others, the contents of this dissertation are original and have not been submitted in whole or in part for consideration for any other degree or qualification in this, or any other University. This dissertation is the result of my own work and includes nothing which is the outcome of work done in collaboration, except where specifically indicated in the text.

Matthias Kraft
2016

Copyright Declaration

The copyright of this thesis rests with the author and is made available under a Creative Commons Attribution Non-Commercial No Derivatives licence. Researchers are free to copy, distribute or transmit the thesis on the condition that they attribute it, that they do not use it for commercial purposes and that they do not alter, transform or build upon it. For any reuse or redistribution, researchers must make clear to others the licence terms of this work.

Matthias Kraft
2016

Acknowledgements

First of all, I want to thank my supervisor Prof. Sir John Pendry, without whom this thesis would not have been possible. His enthusiasm for physics, great physical intuition, mathematical ability and his clear explanations make him, in my view, a model supervisor. Even more so because he always found time for regular meetings, despite his very busy schedule. I am not only grateful for the research environment he provided, but also for the excellent professional development opportunities that came with it, be it travel to conferences, research visits or career advice.

Of course, I must not forget Prof. Yu Luo, who I first met when he was a PostDoc in John's group. He was of great help in the early stages of my PhD, when I had to learn the details of plasmonics and Transformation optics. In both fields, he proved to be an expert and it was good fun learning from him. He has had a large influence on the development of this thesis as well, and special thanks are due. I'm particularly grateful for the opportunity to spend some time on a research visit to his group at Nanyang Technological University, where most of the work on EELS was carried out. Like John, he possesses great physical intuition, an incredible work ethic and has an enviable command of mathematics, so I am fortunate to count him as a friend.

I am, of course, also indebted to our collaborators in the EXSS group. Particularly, Prof. Stefan Maier whose physical insight and experimental knowledge helped to improve our papers and added guidance in terms of the applicability/realisability of our theories. I am also grateful to Dr. Paloma Arroyo Huidobro and Dr. Avi Braun. Discussions with them have always been very fruitful and interesting. I am very glad that Avi agreed to produce plasmonic gratings similar to the ones discussed in this thesis and am hopeful that some interesting physics will come out of the experiments and collaboration. I'm indebted to Paloma as well, who ensured that there is a future for the grating theory developed here, by applying it to a graphene grating. The collaboration with her has been good fun.

Further thanks go to Dr. Antonio Fernández-Domínguez, Dr. Rongkuo Zhao, Dr. Karthik Sasihithlu and Dr. Alberto Favaro for illuminating discussion on Transformation optics and their work.

Special thanks to my office mates Fionn, Adam and Joel, all the others in B817 and my friends from home. Not only have discussions on physics with them been fun, but also the time in the pub.

Last but not least, I would like to thank the special people around me that made all this possible. First of all, my family who supported me all the way through Kindergarten, school, undergraduate degree and now my PhD. I am certainly fortunate to have grown up in a family that always emphasised the importance of education, be it in the natural sciences, humanities or languages. Without them, I doubt I would have ever made it to Imperial. Finally, a big thank you to Lucy, who gives me so much joy in life and to her family for always making me feel welcome at theirs.

Abstract

Symmetries are omnipresent in physics. From classical mechanics, via solid state physics to particle physics, symmetries provide a means for classification and often lead to deep physical insight. In this thesis, we study symmetries in plasmonics using Transformation optics. We show how Transformation optics can be used to reveal, study and make use of symmetries in practical calculations, by studying a range of plasmonic systems. First, we show that an ellipse and spheroids possess a ‘hidden’ rotational symmetry that becomes apparent when transforming them to a rotationally symmetric structure. Next, we investigate plasmonic gratings and show that a whole class of plasmonic gratings (and other periodic structures) can be related to a translationally invariant slab, thereby inheriting all the slabs spectral properties. In studying the plasmonic grating, we extend the Transformation optics approach to treat periodic systems with extent larger than the wavelength in one direction. Finally, we use Transformation optics to study electron energy loss spectroscopy and cathodoluminescence problems in plasmonics, by mapping the plasmonic nanoparticles under investigation to more symmetric ones. Thus, again using the symmetry of the transformed structures to derive analytical solutions to the problem at hand.

Preface and List of Publications

Nowadays, research in physics is almost exclusively done in groups of a few or even many individuals. As a result, it is often quite hard to tell what the exact contribution of each individual is. In this section, I will try to make clear what my share of the work presented in this thesis was, and where credit to others is due.

Chapter 2 gives an introduction to plasmonics and transformation optics. As such, none of the arguments presented in this chapter are original, but instead represent my own short survey of the topics.

In chapter 3 we analyse an ellipse and prolate and oblate spheroids using Transformation optics. I carried out all calculations and numerical simulations for the two-dimensional ellipse. The coordinate transformation of the spheroids to a spherical shell was conceived by Prof. Yu Luo, who also carried out the analytical analysis of this case. The analytics is reproduced here for completeness though. I carried out the numerical simulations of the optical response of the spheroids and compared the results to the analytical calculations. All of the authors of [1], that is Prof. Sir John Pendry, Prof. Stefan Maier, Prof Yu Luo and I contributed to the interpretation of the results in this chapter.

Chapter 4 presents a study of plasmonic gratings using Transformation optics. It is largely, though not exclusively, based on the paper [2]. Prof. John Pendry had the original idea of using a logarithm transformation to study periodic systems, though I derived the exact form of the transformations in chapter 4 that relate a periodic grating to a simple slab and also the one relating a flat half space to a modulated half space. I carried out all the analytical calculations, though I gratefully acknowledge helpful discussion with Prof. John Pendry and Prof. Yu Luo on the technical challenges of the problem. I also carried out all the numerical simulations presented in this chapter and compared them to the analytics. Again, all the authors of [2] contributed to the interpretation of the results.

Finally, chapter 5 extends the Transformation optics approach to study problems in electron energy loss spectroscopy and cathodoluminescence. Here too, I carried out all the analytical calculations and numerical simulations and compared the results. Again,

I gratefully acknowledge discussion with Prof. John Pendry and Prof. Yu Luo on the technical challenges of the analytical calculations. Prof. Yu Luo, in particular, derived the result in Eq.5.25-Eq.5.28, which I quote from another paper [4]. Here too, all authors of [3] contributed to the interpretation of the results.

This thesis is largely based on references [1–3] in the following list of publications. References [4–7] in the list below have been published during the duration of my PhD but are not included in this thesis.

- [1] M. Kraft, J. B. Pendry, S. A. Maier, and Y. Luo, “Transformation optics and hidden symmetries,” *Phys. Rev. B* **89**, 245125 (2014).
- [2] M. Kraft, Y. Luo, S. A. Maier, and J. B. Pendry, “Designing Plasmonic Gratings with Transformation Optics,” *Phys. Rev. X* **5**, 031029 (2015).
- [3] M. Kraft, Y. Luo, and J. B. Pendry, “Transformation Optics: A Time- and Frequency-Domain Analysis of Electron-Energy Loss Spectroscopy,” *Nano Lett.* **16**, 5156–5162 (2016).
- [4] Y. Luo, M. Kraft, and J. B. Pendry, “Harnessing transformation optics for understanding electron energy loss and cathodoluminescence,” [arXiv.org preprint arXiv:1605.09319 \[cond-mat.mes-hall\]](https://arxiv.org/abs/1605.09319) (2016).
- [5] P. A. Huidobro, M. Kraft, R. Kun, S. A. Maier, and J. B. Pendry, “Graphene, plasmons and transformation optics,” *Journal of Optics* **18**, 044024 (2016).
- [6] P. A. Huidobro, M. Kraft, S. A. Maier, and J. B. Pendry, “Graphene as a Tunable Anisotropic or Isotropic Plasmonic Metasurface,” *ACS Nano* **10**, 5499–5506 (2016).
- [7] M. Kraft, A. Braun, Y. Luo, S. A. Maier, and J. B. Pendry, “Bianisotropy and Magnetism in Plasmonic Gratings,” *ACS Photonics* **3**, 764–769 (2016).

Contents

Contents	13
List of Figures	17
List of Tables	27
Nomenclature	29
1 Introduction	31
2 Background	35
2.1 Plasmonics	35
2.2 Transformation optics	40
2.2.1 Derivation of the transformation rules	41
2.2.2 Conformal transformations	43
2.3 Transformation optics in plasmonics	45
3 Hidden symmetries in plasmonic systems I: Ellipses and spheroids	49
3.1 2-D elliptic cylinder	49
3.1.1 Transformation of the geometry and sources	50
3.1.2 Plasmon mode structure: 2-D ellipse	52
3.1.3 Absorption and scattering: 2-D ellipse	53
3.2 3-D spheroid	56
3.2.1 Transformation of the geometry and sources	57
3.2.2 Absorption and scattering: 3-D spheroid	61
3.3 Summary	63
4 Hidden symmetries in plasmonic systems II: plasmonic gratings	65
4.1 Introduction	65
4.2 Transformation of the geometry	68

4.2.1	Semi-infinite periodically modulated plane	68
4.2.2	Nanoparticle chain	69
4.2.3	Periodically modulated plasmonic grating	69
4.2.4	Nanoparticle chain on a flat surface	72
4.2.5	Mathematical details of the transformation	72
4.3	Dispersion relation	75
4.3.1	Half-plane to modulated surface	76
4.3.2	Slab to grating	77
4.4	Optical response: theory	82
4.4.1	Transformation of a plane wave	82
4.4.2	Scattered and induced potential in the slab frame	84
4.4.3	Boundary conditions	87
4.4.3.1	Boundary conditions at the slab interfaces	87
4.4.3.2	Radiation boundary condition	88
4.4.4	Calculating the currents in the grating	89
4.4.5	Reflection and transmission	93
4.5	Optical response: results	95
4.5.1	Reflection, transmission and absorption	95
4.5.2	Realistic permittivities	98
4.5.2.1	Reflection and transmission for real silver	99
4.5.2.2	Field enhancement	99
4.6	Bi-anisotropic effects in plasmonic gratings	101
4.6.1	Parameter retrieval for bi-anisotropic metamaterials	102
4.7	Summary	105
5	Transformation optics applied to Electron Energy-Loss Spectroscopy (EELS)	107
5.1	A very brief introduction to EELS	107
5.2	The fields of a moving charge	110
5.3	EELS for a non-concentric annulus using TO	112
5.3.1	Transformation of the geometry	113
5.3.2	Transformation of the source potential	115
5.3.2.1	An electron passing on the thin side of the non-concentric annulus	115
5.3.2.2	An electron passing the crescent horizontally along its top	117
5.3.2.3	An electron passing on the thick side of the non-concentric annulus	119

5.3.3	Induced potentials and boundary conditions	120
5.3.3.1	Potentials and boundary condition at the interfaces . . .	121
5.3.3.2	Radiative reaction boundary condition	123
5.3.4	Power scattered	127
5.3.5	Power absorption	130
5.3.6	Comparison with COMSOL	133
5.3.6.1	Vertically moving electron	135
5.3.6.2	Horizontally moving electron	139
5.3.6.3	Breakdown of the theory	140
5.3.7	Time-response of the non-concentric annulus	143
5.4	EELS for an ellipse using TO	146
5.4.1	Transformation of the source potential	147
5.4.2	Induced potentials and boundary conditions	148
5.4.3	Power absorbed by the ellipse	150
5.4.4	Power scattered	151
5.4.5	Radiative reaction	153
5.4.5.1	Fictive absorber at the origin	154
5.4.5.2	Fictive absorber surrounding the annulus	156
5.4.5.3	Modified expression for the $l = 1$ scattering coefficients .	157
5.4.6	Comparison with COMSOL	159
5.4.7	Time response of the ellipse	162
5.5	Summary	163
6	Conclusion	165
A	Supporting analytical calculations for a two-dimensional ellipse	169
A.1	Resonance condition for an ellipse	169
A.2	Expansion coefficients: EELS for the ellipse	171
B	Supporting analytical calculations for the grating	173
B.1	The conformal transformation as a Fourier series	173
B.1.1	Real part of Γ	175
B.1.2	Imaginary part of Γ	177
B.1.3	Coordinate transformation as a Fourier series	179
C	Modelling the radiative reaction	181
C.1	Permittivity of the fictive absorber	181
C.2	Polarisability of the fictive absorber	185

D Supplementary material: time-domain simulation files	187
E Copyright permissions for references [62] and [102]	189
Bibliography	195

List of Figures

1.1	Example of a mirror symmetric plasmonic nanoparticle.	31
2.1	The dispersion relation (Eq.2.9) with $\epsilon_d = 1$ and ϵ_m as in Eq.2.7. The blue solid and red dashed lines are the real and imaginary part of k_x . For $\omega < \omega_{sp}$, the wave has the character of a SPP, but for $\omega > \omega_p$ the metal is transparent and the character of the plasmon changes to a propagating transverse electromagnetic wave. In between these regimes k_x is purely imaginary and no propagation is possible (red dashed line).	37
2.2	A dipole and a slab transform to a crescent in a uniform field, as demonstrated in [16].	46
3.1	Schematic illustration of the transformation between an ellipse and an annulus. The transformations of the source are also shown. A constant electric field (red) transforms to a constant electric field (red) plus a dipole (red). Modified from [62].	51
3.2	Resonance frequencies versus the ratio of semi-minor to semi-major axis. Shown are in descending order the first five odd modes (solid lines) and in ascending order the first five even modes (dashed lines). $\omega_p = 8eV$ and $\gamma = 0.032eV$. Modified from [62].	53
3.3	Imaginary part of the electrostatic potential for $m=1$ and $m=3$. Shown are the distributions in the annulus geometry and the elliptic geometry, both for the even (top) and odd (bottom) mode. We assumed a Drude type permittivity (Eq.2.6) ϵ_m with $\omega_p = 8eV$ and $\gamma = 0.032eV$. Reprinted with permission from [62]. Copyright 2014 by the American Physical Society.	54

-
- 3.4 Absorption (left) and scattering (right) cross-section normalised by the physical cross-section a' . Our analytical model (solid lines) is compared to COMSOL simulations (markers) for different values of the semi-major axis a' . The ratio between semi-major to semi-minor axis has been kept constant at $b' = 0.2a'$. We used experimental permittivity data for Silver from Johnson and Christy [65] for ϵ_m and set $\epsilon_d = 1$. This data has also been published in [62]. 56
- 3.5 Shift of the LSP resonances for oblate (top) and prolate (bottom) spheroids. Shown are the modes for $l = 1$ and $l = 4$. The insets show the potential distribution for their respective modes. Reprinted with permission from [62]. Copyright 2014 by the American Physical Society. 60
- 3.6 Absorption (left) and scattering (right) spectra for oblate (top) and prolate (bottom) spheroids under plane wave illumination ($E_{x'} = E_{z'} = E_0$, $E_{y'} = 0$). Shown are spectra for different values of the semi-major axis $a' = 5, 10, 30\text{nm}$ with $b' = 0.2a'$. We used the permittivity data of silver from Johnson and Christy [65] as ϵ_m and set $\epsilon_d = 1$. Reprinted with permission from [62]. Copyright 2014 by the American Physical Society. 62
- 3.7 Comparison between analytically (solid lines) and numerically (open circles) calculated absorption (left) and scattering (right) spectra for oblate (top) and prolate (bottom) spheroids under plane wave illumination ($E_{x'} = E_{y'} = 0$, $E_{z'} = E_0$). Shown are spectra for different values of the semi-major axis $a' = 5\text{nm}$ (black), $a' = 10\text{nm}$ (blue) and $a' = 30\text{nm}$ (red), with $b' = 0.2a'$. We used the permittivity data of silver from Johnson and Christy [65] as ϵ_m and set $\epsilon_d = 1$. Reprinted with permission from [62]. Copyright 2014 by the American Physical Society. 63
- 4.1 Schematic of the step-by-step transformation from a half-plane to a half space with a periodically modulated interface. 68
- 4.2 Schematic of the step-by-step transformation from a half-plane to an array of ‘elliptical’ nanoparticles. 70
- 4.3 Schematic of the step-by-step transformation from a slab to a grating with one periodically modulated and one flat interface. Modified with permission from [102], available under the Creative Commons Attribution 3.0 License. 71

- 4.4 Schematic of the step-by-step transformation from a slab to an array of ‘elliptical’ nanoparticles close to a flat surface. Reprinted with permission from the supplementary material of [102], available under the Creative Commons Attribution 3.0 License. 72
- 4.5 Analytic structure of the transformation in Eq.4.2 for $\gamma = 1$, $y_0 = 0.033$ and $w_0 = 0.6$. The solid lines show the deformation of the cartesian grid in the x - y -frame under transformation to the u - v -frame. The dashed lines indicate the branch cuts running from the branch points to infinity. Reprinted with permission from [102], available under the Creative Commons Attribution 3.0 License. 74
- 4.6 The absorption and scattering spectra for two modulated half planes. The top panel shows spectra for a half plane not obtained via a conformal transformation. The bottom panel shows the spectra for a half-plane obtained from Eq.4.1 with $\gamma = 10^{-8}$ and $y_0 = 0.5$. The period and modulation depth are the same for both structures. The permittivity is given by $\epsilon_m = 1 - \frac{\omega_p^2}{\omega(\omega+i\gamma)}$, $\epsilon_d = 1$, with $\gamma = 0.032eV$ and $\omega_p = 8eV$, in both cases. 76
- 4.7 Dispersion relation of two gratings in the first Brillouin zone. The yellow triangles and green, open circles are COMSOL simulations for a grating with $\gamma = 10^{-8}$, $w_0 = 2.5$ and $\gamma = 10^{-8}$, $w_0 = 1.5$, respectively. In both cases we started with a slab at position $a = 1$ and with thickness $d = 0.5$. The solid lines are analytical calculations. The dashed line corresponds to the light line. The permittivities were $\epsilon_m = 1 - \frac{\omega_p^2}{\omega^2}$, $\epsilon_d = 1$, with $\omega_p = 8eV$. Modified with permission from [102], available under the Creative Commons Attribution 3.0 License. 78
- 4.8 A magnified version of figure 4.7. Shown is the dispersion relation for the grating around the 1st order mode at $\approx 3.55eV$. The solid line corresponds to analytical calculations, the open circles are COMSOL simulations for the weakly modulated grating and the triangles correspond to COMSOL simulations of the strongly modulated grating. a is the lattice constant. Reprinted with permission from the supplementary material of [102], available under the Creative Commons Attribution 3.0 License. 80

- 4.9 Reflectance (top) and transmittance (bottom) for the weakly (left) and strongly (right) modulated grating (shown in figure 4.7). Blue lines correspond to analytical calculations, whereas the red lines with circles are COMSOL simulations. In COMSOL the wave is incident on the modulated side of the grating. The insets show the electric energy density in and close to the grating at the first transmission peak and dip (same color scale). For both analytics and simulations the permittivity of the grating was $\epsilon_m = 1 - \omega_p^2/(\omega(\omega + i\gamma))$ with $\omega_p = 8eV, \gamma = 0.032eV$. The surrounding dielectric is air with $\epsilon_d = 1$. Reprinted with permission from [102], available under the Creative Commons Attribution 3.0 License. . . . 96
- 4.10 Reflectance from the strongly modulated grating for incidence from the right (on modulated side, red dashed) and left (flat side, green crosses). The analytical solution lies between the two curves (blue line). 97
- 4.11 Power absorbed by the grating. Left the weakly modulated grating, analytical solutions are in blue, red dashed solutions correspond to COMSOL and incidence from the right. Right, the strongly modulated grating. Analytical solutions are shown in blue, COMSOL simulations for incidence from the right (red-dashed lines) and incidence from the left (green crosses). 99
- 4.12 Reflection (top) and transmission (bottom) for the weakly (left) and strongly (right) modulated grating (shown in figure 4.7). Blue lines correspond to analytical calculations, whereas the red open circles are COMSOL simulations. In COMSOL the wave is incident on the modulated side of the grating. For both analytics and simulations we used experimental values for the permittivity of silver [65]. The surrounding dielectric is air with $\epsilon_d = 1$ 100
- 4.13 Maximum field enhancement normalised by the incident electric field for the strongly (left) and weakly (right) modulated grating. The field enhancement was calculated using COMSOL with experimental values for the permittivity of silver [65]. $\text{Re}(\epsilon_m) = -3.88, \text{Im}(\epsilon_m) = -0.16$ at $\omega \approx 3.2eV$. Reprinted with permission from [102], available under the Creative Commons Attribution 3.0 License. 101

- 4.14 Effective material parameters for the strongly (solid lines) and weakly (dashed lines) modulated grating. In both cases the equivalent metamaterial was a symmetric slab. The thickness of the slab was set to the maximum thickness of the grating 10.75nm and 26.1nm for the weakly and strongly modulated grating, respectively. The original permittivity of the two gratings was that of silver with permittivity data from [65], whereas the original permeability was 1. 104
- 5.1 Schematic of an electron energy loss problem. An electron (red circle) moves past a metallic nanoparticle at high velocity. The electric field of the moving electron excites localised surface plasmons, leading to an energy transfer from electron to the nanoparticle. The fields induced in the nanoparticle also lead to a scattered field. 108
- 5.2 Transformation of a concentric to a non-concentric annulus. The dashed lines in (c) and (d) show the transformation of the electron trajectories. An electron moving with constant velocity on a straight line in the non-concentric annulus' frame travels on a curved trajectory and with non-uniform velocity in the concentric annulus' frame. Modified with permission from [66]. Copyright 2016 American Chemical Society. 113
- 5.3 The value of the source expansion coefficients a_n^{s-} with $n = 1, 2, 3, 4$ for an electron passing to the left of the nanoparticle (see figure 5.2 (d), red line). The parameters are $\lambda = 1.602 \times 10^{-19}$, $g^2 = 2 \times 10^{-8}$, $x_0 = 1.5$, $x'_e = -0.4g^2$, $c_e = 0.1c$ on the left and $c_e = 0.3c$ on the right. The data for $c_e = 0.1c$ is also shown in the supplementary material of [66]. 117
- 5.4 The absolute value of the source expansion coefficients a_n^{s-} with $n = 1, 2, 3, 4$ for an electron passing along the top of the nanoparticle (see figure 5.2 (d), green line). The parameters are $\lambda = 1.602 \times 10^{-19}$, $g^2 = 2 \times 10^{-8}$, $x_0 = 1.5$, $x'_e = -0.4g^2$, $c_e = 0.1c$ on the left and $c_e = 0.3c$ on the right. The data for $c_e = 0.1c$ is also shown in the supplementary material of [66]. 119
- 5.5 The value of the source expansion coefficients a_n^{s-} with $n = 1, 2, 3, 4$ for an electron passing to the right of the nanoparticle (see figure 5.2 (d), blue line). The parameters are $\lambda = 1.602 \times 10^{-19}$, $g^2 = 2 \times 10^{-8}$, $x_0 = 1.5$, $x'_e = -0.4g^2$, $c_e = 0.1c$ on the left and $c_e = 0.3c$ on the right. 121

- 5.6 The power scattered by the non-concentric annulus. Figure (a) compares the electrostatic results with the result containing the radiative reaction for an electron passing on the crescent's left with $c_e = 0.2c$. Figure (b)-(d) all compare the scattered power for different electron velocities, as indicated in the legend. Figure (b) is for an electron passing on the left side, figure (c) for an electron passing on the right side and in figure (d) the electron passes along the top in the horizontal direction. The geometrical parameters were set to $g^2 = 2 \times 10^{-8}$, $x_0 = 1.5$, $R_0 = \exp(1)$ and $R_1 = \exp(1.2)$. The distance of the electron to the nanoparticle was $\approx 3.3\text{nm}$ for figure (a,b), $\approx 3.6\text{nm}$ for figure (c) and $\approx 2.4\text{nm}$ for figure (d). The permittivity of the nanoparticle is defined in Eq.5.79, the surrounding medium has $\epsilon_d = 1$. The power scattered is given in arbitrary units. 129
- 5.7 The power absorbed by the non-concentric annulus. Figure (a) compares the electrostatic results with the result containing the radiative reaction for an electron passing on the non-concentric annulus' left with $c_e = 0.2c$. Figure (b)-(d) all compare the scattered power for different electron velocities, as indicated in the legend. Figure (b) is for an electron passing on the left side, figure (c) for an electron passing on the right side and in figure (d) the electron passes along the top in the horizontal direction. The geometrical parameters were set to $g^2 = 2 \times 10^{-8}$, $x_0 = 1.5$, $R_0 = \exp(1)$ and $R_1 = \exp(1.2)$. The distance of the electron to the nanoparticle was $\approx 3.3\text{nm}$ for figure (a,b), $\approx 3.6\text{nm}$ for figure (c) and $\approx 2.4\text{nm}$ for figure (d).The permittivity of the nanoparticle is defined in Eq.5.79, the surrounding medium has $\epsilon_d = 1$. The power absorption is given in arbitrary units. 132

- 5.8 The electron energy loss (top) and photon emission (bottom) probability density for a (line) electron passing to the left of the non-concentric annulus. The electron energy loss probability density is in units of $[eV^{-1}$ per electron per unit length]. Similarly the photon emission probability density is in terms of the number of photons emitted in units of $[eV^{-1}$ per electron per unit length]. The area under each of the curves is unity. The solid lines correspond to analytical results, with the accompanying markers corresponding to COMSOL simulations. The geometrical parameters were set to $g^2 = 2 \times 10^{-8}$, $x_0 = 1.5$, $R_0 = \exp(1)$ and $R_1 = \exp(1.2)$, the distance to the particle was $\approx 3.3nm$ and the constant λ defined in Eq.5.15 was set to $1.602 \times 10^{-19}Cm^{-1}$. The data for $c_e = 0.05$ and $c_e = 0.1c$ is also published in [66]. 136
- 5.9 The electron energy loss (top) and photon emission (bottom) probability density for a (line) electron passing to the right of the non-concentric annulus. The electron energy loss probability density is in units of $[eV^{-1}$ per electron per unit length]. Similarly the photon emission probability density is in terms of the number of photons emitted in units of $[eV^{-1}$ per electron per unit length]. The area under each of the curves is unity. The solid lines correspond to analytical results, with the accompanying markers corresponding to COMSOL simulations. The geometrical parameters were set to $g^2 = 2 \times 10^{-8}$, $x_0 = 1.5$, $R_0 = \exp(1)$ and $R_1 = \exp(1.2)$, the distance to the particle was $\approx 3.3nm$ and the constant λ defined in Eq.5.15 was set to $1.602 \times 10^{-19}Cm^{-1}$ 138
- 5.10 The electron energy loss (top) and photon emission (bottom) probability density for a (line) electron passing along the top of the non-concentric annulus. The electron energy loss probability density is in units of $[eV^{-1}$ per electron per unit length]. Similarly the photon emission probability density is in terms of the number of photons emitted in units of $[eV^{-1}$ per electron per unit length]. The area under each of the curves is unity. The solid lines correspond to analytical results, with the accompanying markers corresponding to COMSOL simulations. The geometrical parameters were set to $g^2 = 2 \times 10^{-8}$, $x_0 = 1.5$, $R_0 = \exp(1)$ and $R_1 = \exp(1.2)$, the distance to the particle was $\approx 3.3nm$ and the constant λ defined in Eq.5.15 was set to $1.602 \times 10^{-19}Cm^{-1}$. This data is also published in [66]. 140

- 5.11 The electron energy loss (top) and photon emission (bottom) probability density for a (line) electron passing to the left of the non-concentric annulus. The electron energy loss probability density is in units of $[eV^{-1}$ per electron per unit length]. Similarly the photon emission probability density is in terms of the number of photons emitted in units of $[eV^{-1}$ per electron per unit length]. The area under each of the curves is unity. The solid lines correspond to analytical results, with the accompanying markers corresponding to COMSOL simulations. The geometrical parameters were set to $x_0 = 1.5$, $R_0 = \exp(1)$ and $R_1 = \exp(1.2)$, with g^2 as indicated. The distance to the particle was $\approx 3.3nm$ for the data with $c_e = 0.5c$, but was $\approx 5nm$ for the data with $c_e = 0.1c$. The constant λ defined in Eq.5.15 was set to $1.602 \times 10^{-19} Cm^{-1}$ 142
- 5.12 The top panel shows the electric field distribution at a specific time point (indicated by the arrow). E_v on the left and $|E|$ on the right. The bottom panel shows the time response of the crescent at a particular point (marked by the black dot in the top panel). In this case the electron moves vertically to the left of the nanoparticle. The plots in the bottom panel have been normalised by the maximum source field at the particular point. Modified with permission from [66]. Copyright 2016 American Chemical Society. 144
- 5.13 The top panel shows the electric field distribution at a specific time point (indicated by the arrow). E_v on the left and $|E|$ on the right. The bottom panel shows the time response of the crescent at a particular point (marked by the black dot in the top panel). In this case the electron moves vertically to the left of the nanoparticle. The plots in the bottom panel have been normalised by the maximum source field at the particular point. Modified with permission from [66]. Copyright 2016 American Chemical Society. 145
- 5.14 The transformation of the geometry and the (line) electron's trajectory from the ellipse's frame to the annulus' frame. Modified with permission from the supplementary material of [66]. Copyright 2016 American Chemical Society. 146
- 5.15 The value of the source expansion coefficients a_n^{s-} with $n = 1, 2, 3, 4$ for an electron passing vertically to the right of the ellipse (see figure 5.14. The parameters are $\lambda = 1.602 \times 10^{-19}$, $c' = 10^{-8}$, $u_0 = 0.4$, $x'_e = c' \cosh(u_0) + 2 \times 10^{-9}$, $c_e = 0.1$ on the left and $c_e = 0.3c$ on the right. 148

- 5.16 Transformation of the fictive absorber surrounding the elliptical particle. An absorber with a circular boundary at $r' = a$ and extending to infinity transforms to a small absorber at the origin with radius $r = c'/(2a)$ and an absorber surrounding the annulus with its boundary at $r = 2a/c'$. Both absorbers lead to multiple scattering with the annulus. Modified with permission from the supplementary material of [66]. Copyright 2016 American Chemical Society. 153
- 5.17 The electron energy loss (top) and photon emission (bottom) probability density for a (line) electron passing to the right of the ellipse. The electron energy loss probability density is in units of $[eV^{-1}$ per electron per unit length]. Similarly the photon emission probability density is in terms of the number of photons emitted in units of $[eV^{-1}$ per electron per unit length]. The area under each of the curves is unity. The solid lines correspond to analytical results, with the accompanying markers corresponding to COMSOL simulations. On the left, we compare the electrostatic solution to the one including the radiative reaction of the ellipse for $c_e = 0.3c$. The geometrical parameters were set to $u_0 = 0.4$, $c' = 10^{-8}$ giving an ellipse of width $\approx 22nm$ and height $\approx 8nm$. The distance of the electron to the particle was $2nm$. The constant λ defined in Eq.5.15 was set to $1.602 \times 10^{-19} Cm^{-1}$ 160
- 5.18 The electron energy loss (top) and photon emission (bottom) probability density for a (line) electron passing to the right of the ellipse. The electron energy loss probability density is in units of $[eV^{-1}$ per electron per unit length]. Similarly the photon emission probability density is in terms of the number of photons emitted in units of $[eV^{-1}$ per electron per unit length]. The area under each of the curves is unity. The solid lines correspond to analytical results, with the accompanying markers corresponding to COMSOL simulations. We used permittivity data from [65] for the nanoparticle. All other parameters are the same as in figure 5.17. This data has also been published in the supplementary material of [66]. 161

- 5.19 The top panel shows the electric field distribution at a specific time point (indicated by the arrow). E_u on the left and $|E|$ on the right. The bottom panel shows the time response of the crescent at a particular point (marked by the black dot in the top panel). In this case, the electron moves vertically to the left of the nanoparticle. The plots in the bottom panel have been normalised by the maximum source field at that particular point. 162

List of Tables

2.1	Transformation rules of the various quantities in the Maxwell equations for a general coordinate transformation. Λ is the Jacobian of the coordinate transformation. Note that $\begin{pmatrix} \mathbf{E} \\ \mathbf{H} \end{pmatrix}$ is not to be understood as vector notation, but rather that \mathbf{E}, \mathbf{H} transform in the same way [22].	40
4.1	Summary of branch points	73
5.1	Table giving the total energy loss defined by $\int e_{loss}^-(\omega)d\omega$ in units of [eV per unit length] and the total number of photons emitted. Results for analytical calculations for a line electron passing to the left of the particle are compared with COMSOL simulations.	135
5.2	Table giving the total energy loss defined by $\int e_{loss}^-(\omega)d\omega$ in units of [eV per unit length] and the total number of photons emitted. Results for analytical calculations for a line electron passing to the right of the particle are compared with COMSOL simulations.	137
5.3	Table giving the total energy loss defined by $\int e_{loss}^-(\omega)d\omega$ in units of [eV per unit length] and the total number of photons emitted. Results for analytical calculations for a line electron passing along the top of the particle are compared with COMSOL simulations.	139
5.4	Table giving the total energy loss defined by $\int e_{loss}^-(\omega)d\omega$ in units of [eV per unit length] and the total number of photons emitted. Results for analytical calculations for a line electron passing along the top of the particle are compared with COMSOL simulations.	141

- 5.5 Table giving the total energy loss defined by $\int e_{loss}^-(\omega)d\omega$ in units of [eV per unit length] and the total number of photons emitted. Results for analytical calculations for a line electron passing to the right of the ellipse are compared with COMSOL simulations. This data is for a nanoparticle with experimental permittivity data of silver [65]. 159

Nomenclature

Acronyms / Abbreviations

CL Cathodoluminescence

EELS Electron Energy-Loss Spectroscopy

TO Transformation optics

Chapter 1

Introduction

Symmetry is one of the most fundamental concepts in physics. Beautifully expressed through Noether's theorem, symmetries lead to conservation laws [1], on which so much of classical and quantum physics relies. Homogeneity of time ensures energy conservation, invariance under space translations leads to momentum conservation and rotational symmetry gives rise to conservation of angular momentum, to name a few [2]. These examples alone show the great ability of symmetries to restrict and classify the potential class of solutions to problems in physics. To give a more concrete example from solid state physics, the periodicity of the crystal lattice restricts the class of allowed solutions for the wave functions to periodic ones, via Bloch's theorem [3]. One can thus learn a great deal about the physical properties of the system from the symmetry of the problem alone, without actually solving the underlying equations. This is one of the reasons that makes the study of symmetries worthwhile, especially so in areas of physics where exact solutions (analytical or not) are difficult to obtain.

Plasmonics is such an area, as the often non-regular shape of plasmonic nanoparticles seldom permits fully analytical characterisations of their mode spectrum and optical response. Yet, symmetries are rarely used as a tool to study plasmonic systems. One

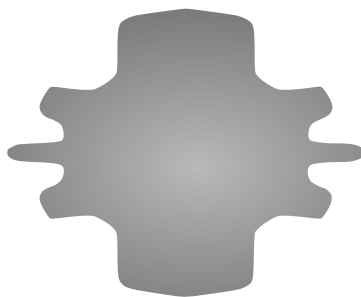


Figure 1.1: Example of a mirror symmetric plasmonic nanoparticle.

of the aims of this thesis is to show that the study of symmetries is worthwhile in plasmonics. Take the particle in figure 1.1. One would be hard-pressed to analytically calculate the plasmon modes of this system. Even in the electrostatic limit, where one needs to solve Laplace's equation $\nabla^2\phi = 0$, this is a hard problem due to the irregular shape of the nanoparticle. However, closer inspection of the geometry reveals that the particle possesses two mirror planes. It immediately follows that the electrostatic potential ϕ has these symmetries as well and they place restrictions on the possible plasmon modes. Arguably, these two mirror symmetries are rather obvious and also only of limited help when it comes to practical calculations of the plasmon modes. In this thesis, we want to go further. We want to investigate if plasmonic nanoparticles possess some additional 'hidden' symmetries that are not apparent at first sight. If so, can we use them to classify and calculate the plasmon modes of the system? Our analytical tool of choice is Transformation optics (TO), which, incidentally, owes its existence to a symmetry in electromagnetism, namely the covariance of Maxwell's equations under coordinate transformations. We thus formulate the following research question addressed in this thesis: *Can TO be used to reveal, study and make use of symmetries in plasmonic systems?*

While the question above sets the theme for most of the thesis, there is however a second, major and more technical point related to TO that we would like to address. Previously, TO has been successfully applied to study plasmonic nanoparticles of sizes far below the wavelength of visible light. In this case, a purely electrostatic treatment is sufficient to describe the plasmon modes and optical response of the particles. Can we relax this restriction and treat systems that have features larger than the wavelength? In this case, currents can flow on a length scale larger than the wavelength of light and thus lead to a magnetic response, rendering a purely electrostatic treatment unfeasible. So the second question we want to address is the following: *Can TO be used to study plasmonic systems of extent greater than the wavelength of light, such that currents can flow on a scale larger than the wavelength?*

The thesis is structured as follows. In chapter 2, we introduce the basic concepts needed to understand this thesis. That is, the basics of plasmonics, TO and how we can use TO to analyse plasmonic systems.

Chapter 3 gives a first glance at revealing and using hidden symmetries with TO, by studying two simple plasmonic systems: a two-dimensional ellipse and three dimensional spheroids. Here, we transform an ellipse (spheroid) to a rotationally symmetric annulus (spherical shell) and show that in addition to mirror symmetries, ellipse and

spheroid posses a hidden rotational symmetry. The physical consequence of this symmetry is a naturally arising dipole selection rule. The plasmon spectra of the original and transformed structure are identical and this reveals a subtle link between geometrical symmetry breaking and plasmon hybridisation. For an ellipse, plasmon modes are divided into two sets of modes, this division occurs because deforming a cylinder into an ellipse lifts the degeneracy of the modes. In the rotationally symmetric annulus, however, the splitting of modes occurs due to hybridisation of plasmons on its inner and outer surface. The mathematical solutions in the original and transformed frames are identical, yet their physical interpretations differ, thus linking two seemingly disparate concepts, hybridisation and symmetry breaking. We show that analogous results hold for the spheroid and spherical shell.

In chapter 4 we study the spectral properties of plasmonic gratings, as well as their optical response. Here, both the question of symmetries and the question of treating systems larger than the wavelength of visible light are addressed. We present a transformation that can map a corrugated surface on a flat half-space, a particle chain on a flat half-space, a chain of particles next to a flat half-space on a symmetric flat slab and a thin modulated grating on a symmetric flat slab. Moreover, the transformation presented contains two free parameters, such that, e.g. a whole class of gratings can be transformed to a symmetric slab. Due to the conformality of the transformation, the plasmon spectrum is conserved and we find that despite the periodicity of the grating, its spectrum is given by that of a translationally invariant slab. This is surprising, since a translationally invariant slab naturally has a gapless spectrum, whereas periodic gratings usually feature band gaps. We thus find that a whole class of periodic gratings features band crossings akin to Dirac points in graphene. For Dirac points in graphene, the physical cause of these band crossings is a special symmetry of the graphene lattice, for our gratings the interpretation is altogether different, as it is precisely the translational invariance (and hence lack of a lattice) of the underlying slab structure that leads to the band crossings. We further calculate the optical response of the grating under plane wave illumination and show the importance of including magnetic effects in the theoretical treatment, as strong currents are present in the gratings that cannot be ignored.

Finally, in chapter 5 we apply TO to a new class of problems in plasmonics. Namely, electron energy loss spectroscopy and cathodoluminescence. This chapter is somewhat less focussed on symmetries. They do, however, play a large role in the sense that they enable us to analytically study these problems. The analytical solution facilitated via TO leads to surprising physical insights. We find that contrary to common belief, an

electron beam does not always couple to every dark mode of a plasmonic structure. For a non-concentric annulus the electron-energy-loss spectrum crucially depends on the velocity of the electron beam and we show that for some velocities specific modes remain inactive despite being probed with an electron. This inactivity is explained through an accidental degeneracy. At the resonance frequency of an inactive mode, the electric field generated by the exciting electron does not contain any contribution that could couple to this particular mode. We find that this phenomenon is very sensitive to the velocity of the electron. This opens up possibilities to switch-on or -off a particular mode in the spectrum. Additionally, we are able to calculate the time-response of the system in a very efficient manner by ‘Fast-Fourier’ transforming our analytical solutions. This allows us, for example, to get an insight into the time scales of the plasmon decay or to find the time when the electric field enhancement is strongest. Through the generation of simulation videos we also clearly ‘see’ how plasmonic nano-particles harvest light and concentrate it near singularities.

Chapter 2

Background

2.1 Plasmonics

Plasmonics is, loosely speaking, the study of the interaction between electromagnetic waves and plasmons. Plasmons are usually described as the quantization of a collective oscillation of the conduction electrons of a metal [4]. They have first been introduced in their quantum form by Bohm and Pines [5] in the early 1950s, but also naturally arise in the context of classical electromagnetism and have thus been known since the early 20th century [6, 7]. In many cases, it is completely adequate to ignore all quantum effects and describe plasmons in the framework of classical electromagnetism, an approach that we will follow here.

Plasmons can be broadly divided into two classes: Plasmons with propagating wave character and plasmons which are localised in space. The former class is subdivided into bulk or volume plasmons and surface plasmon polaritons [4]. We will briefly introduce these different types of plasmons in the following.

Volume plasmons — To understand how each of these types of plasmons arise we start by taking a look at the wave equation for the electric field, as derived from the macroscopic Maxwell equations[4]:

$$\nabla \times \nabla \times \mathbf{E} = -\mu_0 \frac{\partial^2 \mathbf{D}}{\partial t^2}. \quad (2.1)$$

Here μ_0 is the permeability of free space and \mathbf{D} the electric displacement field defined as,

$$\mathbf{D}(\mathbf{r}, t) = \epsilon_0 \int dt' d\mathbf{r}' \epsilon(\mathbf{r} - \mathbf{r}', t - t') \mathbf{E}(\mathbf{r}', t'), \quad (2.2)$$

where ϵ_0 and $\epsilon(\mathbf{r} - \mathbf{r}', t - t')$ are the permittivity of free space and the dielectric function of the medium, respectively [4]. For linear, isotropic media without dispersion this

simplifies to

$$\mathbf{D}(\mathbf{r}, t) = \epsilon_0 \epsilon \mathbf{E}(\mathbf{r}, t). \quad (2.3)$$

The wave equation in Eq.2.1 can be rewritten in Fourier space as [4],

$$\mathbf{k}(\mathbf{k} \cdot \mathbf{E}) - k^2 \mathbf{E} = \epsilon(\mathbf{k}, \omega) \frac{\omega^2}{c^2} \mathbf{E}, \quad (2.4)$$

where \mathbf{k} is the wave vector, $c = \frac{1}{\sqrt{\mu_0 \epsilon_0}}$ and a harmonic time-dependence has been assumed [4]. This equation allows two types of wave solutions; transverse waves with $\mathbf{k} \cdot \mathbf{E} = 0$ and a dispersion relation

$$k^2 = \epsilon(\mathbf{k}, \omega) \frac{\omega^2}{c^2} \quad (2.5)$$

and longitudinal waves with $\mathbf{k} \parallel \mathbf{E}$, for which $\epsilon(\mathbf{k}, \omega) = 0$ [4]. For metals, the dielectric function can, for our purposes, be taken as a Drude model

$$\epsilon(\mathbf{k}, \omega) = \epsilon(\omega) = 1 - \frac{\omega_p^2}{\omega(\omega + i\gamma)}, \quad (2.6)$$

where ω_p is the plasma frequency of the metal and γ a damping term [4]. This dielectric function arises from the plasma model for metals, in which a gas of free and non-interacting electrons moves in the background of fixed ion cores, undergoing collisions with the cores at a frequency γ [4].

In the small damping limit $\gamma \ll \omega$ the dielectric function is

$$\epsilon(\omega) = 1 - \frac{\omega_p^2}{\omega^2}, \quad (2.7)$$

which has a zero at $\omega = \omega_p$. Thus at frequency ω_p the metal supports a longitudinal wave, which corresponds to a collective oscillation of all the electrons in the free electron gas. This oscillation is called a volume plasmon [4]. Since this is a longitudinal mode, it cannot be excited by transverse electromagnetic waves, but can through, e.g., particle impact [4]. In the long wavelength limit ($\mathbf{k} = 0$) this is the only longitudinal mode, other modes exist for finite \mathbf{k} [4].

Substituting Eq.2.7 into Eq.2.5

$$k^2 c^2 = \omega^2 - \omega_p^2, \quad (2.8)$$

we can see that transverse travelling wave solutions can also exist if $\omega > \omega_p$.

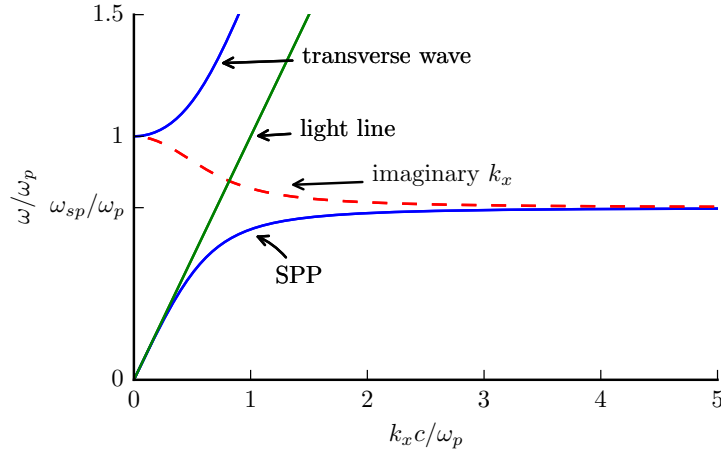


Figure 2.1: The dispersion relation (Eq.2.9) with $\epsilon_d = 1$ and ϵ_m as in Eq.2.7. The blue solid and red dashed lines are the real and imaginary part of k_x . For $\omega < \omega_{sp}$, the wave has the character of a SPP, but for $\omega > \omega_p$ the metal is transparent and the character of the plasmon changes to a propagating transverse electromagnetic wave. In between these regimes k_x is purely imaginary and no propagation is possible (red dashed line).

Surface plasmon polaritons — Contrary to volume plasmons, surface plasmon polaritons (SPPs) do not exist in the bulk of the metal, but rather at the interface between a dielectric and a metal. They are the result of the coupling between a photon and a volume plasmon [4]. As a very simple example, consider a flat interface between metal ($z < 0$) and dielectric ($z > 0$) half spaces with surface normal in the z -direction. The permittivity (ϵ_m (metal) and ϵ_d (dielectric)) in each space is assumed to be homogeneous. The wave equation Eq.2.1 permits two types of solutions; waves of transverse magnetic (TM) and transverse electric (TE) polarisation, but in our case TE waves could only satisfy the boundary conditions at the interface if they were exponentially growing in one of the half spaces and must thus be dismissed [4]. The TM solutions are of the form

$$H_y, E_x, E_z \propto \begin{cases} e^{ik_x x} e^{-k_d z} & z > 0 \\ e^{ik_x x} e^{k_m z} & z < 0 \end{cases}$$

and are thus confined to the interface in the z -direction [4]. Matching the solutions in the two half spaces yields the dispersion relation for SPPs propagating along the metal-dielectric interface [4]

$$k_x = \frac{\omega}{c} \sqrt{\frac{\epsilon_m \epsilon_d}{\epsilon_m + \epsilon_d}}. \quad (2.9)$$

The dispersion relation is shown in figure 2.1. It tells us that SPPs cannot be excited by far-field electromagnetic radiation since their \mathbf{k} -vector lies outside the light cone. One has to resort to special techniques such as prism or grating coupling to excite them [4].

In the example above the SPP would (for $\omega < \omega_{sp}$) propagate without attenuation along the x-direction. This is, of course, not true for real metals where the damping term γ leads to an exponentially decaying wave [4]. Nevertheless, the propagation length can be several micrometers in the optical regime while the confinement in the z-direction lies in the nanometer regime (often far below the wavelength of the incident light) [4]. In the limit of $k_x \rightarrow \infty$ the frequency approaches the surface plasma frequency ω_{sp} and the group velocity of the wave vanishes. This special case of a SPP is called surface plasmon [4].

Localised surface plasmon — As aforementioned, localised surface plasmons (LSPs) are non-propagating collective excitations of the electron gas in a metal, coupled to photons [4]. Contrary to SPPs or longitudinal volume plasmons, LSPs can be excited via far field radiation [4]. LSPs thus arise naturally in metal particles of finite size, in which an incident electromagnetic wave can excite a collective electron oscillation; they manifest themselves in the form of resonances in absorption and scattering spectra, and strong local field enhancements near the metal particle [4]. For particles much smaller than the wavelength of the incident light, the plasmon resonances can be calculated in the quasi-static limit [4], which boils down to solving for the eigenmodes of Laplace's equation in a particular geometry. In the simple example of a small metal sphere in a dielectric the eigenfunctions are given by (in spherical polar coordinates)

$$\psi_{l,m} = (Ar^l + Br^{-l-1})Y_l^m(\theta, \phi), \quad (2.10)$$

where Y_l^m are the spherical harmonics [8]. The resonance condition (sometimes called Fröhlich condition) to excite one of these LSPs is given by [8]

$$\epsilon_m + \frac{l+1}{l}\epsilon_d = 0, \quad (2.11)$$

where $\epsilon_{m,d}$ are the dielectric functions of the metal sphere and dielectric, respectively. For more complicated particle shapes or clusters of particles one often has to rely on numerical simulations as in [9, 10]. However, a number of semi-analytical methods such as the multiple scattering technique [8] or the plasmon hybridisation model [11–13] exist. The hybridisation model especially provides much better physical insight than simple numerical studies. The model explains the plasmonic spectra of more complicated particles by assuming they are made of simpler constituents. For example, a nanoshell can

be thought to be made of a metal sphere and a dielectric void inside a metal [11–13]. One proceeds by calculating the plasmon resonance frequencies and modes of sphere and void; the resonance frequencies and plasmon modes of the shell can then be explained in analogy to molecular orbit theory as bonding and anti-bonding formations of the sphere and void plasmons [11–13]. Another analytical method which has been recently applied to plasmonic systems is TO , which will be discussed in the next two sections.

In plasmonics the SPPs and LSPs play a much more prominent role than the volume plasmons and we will subsequently focus on applications realised by SPPs and LSPs. One of the most interesting features of SPPs is their sub-wavelength field confinement normal to the interface, while still allowing propagation lengths of several micrometers along the interface in the optical regime [4]. This makes them the ideal candidate for waveguiding and super-focusing of light.

Waveguiding has been demonstrated experimentally in several ways. For example, with planar elements guiding can be achieved using surface modulations [4], e.g. Bragg mirrors consisting of regular particle arrays have been demonstrated in [14]. Another approach using closely spaced nanoparticles (spacing \ll wavelength) has been demonstrated with sub-wavelength energy confinement and propagation lengths of about $0.5\mu\text{m}$ [15].

LSPs are also of great interest in applications. Two of their most useful features are an extremely strong field localisation in general and in particular near sharp points (of the order of $10^3 - 10^5$, [16]) of nanoparticles, and a resonance frequency which is strongly influenced by the particles' environment (as can be seen from Eq.2.11).

The strong field localisation, for example, leads to a heating of the nano-particle which can be exploited in biomedical applications such as thermal tumor therapy [17]. In this application, nanoparticles are injected into the tumor cells and then externally heated via near-infrared radiation, killing the tumor cells while leaving the surrounding tissue intact [17]. Another prominent application lies in surface enhanced Raman scattering. Here the strong field localisation leads to an enhancement in the usually very weak Raman scattering signal of single molecules [18]. In conjunction with this, the sensitivity of the plasmon resonance on the local environment allows for biosensing applications and molecule detection, possibly even in the single molecule limit [19].

These are just a select number of possible applications achievable with SPPs and LSPs and it seems very likely that plasmonics will play a part in the technologies of the future.

Physical quantity	Original frame	Transformed frame
Charge density	ρ	$\rho' = \rho / \det(\Lambda)$
Electric field Magnetic field	$\begin{pmatrix} \mathbf{E} \\ \mathbf{H} \end{pmatrix}$	$\begin{pmatrix} \mathbf{E}' \\ \mathbf{H}' \end{pmatrix} = \Lambda^{-1} \begin{pmatrix} \mathbf{E} \\ \mathbf{H} \end{pmatrix}$
Magnetic flux density Electric displacement Current density	$\begin{pmatrix} \mathbf{B} \\ \mathbf{D} \\ \mathbf{J} \end{pmatrix}$	$\begin{pmatrix} \mathbf{B}' \\ \mathbf{D}' \\ \mathbf{J}' \end{pmatrix} = \det(\Lambda)^{-1} \Lambda \begin{pmatrix} \mathbf{B} \\ \mathbf{D} \\ \mathbf{J} \end{pmatrix}$
Permittivity tensor Permeability tensor	$\begin{pmatrix} \epsilon \\ \mu \end{pmatrix}$	$\begin{pmatrix} \epsilon' \\ \mu' \end{pmatrix} = \det(\Lambda)^{-1} \Lambda \begin{pmatrix} \epsilon \\ \mu \end{pmatrix} \Lambda^T$

Table 2.1: Transformation rules of the various quantities in the Maxwell equations for a general coordinate transformation. Λ is the Jacobian of the coordinate transformation. Note that $\begin{pmatrix} \mathbf{E} \\ \mathbf{H} \end{pmatrix}$ is not to be understood as vector notation, but rather that \mathbf{E}, \mathbf{H} transform in the same way [22].

2.2 Transformation optics

TO is a relatively new analytical tool used to design electromagnetic systems with remarkable properties. Since, at the classical level, all electromagnetic interactions are described by Maxwell's equations, it is no surprise that TO draws its power from a particular insight into these equations: explicitly, that the equations are covariant with respect to a change of coordinate system, as long as all the quantities involved transform according to certain rules. The way this is usually interpreted in the context of TO, is that Maxwell's equations in any coordinate system [20]

$$\nabla \cdot \mathbf{D} = \rho \quad \nabla \times \mathbf{E} = -\frac{\partial \mathbf{B}}{\partial t} \quad (2.12)$$

$$\nabla \cdot \mathbf{B} = 0 \quad \nabla \times \mathbf{H} = \frac{\partial \mathbf{D}}{\partial t} + \mathbf{J} \quad (2.13)$$

with the constitutive relations

$$\mathbf{D} = \epsilon_0 \epsilon \mathbf{E} \quad \text{and} \quad \mathbf{B} = \mu_0 \mu \mathbf{H}, \quad (2.14)$$

can always be written in *Cartesian form*, provided that all quantities are redefined according to table 2.1 [21, 22].

This has been known for a long time [23], but little attention was paid to it until it was rediscovered in 1996 to aid numerical simulations of Maxwell's equations [24, 25].

Interest in this rocketed after two seminal papers in 2006 on the design of invisibility cloaks. The paper by Leonhardt took a slightly different approach based on Helmholtz' wave equation which is restricted to the far field [26, 27], whereas the other paper by Pendry et al. worked directly with Maxwell's equations, making their method applicable in both far and near field [27, 28]. Underlying Pendry's approach is the realisation that field lines are 'glued' to the coordinate grid, that is, they can be distorted at *will* by coordinate transformations [28]. In the context of a cloak this means that by opening a hole in the coordinate grid, one excludes all fields from that region. The key insight of TO is that such a coordinate grid can be realised by tailoring the material properties of the medium according to the formulas in table 2.1.

Invisibility cloaks have since been demonstrated experimentally in both microwave [29] and optical [30] regimes. The electromagnetic cloaking concept has subsequently been extended to the space-time regime, thus creating a temporal cloak for an event, rather than a spatial cloak [31, 32]. It has also found applications outside optics; acoustic cloaks have been theorised [33] and demonstrated experimentally both in water [34] and in air [35]

Recently, the TO framework has also been applied to SPPs [36, 37]. This method exploits the fact that most of the energy of the SPPs resides in the dielectric, thus rather than carefully tailoring the permittivity and permeability of dielectric and metal, they only need to modify the material parameters of the dielectric [36, 37]. Following this approach, plasmonic Eaton and Luneburg lenses have been demonstrated experimentally [38], which shows the potential for future applications in, e.g. plasmonic wave guiding.

2.2.1 Derivation of the transformation rules

Here we provide a non-rigorous derivation for some of the transformation rules in table 2.1. Suppose we are currently working in a non-Cartesian coordinate system (x^1, x^2, x^3) that is related to a Cartesian coordinate system (x^1, x^2, x^3) via the Jacobian [39, 40]

$$\Lambda_i^{i'} := \frac{\partial x^{i'}}{\partial x^i}. \quad (2.15)$$

The coordinates then transform as $x^{i'} = \Lambda_i^{i'} x^i$ and the components of the electric field transform as [21]

$$E_{i'} = \Lambda_i^{i'} E_i \quad (2.16)$$

$$E_i = \Lambda_i^{i'} E_{i'} \quad (2.17)$$

and equivalently for the H -field. Here and in the following we assume the *Einstein summation convention* [39, 40].

The transformation rule for the charge density is easy to understand, too. Charge is a conserved (scalar) quantity, but charge density has units of [charge per volume]. A volume element transforms according to [39]

$$d^3x^{i'} = \det(\mathbf{\Lambda})d^3x^i, \quad (2.18)$$

where $\det(\mathbf{\Lambda})$ is the determinant of the Jacobian in Eq.2.15. It thus follows that the charge density should transform as [22]

$$\rho' = \frac{\rho}{\det(\mathbf{\Lambda})}. \quad (2.19)$$

We can now derive the transformation rule for the permittivity tensor. We start from Gauss's law [20] in the non-Cartesian coordinate frame

$$\nabla \cdot (\boldsymbol{\epsilon}' \mathbf{E}') = \rho', \quad (2.20)$$

where $\boldsymbol{\epsilon}'$ is the permittivity tensor in that frame. Rewriting this in component form and using the general expression for the divergence operator [40] yields

$$\frac{1}{\sqrt{g'}} \partial_{i'} (\sqrt{g'} \epsilon^{i'j'} E_{j'}) = \rho', \quad (2.21)$$

where $\partial_{i'} = \frac{\partial}{\partial x^{i'}}$ and g' is the determinant of the metric of the non-Cartesian coordinate system, in our case this is equal to $(\det(\mathbf{\Lambda}))^2$ [40]. Thus

$$\partial_{i'} (\det(\mathbf{\Lambda}) \epsilon^{i'j'} E_{j'}) = \rho' \det(\mathbf{\Lambda}), \quad (2.22)$$

Substituting for $E^{j'}$, ρ' and using that $\partial_{i'} = \partial_i \Lambda_{i'}^i$ gives

$$\partial_i (\det(\mathbf{\Lambda}) \Lambda_{i'}^i \epsilon^{i'j'} \Lambda_{j'}^j E_j) = \rho. \quad (2.23)$$

This is Gauss's law in Cartesian coordinates, we can thus identify the transformation rule for the permittivity tensor

$$\epsilon^{ij} = \det(\mathbf{\Lambda}) \Lambda_{i'}^i \epsilon^{i'j'} \Lambda_{j'}^j. \quad (2.24)$$

Using that $\Lambda_k^{k'} \Lambda_{j'}^k = \delta_{j'}^{k'}$, this can be rewritten as

$$\frac{\Lambda_i^{i'} \epsilon^{ij} \Lambda_j^{j'}}{\det(\Lambda)} = \epsilon^{i'j'} \quad (2.25)$$

$$\frac{\Lambda \epsilon \Lambda^T}{\det(\Lambda)} = \epsilon', \quad (2.26)$$

which is given in table 2.1 and [21].

Transformation rules for other electromagnetic quantities can be obtained in a similar manner. One of particular importance to this thesis is the electrostatic potential ϕ defined via $\mathbf{E} = \nabla\phi$ [20]. Let us derive a transformation rule for the electrostatic potential. In the non-Cartesian coordinate frame it has to satisfy

$$\frac{1}{\det(\Lambda)} \partial_{i'} (\det(\Lambda) \epsilon^{i'j'} \partial_{j'} \phi') = \rho', \quad (2.27)$$

whereas in Cartesian coordinates it must satisfy

$$\partial_i \epsilon^{ij} \partial_j \phi = \rho. \quad (2.28)$$

Substituting for $\epsilon^{i'j'}$ from Eq.2.25 and for ρ' gives

$$\frac{1}{\det(\Lambda)} \partial_{i'} (\Lambda_i^{i'} \epsilon^{ij} \Lambda_j^{j'} \partial_{j'} \phi') = \frac{\rho}{\det(\Lambda)} \quad (2.29)$$

$$\partial_i \epsilon^{ij} \partial_j \phi' = \rho, \quad (2.30)$$

where we have used the transformation rule $\partial_{i'} \Lambda_i^{i'} = \partial_i$ and $\Lambda_j^{j'} \partial_{j'} = \partial_j$. Evidently, ϕ and ϕ' satisfy the same differential equation and we can thus conclude that the electrostatic potential is invariant under coordinate transformations [22] if the permittivity in its defining equation is redefined according to 2.1.

2.2.2 Conformal transformations

The remainder of this thesis will be mainly concerned with a special class of coordinate transformations called conformal transformations. Conformal transformations are restricted to the two-dimensional plane, i.e. we can think of them as transforming (x, y) but leaving the z -coordinates unchanged. Conformal transformations are analytic transformations that preserve the angle between coordinate lines and fulfill the Cauchy-Riemann relations [41]. This implies that for a conformal transformation

$$(x, y) \longrightarrow (x', y')$$

$$\frac{\partial x'}{\partial x} = \frac{\partial y'}{\partial y} \quad (2.31)$$

$$\frac{\partial x'}{\partial y} = -\frac{\partial y'}{\partial x} \quad (2.32)$$

hold. This has profound consequences for the transformation of the permittivity. Starting with an isotropic permittivity in the (x, y, z) –frame, we obtain the permittivity in the (x', y', z') –frame from Eq.2.25 as

$$\epsilon' = \frac{1}{\det(\Lambda)} \begin{pmatrix} \frac{\partial x'}{\partial x} & \frac{\partial x'}{\partial y} & 0 \\ \frac{\partial y'}{\partial x} & \frac{\partial y'}{\partial y} & 0 \\ 0 & 0 & 1 \end{pmatrix} \begin{pmatrix} \epsilon & 0 & 0 \\ 0 & \epsilon & 0 \\ 0 & 0 & \epsilon \end{pmatrix} \begin{pmatrix} \frac{\partial x'}{\partial x} & \frac{\partial y'}{\partial x} & 0 \\ \frac{\partial x'}{\partial y} & \frac{\partial y'}{\partial y} & 0 \\ 0 & 0 & 1 \end{pmatrix} \quad (2.33)$$

$$= \frac{\epsilon}{\det(\Lambda)} \begin{pmatrix} \left(\frac{\partial x'}{\partial x}\right)^2 + \left(\frac{\partial x'}{\partial y}\right)^2 & \frac{\partial x'}{\partial x} \frac{\partial y'}{\partial x} + \frac{\partial x'}{\partial y} \frac{\partial y'}{\partial y} & 0 \\ \frac{\partial y'}{\partial x} \frac{\partial x'}{\partial x} + \frac{\partial y'}{\partial y} \frac{\partial x'}{\partial y} & \left(\frac{\partial y'}{\partial x}\right)^2 + \left(\frac{\partial y'}{\partial y}\right)^2 & 0 \\ 0 & 0 & 1 \end{pmatrix}, \quad (2.34)$$

using the Cauchy-Riemann relations this can be rewritten as

$$\epsilon' = \frac{\epsilon}{\det(\Lambda)} \begin{pmatrix} \left(\frac{\partial x'}{\partial x}\right)^2 + \left(\frac{\partial x'}{\partial y}\right)^2 & 0 & 0 \\ 0 & \left(\frac{\partial x'}{\partial x}\right)^2 + \left(\frac{\partial x'}{\partial y}\right)^2 & 0 \\ 0 & 0 & 1 \end{pmatrix} \quad (2.35)$$

$$= \begin{pmatrix} \epsilon & 0 & 0 \\ 0 & \epsilon & 0 \\ 0 & 0 & \frac{\epsilon}{\det(\Lambda)} \end{pmatrix}, \quad (2.36)$$

where we used that $\det(\Lambda) = \left(\frac{\partial x'}{\partial x}\right)^2 + \left(\frac{\partial x'}{\partial y}\right)^2$. This means that the in-plane components of the permittivity tensor remain invariant under a conformal transformation [42]. What does change is the out-of-plane component, but that is of no concern in two-dimensional calculations.

Two other important properties of conformal maps are that the z –component of the H –field and the two-dimensional electrostatic potential [41] are invariant as well. The latter property will especially be used in this thesis. Both of them are easily proved using the transformation formulas in table 2.1.

2.3 Transformation optics in plasmonics

In the previous two sections, we introduced both Plasmonics and TO as two separate concepts. Here we will link the two and provide the setting for the remainder of this thesis.

Huidobro et al. and Liu et al. were among the first to apply TO techniques to plasmonic systems [36, 37]. However, they still used it as a design tool, i.e. their objective was to design the material parameters of a system such that it would fulfill a specific function. Here, we will introduce an altogether different approach, in which TO is used as an analytical tool to calculate properties of plasmonic systems. At the heart of this new method lie conformal transformations (CTs), which have been applied across different areas of physics to solve problems described by Laplace or Poisson equations [43, 44].

To study the electromagnetic properties of plasmonic nanoparticles in the electrostatic limit and calculate their localised surface plasmon modes, one generally has to solve Laplace's equation [4]

$$\nabla^2\phi(x, y) = 0, \quad (2.37)$$

for the system at hand. How difficult it is to solve this equation largely depends on the shape of the nanoparticle; it is straightforward for highly symmetric nanoparticles such as cylinders, planes, slabs, rings etc. [39]. However, it can become very difficult for less simple structures such as two touching cylinders, overlapping cylinders, crescents, gratings, etc. One way to determine the properties of a complex plasmonic system is to apply a conformal coordinate transformation, which maps the complex system to a simpler one. Since conformal transformations preserve the two-dimensional permittivity and permeability, as well as the electrostatic potential, solving Laplace's equation in the simple geometry automatically yields the solution in the more complex one. To the author's best knowledge, the first to apply this approach to systems of interest in plasmonics were McPhedran et al. [45]. They studied the transport properties of two touching cylinders by transforming it to a slab via an inversion [46]. However, this was before the term 'Plasmonics' was coined and the method has not received much attention until very recently [16, 47]. Aubry et al. realised that just as important as the transformation of the geometry of the nanoparticle is the transformation of the exciting electric field. We briefly outline their approach for the study of a nano crescent below.

Consider a metal slab at position $x = a$, thickness d and infinite extent in the y -direction. The transformation

$$\zeta' = \frac{g^2}{\zeta} \quad \text{with } g \in \mathbb{R}, \quad (2.38)$$

with $\zeta' = x' + iy'$ and $\zeta = x + iy$, transforms the metal slab into a crescent of inner diameter $D_{in} = g^2/a$ and outer diameter $D_{out} = g^2/(a + d)$ [16]. Additionally, a dipole at the origin in the slab frame with potential

$$\phi_s(x, y) = -\frac{1}{2\pi\epsilon_0} \frac{\Delta_x x + \Delta_y y}{x^2 + y^2} = -\frac{1}{2\pi\epsilon_0} \text{Re}\left(\frac{\Delta_\zeta}{\zeta}\right), \quad (2.39)$$

with $\Delta_\zeta = \Delta_x + i\Delta_y$ transforms to

$$\phi_s(x', y') = -\frac{1}{2\pi\epsilon_0 g^2} \text{Re}(\Delta_\zeta \zeta'), \quad (2.40)$$

which is the potential of a constant electric field [16]. The problem of a crescent in a constant electric field is thus equivalent to that of a slab in the vicinity of a dipole, which is far easier to solve, as all calculations can be done in the much simpler slab geometry. A summary of the transformation is shown in figure 2.2.

Aubry et al. used this approach to demonstrate that the crescent structure efficiently ‘harvests’ light across a broadband spectrum and concentrates it at its tip. Similar works by the same group have applied this approach to treat the problem of two kissing cylinders [16], two cylinders separated by a small gap [48] and also two overlapping cylinders [49]. All studies showed a relatively broadband absorption spectrum and strong field localisation at the singularities of the structures [50]. The effect of bluntness on

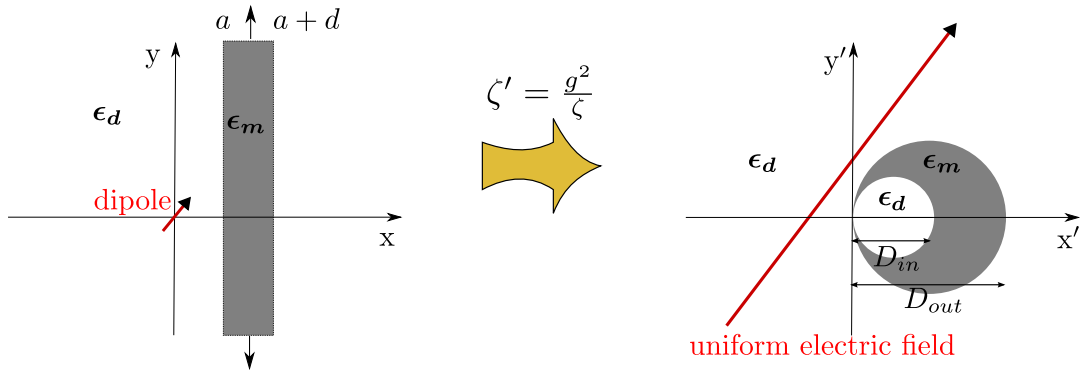


Figure 2.2: A dipole and a slab transform to a crescent in a uniform field, as demonstrated in [16].

the singular features of, e.g. the tip of the crescent, has also been successfully studied using this approach [51]. Broadband absorption and strong field localisation have been shown to be fairly robust to edge bluntness [51]. Radiative effects can also be included by introducing an effective polarisability [52]; this extends the validity of this approach beyond the quasi-static limit [53].

Related studies used the CT approach to calculate the electromagnetic contribution to surface enhanced raman scattering on rough surfaces [54], or to demonstrate the existence of multiple Fano resonances in a non-concentric metal annulus [55].

It can be seen that rather than using TO to design special materials, this approach uses it as an analytical tool to study systems which are hard to tackle analytically with conventional methods. Following the success of the two-dimensional CT approach, Fernandez-Dominguez et al. applied conventional TO in three dimensions in an analogous manner, to study the problem of two touching spheres in the quasi-static limit [56]. A subsequent study extended this method to two spheres separated by a small gap and calculated the van der Waals forces between them [57].

The most recent application of TO as an analytical tool in plasmonics has been to study non-local effects for nearly touching nanoparticles [58]. Luo et al. subsequently refined this technique and introduced a new model to describe non-locality in [59]. Their TO approach paired with the new model for non-locality does not only provide an elegant analytical description of the problem, but also vastly reduces computation times compared to existing methods.

To conclude this section, TO optics is not only a powerful design tool for materials with tailored functions, but is as powerful as an analytic tool in the study of interacting and non-interacting plasmonic systems. In this field it provides one of the few analytic approaches to solve problems, thus providing better physical insight into the physics at hand than numerical schemes. Even if closed form solutions cannot be obtained, TO can tremendously reduce computation times compared to purely numerical methods. It is therefore expected that the use of TO to study plasmonic systems will increase in the years to come.

References [60], [61] and [27] provide excellent reviews on this particular use of TO.

Chapter 3

Hidden symmetries in plasmonic systems I: Ellipses and spheroids

As mentioned in the introduction, symmetries play an important role in many branches of physics and often lead to deep physical insight. Yet, the role of symmetry has seldom been discussed in plasmonics. Here, we demonstrate how TO can be used to reveal hidden symmetries in plasmonic systems. We give two examples: A two-dimensional ellipse, which can be transformed to an annulus and a three-dimensional spheroid, which can be transformed to a spherical shell. All the results presented in the following are based on a paper by the author and colleagues and have been published in [62].

3.1 2-D elliptic cylinder

We are interested in the optical response of an infinitely long elliptic metal cylinder immersed in a dielectric. If we assume the cylinder is directed along the z' -direction, the translational invariance of the problem along z' allows us to treat the problem in two dimensions. We restrict ourselves to the quasi-static limit for now, but will relax this condition later on. In the quasi-static limit we thus face a boundary value problem for Laplace's equation, which can and has been solved by means of elliptic coordinates [63]. Yet, we suggest a different route based on TO that allows us to obtain deeper and somewhat surprising physical insight [62].

3.1.1 Transformation of the geometry and sources

Following the presentation in [62], we solve the problem in the complex plane $\zeta' = x' + iy'$. The equation of an ellipse reads

$$\frac{x'^2}{a'^2} + \frac{y'^2}{b'^2} = 1, \quad (3.1)$$

with semi-major axis $a' = c' \cosh(u_0)$ and semi-minor axis $b' = c' \sinh(u_0)$. Here c' is an arbitrary scale parameter and u_0 determines the eccentricity of the ellipse. Upon application of a Joukowski transformation [43]

$$\zeta' = \frac{c'}{2} \left(\zeta + \frac{1}{\zeta} \right), \quad (3.2)$$

Eq.3.1 transforms into the equation of an annulus with inner radius $R_0 = a' - b' = e^{-u'_0}$ and outer radius $R_1 = a' + b' = e^{u'_0}$ [62]. The real and imaginary parts of ζ', ζ transform according to [43, 62]

$$x' = \frac{c'}{2} x \left(1 + \frac{1}{x^2 + y^2} \right) \quad (3.3)$$

$$y' = \frac{c'}{2} y \left(1 - \frac{1}{x^2 + y^2} \right). \quad (3.4)$$

The transition from a simply connected structure (ellipse) to a doubly connected one (annulus) is due to the multi-valued nature of the inverse of Eq.3.2 [43]. The conformality of the Joukowski transformation above ensures that the in-plane permittivity of the metal ellipse ϵ_m and the surrounding dielectric ϵ_d is preserved [43, 60]. It also means that $\phi(x, y) = \phi'(x', y')$, i.e. if ϕ is a solution to the Laplace equation in the annulus geometry, ϕ' is the corresponding solution in the elliptic geometry [43, 62], as has been discussed in section 2.3. Hence, solutions to Laplace's equation in the elliptic geometry can be found by solving the corresponding problem in the annulus geometry. Due to the rotational symmetry of the annulus, this is a straightforward task and can be done using polar coordinates. TO can hence be used to reveal 'hidden' symmetries in plasmonics, which do not only facilitate analytical treatments, but also give deeper insight into the physics at work [62].

Once the eigenmodes and -values of a system have been calculated (i.e. Laplace's equation has been solved in a particular geometry), the optical response of the system at hand can be calculated by expanding the source potentials in terms of the system's

eigenmodes and using the boundary conditions at the dielectric/metal interface. That is, demanding continuity of the tangential component of the electric field $\mathbf{E} = \nabla\phi$ and of the normal component of the electric displacement field $\mathbf{D} = \epsilon\mathbf{E}$ [20]. To use the TO approach, it is thus of paramount importance that the transformation of the sources is also considered [16, 47], i.e. a constant electric field in the elliptic geometry does not correspond to a constant electric field in the annulus geometry.

Here, we consider the transformation of a constant electric field, which is the quasi-static equivalent of a plane wave illumination. The potential of a constant electric field can be taken as

$$\phi'_s = -E_{x'}x' - E_{y'}y', \quad (3.5)$$

substituting from Eq.3.2 gives [62]

$$\phi_s(x, y) = -\frac{c'}{2}\mathbf{E}'_0 \cdot \mathbf{r} + \frac{\mathbf{p} \cdot \mathbf{r}}{2\pi\epsilon_0 r^2}, \quad (3.6)$$

where

$$\mathbf{E}'_0 = \begin{bmatrix} E_{x'} \\ E_{y'} \end{bmatrix}, \quad \mathbf{r} = \begin{bmatrix} x \\ y \end{bmatrix}, \quad \mathbf{p} = \pi\epsilon_0 c' \begin{bmatrix} E_{x'} \\ -E_{y'} \end{bmatrix}. \quad (3.7)$$

A constant electric field in the elliptic geometry gives rise to a constant electric field plus the field of a line dipole in the annulus geometry [62].

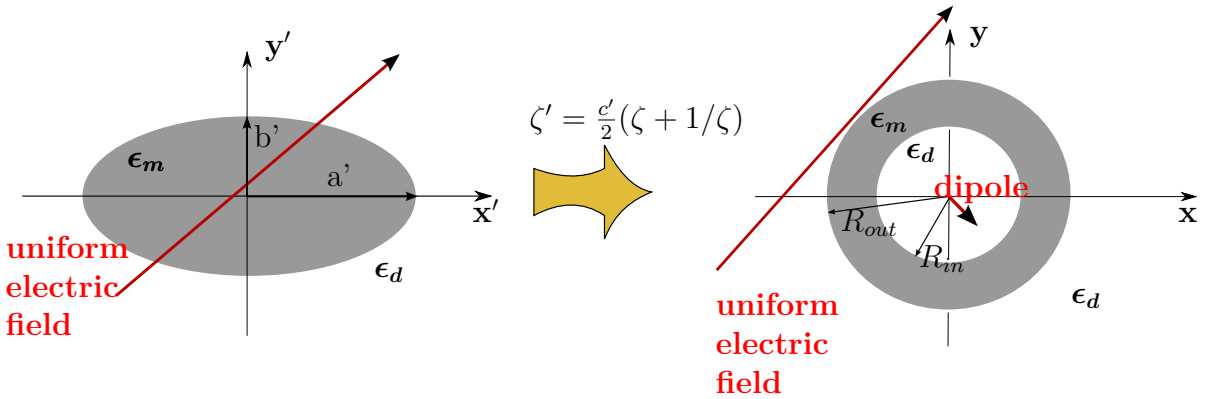


Figure 3.1: Schematic illustration of the transformation between an ellipse and an annulus. The transformations of the source are also shown. A constant electric field (red) transforms to a constant electric field (red) plus a dipole (red). Modified from [62].

The transformation of the geometry and the source is summarised in figure 3.1. In the following, we will focus on the case of a constant electric field in the elliptic geometry.

3.1.2 Plasmon mode structure: 2-D ellipse

As aforementioned the plasmon modes (more precisely LSP modes) of the ellipse can be calculated by solving Laplace's equation in the annulus geometry, since they are the eigenmodes of this system. The resonance condition for one of the LSP modes is encoded into the scattering coefficient of that mode and only depends on the permittivity of the ellipse $\epsilon_m(\omega)$ and the dielectric ϵ_d [4].

For the ellipse this condition is split into even (with respect to reflections about the x' -axis)

$$\tanh(mu_0) = -\frac{\epsilon_d}{\epsilon_m} \quad (3.8)$$

and odd

$$\tanh(mu_0) = -\frac{\epsilon_m}{\epsilon_d} \quad (3.9)$$

modes, with a Drude model for the permittivity $\epsilon_m = 1 - \frac{\omega_p}{\omega(\omega+i\gamma)}$ [62], see appendix A.1. Note that $\tanh(u_0) = b'/a'$ and that ϵ_m is a function of frequency. Thus the resonance condition is crucially dependent on the eccentricity of the ellipse and frequency dependence of its permittivity. The resonance frequency is shown in figure 3.2 for the first five even and odd modes as a function of the ratio of semi-minor to semi-major axis of the ellipse.

Which of these LSP modes can be excited ultimately depends on the type of source. For example, a plane wave only couples to the lowest order (dipolar) modes, whereas a dipole in the near field of the ellipse is able to excite *all* higher order modes as well [62].

The dependence of the resonance frequencies on the eccentricity of the ellipse can be understood in several ways. In the simplest case $b'/a' = 1$, the ellipse becomes a cylinder and all the modes are degenerate at the surface plasma frequency [52]. However, when the cylinder is deformed and the rotational symmetry broken, the modes split. That they split precisely into even and odd modes is a consequence of the fact that even though rotational symmetry has been lost, the ellipse still possesses two mirror planes [62]. That the odd modes shift two higher and the even modes to lower frequencies is easily understood from the potential distribution (figure 3.3). For decreasing $b'/a' \rightarrow 0$ (i.e. thin strip) the separation between the surface charges decreases, thus the energy of the even modes (same charges at top and bottom) decreases while it increases for odd modes (opposite charges at top and bottom), since $Re(\epsilon_m) < 0$ has to be fulfilled [4, 62].

Another way to understand the mode splitting, thereby gaining additional physical insight, is in terms of the potential distribution in the transformed frame (figure 3.3).

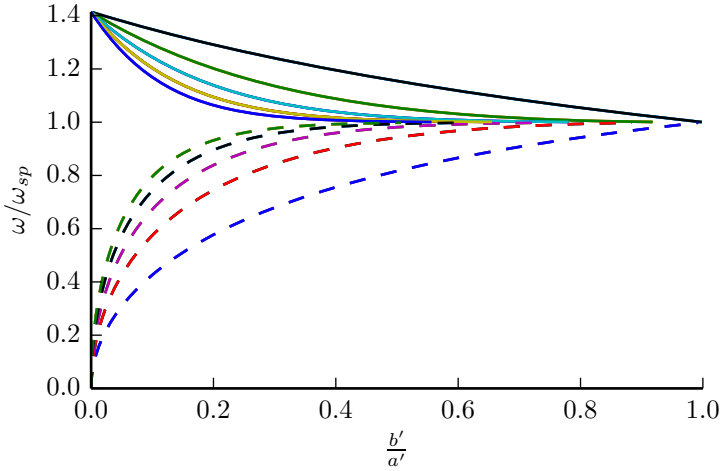


Figure 3.2: Resonance frequencies versus the ratio of semi-minor to semi-major axis. Shown are in descending order the first five odd modes (solid lines) and in ascending order the first five even modes (dashed lines). $\omega_p = 8eV$ and $\gamma = 0.032eV$. Modified from [62].

Since the two geometries are related by a conformal transformation, the potential is the same for each mode in the two geometries. The modes for $m = 1, 3$ are shown in figure 3.3. In the annulus geometry, LSPs are excited on both the outer and inner surface of the annulus. The inner and outer LSPs do, of course, interact and hybridise, which leads to the splitting into odd and even modes. This can be very well understood in terms of the plasmon hybridisation model introduced in section 2.1 [11, 12].

We can conclude that there is a link between symmetry breaking in the elliptic geometry and plasmon hybridisation in the annulus geometry [62]. More such transformation pairs are certain to exist and the connection between symmetry breaking and plasmon hybridisation is likely to be found in transformations with multi-valued inverses.

3.1.3 Absorption and scattering: 2-D ellipse

To determine which modes can be excited by a particular source one can calculate the absorption and scattering spectra of the ellipse. We already mentioned that a plane wave illumination, i.e. a constant electric field will only couple to the two dipolar modes of the ellipse; here we show why. The scattering and absorption cross section of the ellipse can be calculated from its polarisability, the polarisability is itself related to the scattered potential in the far field [64]. Solving the annulus problem and rewriting the scattered potential outside the ellipse in elliptic coordinates $x' = c' \cosh(u') \cos(v')$,

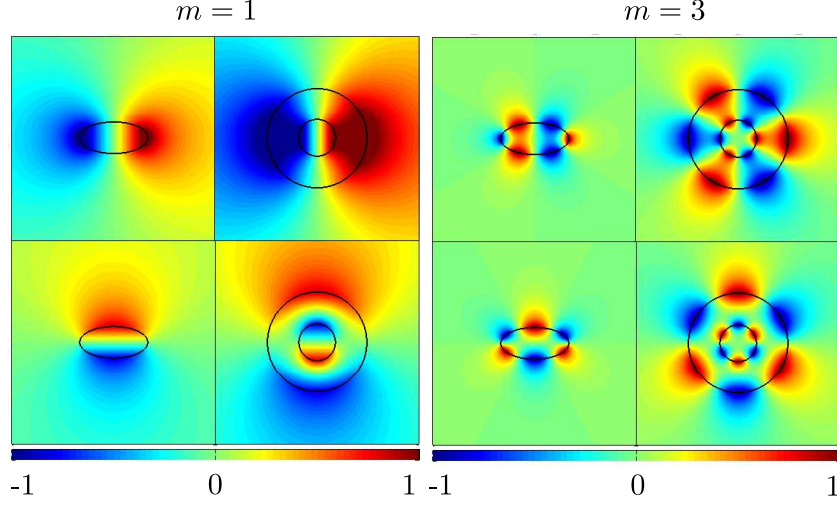


Figure 3.3: Imaginary part of the electrostatic potential for $m=1$ and $m=3$. Shown are the distributions in the annulus geometry and the elliptic geometry, both for the even (top) and odd (bottom) mode. We assumed a Drude type permittivity (Eq.2.6) ϵ_m with $\omega_p = 8eV$ and $\gamma = 0.032eV$. Reprinted with permission from [62]. Copyright 2014 by the American Physical Society.

$y' = c' \sinh(u') \sin(v')$ one obtains (in the elliptic geometry)

$$\phi'_{sca} = -\frac{c'}{2} E_{x'} \gamma_{2d}^x e^{-u'} \cos(v') - \frac{c'}{2} E_{y'} \gamma_{2d}^y e^{-u'} \sin(v'). \quad (3.10)$$

In the far field this can be recast as

$$\phi'_{sca,2d} = -\frac{1}{2} \left(E_{x'} \frac{x'}{x'^2 + y'^2} \gamma_{2d}^x + E_{y'} \frac{y'}{x'^2 + y'^2} \gamma_{2d}^y \right) \quad (3.11)$$

$$= \frac{1}{2\pi\epsilon_0} \frac{\mathbf{P}'_{2d} \cdot \mathbf{r}'}{r'^2}, \quad (3.12)$$

with

$$\mathbf{P}'_{2d} = -\pi\epsilon_0 \begin{pmatrix} \gamma_{2d}^x & 0 \\ 0 & \gamma_{2d}^y \end{pmatrix} \begin{pmatrix} E_{x'} \\ E_{y'} \end{pmatrix}$$

as dipole moment of the ellipse [62]. This leads to a polarisability

$$\alpha'_{2d} = -\pi\epsilon_0 \begin{pmatrix} \gamma_{2d}^x & 0 \\ 0 & \gamma_{2d}^y \end{pmatrix} = \begin{pmatrix} \alpha_{2d}^x & 0 \\ 0 & \alpha_{2d}^y \end{pmatrix}, \quad (3.13)$$

with

$$\gamma_{2d}^x = \frac{(\epsilon'_d - \epsilon'_m)e^{u_0} \cosh(u_0) \sinh(u_0)}{\epsilon'_m \sinh(u_0) + \epsilon'_d \cosh(u_0)} \quad (3.14)$$

$$\gamma_{2d}^y = \frac{(\epsilon'_d - \epsilon'_m)e^{u_0} \cosh(u_0) \sinh(u_0)}{\epsilon'_m \cosh(u_0) + \epsilon'_d \sinh(u_0)}. \quad (3.15)$$

From this it is clear that a plane wave only couples to dipolar modes, since according to Eq.3.8 and Eq.3.9 higher order modes would require the presence of $\cosh(mu_0)$, $\sinh(mu_0)$ and e^{mu_0} in the polarisability [62]. As we write in [62]:

‘This is a surprising result as at first sight the ellipse does not have enough symmetry to select only these two modes for excitation. The hidden symmetry of the system reveals its hand at this point. Externally incident radiation can couple to the higher order modes but only if the ellipse is large enough to invalidate the quasi-static approximation and so to see the higher multipole terms in the field.’

The treatment thus far has been strictly limited to the quasi-static limit, however, we can extend the range of validity of this approach by taking radiation damping into account. This can be done by defining an effective polarisability as in [52, 53] such that

$$\alpha_{2d}^{eff,x'/y'} = \frac{\alpha_{2d}^{x'/y'}}{1 - i\frac{k^2}{8}\alpha_{2d}^{x'/y'}}. \quad (3.16)$$

Such a treatment extends the validity of our approach from a particle size of a few nanometers to a few tens of nanometers and sometimes more [53]. However, it does not invalidate the selection rule because it only takes into account the radiative reaction of the ellipse, but not higher order terms in the incident radiation.

The extinction and scattering cross-sections are related to the polarisability via $\sigma_{ext}^{x'/y'} = k\text{Im}(\alpha_{2d}^{eff,x'/y'})$ and $\sigma_{sca}^{x'/y'} = \frac{k^3}{8}|\alpha_{2d}^{eff,x'/y'}|^2$ [53, 64]. The absorption cross-section is simply the difference between the two $\sigma_{abs}^{x'/y'} = \sigma_{ext}^{x'/y'} - \sigma_{sca}^{x'/y'}$ [64]. The total cross-sections are then the sum of the cross-sections for x' and y' as long as the incident field satisfies $E'_x = E'_y$ [62].

Figure 3.4 shows the scattering and absorption cross-section for a metal ellipse in vacuum under plane wave illumination. We used permittivity data for silver from Johnson and Christy [65]. The cross-sections have been normalised by the physical cross-section a' . We compare our analytical solutions to COMSOL simulations. For semi-major a' equal to five or ten nanometers, the agreement is excellent and the two peaks in the

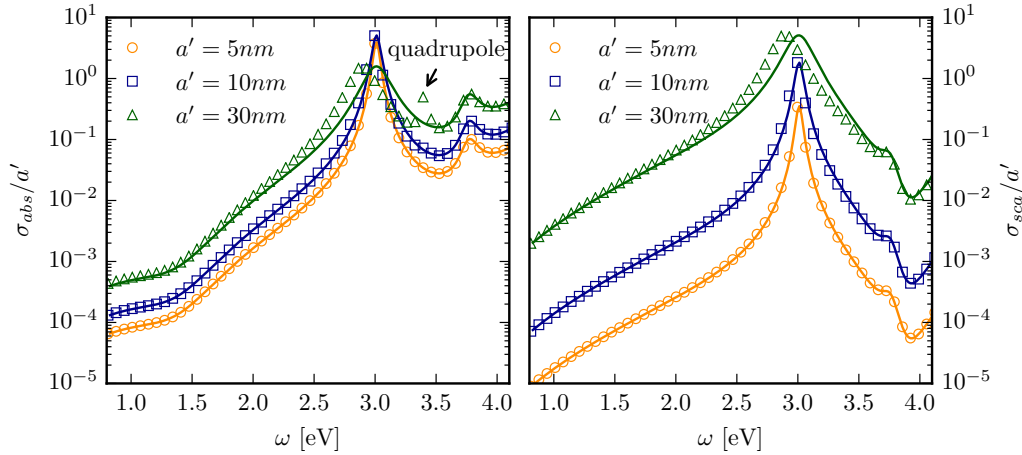


Figure 3.4: Absorption (left) and scattering (right) cross-section normalised by the physical cross-section a' . Our analytical model (solid lines) is compared to COMSOL simulations (markers) for different values of the semi-major axis a' . The ratio between semi-major to semi-minor axis has been kept constant at $b' = 0.2a'$. We used experimental permittivity data for Silver from Johnson and Christy [65] for ϵ_m and set $\epsilon_d = 1$. This data has also been published in [62].

absorption and scattering cross-section correspond to the two dipolar modes. This confirms the selection rule predicted above. For $a' = 30nm$ the agreement is still good, but there is another peak arising in the absorption spectrum at $\approx 3.4eV$, which corresponds to a quadrupole mode. This is the result of the breakdown of the quasi-static approximation for the incoming plane wave, as the ellipse is now big enough to ‘see’ the higher order modes of the incoming radiation, which then couple to the ellipse’s quadrupole mode. The scattering cross-section is still dominated by the two dipole modes, though. Additionally, the simulations for both, absorption and scattering cross-section, show a slight red-shift compared to the analytical result, indicating the onset of retardation effects [64].

3.2 3-D spheroid

In this section, we present an extension of the two-dimensional case into three dimensions. That is we study oblate and prolate spheroids by transforming them to spherical shells. The analytical calculations are as presented in [66] and have been done by Prof. Yu Luo, but we include them here for completeness and to demonstrate that the ‘hid-

den' symmetries can carry over to three dimensions, too. The numerical simulations have been done by the author.

3.2.1 Transformation of the geometry and sources

A straightforward extension of the transformation in Eq.3.2 to three dimensions allows us to transform a spheroid into a spherical shell. The transformation $\rho' = \frac{1}{2}(r - \frac{1}{r})\sin(\theta)$, $z' = \frac{1}{2}(r + \frac{1}{r})\cos(\theta)$ and $\varphi' = \varphi$, where r, θ and ϕ are spherical polar coordinates, takes a prolate spheroid to a spherical shell [66]. For an oblate spheroid one must use $\rho' = \frac{1}{2}(r + \frac{1}{r})\sin(\theta)$, $z' = \frac{1}{2}(r - \frac{1}{r})\cos(\theta)$ and $\varphi' = \varphi$ [62]. Contrary to the 2-D case, the permittivity and permeability are not preserved by this transformation, but transform as described in table 2.1. Since we work in the quasi-static limit, we will focus on the transformation of the permittivity, which is given in component form by

$$\epsilon_{r,d/m}^p = \epsilon_{\theta,d/m}^p = \frac{1-r^2}{2r^2}\epsilon'_{d/m}, \quad (3.17)$$

$$\epsilon_{\varphi,d/m}^p = \frac{1+r^4-2r^2\cos(2\theta)}{2r^2(1-r^2)}\epsilon'_{d/m}, \quad (3.18)$$

for the prolate transformation and by

$$\epsilon_{r,d/m}^o = \epsilon_{\theta,d/m}^o = -\frac{1+r^2}{2r^2}\epsilon'_{d/m}, \quad (3.19)$$

$$\epsilon_{\varphi,d/m}^o = -\frac{1+r^4+2r^2\cos(2\theta)}{2r^2(1+r^2)}\epsilon'_{d/m}, \quad (3.20)$$

in the oblate case. The source potential transforms in the same way as in the two-dimensional case under these two transformations. To find the eigenmodes of the spheroids in the quasi-static limit one then has to solve [20]

$$\nabla \cdot (\epsilon^{p/o} \cdot \nabla \Phi) = 0, \quad (3.21)$$

with the only non-zero components of the permittivity tensor $\epsilon^{p/o}$ given in Eqs.3.17-3.20. The space dependence of the permittivity makes the spherical shell an inhomogeneous system, which makes it harder to solve than a simple spherical shell with a constant permittivity. Fortunately, the special form of the permittivity tensor in Eq.3.17-3.20 still allows for a solution in terms of spherical harmonics. Below, we provide a derivation of the electrostatic potential satisfying Eq.3.21 for the oblate spheroid. We follow the derivation in [62] exactly.

Expanding and rearranging Eq.3.21 leads to

$$\frac{1}{r^2} \frac{\partial}{\partial r} (1-r^2) \frac{\partial}{\partial r} \Phi + \frac{1-r^2}{r^4 \sin \theta} \frac{\partial}{\partial \theta} (\sin \theta) \frac{\partial}{\partial \theta} \Phi + \left[\frac{1-r^2}{r^4 \sin^2 \theta} + \frac{4}{r^2 (1-r^2)} \right] \frac{\partial^2}{\partial \varphi^2} \Phi = 0.$$

An ansatz of the form $\Phi = Z(r)\Xi(\theta)\phi(\varphi)$ will, after using some trigonometric identities and rearranging give three separated equations

$$\frac{r^2}{1-r^2} \frac{d}{dr} (1-r^2) \frac{dZ}{dr} - \left[l(l+1) + \frac{4m^2 r^2}{(1-r^2)^2} \right] Z = 0$$

$$\frac{1}{\sin \theta} \frac{d}{d\theta} \sin \theta \frac{d\Xi}{d\theta} + \left[l(l+1) - \frac{m^2}{\sin^2 \theta} \right] \Xi = 0$$

$$\frac{d^2 \Phi}{d\varphi^2} = -m^2 \phi.$$

The radial equation can, after a change of variable $\psi = \frac{1}{2}(r + 1/r)$ be recast into the form of the associated Legendre differential equation [20]. The general solution can thus be written down as

$$Z(r) = A_1 P_l^m \left[\frac{1}{2} \left(r + \frac{1}{r} \right) \right] + A_2 Q_l^m \left[\frac{1}{2} \left(r + \frac{1}{r} \right) \right], \quad (3.22)$$

where P_l^m and Q_l^m are the associated Legendre polynomials of the first and second kind, respectively [20]. The angular differential equations above are simply the defining equations of the spherical harmonics Y_l^m [20]. Hence, the eigenmodes of the system are products of the form

$$\Phi_l^m = \left(A_1 P_l^m \left[\frac{1}{2} \left(r + \frac{1}{r} \right) \right] + A_2 Q_l^m \left[\frac{1}{2} \left(r + \frac{1}{r} \right) \right] \right) Y_l^m(\theta, \phi). \quad (3.23)$$

This is quite a surprising result. It means that the angular dependence of the eigenmodes of the spheroid is still given in terms of spherical harmonics and unique angular momentum numbers m, l . Thus, in contrast to a previous study [57], good angular momentum numbers in the spherical shell frame carry over as good angular momentum numbers in the spheroidal frame, i.e. there is no mixing of modes under the transformation. Again, this is a consequence of the spheroidal system's hidden symmetry, which has been revealed by our transformation [62]. As an aside, the space dependence of the permittivity only manifests itself in the radial part of the solution in Eq.3.23 which depends on both angular momentum numbers m, l (for a spherical shell it only depends on l) [62].

The most general solution for the potential in the prolate spheroidal geometry is a superposition of all the fundamental modes. Yet, along the axis of the spheroid ($\rho' = 0 \rightarrow r = 1$) the potential must remain finite, since the associated Legendre polynomials of the second kind diverge at these points, the potential inside the spheroid must thus be of the form

$$\Phi^{\text{in}} = \sum_{l=1}^{\infty} \sum_{m=-l}^l a_{l,m}^{\text{in}} P_l^m \left[\frac{1}{2} \left(r + \frac{1}{r} \right) \right] Y_l^m(\theta, \varphi).$$

Outside the spheroid the scattered part of the potential can be obtained as

$$\Phi^{\text{sca}} = \sum_{l=1}^{\infty} \sum_{m=-l}^l a_{l,m}^{\text{sca}} \left\{ i \frac{\pi}{2} P_l^m \left[\frac{1}{2} \left(r + \frac{1}{r} \right) \right] + Q_l^m \left[\frac{1}{2} \left(r + \frac{1}{r} \right) \right] \right\} Y_l^m(\theta, \varphi),$$

since the electric field must vanish at infinity. The remaining unknown coefficients are then determined by demanding continuity of the tangential component of the electric field and the normal component of the electric displacement field at the spheroid/dielectric interface [20]. This leads to the expansion coefficients

$$a_{l,m}^{\text{sca}} = \frac{(\varepsilon - 1) P_l^m(\tau) P_l^{m'}(\tau)}{P_l^m(\tau) G_l^{m'}(\tau) - \varepsilon G_l^m(\tau) P_l^{m'}(\tau)} a_{l,m}^{\text{S}}$$

$$a_{l,m}^{\text{in}} = \frac{P_l^m(\tau) G_l^{m'}(\tau) - G_l^m(\tau) P_l^{m'}(\tau)}{P_l^m(\tau) G_l^{m'}(\tau) - \varepsilon G_l^m(\tau) P_l^{m'}(\tau)} a_{l,m}^{\text{S}}$$

with $\tau = (R^{\text{out}} + 1/R^{\text{out}})/2$ and $G_l^m(\cdot) = i\pi P_l^m(\cdot)/2 + Q_l^m(\cdot)$ [62]. $a_{l,m}^{\text{S}}$ are the expansion coefficients for the source potential and are thus obtained once a source is specified. Irrespective of the source coefficients, the resonance condition for the excitation of LSP modes is set by the zeros of the denominator of the expansion coefficients $a_{l,m}^{\text{in}}$ and $a_{l,m}^{\text{sca}}$. It can be easily obtained for any order mode, which has not been possible previously [62], due to high computational demands of other methods [67–69]. An analogous calculation can be carried out for oblate spheroids.

Figure 3.5 shows the shift of the LSP resonance versus the ratio of semi-minor to semi-major axis b'/a' . To understand their behaviour we start with the simplest case again. If $b'/a' = 1$ the spheroids turn into spheres such that modes with the same quantum number l but different m are degenerate, which is expected [20]. For oblate spheroids the behaviour of the modes is determined by the distribution of the surface charges in a similar way to the two-dimensional case. When $l - m$ is an even number charges on the ‘top’ and ‘bottom’ of the oblate spheroid have the same sign, thus decreasing the distance between them (i.e. decreasing b'/a') reduces the energy of the configuration

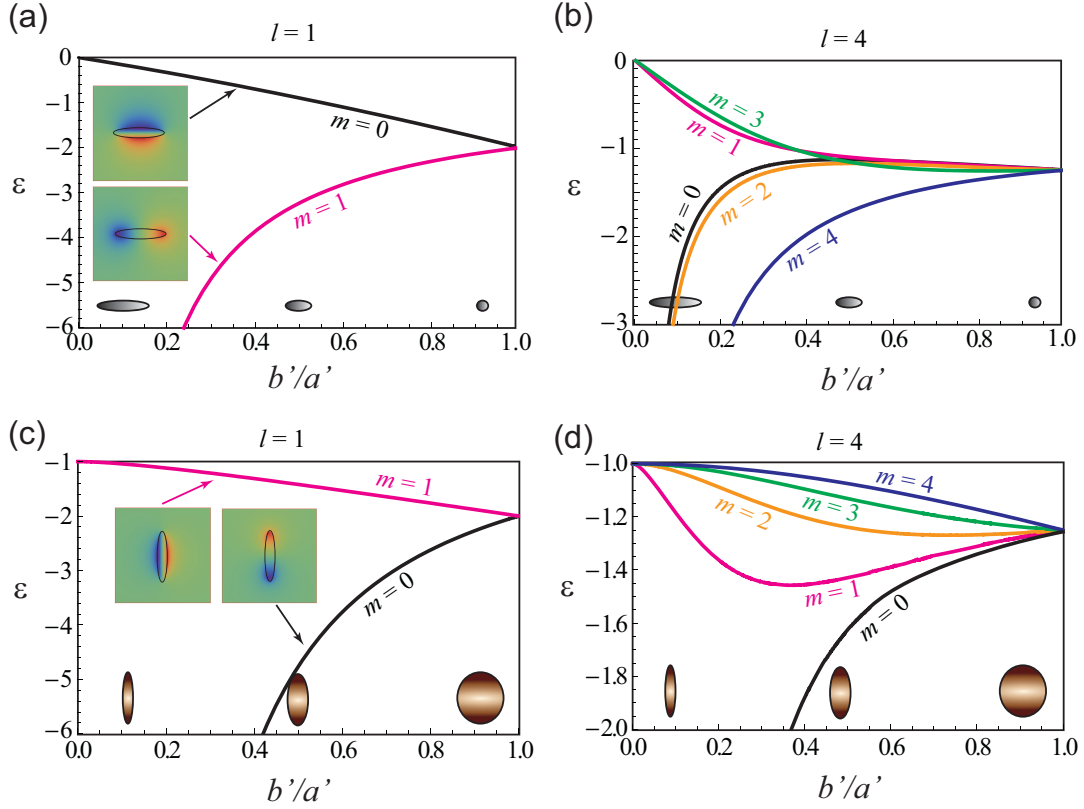


Figure 3.5: Shift of the LSP resonances for oblate (top) and prolate (bottom) spheroids. Shown are the modes for $l = 1$ and $l = 4$. The insets show the potential distribution for their respective modes. Reprinted with permission from [62]. Copyright 2014 by the American Physical Society.

and the modes shift to zero frequency ($\epsilon \rightarrow -\infty$) [62]. The opposite is true for modes with $l - m$ being odd and the modes shift to the plasma frequency ω_p ($\epsilon = 0$) [62].

This behaviour cannot be observed for the prolate spheroid, where only modes with $m = 0$ shift to zero frequency, whereas all the other modes shift to the surface plasma frequency ($\epsilon = -1$). This is because, for $m \neq 0$, the prolate spheroid effectively turns into an infinitely long cylinder when $b'/a' \rightarrow 0$, for which all modes are degenerate at the surface plasma frequency [52, 62].

Degeneracy of LSP modes usually has some underlying symmetry at its roots. When this symmetry is broken the degeneracy is lifted and the modes split. This has been observed both for a two-dimensional ellipse and now for three-dimensional spheroids. Both systems also have in common that the splitting of the modes can also be understood in terms of plasmon hybridisation in the transformed frame, thus hinting at a connection between symmetry breaking and plasmon hybridisation. But, it should be mentioned that the modes obtained in the spherical shell geometry are not only the result of plasmon

hybridisation, but also due to the space dependence of the permittivity [62]. As such their spectrum is a little more complicated, but also richer than that of simple core-shell structures [70].

3.2.2 Absorption and scattering: 3-D spheroid

The absorption and scattering spectrum can be calculated from the polarisability, as in the two-dimensional case. Here we are interested in the absorption/scattering spectra for a prolate spheroid under plane wave illumination, the oblate case is derived in an analogous manner. In the quasi-static limit the source potential reads [62]

$$\Phi_s = -E_x x' - E_z z'. \quad (3.24)$$

As an expansion of associated Legendre polynomials this leads to the source coefficients

$$a_{1,1}^s = iE_x \quad a_{1,0}^s = -E_z, \quad (3.25)$$

with all higher order coefficients being zero. Hence, the only non-zero scattering coefficients will be $a_{1,1}^{sca}$ and $a_{1,0}^{sca}$. The polarisability is then obtained from the scattered potential at infinity as [62],

$$\begin{aligned} \Phi^{sca}(r' \rightarrow \infty) &= a_{1,0}^{sca} \left\{ i \frac{\pi}{2} P_1^0 \left[\frac{1}{2} \left(r + \frac{1}{r} \right) \right] + Q_1^0 \left[\frac{1}{2} \left(r + \frac{1}{r} \right) \right] \right\} \cos(\theta) \\ &- a_{1,1}^{sca} \left\{ i \frac{\pi}{2} P_1^1 \left[\frac{1}{2} \left(r + \frac{1}{r} \right) \right] + Q_1^1 \left[\frac{1}{2} \left(r + \frac{1}{r} \right) \right] \right\} \sin(\theta) \cos(\varphi) \\ &= \frac{-2i a_{1,1}^{sca}}{3r^3} x - \frac{a_{1,0}^{sca}}{3r^3} z = \frac{1}{4\pi\epsilon_0} \frac{\gamma_{x'} E_{x'} x + \gamma_{z'} E_{z'} z}{r^3}, \end{aligned}$$

with the polarisabilities $\gamma_{x'}^p = -\frac{8i\pi\epsilon_0}{E_{x'}} a_{1,1}^{sca}$ and $\gamma_{z'}^p = -\frac{4\pi\epsilon_0}{3E_{z'}} a_{1,0}^{sca}$. Radiation damping can be accounted for by defining an effective polarisability, as in the two-dimensional case [22, 52]. We obtain the extinction and scattering cross-sections as,

$$\sigma_{ext}^{x'/z'} = k \text{Im} \left(\frac{1}{\epsilon_0 / \gamma_{x'/z'}^p - ik^3 / (6\pi)} \right), \quad (3.26)$$

$$\sigma_{sca}^{x'/z'} = \frac{k^4}{6\pi} \left| \frac{1}{\epsilon_0 / \gamma_{x'/z'}^p - ik^3 / (6\pi)} \right|^2. \quad (3.27)$$

The same expressions apply in the oblate case, but with $\gamma_{x'/z'}^p \rightarrow \gamma_{x'/z'}^o$. It is interesting to see that, similar to the two-dimensional ellipse, the polarisability only depends on the dipolar scattering coefficient ($l = 1$), indicating that the same selection

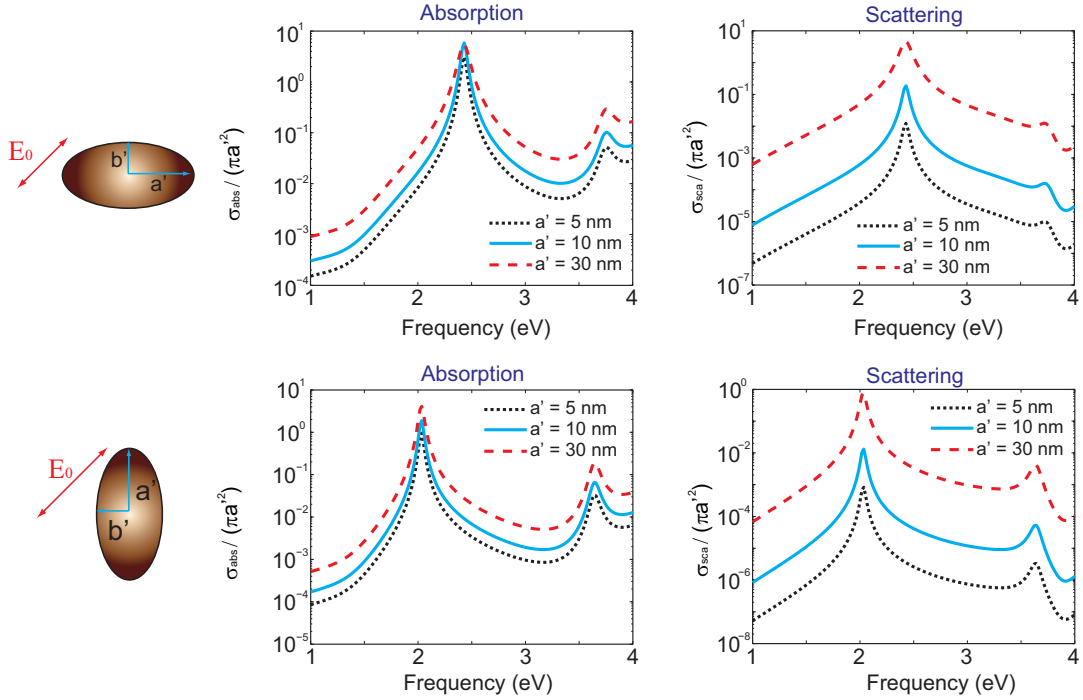


Figure 3.6: Absorption (left) and scattering (right) spectra for oblate (top) and prolate (bottom) spheroids under plane wave illumination ($E_{x'} = E_{z'} = E_0$, $E_{y'} = 0$). Shown are spectra for different values of the semi-major axis $a' = 5, 10, 30$ nm with $b' = 0.2a'$. We used the permittivity data of silver from Johnson and Christy [65] as ϵ_m and set $\epsilon_d = 1$. Reprinted with permission from [62]. Copyright 2014 by the American Physical Society.

rules hold. Again, this is a consequence of the spheroid's hidden symmetry, which is much more prominent after the transformation to the rotationally symmetric shell.

Analytical results for both oblate and prolate spheroids are shown in figure 3.6, providing further evidence of the selection rule. Note that the absorption cross-section for a prolate spheroid remains one order of magnitude larger than the scattering cross-section even for $a' = 30$ nm [62]. This makes the prolate spheroid a good candidate for applications in which plasmonic particles are needed where radiation damping has to be suppressed [62].

Figure 3.7 shows a comparison of our analytical calculation with COMSOL simulations. Numerical and analytical spectra match very well, providing further verification of our analytical approach.

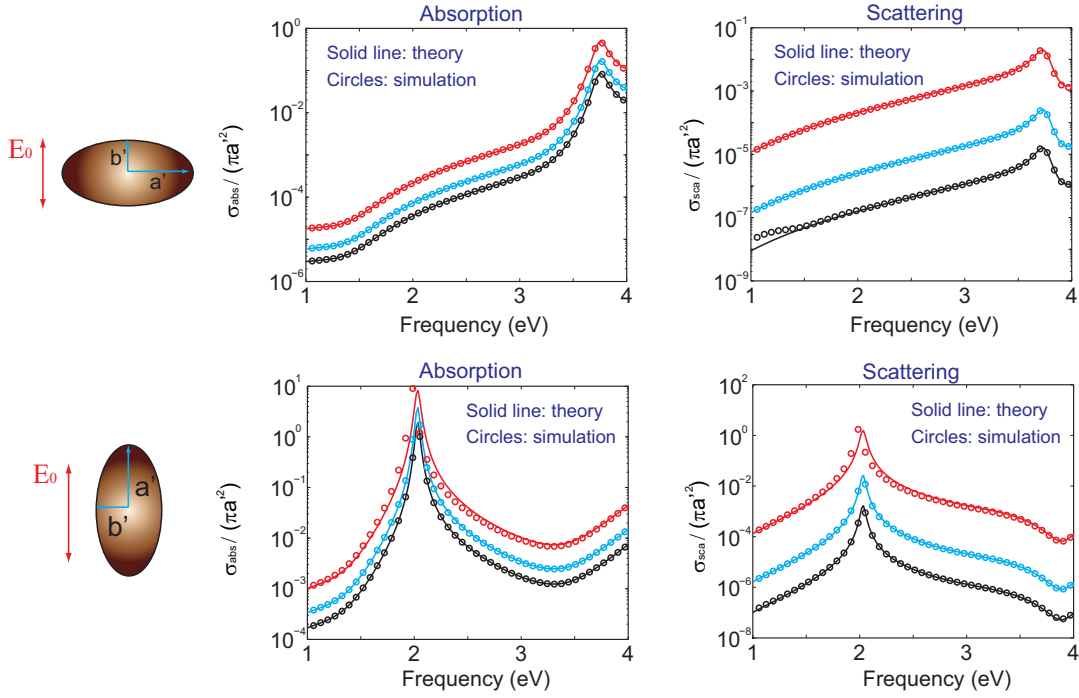


Figure 3.7: Comparison between analytically (solid lines) and numerically (open circles) calculated absorption (left) and scattering (right) spectra for oblate (top) and prolate (bottom) spheroids under plane wave illumination ($E_{x'} = E_{y'} = 0$, $E_{z'} = E_0$). Shown are spectra for different values of the semi-major axis $a' = 5\text{nm}$ (black), $a' = 10\text{nm}$ (blue) and $a' = 30\text{nm}$ (red), with $b' = 0.2a'$. We used the permittivity data of silver from Johnson and Christy [65] as ϵ_m and set $\epsilon_d = 1$. Reprinted with permission from [62]. Copyright 2014 by the American Physical Society.

3.3 Summary

In this chapter, we studied the plasmonic properties of a two-dimensional ellipse and prolate and oblate spheroids, using the TO framework. Both, the two- and three-dimensional structures were shown to possess ‘hidden’ rotational symmetries. These symmetries, while not obvious from the original geometry, became apparent upon transformation to the more symmetrical annulus and spherical shell, respectively. This meant that the plasmon modes for the ellipse and spheroids could be classified in terms of the symmetries of their more symmetrical counterparts. This did not only facilitate the derivation of analytical solutions for plasmon modes, absorption and scattering spectra, but also gave two key insights. First, it allowed us to derive ‘dipole’ selection rules in the scattering and absorption spectra. These were easy to obtain in the annulus/shell geometries and the reason that they also hold in the ellipse/spheroid frames, is that the transformation between the two geometries did not lead to a mixing of eigenmodes. That

is, both systems are simultaneously diagonalisable. Second, we obtained the plasmon resonance conditions as a function of the shape parameters of the ellipse/spheroid. This showed a splitting of the modes, when the ellipse/spheroids were deformed from a cylinder/sphere, i.e. the modes split because the rotational symmetry was broken. However, in the annulus/shell frame this splitting could be attributed to plasmon hybridisation and there thus seems to be a connection between the symmetry breaking in one frame and plasmon hybridisation in the other.

Chapter 4

Hidden symmetries in plasmonic systems II: plasmonic gratings

4.1 Introduction

Metallic gratings have a long standing history in optics research, spanning over a hundred years. The interaction of electromagnetic radiation and metallic gratings is rich in physics and full of subtleties, one of the earliest and most prominent being the discovery of Wood's anomalies in 1902, by Wood [71]. Wood discovered very sharp (in wavelength) bright and dark bands in the spectrogram of a metallic grating [71, 72]: an unexpected result which could not be explained by theory at the time [71].

The first theoretical explanation of Wood's anomalies came with Lord Rayleigh's article 'On the Dynamical Theory of Gratings' in 1907 [73]. He explained the effect by the vanishing and emergence of higher diffraction orders [73]. If a plane wave is incident normally on a grating, one can observe higher order diffraction modes at particular angles determined by $d \sin(\theta_m) = m\lambda$ (d is the grating's period). At some critical wavelength, the m -th diffraction mode will travel parallel to the surface; increase the wavelength ever so slightly and this diffraction order will vanish. This means the energy previously contained in this m -th diffraction mode is distributed over all the other, still visible, modes and leads to a sudden change in their intensity [72, 73]. This change is what Wood observed [71].

Fano and Hessel et. al. later showed that there are two types of Wood anomalies: the ones explained by Rayleigh and a second due to resonances in the grating itself (think waveguide or plasmon modes) [72, 74–76]. The latter type is associated with the interference of a resonant and non-resonant mode leading to the characteristic asymmetric line shape, now famously known as a Fano resonance [74, 75].

We have come a long way since then, but investigations into Wood anomalies and Fano resonances continue to the present day [77–81]. Research into one- or two-dimensional metallic gratings has also continued and led to the discovery of such important effects as extraordinary optical transmission (EOT) [82, 83]. It goes without saying that there is a broad range of existing and potential applications for these gratings, however, in the following we will focus on only two of these: Plasmonic gratings¹ in sensing and photovoltaics.

The common goal in sensing is to design a device capable of detecting a particular substance, which could be a chemical compound or a biological sample. It has already been shown that plasmonic nanoparticles are ideally suited to detect small changes in the refractive index of the material surrounding the particle [4, 19, 84]. This is due to the sensitivity of the nanoparticle’s plasmon resonance to the local environment of the particle [4, 19, 84]. Several studies optimising plasmonic grating designs for this particular effect exist and have been implemented successfully [85–87].

One of the most promising techniques for molecular sensing with the potential to go all the way to single molecule detection is Surface Enhanced Raman Scattering (SERS) [4, 18, 88]. This particular technique is ideally suited for plasmonic systems, since its efficiency is extremely sensitive to the local electric field strength (the probability of Raman scattering taking place is proportional to $|E|^4$) [4, 88]. All plasmonic particles show an enhanced local electric field at the plasmon resonance [4]. Moreover, some special systems are able to harvest light over the whole visible spectrum and concentrate its energy into hotspots, e.g. kissing cylinders and spheres [47, 57]. These structures give spectacular field enhancements of the order of 10^3 at the hotspot, the only problem being that it is a rare event that a target molecule sits exactly at the hotspot.

This is where plasmonic gratings come in. They, too, have the ability to harvest incoming electromagnetic radiation and couple it to higher order plasmon resonances showing strong field enhancements in the gap of the gratings [89, 90]. The field enhancements may not be as strong as for kissing cylinders; however, it is much easier to produce a regular grating on a larger scale, featuring many more hotspots than possible with kissing cylinders/spheres. This greatly enhances the probability of a target molecule being situated at the hotspot and thus increases the efficiency of SERS [89, 90].

¹Metallic gratings can be considered plasmonic if the frequency of the exciting source is below the plasma frequency of the metal.

A problem of thin film solar cells ($2\mu m$) compared to conventional ‘thick’ solar cells ($180 - 300\mu m$) is that, due to their small thickness, a lot of the incoming radiation simply passes through the cell without interaction [91]. Plasmonic improvements of thin film solar cells thus focus on trapping more of the incoming light in the thin photovoltaic device by integrating plasmonic elements in it [91]. Several design approaches exist [91–97]. A metal film with a single groove at the back of a semiconductor solar cell can couple incident light into a surface plasmon polariton, which propagates at the semi-conductor metal interface and thus enhances the energy absorption of the device [91, 97]. Other approaches place arrays of plasmonic nanoparticles on the semiconductor surface, leading to multi-scattering events between the particles and the light reflected at the back of the solar cell. This increases the optical path length and again the energy absorption [91, 98]. Yet another approach is to embed the plasmonic particles into the semiconductor, such that the localised surface plasmons trap the light inside it. In many of these designs plasmonic gratings play a prominent role [91, 92, 94–96, 99, 100].

Without a doubt, an accurate theoretical description of the interaction of light with plasmonic gratings is desirable. The question is, why use Transformation optics? Many analytical and semi-analytical methods exist, which give reasonably accurate results with some limitations. Rayleigh theory, as the most prominent example, works well only for shallow gratings and cannot predict the field inside the grooves as it only considers outgoing waves [73]. Green’s function methods and multiple scattering give good results, but are often mathematically heavy and rely on the inversion of large matrices, thus hiding the physics from view [101]. Of course, with today’s computational power, a brute force numerical method using software packages such as COMSOL can give accurate results within a couple of hours, albeit giving little physical insight.

Still, I believe Transformation has a place here. Transformation optics has previously been shown to give unique physical insights into plasmonic systems by reducing complex problems to rather simple ones, allowing for a concise and elegant mathematical description. This is something current analytical and numerical methods lack. Furthermore, applications often demand optimisation of design parameters. This is where numerical methods are most often applied. However, even if a single run only takes of the order of hours, optimising the design by changing the geometry can quickly boost simulation times to days and weeks. Here, I believe, a simple fully analytical description of plasmonic gratings in the Transformation optics framework has a major advantage.

4.2 Transformation of the geometry

Transformation optics is at its best when it can be used to reveal a connection between seemingly unrelated geometries. In this section, we show how a specific class of transformations can be used to design several classes of plasmonic systems: semi-infinite modulated planes, nanoparticle chains, thin gratings and nanoparticle chains on top of a surface.

4.2.1 Semi-infinite periodically modulated plane

We start with the simplest case. Starting from a half-plane with metal-dielectric boundary at $x = 0$, we can generate a semi-infinite modulated surface with period $2\pi\gamma$ using the conformal transformation

$$w = \gamma \log(e^\zeta - iv_0), \quad (4.1)$$

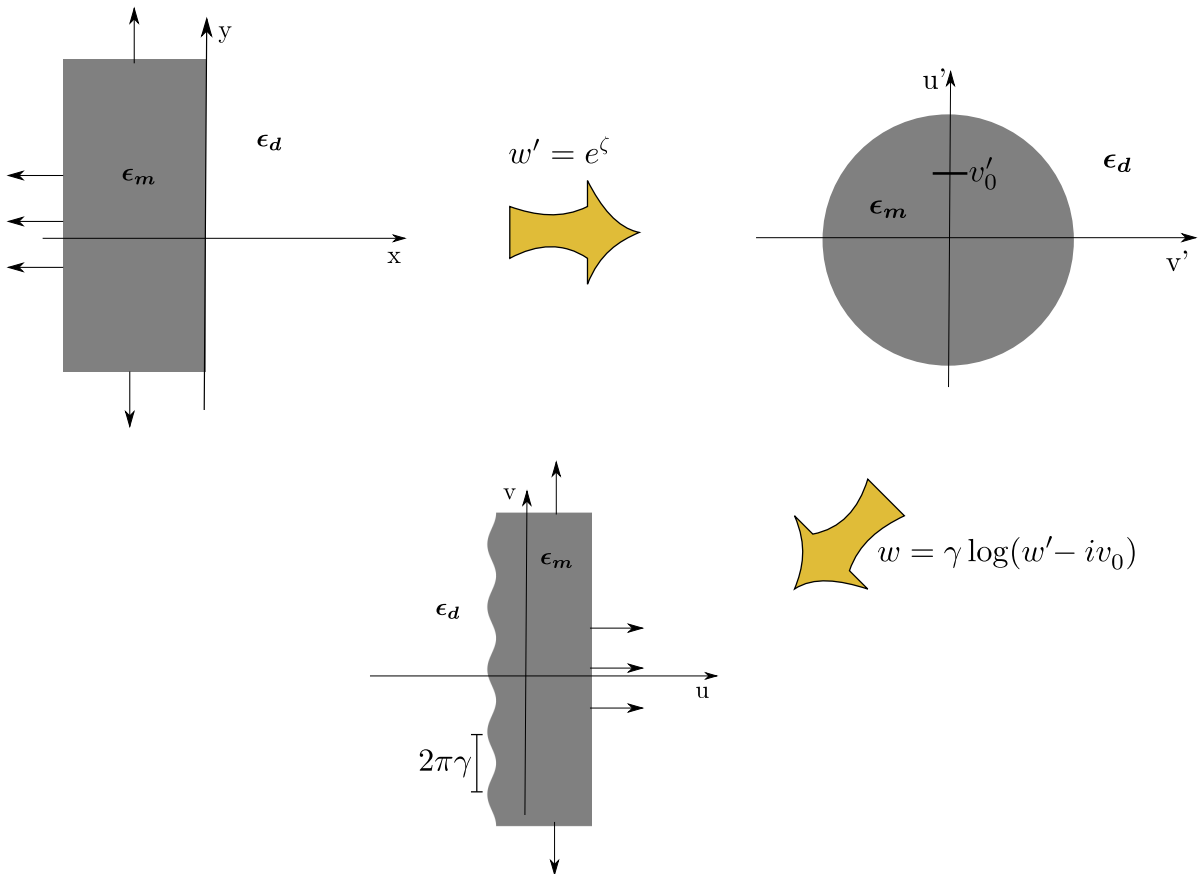


Figure 4.1: Schematic of the step-by-step transformation from a half-plane to a half-space with a periodically modulated interface.

where $w = u + iv$ and $\zeta = x + iy$. The effect of this transformation is summarised in figure 4.1. It works by transforming a half-plane into a circle by the well known exponential map [41]. A modulated half-plane is then obtained by taking a shifted logarithm transform [102]. Note that this transformation ‘swaps’ left and right, as depicted in figure 4.1. It is also worth noting that the transformation has branch points at $\zeta = \infty$ and $\zeta = \log(|v_0|) + i(\pi/2 + 2\pi n)$ for integer n .

There are two free parameters in this transformation. The first one, γ , determines the periodicity of the modulated surface and the second one, v_0 , sets the amplitude of the modulations on the surface. Changing the amplitude does, however, also change the modulation profile. Eq.4.1 thus relates a whole *class* of periodically modulated surfaces to a simple half-plane. Given that the electrostatic potential is conserved under conformal maps [41, 43], there is a whole class of periodically modulated surfaces, which is, in the electrostatic limit, physically equivalent to a simple half-plane. This has profound physical implications, which we will explore in later sections.

4.2.2 Nanoparticle chain

The same transformation can also be used to map a half-plane into a chain of plasmonic nanoparticles, as is shown in figure 4.2. The key to designing nanoparticles instead of a modulated half-space, is to choose the inversion point v_0 to be outside the metallic cylinder. Just on the perimeter of the metallic circle the transformation yields an infinitely modulated periodic surface, increase v_0 a little further and the lines of constant radius in the cylindrical frame form closed loops again. The closer v_0 is to the metallic circle, the more elongated the nanoparticles will be. If v_0 is increased, the nanoparticles become more circular. The periodicity of the array is the same as that for the modulated surface, namely $2\pi\gamma$.

The conformal transformation in Eq.4.1 really is very powerful, as it does not only relate a whole *class* of modulated surfaces to a simple planar half-space, but also a *class* of nanoparticle chains with variable particle shape. Note that conformal maps have previously been used to study particle arrays by McPhedran et al. [45, 46].

4.2.3 Periodically modulated plasmonic grating

The conformal transformation in Eq.4.1 is easily extended to treat thin plasmonic gratings. Here, the starting point is a semi-infinite plasmonic slab of thickness d , with its left interface at position $x = x_0$. The standard exponential map $\omega' = e^\zeta$ transforms this slab to a concentric annulus [27], rather than a solid cylinder. It is well known that a non-

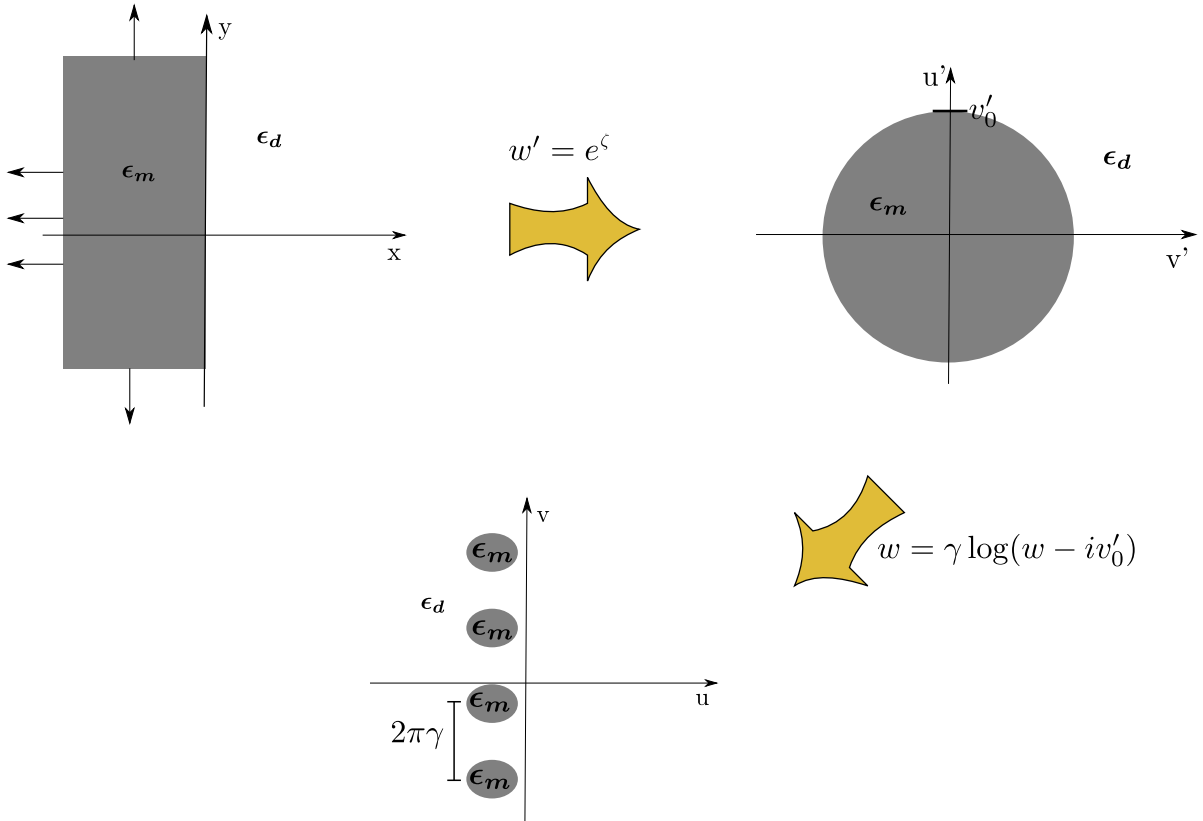


Figure 4.2: Schematic of the step-by-step transformation from a half-plane to an array of ‘elliptical’ nanoparticles.

concentric annulus can be obtained from a standard Moebius transformation [41, 43], $\zeta' = \frac{1}{w' - iw_0}$. Finally, it is possible to move from a non-concentric annulus to a plasmonic grating by a shifted logarithm transformation, such that the complete transformation from slab to plasmonic grating reads

$$w = \gamma \log\left(\frac{1}{e^\zeta - iw_0} + iy_0\right), \quad (4.2)$$

with $w_0, y_0 \in \mathbb{R}^+$ [102]. The effect of this transformation is summarised in figure 4.3. To obtain a grating with one flat and one corrugated side, as it is shown in figure 4.3, y_0 cannot be chosen independently of w_0 . A logarithmic transformation can only map a circle into a straight line if the circle is centred around the inversion point of the logarithm, in this case y_0 . A circle not centred around y_0 will transform to a periodically modulated line. Thus to obtain a flat surface y_0 must be at the centre of the inner circle in the ζ' -frame of figure 4.3, the centre of this inner circle is itself dependent on the transformation parameter w_0 and the position of the original slab interfaces, x_0 and

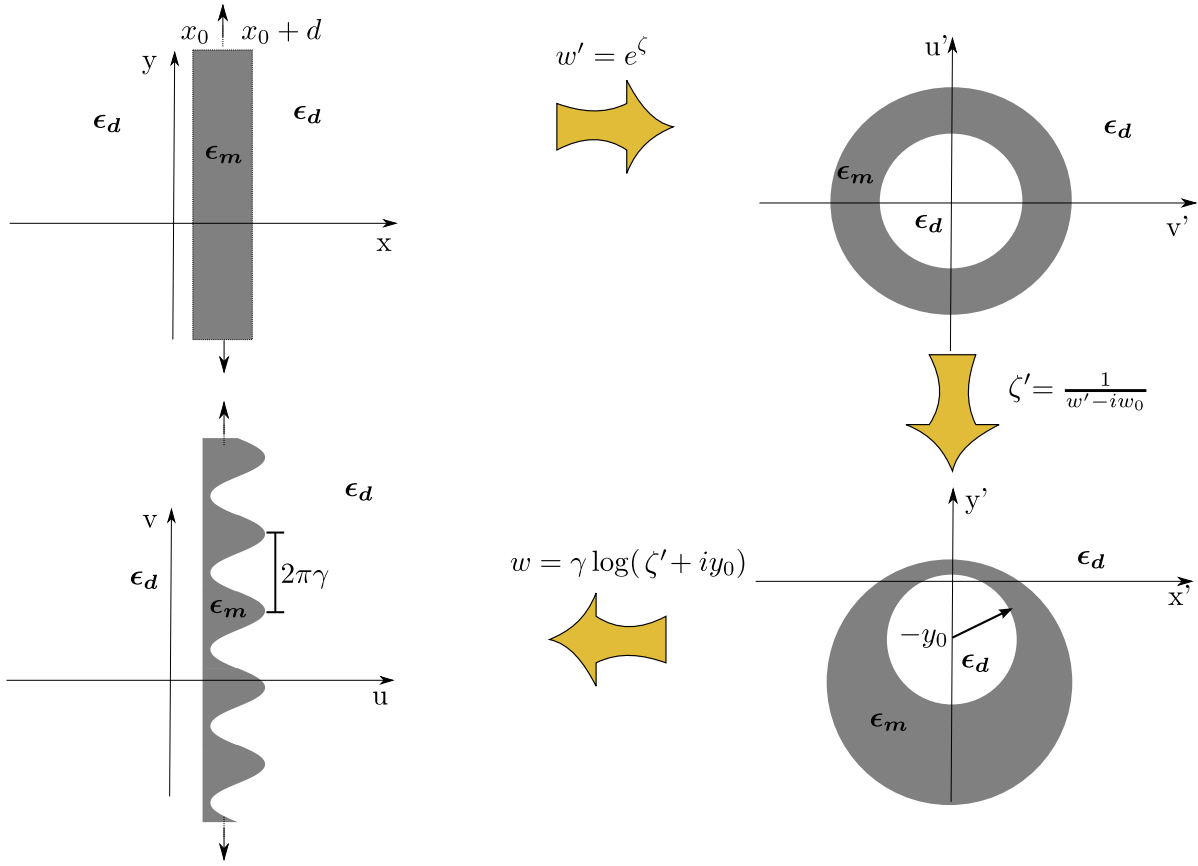


Figure 4.3: Schematic of the step-by-step transformation from a slab to a grating with one periodically modulated and one flat interface. Modified with permission from [102], available under the Creative Commons Attribution 3.0 License.

$x_0 + d$. It can be determined as $\frac{w_0}{(e^{2(x_0+d)} - w_0^2)}$ [102]. A plasmonic grating with one flat and one corrugated side can thus be obtained if $y_0 = \frac{w_0}{(e^{2(x_0+d)} - w_0^2)}$ [102].

As has been stated many times, a conformal transformation preserves the in-plane permittivity and permeability [42], meaning that slab and grating have the same material parameters and the two systems are completely equivalent, as far as electrostatics is concerned.

The great flexibility of the transformation in Eq.4.2 has to be stressed. Similar to the case of a half-plane, there are two free parameters. One, γ , sets the periodicity of the grating, the other, w_0 , determines its shape and modulation depth. So again, a whole *class* of gratings can be related to a simple semi-infinite slab by the single transformation given in Eq.4.2. In contrast to the case of a half-plane, the restriction on y_0 can be relaxed and the gratings second interface can also be modulated. This

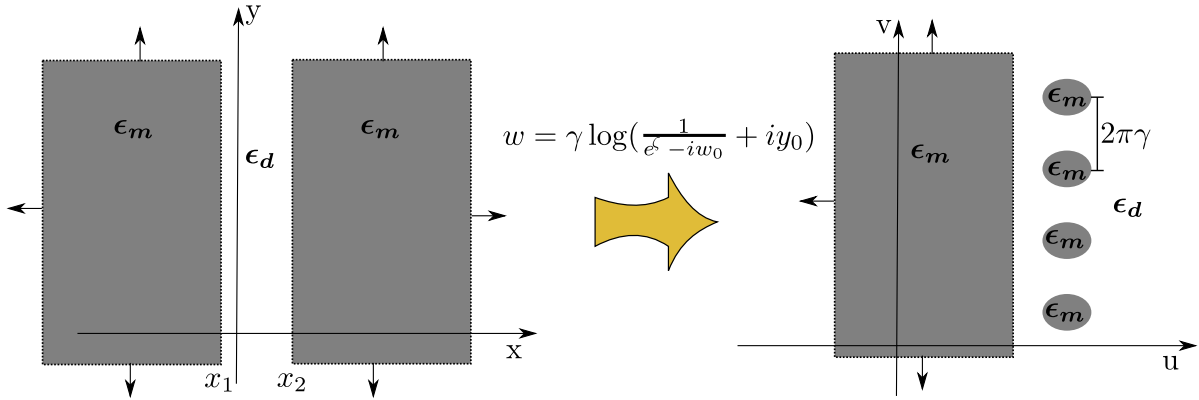


Figure 4.4: Schematic of the step-by-step transformation from a slab to an array of ‘elliptical’ nanoparticles close to a flat surface. Reprinted with permission from the supplementary material of [102], available under the Creative Commons Attribution 3.0 License.

allows us to treat a vast number of different, yet very special, plasmonic gratings within a unified framework.

4.2.4 Nanoparticle chain on a flat surface

Similar to the transformation from a simple slab to a periodic grating, it is possible to obtain a chain of nanoparticles on top of a metallic surface. In this case the system to start from is a metal-insulator-metal waveguide [102]. This will be transformed to a chain of ‘elliptical’ nanoparticles if $x_1 < \log(w_0)$ and $y_0 = \frac{w_0}{(e^{2x_2} - w_0^2)}$. The first of these conditions ensures that the area left of x_1 is transformed into a chain of nanoparticles rather than a continuous surface, while the second one leads to a flat surface upon transformation of the area right of x_2 . An intuitive explanation for this behaviour will follow in the next section.

4.2.5 Mathematical details of the transformation

Much of the remainder of this text will be concerned with the transformation from a simple slab to a thin plasmonic grating, so it pays to take a closer look at the conformal transformation in Eq.4.2, here again

$$w = \gamma \log\left(\frac{1}{e^\zeta - iw_0} + iy_0\right). \quad (4.3)$$

Branch point type	$\log(0)$	$\log(\infty)$
Slab frame	$\log(w_0 + 1/y_0) + i(\pi/2 + 2\pi k)$	$\log(w_0) + i(\pi/2 + 2\pi k)$
Grating frame	$\log(y_0 + 1/w_0) + i(\pi/2 + 2\pi k)$	$\log(y_0) + i(\pi/2 + 2\pi k)$

Table 4.1: Summary of branch points

First of all, the inverse transformation has the same functional form and is given by

$$\zeta = \log\left(\frac{1}{e^{w/\gamma} - iy_0} + iw_0\right). \quad (4.4)$$

Second, the complex logarithm has branch points at the origin and infinity. Therefore the transformation has branch points whenever the argument of the logarithm vanishes or diverges. This holds true for the inverse transformation as well. The position of the branch points for the transformation and its inverse are summarised in table 4.1. Yet, a more intuitive feeling for the analytic structure of the transformation can be obtained from figure 4.5 [102].

As has been pointed out in several papers [60, 102], the effect of any coordinate transformation can be imagined as a ‘stretching’ and ‘pulling’ of the original coordinate grid, to deform the grid according to the underlying transformation. In essence, this is what is shown in figure 4.5. The original Cartesian grid is distorted into the irregular mesh shown in figure 4.5 [102]. Note that the contour lines meet at right angles; the defining property of a conformal transformation [41, 43]. As has been pointed out in [102], there are number of interesting points to recognise here. Specifically, the points where the contour lines ‘bunch up’ correspond to the branch points of the transformation; they equate to points at infinity in the slab frame, but are transformed into two periodic arrays of singularities in the grating frame. Their position is given in table 4.1. Furthermore, following a single contour line in-between the branch points shows how one can generate a grating with a flat and corrugated side. Right in the centre between the branch points there is single contour line, whose shape remains unaltered. Yet, all other contour lines have a ‘wavy’ shape and repeat with period $2\pi\gamma$ [102]. The modulation of these lines gets stronger and stronger the closer they lie to the branch points of the transformation, until, right at the branch point, they become infinitely modulated [102]. Finally, the behaviour of the contour lines past the branch points explains how the transformation can be used to model a chain of nanoparticles above a substrate. Once the contour lines move past a branch point, they do not form a continuous line anymore, but instead break up and loop around the branch point, i.e. they form an array

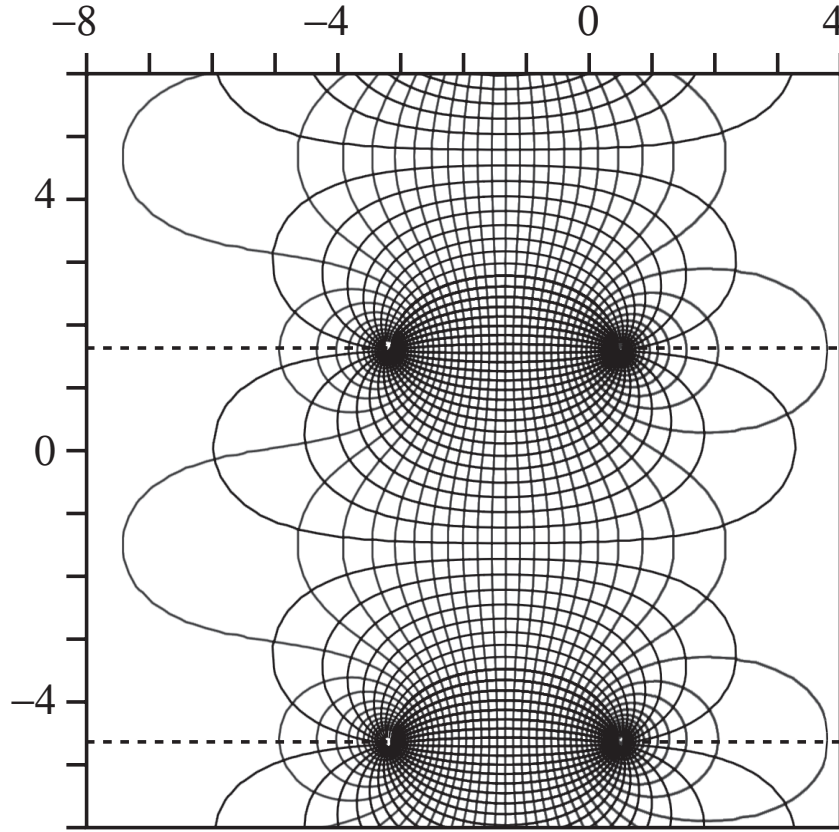


Figure 4.5: Analytic structure of the transformation in Eq.4.2 for $\gamma = 1$, $y_0 = 0.033$ and $w_0 = 0.6$. The solid lines show the deformation of the cartesian grid in the x - y -frame under transformation to the u - v -frame. The dashed lines indicate the branch cuts running from the branch points to infinity. Reprinted with permission from [102], available under the Creative Commons Attribution 3.0 License.

of discrete particles rather than a continuous surface [102]. This effect is schematically shown in figure 4.4 [102].

For later manipulations it is also beneficial to rewrite the transformation in Eq.4.2 in a slightly more amendable form. It turns out that in the region between the branch points, i.e. for $\log(w_0) < x < \log(w_0 + 1/y_0)$, the transformation can be written as a Fourier series. This allows us to obtain explicit expressions for the u - and v -coordinate

[102]

$$u = \gamma \left[\log(1 + y_0 w_0) - x + \sum_{\substack{g=-\infty \\ g \neq 0}}^{\infty} (d_g^+ e^{|g|x} + d_g^- e^{-|g|x}) e^{igy} \right] \quad (4.5)$$

$$v = \gamma \left[-y + \sum_{\substack{g=-\infty \\ g \neq 0}}^{\infty} (h_g^+ e^{|g|x} + h_g^- e^{-|g|x}) e^{igy} \right], \quad (4.6)$$

with

$$h_g^+ = \frac{e^{-i\frac{\pi}{2}g} \operatorname{sign}(g)i}{2|g| (w_0 + 1/y_0)^{|g|}} \quad (4.7)$$

$$h_g^- = \frac{i\operatorname{sign}(g)e^{-i\frac{\pi}{2}g}}{2|g|} w_0^{|g|} \quad (4.8)$$

$$d_g^+ = \frac{e^{-i\frac{\pi}{2}g} - 1}{2|g| (w_0 + 1/y_0)^{|g|}} \quad (4.9)$$

$$d_g^- = \frac{e^{-i\frac{\pi}{2}g}}{2|g|} w_0^{|g|}. \quad (4.10)$$

This representation is particularly useful as it is already in terms of the eigenfunctions of the slab frame. See appendix B.1 for a derivation of the above Fourier series.

To conclude this section, we have presented two conformal transformations, which allow the transformation of a half-plane into a modulated surface or a particle chain and a simple slab into a thin grating or a nanoparticle chain on a substrate. The richness of these transformations should not go unnoticed. In each case it is possible to treat a whole *class* of structures within a unified framework by simply tweaking the free parameters of the transformations. This will not only lead to mathematical simplicity, but also give physical insight into the behaviour of these classes of structures.

4.3 Dispersion relation

One of the fundamental properties, if not the most fundamental, of a physical system is its spectrum. For nanoparticles of size smaller than the wavelength of light or extended systems with feature sizes smaller than the wavelength, the plasmonic spectrum is, to a good approximation, given by the electrostatic spectrum [20, 52]. That is, it is given by

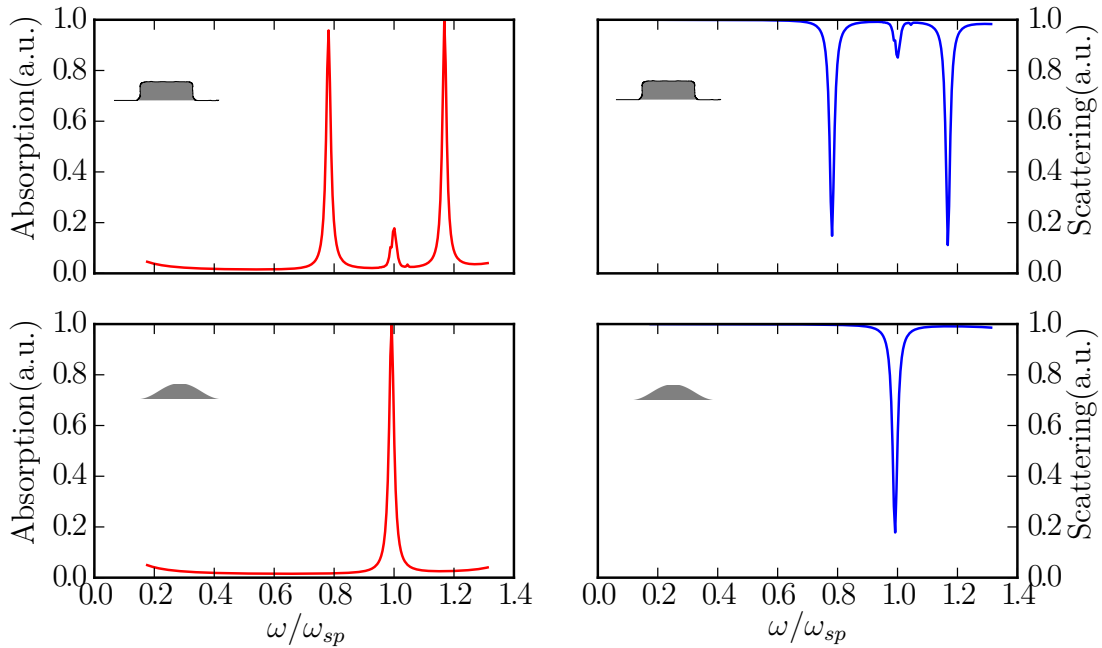


Figure 4.6: The absorption and scattering spectra for two modulated half planes. The top panel shows spectra for a half plane not obtained via a conformal transformation. The bottom panel shows the spectra for a half-plane obtained from Eq.4.1 with $\gamma = 10^{-8}$ and $y_0 = 0.5$. The period and modulation depth are the same for both structures. The permittivity is given by $\epsilon_m = 1 - \frac{\omega_p^2}{\omega(\omega+i\gamma)}$, $\epsilon_d = 1$, with $\gamma = 0.032eV$ and $\omega_p = 8eV$, in both cases.

the solutions to a modified Laplace's equation,

$$\nabla \cdot (\epsilon \nabla) \phi = 0. \quad (4.11)$$

Let us reiterate that the electrostatic potential is conserved under conformal transformations and so is the spectrum [41, 43]. This has some interesting consequences for the structures introduced in the previous section.

4.3.1 Half-plane to modulated surface

In the previous section we showed that a whole class of periodically modulated half-spaces could be designed via a conformal map (Eq.4.1), with a completely flat half-plane as underlying ‘mother’ structure [102]. Since the spectrum is conserved under conformal maps, this whole class of periodically modulated half-planes inherits its spectral proper-

ties from one and the same half-plane. It is well known that all the plasmon resonance modes are degenerate at the surface plasma frequency for a half-plane [4, 20].

Figure 4.6 provides a test of this assertion. It shows the absorption and scattering spectra for two different periodically modulated half-spaces. The lower of the two has been obtained from the conformal transformation given in Eq.4.1, the upper features a simple rectangular grating with rounded corners, the period and modulation depth is the same for both. In both cases the incident source is given by a plane wave at normal incidence and with the electric field polarised in the plane of incidence. Since both modulated surfaces have the ability to couple light into higher order Fourier modes due to their periodic modulation, one could expect absorption and scattering spectra with several distinct peaks. This is exactly what can be observed for the rectangular surface with peaks emerging on either side of the surface plasma frequency. However, there is only one peak visible for the modulated half-space designed from a conformal map. This indicates that the plasmon modes of this structure are indeed degenerate at the surface plasma frequency. This is a highly intriguing result and can only be explained via the *hidden* symmetry of the modulated surface, i.e. its relation to the much more symmetrical half-*plane*.

Of course, a simple plot of the absorption and scattering spectra does not constitute a proof of the claim that the plasmon modes for the special class of periodically modulated half-spaces discussed here are all degenerate. For this a rigorous numerical eigenmode analysis is necessary. However, the remainder of this report will focus on the much more interesting class of thin plasmonic gratings and an eigenmode analysis is carried out for those structures instead. Nonetheless, the absorption and scattering spectra in figure 4.6 indicate that we are on the right track.

4.3.2 Slab to grating

The conformal map in Eq.4.3 relates a class of periodically modulated plasmonic gratings to a simple infinite slab. As has been mentioned many times, the conformality of the map between the two structures ensures that their plasmon spectra are the same. Calculating the dispersion relation of a plasmonic grating is normally a laborious task, but not so here, for the plasmon dispersion relation of the related slab is well known and very easy to calculate. It is given by [102, 103]

$$e^{d|k_y|} = \pm \left(\frac{\epsilon_m - \epsilon_d}{\epsilon_m + \epsilon_d} \right), \quad (4.12)$$

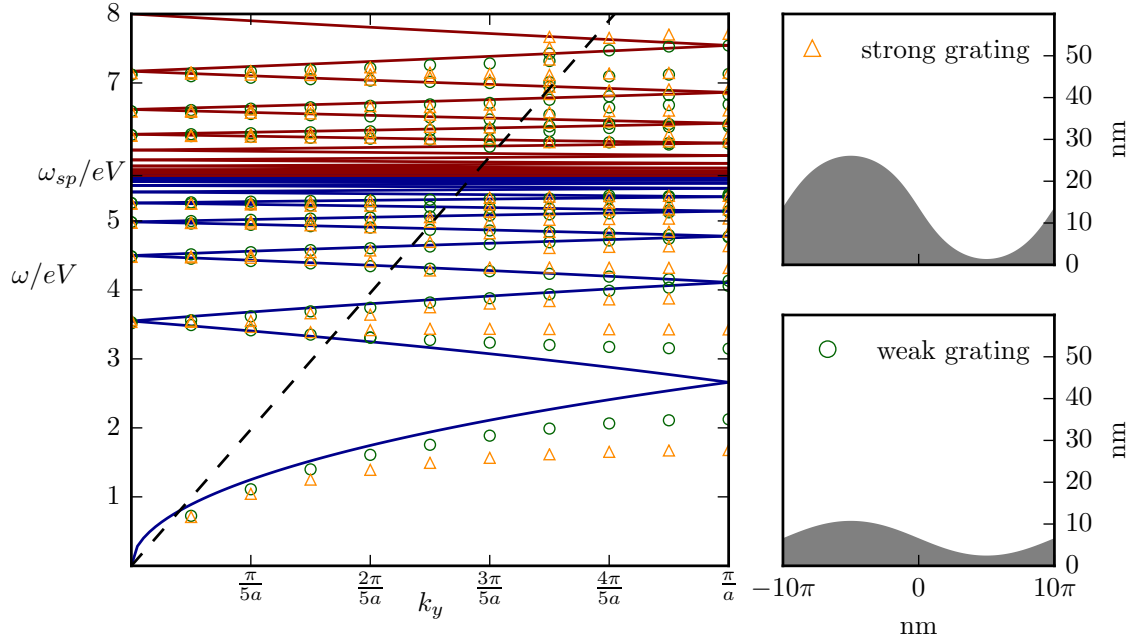


Figure 4.7: Dispersion relation of two gratings in the first Brillouin zone. The yellow triangles and green, open circles are COMSOL simulations for a grating with $\gamma = 10^{-8}$, $w_0 = 2.5$ and $\gamma = 10^{-8}$, $w_0 = 1.5$, respectively. In both cases we started with a slab at position $a = 1$ and with thickness $d = 0.5$. The solid lines are analytical calculations. The dashed line corresponds to the light line. The permittivities were $\epsilon_m = 1 - \frac{\omega_p^2}{\omega^2}$, $\epsilon_d = 1$, with $\omega_p = 8eV$. Modified with permission from [102], available under the Creative Commons Attribution 3.0 License.

where d is the thickness of the slab. Once more, the simplicity of this expression highlights the elegance of the transformation optics approach. It is worth noting that this is also the plasmon resonance condition of the class of nanoparticles on a surface generated in figure 4.4.

The dispersion relation in Eq.4.12 is quite unusual for a periodic grating, as its spectrum is continuous, whereas one usually expects band gaps in the spectrum [3]. The absence of forbidden energy regions for our class of periodic gratings can only be explained as a result of the hidden symmetry of the underlying slab system. The infinite slab is translationally invariant, so its spectrum is naturally gap less.

Apparently the plasmons generated on the grating's surface know nothing about the periodic modulation due to this hidden symmetry. It is thus appropriate to refer to the class of gratings (or nanoparticles on a surface) generated by Eq.4.3 as a *symmetry* class [102].

In the following, we will provide a detailed comparison between the analytical dispersion relation obtained from Eq.4.12 and a full electrodynamical numerical simulation using the ‘eigenfrequency solver’ of the COMSOL Multiphysics software package. We can hence test the validity of these analytical expressions and make statements about their applicability.

Figure 4.7 shows the dispersion relation for two different gratings generated from Eq.4.3 [102]. In both cases we assumed the grating to have the permittivity of a lossless Drude model $\epsilon_m = 1 - \frac{\omega_p^2}{\omega^2}$ with $\omega_p = 8eV$ and to be surrounded by air ($\epsilon_d = 1$). The two gratings considered possess the same permittivity and period, but vary in their modulation depth. Compared to previous analytical studies [101], both gratings can be considered to be strongly modulated with modulation depth to period ratios of $\approx 16\%$ and $\approx 40\%$, respectively. This should be kept in mind for the remainder of this chapter, as we will refer to the grating with $\approx 16\%$ modulation as weakly modulated even though its modulation is still substantial.

The solid lines in figure 4.7 give the analytical dispersion relation for the even (blue) and odd (red) plasmon modes. As the weakly and strongly modulated grating are derived from the same slab our theory predicts that their dispersion relations are identical [102]. This can be checked by comparing to the numerically obtained dispersion relation for the strongly (purple triangles) and weakly modulated grating (green circles). The black dashed line corresponds to the light line. Before analysing the results in detail, let us note that the dispersion relation is shown in the first Brillouin zone using the reduced zone scheme [3]. That is, points at $k_y = k_y^0 + 2\pi m/a$, where $m \in \mathbb{Z}_0$, $k_y^0 \in [0, \pi/a]$ with a being the grating’s period are ‘folded’ back into the region $0 \leq k_y \leq \pi/a$. For example, points with $k_y = 2\pi/a, 4\pi/a$, etc. are folded back onto the $k_y = 0$ -axis. This means that the mode at $\approx 3.5eV$ should really be thought of as the mode at $\omega(k_y = 2\pi/a)$ on the standard dispersion curve. Thus despite this mode appearing to be left of the light line in this reduced zone picture, it actually is far to the right of the light line already, if one simply plots the standard dispersion curve $\omega(k_y)$ without folding back [102].

Comparing the analytical and numerical solutions we find excellent agreement near the zone centre. Yet for larger values of k_y the agreement between numerical and analytical solutions worsens and the numerical solutions for the weakly and strongly modulated grating diverge [102]. Most importantly, at the zone edge the numerical solutions feature a large band gap contradicting the analytical prediction of a gapless spectrum [102].

Furthermore, a magnified version of the dispersion relation around the mode at $\omega \approx 3.5eV$ (see figure 4.8) shows that at $k_y = 0$ there is also a small band gap. However, this band gap is of the order of a few milli electron-volts [102]. Such an energy differ-

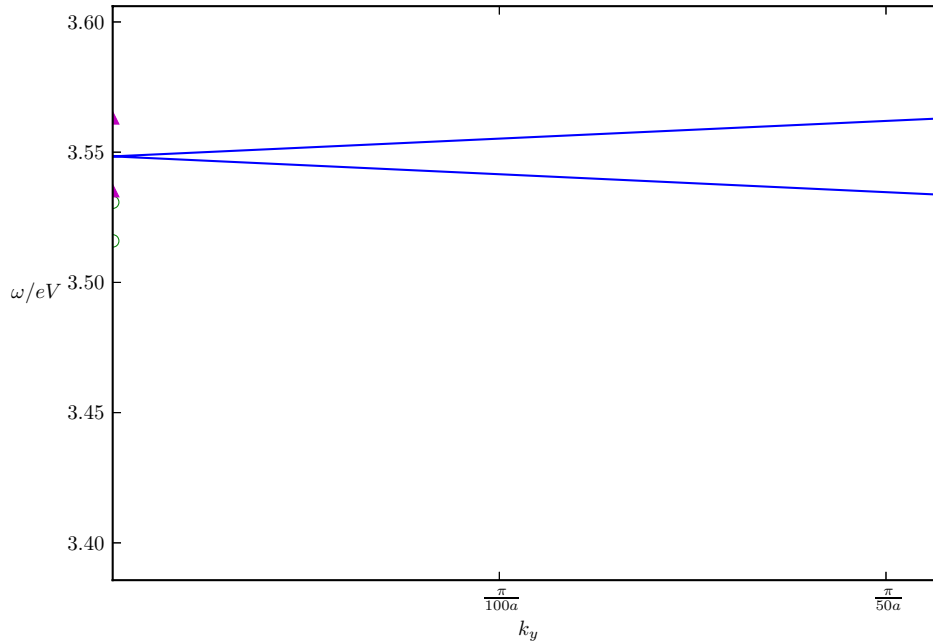


Figure 4.8: A magnified version of figure 4.7. Shown is the dispersion relation for the grating around the 1st order mode at $\approx 3.55eV$. The solid line corresponds to analytical calculations, the open circles are COMSOL simulations for the weakly modulated grating and the triangles correspond to COMSOL simulations of the strongly modulated grating. a is the lattice constant. Reprinted with permission from the supplementary material of [102], available under the Creative Commons Attribution 3.0 License.

ence which could be resolved in high precision optical measurements in the absence of radiation damping, but is very difficult to access in other experimental set-ups such as electron energy loss spectroscopy. As will be shown in a later section, even numerical simulations do not show this splitting, as the broadening of the resonance peak due to radiation damping is much larger than a few milli electron-volts. Therefore, at $k_y = 0$ the special class of gratings studied here does possess a *near zero* band gap [102]. These ‘degeneracy points’ can only be explained in terms of the hidden translational symmetry of the gratings. The absence of an appreciable band gap at the zone centre and the excellent agreement between analytical and numerical calculations for small k_y is a strong indicator that transformation optics indeed allows one to design a whole symmetry class of plasmonic gratings with equivalent spectral properties near the zone centre [102].

Before analysing the short-comings of the analytical approach it is worth discussing the ‘degeneracy points’ at the zone centre in view of another famous occurrence of degeneracy: the Dirac point. The biggest similarity between Dirac points and the degeneracy

points of the grating is the absence of an appreciable band gap, which leads to a finite group velocity at the zone centre [102]. However, near Dirac points the dispersion relation takes its famous conical shape [104–106]. This is not the case for the grating [102]. Moreover, the physical origin between the degeneracy points found in the gratings’ spectra and Dirac points is altogether different. Dirac points in graphene [104], photonic crystals [105] and other analogous plasmonic systems [106] are all due to a special symmetry of the underlying ‘crystal lattice’, e.g. a honeycomb lattice [102]. On the contrary, the emergence of the ‘degeneracy points’ for the grating is not due to any special symmetry of the lattice. In fact, it is the *absence of the lattice* causing the degeneracy [102]. This only becomes obvious upon transformation to the translationally invariant slab.

The analytical theory presented here is very successful in predicting the dispersion relation near the zone centre. Yet it fails very badly near the zone edge and there is also a slight band gap at the zone centre. Two reasons for the theory’s limitations can be identified.

The first and relatively minor effect is due to the electrostatic approximation [102]. The electrostatic potential is conserved under conformal transformations, because the in-plane permittivity and permeability are conserved and the electrostatic fields are confined in-plane. The out-of-plane permittivity and permeability, however, do change (see section 2.2.2). Due to the periodicity of the transformation these out-of-plane components will be periodic functions [102]. The plasmon modes of a deeply sub-wavelength grating as studied here are mostly confined to the in-plane and dominated by electrostatics [102]. Nonetheless, there is a small out-of-plane magnetic component, which will ‘feel’ the modified out-of-plane permittivity and permeability when transforming between grating and slab frame. It is this magnetic effect which gives rise to the small band gap at the zone centre [102].

The second and stronger limitation is due to the analytical structure of the conformal transformation in Eq.4.3. Modes at the zone centre have the same periodicity as the grating [102]. This naturally leads to continuous solutions in the grating frame without any discontinuities across the branch cuts shown in figure 4.5. If the modes do not have the same periodicity as the grating, unphysical discontinuities in the potential arise across the branch cuts [102]. This indicates that the boundary conditions for finite k_y and thus the eigenmodes are not correct [102]. In principle, it should be possible to avoid these discontinuities by applying additional boundary conditions at the Branch cuts. However, this has proven tricky in the past. This provides a technical reason for

the failure of the theory, but gives very little physical insight. Physically, the appearance of the band gap at the zone edge is due to Bragg scattering [101]. Hence, a more intuitive explanation of the failure of our theory is that it lacks the ability to treat Bragg scattering [102]. We would thus like to stress that the large band gap at the zone edge is *not* due to magnetic effects and that the electrostatic approximation holds there.

To summarise, the transformation optics approach allows us to design a whole symmetry class of plasmonic gratings with unusual properties, explained only by the hidden symmetry of the ‘mother’ structure. Unfortunately, this approach seems unable to predict the dispersion relation near the zone edge. Yet from a practical point of view this is not a major obstacle, as long as one is interested in the response of the grating under the illumination of light. Light essentially carries zero momentum, so the only modes that can be excited by a far field light source are the ones close to the zone centre, which are exactly the ones that can be predicted very accurately using the present theory.

4.4 Optical response: theory

In this section, we will show how the Transformation optics approach outlined in the previous sections can be used to calculate the optical response of a thin plasmonic grating. Specifically, we will consider the electromagnetic scattering problem for a plane wave at normal incidence on the grating. A plane wave polarised along the vertical direction has zero momentum in this direction, i.e. $k_y = 0$. Following the discussion in the previous section a good agreement between theory and full electrodynamic simulations can be expected in this case.

4.4.1 Transformation of a plane wave

In the grating frame, a plane wave with the electric field polarised along the vertical (v -) direction and incident on the modulated side of the grating, i.e. from the right, can be written as [102]

$$\mathbf{H}^{sou} = -\frac{\omega\epsilon_0\epsilon}{k} E^{sou} e^{-iku} \hat{z}. \quad (4.13)$$

Note, that the z -component of the \mathbf{H} -field is conserved under conformal transformations (see section 2.2.2). That is, the plane wave constituting the exciting source in the grating frame is easily transferred to the slab frame. Thus to first order in k the exciting

source field in the slab frame is given by [102]

$$\mathbf{H}^{sou} \approx - \left(\frac{\omega \epsilon_0 \epsilon}{k} E^{sou} + i\omega \epsilon_0 \epsilon E^{sou} u \right) \hat{z}. \quad (4.14)$$

A simple substitution for the u -coordinate from Eq.4.5 then gives the \mathbf{H} -field in terms of the slab frame coordinates [102]

$$\mathbf{H}^{sou} = - \frac{\omega \epsilon_0 \epsilon}{k} E^{sou} \left(1 - ik\gamma \left[\log(1 + y_0 w_0) - x + \sum_{\substack{g=-\infty \\ g \neq 0}}^{\infty} (d_g^+ e^{|g|x} + d_g^- e^{-|g|x}) e^{igy} \right] \right) \hat{z}, \quad (4.15)$$

which is valid for $\log(w_0) < x < \log(w_0 + 1/y_0)$. For later manipulations it will be advantageous to express the exciting source in terms of an electrostatic potential ϕ_{sou} . We thus proceed by first calculating the electric field in the slab frame from Ampere's law [20],

$$\nabla \times \mathbf{H}^{sou} = -i\omega \epsilon_0 \epsilon \mathbf{E}^{sou} \quad (4.16)$$

$$\partial_y H_z \hat{x} - \partial_x H_z \hat{y} = -i\omega \epsilon_0 \epsilon \mathbf{E}^{sou}. \quad (4.17)$$

Thus

$$-i\omega \epsilon_0 \epsilon E_x = i\omega \epsilon_0 \epsilon \gamma E^{sou} \partial_y \sum_{\substack{g=-\infty \\ g \neq 0}}^{\infty} (d_g^+ e^{|g|x} + d_g^- e^{-|g|x}) e^{igy} \quad (4.18)$$

$$E_x = -\gamma E^{sou} \sum_{\substack{g=-\infty \\ g \neq 0}}^{\infty} ig (d_g^+ e^{|g|x} + d_g^- e^{-|g|x}) e^{igy}, \quad (4.19)$$

and

$$\begin{aligned} E_y &= \gamma E^{sou} \partial_x \left[-x + \sum_{\substack{g=-\infty \\ g \neq 0}}^{\infty} (d_g^+ e^{|g|x} + d_g^- e^{-|g|x}) e^{igy} \right] \\ &= \gamma E^{sou} \left[-1 + \sum_{\substack{g=-\infty \\ g \neq 0}}^{\infty} |g| (d_g^+ e^{|g|x} - d_g^- e^{-|g|x}) e^{igy} \right]. \end{aligned} \quad (4.20)$$

Integrating the x -component of $\mathbf{E}^{sou} = -\nabla\phi^{sou}$ gives ϕ^{sou} up to a function of y

$$\phi = \gamma E^{sou} \sum_{\substack{g=-\infty \\ g \neq 0}}^{\infty} \frac{ig}{|g|} \left(d_g^+ e^{|g|x} - d_g^- e^{-|g|x} \right) e^{igy} + \text{Const}(y), \quad (4.21)$$

with $\text{Const}(y)$ clearly given by $\gamma E^{sou} y$. Finally, for $\log(w_0) < x < \log(w_0 + 1/y_0)$ [102]

$$\phi^{sou} = \gamma E^{sou} \left[\sum_{\substack{g=-\infty \\ g \neq 0}}^{\infty} i \text{sign}(g) \left(d_g^+ e^{|g|x} - d_g^- e^{-|g|x} \right) e^{igy} + y \right]. \quad (4.22)$$

It is an interesting feature of this expression that it does not depend on the free space wave vector k . This means a plane wave travelling in the opposite direction in the grating frame will lead to the exact same potential in the slab frame.

4.4.2 Scattered and induced potential in the slab frame

The expression for the source potential in Eq.3.6 is, conveniently, already written in terms of the eigenfunctions of the slab geometry. To find the response of the slab to this incident potential we start by writing down general expressions for the potential in the three regions of interest, i.e. to the left and right of the slab, as well as inside. Hence, the total potential Φ can be written as [102]

$$\Phi = \begin{cases} \phi_L = \phi^{sou} + \phi_L^{near} + \phi_L^{rad} & \log(w_0) < x < x_0 \\ \phi_I = \phi_{ins}^{near} & x_0 < x < x_0 + d \\ \phi_R = \phi_R^{near} + \phi_R^{rad}. & x_0 + d < x < \log(w_0 + 1/y_0) \end{cases} \quad (4.23)$$

As the conformal transformation from grating to slab reverses left and right, the source potential is now incident on the left side of the grating [102]. The fields inside the slab will be completely dominated by electrostatics, as the original grating is very thin compared to the wavelength. The source potential in Eq.3.6 thus suggests the following form for the potential inside the slab [102],

$$\phi_{ins}^{near} = \sum_{\substack{g=-\infty \\ g \neq 0}}^{\infty} \left(c_g^- e^{igy} e^{-|g|x} + c_g^+ e^{igy} e^{|g|x} \right) + E_0^v y. \quad (4.24)$$

Outside the slab, the story is a little different. Here there will be electrostatic near field contributions which must decay to zero as $x \rightarrow \infty$, i.e. to the left of the slab the near field contributions take the form [102]

$$\phi_L^{nrea} = \sum_{\substack{g=-\infty \\ g \neq 0}}^{\infty} b_g^{sca} e^{igy} e^{|g|x}, \quad (4.25)$$

whereas to the right they are given by [102]

$$\phi_R^{nrea} = \sum_{\substack{g=-\infty \\ g \neq 0}}^{\infty} e_g^{sca} e^{igy} e^{-|g|x}. \quad (4.26)$$

If the world was completely governed by electrostatics, the expansion coefficients could now be determined from the boundary conditions at the two interfaces of the slab and the scattering problem would be solved. However, we know that in reality energy conservation demands that the grating provides a radiative reaction in the form of an electromagnetic wave carrying energy away from the grating [20, 52]. This radiative reaction is encoded in the functions ϕ_L^{rad} and ϕ_R^{rad} [102]. A moment's thought will reveal their form in the slab frame.

In the original grating frame there is a plane wave incident on the grating with the electric field polarised along the vertical direction. This field leads to a potential decrease/increase along the vertical direction of the grating and sets the electrons of the metal in motion, i.e. it produces a current [102]. Since this current can oscillate on a scale much larger than the wavelength of light, it will lead to the radiation of electromagnetic waves [20]. Because the grating is very thin in the horizontal direction the contribution of the currents in this direction to the radiated wave will be small [102]. Thus only the vertical currents are of relevance, which means the thin grating effectively 'looks' like a uniform thin current sheet with an effective surface current [102]. Apart from working in the quasi-static limit, this is the major assumption we will make about the response of the grating.

It is well known that a uniform sheet of current radiates plane electromagnetic waves along the direction of its surface normal [107], that is in the grating frame the fields determining the radiative reaction are given by [102]

$$\mathbf{H}^{ref} = \frac{\omega\epsilon\epsilon_0}{k} E^{ref} e^{iku} \hat{z} \quad (4.27)$$

$$\mathbf{H}^{tra} = -\frac{\omega\epsilon\epsilon_0}{k} E^{tra} e^{-iku} \hat{z}. \quad (4.28)$$

Finally, Eq.3.6 determines the form of $\phi_{L/R}^{rad}$ as [102]

$$\phi_L^{rad} = \gamma E^{ref} \left[\sum_{\substack{g=-\infty \\ g \neq 0}}^{\infty} i \text{sign}(g) \left(d_g^+ e^{|g|x} - d_g^- e^{-|g|x} \right) e^{igy} + y \right] \quad (4.29)$$

$$\phi_R^{rad} = \gamma E^{tra} \left[\sum_{\substack{g=-\infty \\ g \neq 0}}^{\infty} i \text{sign}(g) \left(d_g^+ e^{|g|x} - d_g^- e^{-|g|x} \right) e^{igy} + y \right]. \quad (4.30)$$

To sum up, the potential in all three regions is given by [102]

$$\begin{aligned} \phi_L = & \gamma (E^{sou} + E^{ref}) \left[\sum_{\substack{g=-\infty \\ g \neq 0}}^{\infty} i \text{sign}(g) \left(d_g^+ e^{|g|x} - d_g^- e^{-|g|x} \right) e^{igy} + y \right] \\ & + \sum_{\substack{g=-\infty \\ g \neq 0}}^{\infty} b_g^{sca} e^{igy} e^{|g|x} \end{aligned} \quad (4.31)$$

$$\begin{aligned} \phi_R = & \gamma E^{tra} \left[\sum_{\substack{g=-\infty \\ g \neq 0}}^{\infty} i \text{sign}(g) \left(d_g^+ e^{|g|x} - d_g^- e^{-|g|x} \right) e^{igy} + y \right] \\ & + \sum_{\substack{g=-\infty \\ g \neq 0}}^{\infty} e_g^{sca} e^{igy} e^{-|g|x} \end{aligned} \quad (4.32)$$

$$\phi_I = \sum_{\substack{g=-\infty \\ g \neq 0}}^{\infty} \left(c_g^- e^{igy} e^{-|g|x} + c_g^+ e^{igy} e^{|g|x} \right) + E_0^v y \quad (4.33)$$

The unknown coefficients e_g^{sca} , b_g^{sca} , c_g^- , c_g^+ and E_0^v have to be determined from the boundary conditions.

4.4.3 Boundary conditions

In this and the next section we will determine the unknown coefficients $e_g^{sca}, b_g^{sca}, c_g^-, c_g^+$ and E_0^v to obtain the induced and scattered fields in the slab frame, as well as the radiative reaction parts.

4.4.3.1 Boundary conditions at the slab interfaces

Maxwell's equations demand the continuity of the tangential component of the electric field and normal component of the electric displacement field at an interface between two media [20]. That is at the two slab interfaces x_0 and $x_0 + d$

$$-\epsilon \frac{d\phi}{dx}, \quad (4.34)$$

and

$$-\frac{d\phi}{dy}, \quad (4.35)$$

must be continuous. Since this must hold for any mode g , applying these two boundary conditions at the slab interfaces leads to the following set of equations [102]

$$\begin{aligned}
 (E^{sou} + E^{ref}) &= E_0^v \\
 E_0^v &= E^{tra} \\
 \gamma(E^{sou} + E^{ref}) \left[i\text{sign}(g) \left(d_g^+ e^{|g|x_0} - d_g^- e^{-|g|x_0} \right) \right] + b_g^{sca} e^{|g|x_0} &= \\
 \left(c_g^- e^{-|g|x_0} + c_g^+ e^{|g|x_0} \right) &= \\
 \left(c_g^- e^{-|g|(x_0+d)} + c_g^+ e^{|g|(x_0+d)} \right) &= \\
 \gamma E^{tra} \left[i\text{sign}(g) \left(d_g^+ e^{|g|(x_0+d)} - d_g^- e^{-|g|(x_0+d)} \right) \right] + e_g^{sca} e^{-|g|(x_0+d)} &= \\
 \gamma(E^{sou} + E^{ref}) \left[i\text{sign}(g) \left(d_g^+ e^{|g|x_0} + d_g^- e^{-|g|x_0} \right) \right] + b_g^{sca} e^{|g|x_0} &= \\
 \epsilon \left(-c_g^- e^{-|g|x_0} + c_g^+ e^{|g|x_0} \right) &= \\
 \epsilon \left(-c_g^- e^{-|g|(x_0+d)} + c_g^+ e^{|g|(x_0+d)} \right) &= \\
 \gamma E^{tra} \left[i\text{sign}(g) \left(d_g^+ e^{|g|(x_0+d)} + d_g^- e^{-|g|(x_0+d)} \right) \right] - e_g^{sca} e^{-|g|(x_0+d)}. & \quad (4.36)
 \end{aligned}$$

In principle, the mode number g runs from $-\infty$ to ∞ , but in practice the contribution of high order modes to the scattering quickly decreases and a finite number of terms suffices to achieve convergence. If the highest mode number considered is G , the boundary

conditions in Eq.4.36 constitute a set of $4G + 2$ equations. One too few, as there are $4G + 3$ undetermined coefficients [102]!

Normally, the boundary conditions in Eq.4.34-4.35 are enough to determine the expansion coefficients for the different modes. However, we introduced a radiative reaction term into the electrostatic potentials to model the grating's ability to re-radiate electromagnetic waves, thereby introducing two additional variables E^{ref} and E^{tra} . It is these two variables which lead to an underdetermined set of equations [102]. To determine them we need to introduce an additional boundary condition. This will be the subject of the next section.

Treating E^{ref} as known for the moment, it is straightforward to solve the system of boundary equations in Eq.4.36 to yield the expansion coefficients [102],

$$\begin{aligned}
b_g^{sca} &= \frac{e^{-x_0|g|} \left((\epsilon + 1)(A_g \epsilon - C_g) e^{2d|g|} - (\epsilon - 1)(A_g \epsilon + C_g) + 2\epsilon(B_g - D_g) e^{d|g|} \right)}{(\epsilon + 1)^2 e^{2d|g|} - (\epsilon - 1)^2} \\
c_g^- &= \frac{e^{(x_0+d)|g|} \left(-(\epsilon + 1)(A_g + C_g) e^{d|g|} + B_g(\epsilon - 1) + D_g(1 - \epsilon) \right)}{(\epsilon + 1)^2 e^{2d|g|} - (\epsilon - 1)^2} \\
c_g^+ &= \frac{e^{-x_0|g|} \left((\epsilon + 1)(B_g - D_g) e^{d|g|} - (\epsilon - 1)(A_g + C_g) \right)}{(\epsilon + 1)^2 e^{2d|g|} - (\epsilon - 1)^2} \\
e_g^{sca} &= - \frac{e^{(x_0+d)|g|} \left(2\epsilon(A_g + C_g) e^{d|g|} + (\epsilon + 1) e^{2d|g|} (B_g \epsilon + D_g) + (\epsilon - 1)(D_g - B_g \epsilon) \right)}{(\epsilon + 1)^2 e^{2d|g|} - (\epsilon - 1)^2},
\end{aligned} \tag{4.37}$$

with

$$A_g = -\gamma(E^{sou} + E^{ref}) \left[i \text{sign}(g) \left(d_g^+ e^{|g|x_0} - d_g^- e^{-|g|x_0} \right) \right] \tag{4.38}$$

$$B_g = \gamma E^{tra} \left[i \text{sign}(g) \left(d_g^+ e^{|g|(x_0+d)} - d_g^- e^{-|g|(x_0+d)} \right) \right] \tag{4.39}$$

$$C_g = \gamma(E^{sou} + E^{ref}) \left[i \text{sign}(g) \left(d_g^+ e^{|g|x_0} + d_g^- e^{-|g|x_0} \right) \right] \tag{4.40}$$

$$D_g = -\gamma E^{tra} \left[i \text{sign}(g) \left(d_g^+ e^{|g|(x_0+d)} + d_g^- e^{-|g|(x_0+d)} \right) \right]. \tag{4.41}$$

4.4.3.2 Radiation boundary condition

To unambiguously determine all expansion coefficients it is necessary to introduce an additional boundary condition. This can be obtained from an approximation made regarding the radiative reaction. The key assumption to obtain the form of the radiative reaction $\phi_{L/R}^{rad}$ was to approximate the grating as a thin current sheet supporting a finite and continuous surface current in the v -direction. If this approximation is a

good approximation to model the far field response of the grating, Maxwell's equations provide an additional boundary condition in the grating frame [102]. They demand that the \mathbf{H} -field is discontinuous across an idealised current sheet with the discontinuity determined by the surface current [20], i.e.

$$\mathbf{n} \times (\mathbf{H}_R - \mathbf{H}_L) = \mathbf{J}. \quad (4.42)$$

The far field contributions to $\mathbf{H}_{R/L}$ are given in equations 4.13, 4.27 and 4.28. Thus if the effective current sheet is at position u_0 and the surface current is in the vertical direction such that $\mathbf{J} = J_v \hat{v}$, the boundary condition 4.42 becomes,

$$\frac{\omega\epsilon_0}{k} E^{sou} e^{-iku_0} - \frac{\omega\epsilon_0}{k} E^{ref} e^{iku_0} - \frac{\omega\epsilon_0}{k} E^{tra} e^{-iku_0} = J_v. \quad (4.43)$$

To second order in ku_0 this simplifies to [102]

$$\frac{\omega\epsilon_0}{k} E^{sou} - \frac{\omega\epsilon_0}{k} E^{ref} - \frac{\omega\epsilon_0}{k} E^{tra} = J_v. \quad (4.44)$$

This equation provides an additional link between E^{ref} and E^{tra} and thus allows us to unambiguously determine the radiative reaction of the grating [102]. However, one last hurdle has to be overcome before this is possible, finding the effective current J_v .

4.4.4 Calculating the currents in the grating

In the previous section, we assumed that the grating could be approximated as a thin current sheet with an effective and uniform surface current J_v . Here we will calculate this current.

As aforementioned, the grating is very thin, meaning that the currents in the horizontal direction do not contribute appreciably to the radiative reaction. This justifies the assumption of a thin current sheet with current only along the vertical v -direction. However, the vertical component of the current in the grating still depends on the position (u, v) . To overcome this and obtain an effective uniform current J_v we thus calculate the total current inside the grating over a single unit cell and average over the height of said cell, i.e. $J_v = J_{tot}/(2\pi\gamma)$ [102]. The total current is given by [102]

$$J_{tot} = \int_{S_g} dv du j_v^{gra}, \quad (4.45)$$

where S_g is the surface of a single unit cell of the grating.

This expression is still not straightforward to calculate as S_g is a somewhat complicated surface and the form of the current j_v^{gra} is not known. Here, Transformation optics comes to the rescue, because this current can be evaluated in the slab frame [102]. Transformation optics demands that the v -component of the current in the grating is related to the current in the slab frame via [102]

$$j_v^{gra} = \frac{1}{\det(\Lambda)} \left(\frac{\partial v}{\partial x} j_x + \frac{\partial v}{\partial y} j_y \right), \quad (4.46)$$

where Λ is the Jacobian of the transformation given by

$$\Lambda = \begin{pmatrix} \frac{\partial u}{\partial x} & \frac{\partial u}{\partial y} & 0 \\ \frac{\partial v}{\partial x} & \frac{\partial v}{\partial y} & 0 \\ 0 & 0 & 1 \end{pmatrix}. \quad (4.47)$$

It is also well known that the integration area transforms as [39]

$$\int_{S_g} dudv = \int_{S_s} dx dy \det(\Lambda), \quad (4.48)$$

where S_s is the surface of a single unit cell in the slab frame. The expression for J_{tot} in terms of the slab frame coordinates thus becomes [102]

$$J_{tot} = \int_{x_0}^{x_0+d} dx \int_0^{2\pi} dy \left(\frac{\partial v}{\partial x} j_x + \frac{\partial v}{\partial y} j_y \right). \quad (4.49)$$

This expression is much more susceptible for evaluation, as the integration area is very simple and the partial derivatives $\frac{\partial v}{\partial x}$ and $\frac{\partial v}{\partial y}$ are known from Eq.4.5 as [102],

$$\frac{\partial v}{\partial x} = \gamma \left[\sum_{\substack{g=-\infty \\ g \neq 0}}^{\infty} |g| \left(h_g^+ e^{|g|x} - h_g^- e^{-|g|x} \right) e^{igy} \right] \quad (4.50)$$

$$\frac{\partial v}{\partial y} = \gamma \left[-1 + \sum_{\substack{g=-\infty \\ g \neq 0}}^{\infty} ig \left(h_g^+ e^{|g|x} + h_g^- e^{-|g|x} \right) e^{igy} \right]. \quad (4.51)$$

Likewise the currents inside the slab can be obtained from Ohm's law [4] as [102]

$$j_x = -i\omega(\epsilon_m - 1)\epsilon_0 \left(-\frac{\partial\phi_I}{\partial x} \right) \quad (4.52)$$

$$j_y = -i\omega(\epsilon_m - 1)\epsilon_0 \left(-\frac{\partial\phi_I}{\partial y} \right), \quad (4.53)$$

with the potential defined in Eq.4.33. Evaluating the partial derivatives yields the two components of the current [102]

$$j_x = i\omega(\epsilon_m - 1)\epsilon_0 \sum_{\substack{g=-\infty \\ g \neq 0}}^{\infty} |g| \left(c_g^+ e^{igy} e^{|g|x} - c_g^- e^{igy} e^{-|g|x} \right) \quad (4.54)$$

$$j_y = i\omega(\epsilon_m - 1)\epsilon_0 \left[\sum_{\substack{g=-\infty \\ g \neq 0}}^{\infty} ig \left(c_g^+ e^{igy} e^{|g|x} + c_g^- e^{igy} e^{-|g|x} \right) + E_0^v \right]. \quad (4.55)$$

The integral in Eq.4.49 can now be evaluated. The contribution of the x -components reads

$$\begin{aligned} J_{tot}^x &= \int_{x_0}^{x_0+d} dx \int_0^{2\pi} dy \frac{\partial v}{\partial x} j_x \\ &= i\omega(\epsilon_m - 1)\epsilon_0 \gamma \int_{x_0}^{x_0+d} dx \int_0^{2\pi} dy \left[\sum_{\substack{g=-\infty \\ g \neq 0}}^{\infty} |g| \left(c_g^+ e^{|g|x} - c_g^- e^{-|g|x} \right) e^{igy} \right] \\ &\quad \times \left[\sum_{\substack{p=-\infty \\ p \neq 0}}^{\infty} |p| \left(h_p^+ e^{|p|x} - h_p^- e^{-|p|x} \right) e^{ipy} \right]. \end{aligned} \quad (4.56)$$

The integral over y is trivial to perform as $\int_0^{2\pi} e^{i(g+p)y} dy = 2\pi\delta_{g,-p}$, hence

$$\begin{aligned} J_{tot}^x &= i\omega(\epsilon_m - 1)\epsilon_0 2\pi \gamma \sum_{\substack{p=-\infty \\ p \neq 0}}^{\infty} \int_{x_0}^{x_0+d} dx \left[|p|^2 \left(c_{-p}^+ e^{|p|x} - c_{-p}^- e^{-|p|x} \right) \right. \\ &\quad \times \left. \left(h_p^+ e^{|p|x} - h_p^- e^{-|p|x} \right) \right] \\ &= i\omega(\epsilon_m - 1)\epsilon_0 2\pi \gamma \sum_{\substack{p=-\infty \\ p \neq 0}}^{\infty} \int_{x_0}^{x_0+d} dx |p|^2 \left[c_{-p}^+ h_p^+ e^{2|p|x} + c_{-p}^- h_p^- e^{-2|p|x} \right. \\ &\quad \left. - \left(c_{-p}^+ h_p^- + c_{-p}^- h_p^+ \right) \right]. \end{aligned} \quad (4.57)$$

This integral can now be evaluated since

$$\begin{aligned} \int_{x_0}^{x_0+d} e^{\pm 2|p|x} dx &= \frac{e^{\pm 2|p|x}}{\pm 2|p|} \Big|_{x_0}^{x_0+d} \\ &= \frac{1}{\pm 2|p|} \left(e^{\pm 2|p|(x_0+d)} - e^{\pm 2|p|x_0} \right). \end{aligned} \quad (4.58)$$

Finally the x -contribution to the total current is given by

$$\begin{aligned} J_{tot}^x &= i\omega(\epsilon_m - 1)\epsilon_0 2\pi\gamma \sum_{\substack{p=-\infty \\ p \neq 0}}^{\infty} |p|^2 \left[\frac{c_{-p}^+ h_p^+}{2|p|} \left(e^{2|p|(x_0+d)} - e^{2|p|x_0} \right) \right. \\ &\quad \left. - \frac{c_{-p}^- h_p^-}{2|p|} \left(e^{-2|p|(x_0+d)} - e^{-2|p|x_0} \right) - (c_{-p}^+ h_p^- d + c_{-p}^- h_p^+ d) \right]. \end{aligned} \quad (4.59)$$

The contribution from the y -component can be evaluated similarly and gives

$$\begin{aligned} J_{tot}^y &= i\omega(\epsilon_m - 1)\epsilon_0 2\pi\gamma \left(-E_0^v \gamma d + \sum_{\substack{p=-\infty \\ p \neq 0}}^{\infty} |p|^2 \left[\frac{c_{-p}^+ h_p^+}{2|p|} \left(e^{2|p|(x_0+d)} - e^{2|p|x_0} \right) \right. \right. \\ &\quad \left. \left. - \frac{c_{-p}^- h_p^-}{2|p|} \left(e^{-2|p|(x_0+d)} - e^{-2|p|x_0} \right) + (c_{-p}^+ h_p^- d + c_{-p}^- h_p^+ d) \right] \right). \end{aligned} \quad (4.60)$$

Adding the two gives the final result for the total current [102]

$$\begin{aligned} J_{tot} &= i\omega(\epsilon_m - 1)\epsilon_0 2\pi\gamma \left(-E_0^v \gamma d + \sum_{\substack{p=-\infty \\ p \neq 0}}^{\infty} |p| \right. \\ &\quad \left. \times \left[(c_{-p}^+ h_p^+ \left(e^{2|p|(x_0+d)} - e^{2|p|x_0} \right) - c_{-p}^- h_p^- \left(e^{-2|p|(x_0+d)} - e^{-2|p|x_0} \right)) \right] \right). \end{aligned} \quad (4.61)$$

At the moment it is not yet clear how this expression can help to find a simple relation between E^{ref} and E^{sou} . The usefulness of this formula becomes a little more obvious if we use the fact that $E_0^v = E^{tra} + E^{ref}$ (see Eq.4.36) and that the expansion coefficients c_g^\pm are proportional to $(E^{tra} + E^{ref})\gamma$ (see Eq.4.37) such that we can write [102]

$$c_g^\pm = (E^{sou} + E^{ref})\gamma c_{2,g}^\pm. \quad (4.62)$$

Hence, the expression for the total current becomes [102]

$$J_{tot} = i\omega(\epsilon_m - 1)\epsilon_0 2\pi\gamma^2 (E^{sou} + E^{ref})N, \quad (4.63)$$

with

$$N = -d + \sum_{\substack{p=-\infty \\ p \neq 0}}^{\infty} |p| \left[(c_{2,-p}^+ h_p^+ (e^{2|p|(x_0+d)} - e^{2|p|x_0}) - c_{2,-p}^- h_p^- (e^{-2|p|(x_0+d)} - e^{-2|p|x_0})) \right]. \quad (4.64)$$

It pays off to inspect the expression for the total current before proceeding to solve the remaining boundary condition. It is clear from Eq.4.64 that every single Fourier mode contributes to the averaged total current in the grating frame. As aforementioned, the current directly leads to the radiation of electromagnetic waves. Eq.4.63 and Eq.4.64 thus describe the grating's ability to out-couple a fraction of each induced Fourier mode into a plane electromagnetic wave [102]. This is the radiative reaction of the grating. It is in contrast to the radiative reaction of a slab. In a slab, the current from the higher order modes would average to zero and the only contribution would come at $\omega \rightarrow 0$ from the zeroth order mode.

The results are, however, to be expected from the transformation. We showed previously that a plane wave in the grating frame transforms into a sum of Fourier modes in the slab frame, it is thus not unexpected that a single Fourier mode in the slab frame also contributes to a plane wave in the grating frame upon transformation [102].

4.4.5 Reflection and transmission

In this section, we use the expression for the current and the radiation boundary condition in Eq.4.44 to derive expressions for the transmission and reflection coefficient, as well as the power absorption in the grating.

Starting from the additional radiation boundary condition in Eq.4.44

$$\frac{\omega\epsilon_0}{k} E^{sou} - \frac{\omega\epsilon_0}{k} E^{ref} - \frac{\omega\epsilon_0}{k} E^{tra} = J_v, \quad (4.65)$$

E^{ref} and E^{tra} can, at last, be determined unambiguously. Substituting the expression for the current while noting that $J_v = J_{tot}/(2\pi\gamma)$ yields

$$\frac{\omega\epsilon_0}{k} E^{sou} - \frac{\omega\epsilon_0}{k} E^{ref} - \frac{\omega\epsilon_0}{k} E^{tra} = i\omega(\epsilon_m - 1)\epsilon_0\gamma(E^{sou} + E^{ref})N. \quad (4.66)$$

Since the set of boundary conditions in Eq. 4.36 gives another relation between reflected and transmitted field, $E^{tra} = E^{sou} + E^{ref}$, these two simultaneous equations are easily

solved. They give [102]

$$E^{ref} = \frac{ik(\epsilon_m - 1)\gamma N}{2 - ik(\epsilon_m - 1)\gamma N} E^{sou} \quad (4.67)$$

$$E^{tra} = \frac{2}{2 - ik(\epsilon_m - 1)\gamma N} E^{sou}. \quad (4.68)$$

E^{ref} and E^{tra} represent the amplitude of two outgoing plane waves carrying energy to infinity. One associated with reflection, the other with transmission. Since both are proportional to the amplitude of the plane wave source E^{sou} , the reflection (r) and transmission (t) coefficients of the metallic grating under investigation can be easily inferred from $E^{ref} = rE^{sou}$ and $E^{tra} = tE^{sou}$. Thus [102],

$$r = \frac{ik(\epsilon_m - 1)\gamma N}{2 - ik(\epsilon_m - 1)\gamma N} \quad (4.69)$$

$$t = \frac{2}{2 - ik(\epsilon_m - 1)\gamma N}. \quad (4.70)$$

The ratio of the power absorbed can then be simply calculated from [102]

$$\frac{Q}{P_{sou}} = 1 - |r|^2 - |t|^2, \quad (4.71)$$

where P_{sou} is the power contained in the source wave.

The two equations for reflection and transmission coefficients have the same form as the reflection and transmission from a two-dimensional conducting sheet [108],

$$r = \frac{-\sigma Z_0}{2 + \sigma Z_0} \quad (4.72)$$

$$t = \frac{2}{2 + \sigma Z_0}, \quad (4.73)$$

where σ is the surface conductivity and Z_0 corresponds to the impedance of free space $Z_0 = \sqrt{\mu_0/\epsilon_0}$. The far field response of the grating can thus be described by a two-dimensional conducting sheet with an effective surface conductivity given by $\sigma_{eff} = ik(\epsilon_m - 1)\gamma N/Z_0$ [102]. Of course this should not come as a surprise, because the main assumption when modelling the grating's far field response was that it can be described as a thin current sheet, yet, Eq.4.69 and Eq.4.70 provide a neat formal analogy.

The simplicity of the reflection and transmission coefficients also allows to obtain an intuitive understanding of the grating's optical response before computing the result.

The transformation parameter γ determines the overall system size (the system increases monotonically with γ). Thus, if γ becomes very large the grating becomes very thick and, as one would expect, the transmission coefficient decreases. Furthermore, the factor $(\epsilon_m - 1)$ ensures that the reflection vanishes if the permittivity of the grating approaches that of its surroundings (in this case air with unit permittivity). All the structural information about the grating is encoded into the factor N defined in Eq.4.64. It depends on frequency via the coefficients $c_{2,\pm p}^\pm$ and the geometrical information is encoded in both $c_{2,-p}^\pm$ and h_p^\pm . It can be shown from the defining equations for $c_{2,-p}^\pm$ and h_p^\pm that their products $c_{2,-p}^\pm h_p^\pm$ decay slower versus p , the larger the grating's modulation depth. This is also an intuitive result as one might expect that a very strongly corrugated surface is quite efficient in diffracting plane waves into higher order modes. This is then reflected in the reflection and transmission coefficients.

Eq.4.69 and Eq.4.70 seem to make intuitive sense, the next section will provide a quantitative analysis of their validity.

4.5 Optical response: results

In this section, we will test our theory's prediction by comparison with full electrodynamic simulations using the 'frequency domain solver' of the COMSOL Multiphysics software. Reflection, transmission and absorption spectra are discussed, as well as the maximum field enhancement obtainable in the structures.

4.5.1 Reflection, transmission and absorption

Eq.4.69 and Eq.4.70 give the reflection and transmission coefficients for a plane wave normally incident on the grating. Figure 4.9 shows a comparison between the analytical results and full electrodynamic COMSOL simulations for the weakly and strongly modulated grating. The COMSOL simulations have been performed in the frequency domain, with exciting and receiving ports to model the source. The plane wave has been chosen to be incident on the modulated side of the gratings. The discussion follows the one in [102].

The agreement between analytics and simulations is near perfect for the weakly modulated grating. Only slight discrepancies arise in the peak heights of the transmittance spectrum. Note that both gratings are nearly transparent around $\omega = 3eV$, as the transmittance approaches unity [102]. The excellent agreement in the peak position for both gratings should not come as a surprise with regards to our earlier discussion of the

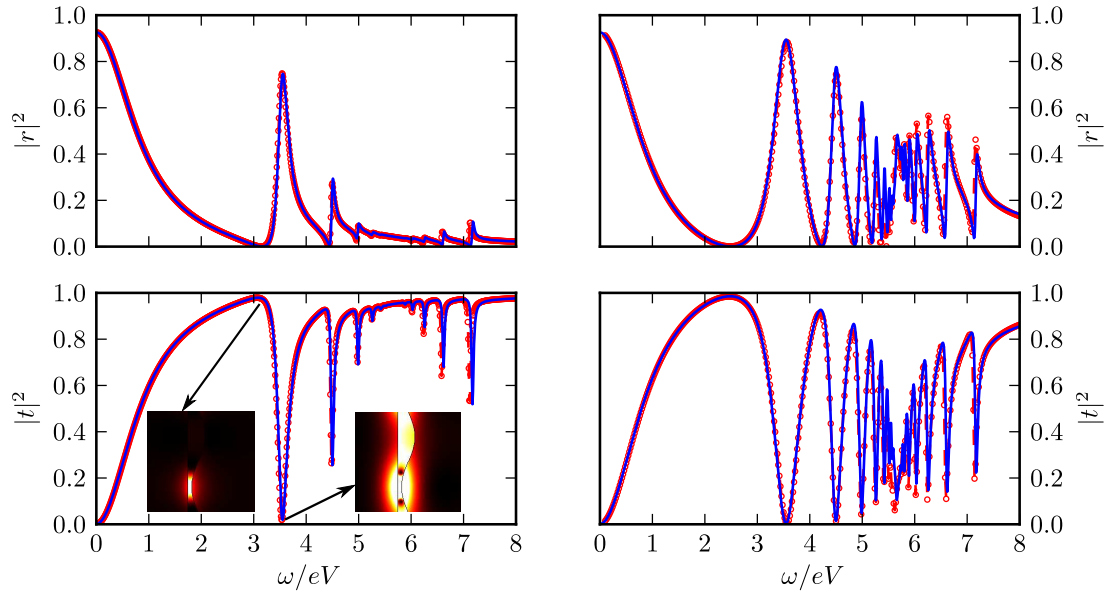


Figure 4.9: Reflectance (top) and transmittance (bottom) for the weakly (left) and strongly (right) modulated grating (shown in figure 4.7). Blue lines correspond to analytical calculations, whereas the red lines with circles are COMSOL simulations. In COMSOL the wave is incident on the modulated side of the grating. The insets show the electric energy density in and close to the grating at the first transmission peak and dip (same color scale). For both analytics and simulations the permittivity of the grating was $\epsilon_m = 1 - \omega_p^2/(\omega(\omega + i\gamma))$ with $\omega_p = 8eV, \gamma = 0.032eV$. The surrounding dielectric is air with $\epsilon_d = 1$. Reprinted with permission from [102], available under the Creative Commons Attribution 3.0 License.

dispersion relation (see figure 4.7), but can be considered a clear success of the theory [102]. It confirms our earlier statement that in the quasi-static limit, the plasmon resonance condition is solely determined by the underlying slab structure, for excitations with k_y near the zone centre [102].

A feature shared by the weakly and strongly modulated grating that is noteworthy is the reflection peak at zero frequency [102]. The reflectivity rises in both spectra as the frequency is lowered towards zero, signifying a coupling to the zeroth-order mode ($g = 0$). Previous Transformation optics studies [47, 55, 62] did not report any coupling to the zeroth order mode, as there is a fundamental difference between the systems studied in, e.g. Refs. [47, 55, 62], and the gratings: the gratings are able to support continuous currents on a scale larger than the wavelength, something the structures in [47, 55, 62] cannot. This provides the coupling to the lowest order mode [102].

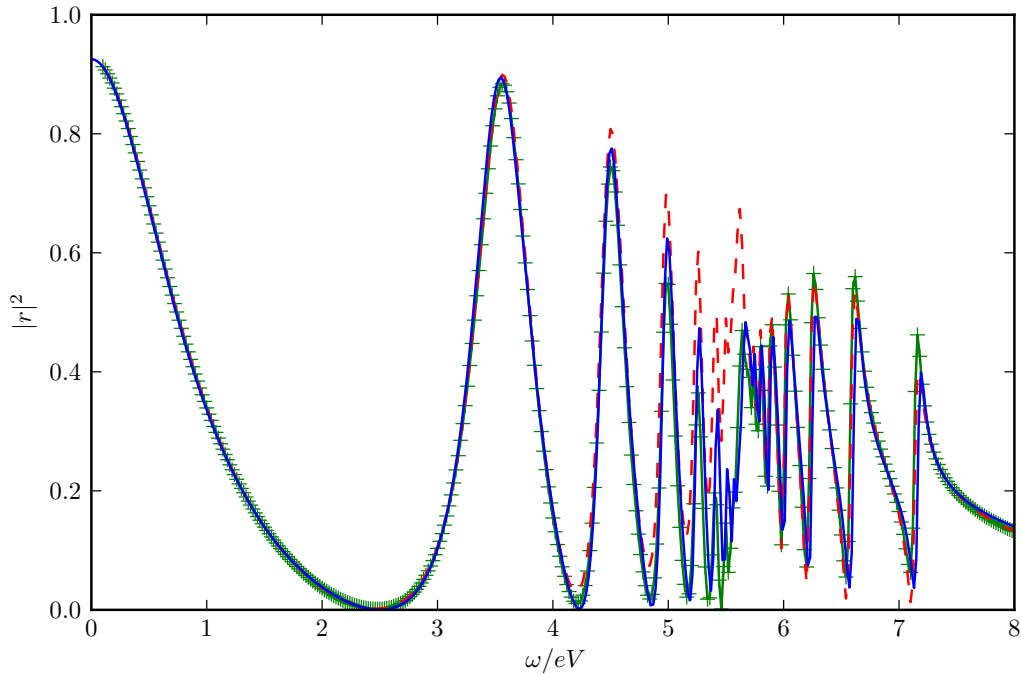


Figure 4.10: Reflectance from the strongly modulated grating for incidence from the right (on modulated side, red dashed) and left (flat side, green crosses). The analytical solution lies between the two curves (blue line).

A close inspection of the reflection spectra in figure 4.9 reveals that the resonances have an asymmetric line shape akin to a Fano resonance [77, 79, 81, 109]. Again this is most easily understood using the Transformation optics framework. Figure 4.3 gives a conformal transformation from an asymmetric annulus to the gratings under consideration. Asymmetric annuli have been shown to support multiple Fano resonances; a detailed study based on Transformation optics can be found in [55]. Figure 4.9 has two insets showing the electric energy density distribution. It is apparent that the energy is much more concentrated around the structure at the transmission dip than it is at the transmission peak [102]. This is in agreement with the study in [55].

The question arises why the line shape for the strongly modulated grating is so much more symmetric. Most likely the stronger radiation damping leads to a peak broadening which covers the asymmetry [102].

While the agreement between theory and simulations is excellent for most of the spectrum, there are some discrepancies at the higher order modes near the surface plasma frequency ($\approx 5.6eV$). These higher order modes are not present for the weakly modu-

lated grating, as it is not able to couple to them due to the rapid decay of the expansion coefficients [102]. However, the strongly modulated grating is able to couple to them as the expansion coefficients decay more slowly with increasing mode number and discrepancies near the surface plasma frequency become visible [102]. The problem is easy to understand intuitively, yet tricky to solve technically. Imagine a moderately thick grating with a flat side and a modulated side. If a plane wave is incident on the flat side there will, first of all, be a reflection into the zeroth order mode as the flat side cannot provide any momentum to couple to the higher order modes. As the transmitted part of the wave travels through the grating towards the modulated side it loses energy due to resistive losses. That is, the wave will be attenuated by the time it reaches the modulated interface where it can couple to the higher order modes. On the contrary, if the plane wave is incident on the modulated side, the grating can immediately couple to the higher order modes, meaning that more of the energy is funneled into these modes as the wave has not been attenuated yet. This leads to a difference in the reflection coefficient for a wave incident on the flat or modulated side and also means that the out-coupling into radiation is different on both sides. The transmission coefficients are of course identical, as they must be due to reciprocity [110]. Figure 4.10 shows this behaviour. As predicted, the wave incident on the modulated side (red dashed line) couples more strongly to the higher order modes. The problem with the analytics is that it does not capture this behaviour for two reasons. First, the source potential obtained in the slab frame is independent of the direction of incidence in the grating frame. Second, the assumption that the grating can be modelled as a thin current sheet means that the grating radiates equally to either side.

Finally, figure 4.11 gives the ratio of the absorbed to incident power as calculated from Eq.4.71. Again the agreement between analytics and theory is excellent, with the exception of the modes around the surface plasma frequency. Note that the absorption reaches around 70%, which is significant for such a thin grating.

4.5.2 Realistic permittivities

In the previous section, we looked at the optical response of our TO-designed grating using a Drude model for its permittivity. While this gave rise to a set of well defined and sharp resonances, which allowed us to accurately compare our theory with numerical simulations, it is not the most realistic model for permittivity. Here, we take the permittivity of the grating to be that of silver, using the experimental data published in [65].

4.5.2.1 Reflection and transmission for real silver

Here, we give the reflection and transmission of the weakly and strongly modulated grating for a silver grating surrounded by a dielectric with $\epsilon_d = 1$. Figure 4.12 compares analytical results with COMSOL simulations. As expected, the graphs show fewer resonances, as losses are much stronger than previously. As previously, the strongly modulated grating is more efficient in exciting higher order modes near the surface plasma frequency (here around $\approx 3.67eV$) than the weakly modulated grating. Yet, even for the strongly modulated grating the higher order modes are strongly damped, which leads to a much better agreement between analytics and numerics in the reflection than previously. However, small discrepancies remain for the same reasons as in the Drude model case. The overall agreement between analytics and numerical simulations is still excellent and our theory correctly predicts the response of gratings with realistic material parameters, as well.

4.5.2.2 Field enhancement

As has been pointed out in the introduction, applications of plasmonic gratings include surface-enhanced Raman spectroscopy (SERS), where the strong field enhancements in the grating's grooves lead to an enhanced Raman signal. Here, we briefly touch upon

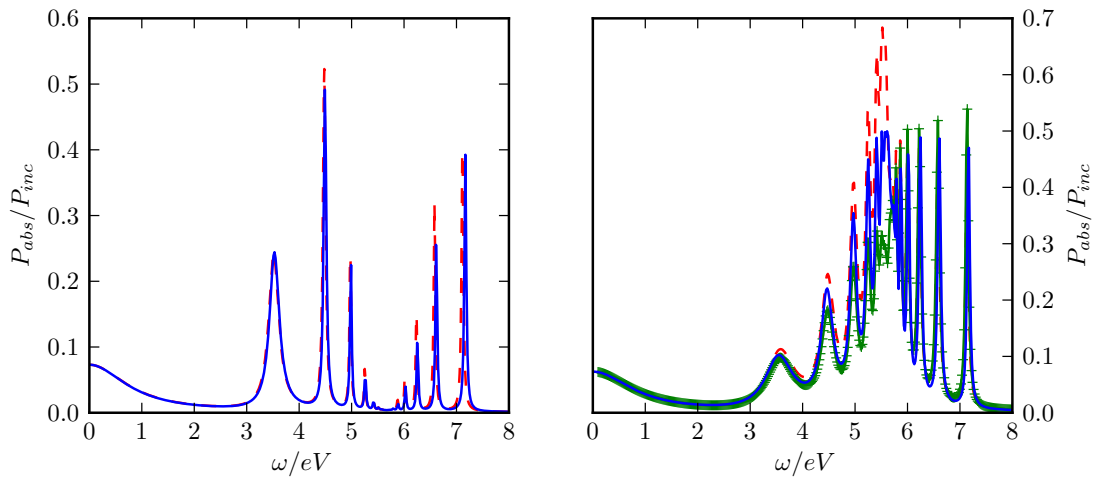


Figure 4.11: Power absorbed by the grating. Left the weakly modulated grating, analytical solutions are in blue, red dashed solutions correspond to COMSOL and incidence from the right. Right, the strongly modulated grating. Analytical solutions are shown in blue, COMSOL simulations for incidence from the right (red-dashed lines) and incidence from the left (green crosses).

the viability of using the gratings studied here for SERS. Figure 4.13 shows the field enhancement for the weak and strong grating with realistic values of the permittivity [65]. It is apparent that most of the energy is concentrated near the thinnest parts of the grating, thus forming a periodic array of hotspots [102]. The formation of hotspots is easily understood from the transformation [102]. In the equivalent slab system the energy is spread out evenly in the slab due to its translational invariance. Hence, figure 4.5 provides an explanation for the hotspots. At the thinnest part of the grating the contour lines lie most dense, thus space is squashed and the energy has to be squeezed into a smaller area than at the ‘fat’ part of the grating. As can be expected, the field enhancement is larger for the strongly modulated grating (~ 30) than for the weakly modulated one (~ 20). Unfortunately, both values are smaller than in previous transformation optics based studies [47] and also other grating designs [89], where enhancement factors of about ~ 200 have been reported. It does appear that there are better suited

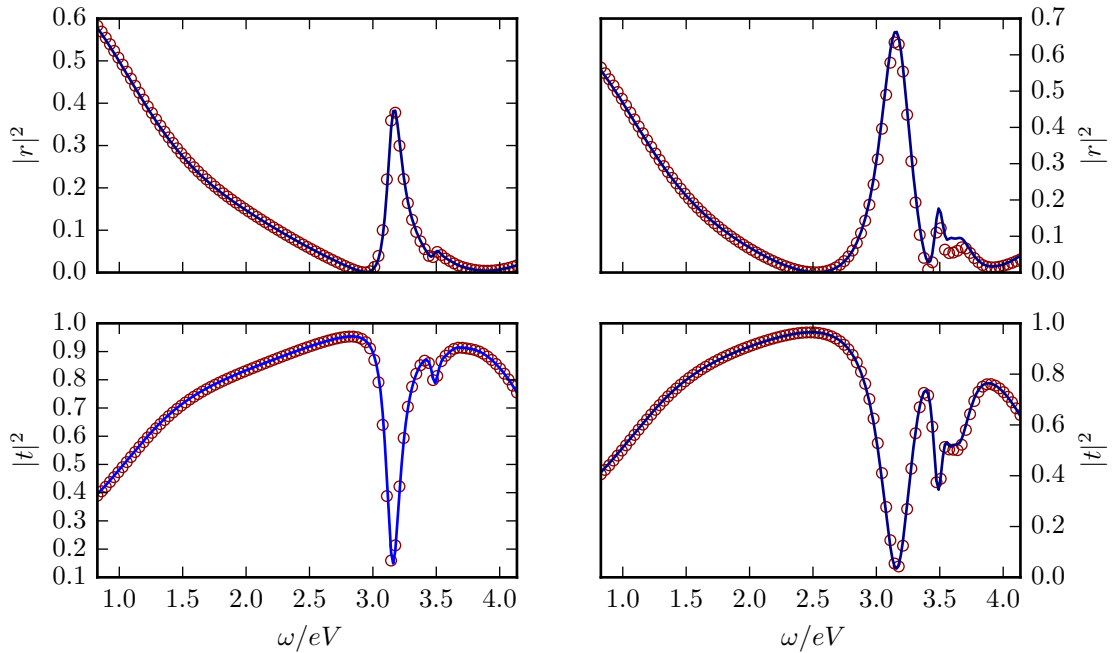


Figure 4.12: Reflection (top) and transmission (bottom) for the weakly (left) and strongly (right) modulated grating (shown in figure 4.7). Blue lines correspond to analytical calculations, whereas the red open circles are COMSOL simulations. In COMSOL the wave is incident on the modulated side of the grating. For both analytics and simulations we used experimental values for the permittivity of silver [65]. The surrounding dielectric is air with $\epsilon_d = 1$.

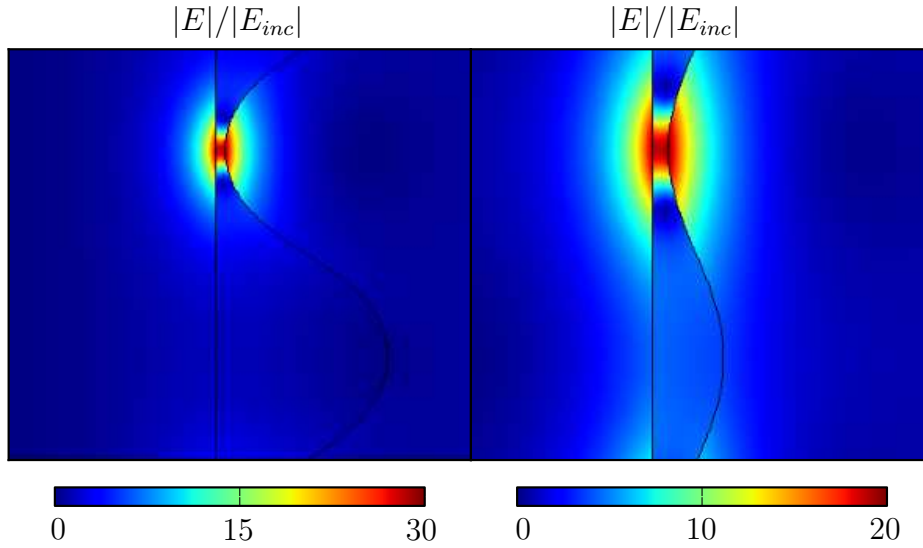


Figure 4.13: Maximum field enhancement normalised by the incident electric field for the strongly (left) and weakly (right) modulated grating. The field enhancement was calculated using COMSOL with experimental values for the permittivity of silver [65]. $\text{Re}(\epsilon_m) = -3.88$, $\text{Im}(\epsilon_m) = -0.16$ at $\omega \approx 3.2eV$. Reprinted with permission from [102], available under the Creative Commons Attribution 3.0 License.

grating designs if one is interested in SERS, however, it should be stressed that no optimisation procedures have been implemented and that the field enhancement could probably be increased beyond the current values.

4.6 Bi-anisotropic effects in plasmonic gratings

In the previous section we calculated the optical response of our plasmonic grating under plane wave illumination at normal incidence and compared to numerical simulations. The agreement was mostly excellent, however some discrepancies arose for higher order modes. Due to the strong decay of these high order modes, the reflection of the grating was different for illumination on the flat or corrugated side of the grating. This effect could not be described analytically using our simple ‘current sheet’ model with an effective surface conductivity. In fact, different reflection properties for waves incident from opposite directions are a signature of bi-anisotropy. While bi-anisotropic effects

could not be incorporated into our analytical model, they can still be characterised using numerical simulations.

4.6.1 Parameter retrieval for bi-anisotropic metamaterials

A uniaxial bi-anisotropic medium is characterised via its ability to couple electric and magnetic fields, which naturally leads to different reflection properties for left and right travelling waves [110]. Specifically, the introduction of a magneto-electric coupling leads to a redefinition of the auxiliary fields \mathbf{D} and \mathbf{B} according to [111]:

$$\begin{aligned}\mathbf{D} &= \boldsymbol{\epsilon}\mathbf{E} + \boldsymbol{\xi}\mathbf{H} \\ \mathbf{B} &= \boldsymbol{\mu}\mathbf{H} + \boldsymbol{\zeta}\mathbf{E},\end{aligned}$$

with

$$\boldsymbol{\epsilon} = \begin{pmatrix} \epsilon_x & 0 & 0 \\ 0 & \epsilon_y & 0 \\ 0 & 0 & \epsilon_z \end{pmatrix}, \boldsymbol{\mu} = \begin{pmatrix} \mu_x & 0 & 0 \\ 0 & \mu_y & 0 \\ 0 & 0 & \mu_z \end{pmatrix} \quad (4.74)$$

and

$$\boldsymbol{\xi} = \begin{pmatrix} 0 & 0 & 0 \\ 0 & 0 & 0 \\ 0 & -i\xi_0 & 0 \end{pmatrix}, \boldsymbol{\zeta} = \begin{pmatrix} 0 & 0 & 0 \\ 0 & 0 & i\xi_0 \\ 0 & 0 & 0 \end{pmatrix}. \quad (4.75)$$

ξ_0 is the magneto-electric coupling parameter and determines the strength of the bi-anisotropy. It can be shown [110, 111] that the reflectivity of a slab of such a material depends on the direction of incidence, whereas the transmission does not (due to reciprocity, [110]). It thus shows the same properties as our strongly modulated grating, indicating that the grating can be modeled as a thin bi-anisotropic slab with an effective $\boldsymbol{\epsilon}^{eff}$, $\boldsymbol{\mu}^{eff}$ and ξ_0^{eff} .

For a wave travelling along the x -direction such that $\mathbf{H}^{sou} = -\frac{\omega\epsilon_0}{k} E^{sou} e^{-ik_0 u} \hat{z}$, the relevant components of the permittivity tensor are ϵ_y^{eff} and μ_z^{eff} . They can be retrieved from the scattering (S-)parameters

$$\mathbf{S} = \begin{pmatrix} S_{11} & S_{12} \\ S_{21} & S_{22} \end{pmatrix} \quad (4.76)$$

as follows. First, determine the effective refractive index $n^{eff} = \pm \sqrt{\mu_z^{eff} \epsilon_y^{eff} - (\xi_0^{eff})^2}$ from [111]

$$\cos(n^{eff} k_0 d) = \frac{1 - S_{11} S_{22} + S_{21}^2}{2S_{21}}, \quad (4.77)$$

under the ‘passive medium’ condition $\text{Im}(n^{eff}) \geq 0$. Here d is the thickness of the effective medium slab [111]. The effective permittivity, permeability, magneto-electric coupling parameter and the left and right incidence surface impedances are then obtained from [111]

$$\xi_0^{eff} = \frac{n^{eff}}{-2 \sin(n^{eff} k_0 d)} \left(\frac{S_{11} - S_{22}}{S_{21}} \right) \quad (4.78)$$

$$\mu_z^{eff} = \frac{i n^{eff}}{\sin(n^{eff} k_0 d)} \left(\frac{2 + S_{11} + S_{22}}{2S_{21}} - \cos(n^{eff} k_0 d) \right) \quad (4.79)$$

$$\epsilon_y^{eff} = \frac{(n^{eff})^2 + (\xi_0^{eff})^2}{\mu_z^{eff}}, \quad (4.80)$$

$$z_{\pm}^{eff} = \frac{\mu_z^{eff}}{n^{eff} \pm \xi_0^{eff}}. \quad (4.81)$$

Here, the ‘passive medium’ condition demands that $\text{Re}(z_{\pm}^{eff}) \geq 0$.

The S-parameters are readily obtained from COMSOL simulations, note that S_{11}/S_{22} are related to the reflection coefficients and S_{12}/S_{21} determine the transmission coefficients.

Figure 4.14 shows the effective material parameters for the weakly (dashed lines) and strongly (solid lines) modulated grating. Here, we used permittivity data for silver [65] for the grating and assumed $\epsilon_d = 1$. The effective material parameters are then obtained from Eq.4.78-Eq.4.80 using the left and right reflection, and transmission coefficients obtained from COMSOL simulations. Focussing on the effective permittivity, we observe that at low frequencies the real part of the effective permittivity becomes very large and negative. This is to be expected, as silver is a metal and thus is completely opaque at low frequencies. This means the modulation of the grating is not too important at these frequencies, as the grating simply reflects all incoming light and essentially behaves like a slab. Thus the effective permittivity behaves as the real permittivity and attains large negative values. Things are more interesting at higher frequencies. Whereas the real part of the permittivity of silver behaves as an (almost) strictly increasing function of frequency [65], the effective permittivity shows several resonances, corresponding to the plasmons excited in the grating (see figure 4.12). As expected, the resonances

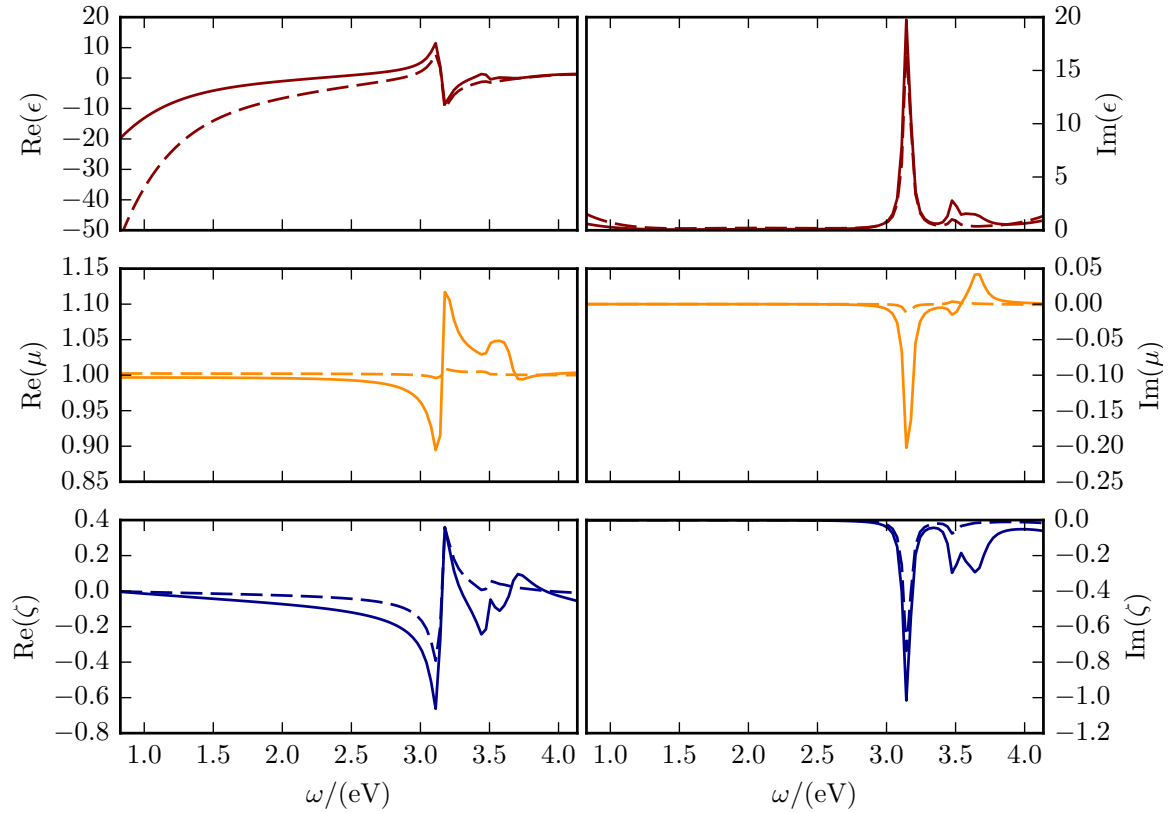


Figure 4.14: Effective material parameters for the strongly (solid lines) and weakly (dashed lines) modulated grating. In both cases the equivalent metamaterial was a symmetric slab. The thickness of the slab was set to the maximum thickness of the grating 10.75nm and 26.1nm for the weakly and strongly modulated grating, respectively. The original permittivity of the two gratings was that of silver with permittivity data from [65], whereas the original permeability was 1.

are stronger for the more strongly modulated grating, especially at the surface plasma frequency ($\approx 3.67\text{eV}$). This difference is even more prominent for the effective magnetic response. The most interesting parameter in figure 4.14 is ξ_0^{eff} , which leads to the coupling between the electric and magnetic fields. For a completely symmetric system, such as a slab or a conductive sheet, this parameter will be exactly zero. However, as is evident from figure 4.14, it is non-zero for the two gratings. We see that the coupling parameter ξ_0^{eff} is of the same order as the effective permeability and should thus be included in a complete description of the grating's properties.

A more thorough simulation based and experimentally verified study of the role of bianisotropy in plasmonic gratings has been published in [112].

4.7 Summary

In this chapter, Transformation optics has been applied to analyse plasmonic gratings for the first time. It was shown how a whole *symmetry class* of gratings can be treated within a unified framework by relating it to a simple slab via a conformal map. The gratings thus designed showed some very interesting behaviour; they exhibited ‘degeneracy points’ in the dispersion relation caused by the hidden symmetry of the underlying slab structure and they efficiently concentrated energy into hotspots (even though the light harvesting was less impressive than in previous studies). Both these effects could be predicted using the analytical theory developed in the report. The agreement between theory and numerical simulations has been excellent in limiting cases, however, the range of applicability is limited. The present theory is able to accurately predict the energy band structure near the Brillouin zone centre, which is enough if one is interested in the gratings’ response to far field light sources. However, it currently fails in predicting the band structure near the zone edge, which means it is not suitable to calculate the grating’s response to near field excitations (e.g. point dipoles). The second short-coming of the theory is its inability to distinguish the reflection coefficient of the grating for incidence from one side or the other. For non-symmetric lossy gratings the reflection coefficients are different and render the gratings ‘bi-anisotropic’. This ‘bi-anisotropic’ has been studied numerically and quantified. As expected, it is relatively small in our case, which explains the good agreement with our theory. However, for ‘thicker’ and even more asymmetric gratings this effect is likely to become stronger and should be included for an accurate calculation of the transmission and reflection properties of such gratings.

Chapter 5

Transformation optics applied to Electron Energy-Loss Spectroscopy (EELS)

5.1 A very brief introduction to EELS

In the previous two chapters, hidden symmetries were pivotal to our analyses of the optical response of the ellipse, spheroids and the plasmonic grating. The properties and response under plane wave illumination of all three systems have been studied by transforming them to geometries with much higher symmetry. In this chapter, we will apply the same formalism, but to a new application of TO. Namely, the study of Electron Energy-Loss Spectroscopy and Cathodoluminescence problems.

Let us briefly outline a theorist's take on what constitutes the most basic electron energy loss and CL studies. Figure 5.1 illustrates the basic problem. An electron moves past a (spherical) nanoparticle at high velocity. Associated with the moving electron is an electric field containing a broad range of frequencies. This electric field leads to an induced field in the nanoparticle and, if the particle supports them, can excite plasmons. The electron thus transfers some of its energy to the nanoparticle. In EELS one measures the energy lost by the electron as a function of frequency to obtain information about the spectral properties of the nanoparticle. Complementary to this are CL measurements. In those, one measures the photons scattered by the nanoparticle.

The aim of this chapter is thus to use TO to calculate the energy lost by a fast moving electron when it moves past a nanoparticle and to calculate the nanoparticle's photon emission spectrum. We rely on several assumptions in our approach. First,

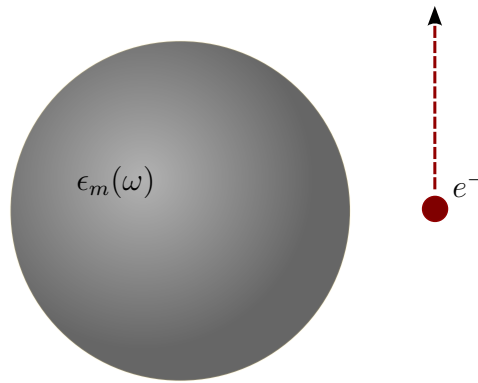


Figure 5.1: Schematic of an electron energy loss problem. An electron (red circle) moves past a metallic nanoparticle at high velocity. The electric field of the moving electron excites localised surface plasmons, leading to an energy transfer from electron to the nanoparticle. The fields induced in the nanoparticle also lead to a scattered field.

we work in the electrostatic limit (with the exception of radiative losses, which we can introduce). This places limits on the particle's size [20]. Second, and following from the first, we ignore relativistic effects, so we cannot treat highly relativistic electrons, though the non-relativistic approximation goes a long way. Third, we assume that the energy lost by the electron is small compared to its total energy, such that its trajectory is unaltered and its velocity remains constant. Last, and most importantly, we will apply the TO approach to two-dimensional geometries. That is we assume invariance in the solution along the third dimension, which means that instead of calculating the system's response with respect to a point charge, we do it for a line charge. Of course, in realistic experiments this is not the case, as the exciting electron is a three-dimensional point particle. However, there is a workaround. In realistic experiments on two-dimensional nanoparticles, i.e. where one dimension is much larger than the other two, a real electron is going to transfer energy in the two-dimensional plane, as well as out-of-plane. If the electron transfers energy in the out-of-plane direction, there will be a change in its out-of-plane momentum, too. Thus, if the electrons that have changed their out-of-plane momentum are filtered out, one is left with the ones that have not lost any energy out-of-plane. These can be considered as effectively two-dimensional, as there was no change in their out-of-plane momentum. It is the energy lost by those electrons that can be calculated in a two-dimensional calculation. This is absolutely crucial and has to be kept in mind for the remainder of this chapter. In the following analytical treatment we may speak of a line electron or simply electron at times, but it is understood that we always mean a line electron, as it is a two-dimensional calculation.

The results presented in this chapter are by and large based on the paper [66] and its supplementary material, including the introduction below.

Historically, EELS has been pivotal to the development of plasmonics as we know it today. Starting from the experimental discovery and characterisation of plasmons more than half a century ago [113–115] up to present day investigations into quantum effects of plasmonic systems [116–118], EELS (and CL) have proved valuable tools in fundamental studies of plasmonic systems. Correspondingly large, is the literature associated with it. We can thus only aim to refer to a select few studies that have influenced the field in the past decade, but even here we cannot claim a complete list.

Of particular appeal are the high spatial resolution achieved in EELS (see [119], p.13), which is of importance in the study of plasmonic particles with nanometer sized features. The high resolution paired with the ability to excite ‘dark’ modes [120], which cannot be excited by external radiation, makes EELS ideally suited to create maps of the plasmon’s field patterns [120–125] and collect information about the local density of states [126, 127]. As mentioned, this also allowed investigations into quantum effects of closely spaced nanoparticles [116–118], where quantum tunneling becomes a possibility [116, 128]. EELS measurements can be complemented by CL measurements, in which the photons emitted from the nanoparticle are measured, rather than the electrons itself [119]. This technique, too, has been applied in recent state-of-the-art plasmonic experiments with great success [119, 123, 129, 130]. Reference [131] and [132] provide nice reviews of the subject.

Experiments are supported by a wide range of theoretical techniques to model EELS. A recent paper by Cao et. al. [133] implemented a finite-difference time-domain (FDTD) simulation using the commercial software package Lumerical. In their introduction, the authors give a nice overview of numerical techniques available for the study of EELS experiments, from which we quote the following passage [133]:

“For such simulations a myriad of different numerical techniques have been developed in the past years, including boundary element method (BEM)[134, 135], discrete dipole approximation (DDA)[136–138], finite-element method (FEM)[118, 125, 139], finite-difference time-domain (FDTD) method [140] and discontinuous Galerkin time-domain (DGTD) method [141]. Although these methods are able to predict and interpret experimental EELS spectra, they possess some of the following significant drawbacks: (i) the need for large computational resources [136–138], (ii) limitations to nonpenetrating electron trajectories [137–139, 141], (iii) requiring highly symmetrical ge-

ometries [134–138], and (iv) complexity (i.e., programming skills required, absence of user-friendly interface) [134–141].”

Clearly, there are numerous computational methods to obtain EELS spectra, all of which seem to have one limitation or another, such that there is no *de facto* standard for EELS computations yet. Analytical methods also exist, but are limited to a only a few geometries. Examples where the response of metal/dielectric particles and surfaces under excitation with electron beams have been studied include [132]: planar surfaces [142, 143], spheres [144, 145], coupled spheres [146] and cylinders [147], ellipsoids [148] and parabolic wedges [143]. Though this list may not be exhaustive, Garcia de Abajo remarks [132]:

“...the list of structures that can be accessed with analytical tools is short and we need in general to rely on numerical methods for more complicated shapes.”

TO has proved a valuable tool in the analysis of plasmonic systems with complicated geometries [27]; while we do not expect the remainder of this chapter to completely change the validity of the above statement, we strongly believe that a TO approach to EELS and CL can significantly extend the list of structures that can be analysed analytically. This chapter introduces such an approach (see [61, 66, 149]) and we apply it to a non-concentric annulus and an ellipse.

First, we calculate the electrostatic potential of a moving charge. Then we present a detailed derivation of the electron energy loss probability and photon emission probability for a two-dimensional non-concentric annulus that is excited by an electron beam. As a second example, we derive the same quantities for a two-dimensional ellipse. All calculations are done in frequency space and are fully analytical, which allows us to obtain time-domain solutions by an inverse fourier transform in a very time efficient manner. The results presented here are based on [66] and influenced by [149].

5.2 The fields of a moving charge

As a first step in the calculation of the energy loss and photon scattering spectrum the field associated with the exciting source has to be calculated. In the case presented here, the line electron moves on a straight trajectory and with constant velocity c_e . There are many ways to calculate the potential associated with this moving line charge, but the most elegant is arguably to start from the electrostatic potential of a stationary line

charge and Lorentz boost it to velocity c_e [20]. The outline of this calculation for an electron moving along the vertical direction is given below. The four-vector potential \mathbf{A} for a stationary line charge is given by,

$$\mathbf{A} = \begin{pmatrix} \phi/c \\ A_1 \\ A_2 \\ A_3 \end{pmatrix} = \Phi = \begin{pmatrix} \frac{-\lambda}{2\pi\epsilon_0 c} \log \sqrt{x_1^2 + x_2^2} \\ 0 \\ 0 \\ 0 \end{pmatrix}, \quad (5.1)$$

where c is the velocity of light, λ is the charge per unit length, ϵ_0 the permittivity of free space and x_1 and x_2 two orthogonal Cartesian coordinates. Boosting the line charge along the x_2 -direction with velocity c_e changes the coordinates to

$$t' = \gamma(t - \frac{\beta}{c}x_2) \quad (5.2)$$

$$y' = \gamma(x_2 - vt), \quad (5.3)$$

$$x' = x_1 \quad (5.4)$$

$$z' = x_3 \quad (5.5)$$

where $\beta = c_e/c$. Expressed in terms of the primed coordinates this reads.

$$t = \gamma(t' + \frac{\beta}{c}y') \quad (5.6)$$

$$x_2 = \gamma(y' + vt'). \quad (5.7)$$

Similarly the four potential changes to

$$\phi'/c = \gamma(\phi/c - A_2\beta) = \gamma\phi/c \quad (5.8)$$

$$A_{y'} = \gamma(A_2 - \beta\phi/c) = \gamma\beta\phi/c \quad (5.9)$$

$$A_{x'} = A_1 \quad (5.10)$$

$$A_{z'} = A_3. \quad (5.11)$$

In the following, we will restrict ourselves to the non-relativistic limit, in which $\beta \ll 1$. In that case, we can ignore the contribution from $A_{y'}$ and work in the electrostatic regime, i.e. the electrostatic potential is given by

$$\phi'(x', y', t) = \frac{-\lambda\gamma}{2\pi\epsilon_0} \log \sqrt{(x')^2 + \gamma^2(y' + c_e t)^2}. \quad (5.12)$$

To simplify matters we will carry out our analysis in the frequency domain, so we have to ‘Fourier transform’ the potential with respect to time. That is: evaluate the integral

$$\phi'(\omega) = \frac{-\lambda\gamma}{4\pi^2\epsilon_0} \int_{-\infty}^{\infty} dt \log \sqrt{(x')^2 + \gamma^2(y' + c_e t)^2} e^{-i\omega t}. \quad (5.13)$$

Despite the formal divergence of the integrand at $|t| = \infty$ this expression can be evaluated by differentiating under the integral sign. After using $\gamma \approx 1$, we obtain

$$\phi'(x', y', \omega) = -\frac{\lambda}{4\pi\epsilon_0\omega} e^{-i\frac{\omega}{c_e}y'} e^{-|x'| \frac{\omega}{c_e}} \quad \text{for } \omega > 0, \quad (5.14)$$

as in [149]. For a line charge moving in the vertical direction at position $x' = x'_e$ this changes to

$$\phi' = -\frac{\lambda}{4\pi\epsilon_0\omega} e^{-i\frac{\omega}{c_e}y'} e^{-|x'-x'_e| \frac{\omega}{c_e}}. \quad (5.15)$$

Equivalently, the potential of a line charge moving in the horizontal direction at position $y' = y'_e$ is given by

$$\phi' = -\frac{\lambda}{4\pi\epsilon_0\omega} e^{-i\frac{\omega}{c_e}x'} e^{-|y'-y'_e| \frac{\omega}{c_e}}. \quad (5.16)$$

5.3 EELS for a non-concentric annulus using TO

In this section, we will perform a theoretical analysis of EELS and CL for a two-dimensional non-concentric annulus. We will calculate the electrostatic response of the metallic, non-concentric annulus when a (line) electron moves past it on a straight trajectory. The main objective is to derive experimentally measurable quantities. In EELS/CL this would be the electron energy loss probability and the photon emission spectrum, both as a function of frequency. These two quantities can be inferred from the power absorption in the non-concentric annulus and the power scattered by it. The calculation of these, is most easily carried out by transforming the non-concentric annulus to a more symmetrical structure, i.e. a concentric annulus. This is where TO comes in. Again, the transformation to a more symmetrical structure allows us to derive fully analytic solutions to the problem at hand, albeit in the electrostatic limit. A nice consequence of this is that a fully analytic solution to the EELS scenario considered here, makes it possible to obtain the time-domain response in a computationally efficient manner, by a simple ‘Fast Fourier Transform’ of the frequency space solution.

This section is structured as follows. We start by transforming the geometry then we derive the electrostatic potential of the moving line electron in the symmetric annulus

frame. From that we solve the electrostatic scattering problem by applying the usual boundary conditions demanded by Maxwell's equations at the interfaces [20]. We include the radiative reaction of the nanoparticle and then derive the power scattered and power absorbed by it. These are converted into electron energy loss and photon emission probabilities, and finally results are compared to fully electrodynamic simulations using COMSOL Multiphysics [66].

It must be noted that most of the results presented here have been published previously in [66] and the accompanying supplementary material. Any results not included in [66] can be easily derived from it. We closely follow the presentation of the supplementary material of [66].

5.3.1 Transformation of the geometry

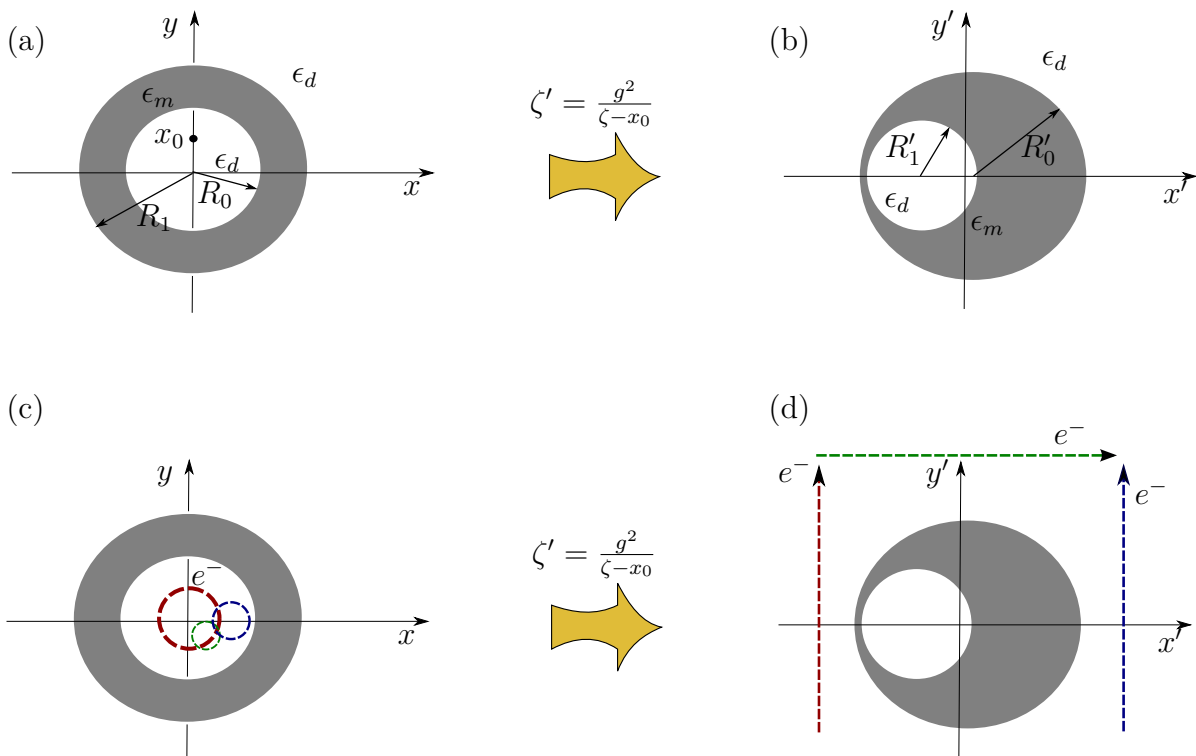


Figure 5.2: Transformation of a concentric to a non-concentric annulus. The dashed lines in (c) and (d) show the transformation of the electron trajectories. An electron moving with constant velocity on a straight line in the non-concentric annulus' frame travels on a curved trajectory and with non-uniform velocity in the concentric annulus' frame. Modified with permission from [66]. Copyright 2016 American Chemical Society.

It is well known that a non-concentric annulus can be transformed to a concentric one by means of a Möbius transformation [27, 41] and vice versa. Starting with a concentric annulus described by the complex number $\zeta = x + iy$ (virtual frame), a non-concentric annulus (physical frame) can be obtained from the following Moebius transformation

$$\zeta' = \frac{g^2}{\zeta - x_0}, \quad (5.17)$$

where $\zeta' = x' + iy'$ and $g, x_0 \in \mathbb{R}$ [27, 41]. Inner and outer boundary (R_0 and R_1) of the concentric annulus are easily related to the position and radius of the inner and outer boundary of the non-concentric annulus [27]. The position and radius of the dielectric inclusion are given by $y' = 0, x' = \frac{g^2 x_0}{R_1^2 - x_0^2}$ and $R'_1 = \left(\frac{g^4}{R_1^2 - x_0^2} + x_0^2 \right)^{1/2}$. Similarly, the surrounding metallic circle is centred at $y' = 0, x' = \frac{g^2 x_0}{R_0^2 - x_0^2}$ and has radius $R'_0 = \left(\frac{g^4}{R_0^2 - x_0^2} + x_0^2 \right)^{1/2}$.

Figure 5.2 ((a) and (b)) show the effect of the transformation in Eq.5.17 schematically. As previously, the conformality of the transformation ensures that the in-plane components of the permittivity and permeability are conserved [42].

Evidently, a non-concentric annulus possesses a hidden rotational symmetry, too. As was the case for the ellipse and the plasmonic grating studied in the previous two chapters, this hidden symmetry facilitates the determination of the plasmon modes of that system, as they are given by the ones of the concentric annulus. The task at hand is thus to determine how these modes respond in the presence of the fields of a fast moving electron. This is where difficulties can arise.

Figure 5.2 ((c) and (d)) hints at where these difficulties lie. While the trajectory of a fast moving electron in the non-concentric annulus frame is taken as a straight line (figure 5.2 (d)), it is far from trivial in the concentric annulus frame. Since charge is a conserved quantity, the electron trajectory in the annulus frame is simply obtained by transforming each point of the trajectory in the non-concentric frame via Eq.5.17. The three straight trajectories in figure 5.2 (d) transform to the three circles shown in 5.2 (c). Thus, the electrons move on a circle in the concentric annulus frame, however, because the transformation does not compress space uniformly, the electrons will move with a space dependent velocity. This makes it difficult to calculate the electric fields associated with the electrons directly. Progress can be made in the physical frame, however, as the electrostatic potential of an electron moving on a straight trajectory with constant velocity has already been obtained in Eq.5.15. The electrostatic source potential must then be transformed into the virtual frame by substituting coordinates.

5.3.2 Transformation of the source potential

In this subsection, we determine the electrostatic source potential of the moving electron in the annulus frame. The potential in the non-concentric annulus frame by for a line charge moving in the vertical direction at position $x' = x'_e$ is given by

$$\phi' = -\frac{\lambda}{4\pi\epsilon_0\omega} e^{-i\frac{\omega}{c_e}y} e^{-|x-x'_e|\frac{\omega}{c_e}}. \quad (5.18)$$

and

$$\phi' = -\frac{\lambda}{4\pi\epsilon_0\omega} e^{-i\frac{\omega}{c_e}x} e^{-|y-y'_e|\frac{\omega}{c_e}} \quad (5.19)$$

for a line charge moving in the horizontal direction at position $y' = y'_e$, as has been shown previously (see section 5.2). Since the transformation between annulus and non-concentric annulus is conformal, we obtain the potential in the annulus frame simply by substituting coordinates (see section 2.3). However, to determine the response of the annulus' plasmon modes, the potential has to be expanded in terms of these. In practice, this can be the most challenging step in solving the whole problem. In the following, we consider the potential for a line electron moving past the non-concentric annulus in the vertical direction to its left and right, and a line electron moving horizontally past its top.

5.3.2.1 An electron passing on the thin side of the non-concentric annulus

Here, we find the expansion of the source potential in terms of the plasmon eigenmodes of the annulus for an electron moving to the left of the non-concentric annulus (red line in figure 5.2). In this case, the source potential incident at the non-concentric annulus is given by

$$\phi^{sou}(x', y') := \phi' = \frac{\lambda}{4\pi\epsilon_0\omega} \exp\left[\frac{\omega}{c_e}(iy' - x' + x'_e)\right] \quad (5.20)$$

$$= \frac{\lambda \exp\left[\frac{\omega}{c_e}x_e\right]}{4\pi\epsilon_0\omega} \exp\left[-\frac{\omega}{c_e}(\zeta')^*\right], \quad (5.21)$$

since $x'_e < x$ at the surface of the nanoparticle [66]. The potential in the annulus frame is then obtained by substituting ζ' from Eq.5.17

$$\phi^{sou}(x, y) = \frac{\lambda \exp\left[\frac{\omega}{c_e} x_e\right]}{4\pi\epsilon_0\omega} \exp\left[-\frac{\omega}{c_e} \left(\frac{g^2}{\zeta - x_0}\right)^*\right] \quad (5.22)$$

$$= \frac{\lambda \exp\left[\frac{\omega}{c_e} x_e\right]}{4\pi\epsilon_0\omega} \exp\left[-\frac{\omega}{c_e} \left(\frac{g^2}{re^{i\phi} - x_0}\right)^*\right]. \quad (5.23)$$

As has been shown in Chapter 3, the plasmon eigenmodes of the annulus are of the form $r^{\pm n} e^{\pm in\phi}$. Hence, the potential above should be expanded in this form and can be found as

$$\phi^{sou} = \sum_{n=0}^{\infty} a_n^{s\pm} \left(\frac{r}{x_0}\right)^{\pm n} e^{\mp in\phi}, \quad (5.24)$$

with the expansion coefficients given by [66, 149]

$$a_0^{s+} = \frac{\lambda \exp\left[\frac{\omega}{c_e} x'_e + \frac{\omega g^2}{c_e x_0}\right]}{4\pi\epsilon_0\omega} \quad (5.25)$$

$$a_n^{s+} = \frac{\lambda \exp\left[\frac{\omega}{c_e} x'_e + \frac{\omega g^2}{c_e x_0}\right]}{4\pi\epsilon_0\omega} \sum_{k=1}^n \frac{(n-1)!}{k!(k-1)!(n-k)!} \left(\frac{\omega g^2}{c_e x_0}\right)^k \quad (5.26)$$

$$a_0^{s-} = \frac{\lambda \exp\left[\frac{\omega}{c_e} x'_e\right]}{4\pi\epsilon_0\omega} \quad (5.27)$$

$$a_n^{s-} = \frac{\lambda \exp\left[\frac{\omega}{c_e} x'_e\right]}{4\pi\epsilon_0\omega} \sum_{k=1}^n \frac{(n-1)!}{k!(k-1)!(n-k)!} \left(-\frac{\omega g^2}{c_e x_0}\right)^k. \quad (5.28)$$

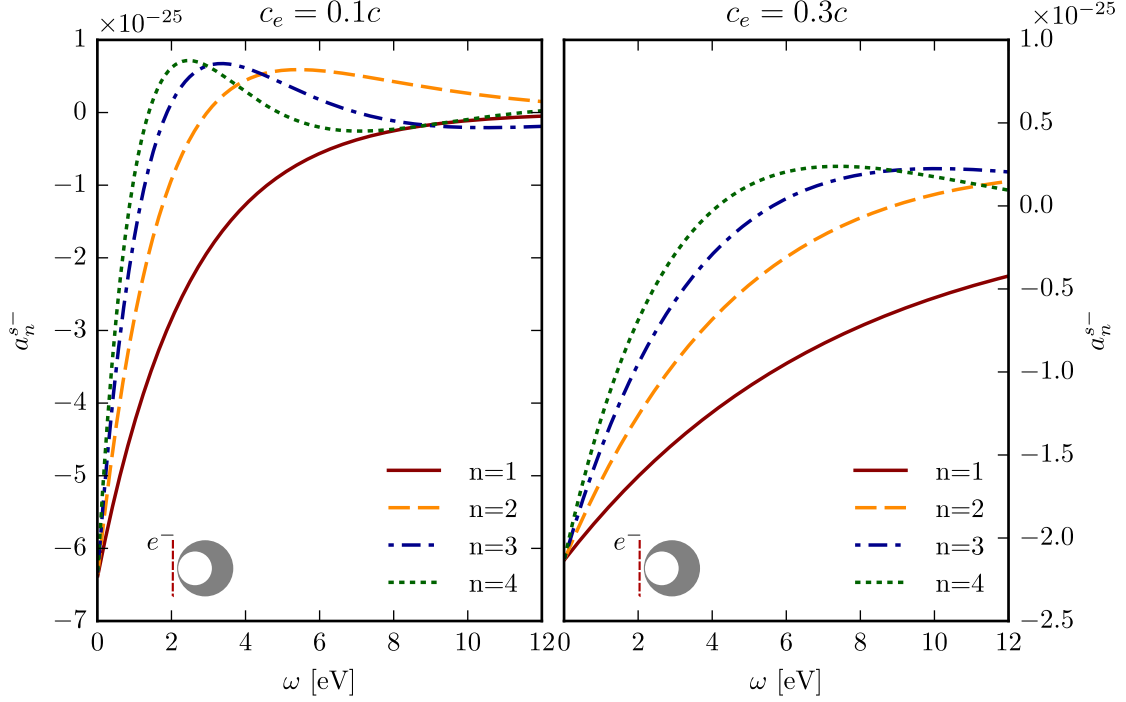


Figure 5.3: The value of the source expansion coefficients a_n^{s-} with $n = 1, 2, 3, 4$ for an electron passing to the left of the nanoparticle (see figure 5.2 (d), red line). The parameters are $\lambda = 1.602 \times 10^{-19}$, $g^2 = 2 \times 10^{-8}$, $x_0 = 1.5$, $x'_e = -0.4g^2$, $c_e = 0.1c$ on the left and $c_e = 0.3c$ on the right. The data for $c_e = 0.1c$ is also shown in the supplementary material of [66].

It is essential for the understanding of the electron energy loss and photon emission spectra to examine the behaviour of these expansion coefficients in more detail. First, it can be noted that the coefficients in Eq.5.25-Eq.5.28 are purely real [66]. Second, they decay with distance from the nanoparticle and decay faster the slower the electron. Third, the coefficients in Eq.5.28, which determine the fields on the surface of the nanoparticle, exhibit damped oscillations with respect to the parameter $-\frac{\omega g^2}{c_e x_0}$ [66]. This behaviour is shown in figure 5.3. Note that the expansion coefficients pass through zero at some points, indicating that the source does not contain these modes at the particular frequency where they are zero [66]. The positions of these zeros move to higher frequency for higher velocities.

5.3.2.2 An electron passing the crescent horizontally along its top

Here, we calculate the expansion of the source potential in terms of the plasmon eigenmodes of the annulus, in the case of an electron moving along the top of the non-

concentric annulus (green line in figure 5.2). The potential is given by

$$\phi^{sou} := \phi' = \frac{\lambda}{4\pi\epsilon_0\omega} \exp\left[\frac{\omega}{c_e}(ix' + y' - y'_e)\right] \quad (5.29)$$

$$= \frac{\lambda \exp\left[-\frac{\omega}{c_e}y'_e\right]}{4\pi\epsilon_0\omega} \exp\left[i\frac{\omega}{c_e}(\zeta')^*\right]. \quad (5.30)$$

since $y'_e > y'$ at the surface of the crescent [66]. Substituting coordinates again, this gives the potential in the annulus frame as [66]

$$\phi^{sou}(r, \phi) = \frac{\lambda \exp\left[-\frac{\omega}{c_e}y'_e\right]}{4\pi\epsilon_0\omega} \exp\left[i\frac{\omega}{c_e}\left(\frac{g^2}{re^{i\phi} - x_0}\right)^*\right], \quad (5.31)$$

which can be expanded as [66, 149]

$$\phi^{sou} = \sum_{n=0}^{\infty} a_n^{s\pm} \left(\frac{r}{x_0}\right)^{\pm n} e^{\mp in\phi}, \quad (5.32)$$

with

$$a_0^{s-} = \frac{\lambda \exp\left[-\frac{\omega}{c_e}y'_e\right]}{4\pi\epsilon_0\omega} \quad (5.33)$$

$$a_n^{s-} = \frac{\lambda \exp\left[-\frac{\omega}{c_e}y'_e\right]}{4\pi\epsilon_0\omega} \sum_{k=1}^n \frac{(n-1)!}{k!(k-1)!(n-k)!} \left(i\frac{\omega g^2}{c_e x_0}\right)^n \quad (5.34)$$

$$a_0^{s+} = \frac{\lambda \exp\left[-\frac{\omega}{c_e}y'_e - i\frac{\omega g^2}{c_e x_0}\right]}{4\pi\epsilon_0\omega} \quad (5.35)$$

$$a_n^{s+} = \frac{\lambda \exp\left[-\frac{\omega}{c_e}y'_e - i\frac{\omega g^2}{c_e x_0}\right]}{4\pi\epsilon_0\omega} \sum_{k=1}^n \frac{(n-1)!}{k!(k-1)!(n-k)!} \left(-\frac{i\omega g^2}{c_e x_0}\right)^k. \quad (5.36)$$

This time the expansion coefficients in Eq.5.34 and Eq.5.36 feature both, real and imaginary parts. They still decay with increasing distance from the source and with decreasing electron velocity, but their behaviour with respect to the parameter $\frac{i\omega g^2}{c_e x_0}$ is rather different than in the previous case [66]. A detailed view is given in figure 5.4. Here we plot the absolute value of the expansion coefficients a_n^{s-} , as they are complex numbers. The coefficients do not exhibit any oscillatory behaviour in their absolute value and do not pass through zero [66]. Thus the source contains contributions from all the modes at all frequencies in the range shown here.

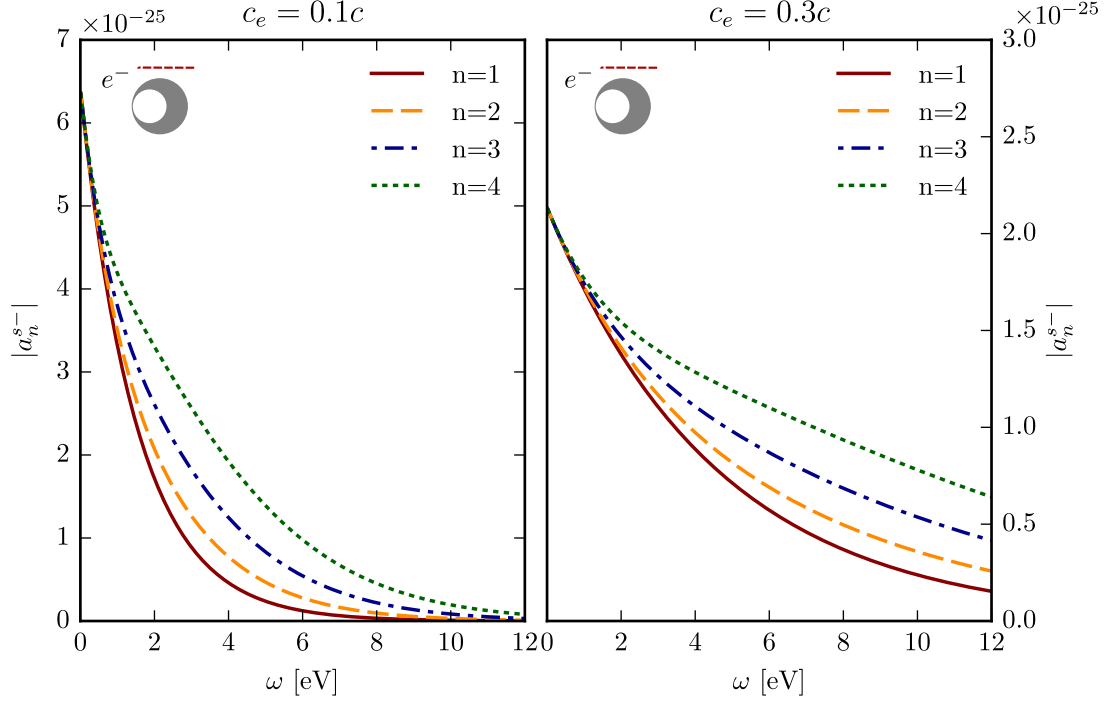


Figure 5.4: The absolute value of the source expansion coefficients a_n^{s-} with $n = 1, 2, 3, 4$ for an electron passing along the top of the nanoparticle (see figure 5.2 (d), green line). The parameters are $\lambda = 1.602 \times 10^{-19}$, $g^2 = 2 \times 10^{-8}$, $x_0 = 1.5$, $x'_e = -0.4g^2$, $c_e = 0.1c$ on the left and $c_e = 0.3c$ on the right. The data for $c_e = 0.1c$ is also shown in the supplementary material of [66].

5.3.2.3 An electron passing on the thick side of the non-concentric annulus

Last but not least, we consider the case of an electron passing to the right of the crescent, where $x_e > x$ at the surface of the crescent. This means the incident potential is given by

$$\phi^{sou} = \frac{\lambda}{4\pi\epsilon_0\omega} \exp\left[\frac{\omega}{c_e}(iy' + x' - x'_e)\right] \quad (5.37)$$

$$= \frac{\lambda \exp\left[-\frac{\omega}{c_e}x'_e\right]}{4\pi\epsilon_0\omega} \exp\left[\frac{\omega}{c_e}\zeta'\right]. \quad (5.38)$$

in the non-concentric annulus frame and by

$$\phi^{sou}(r, \phi) = \frac{\lambda \exp\left[-\frac{\omega}{c_e}x'_e\right]}{4\pi\epsilon_0\omega} \exp\left[\frac{\omega}{c_e}\left(\frac{g^2}{re^{i\phi} - x_0}\right)\right] \quad (5.39)$$

in the normal annulus frame. As before, this can be expanded as a series over the plasmon eigenmodes of the system, i.e

$$\phi = \sum_{n=0}^{\infty} a_n^{s\pm} \left(\frac{r}{x_0}\right)^{\pm n} e^{\pm in\phi}, \quad (5.40)$$

depending on whether $r > x_0$ or $r < x_0$. Note though, the difference in the sign of the phase factor compared to the previous two cases. The expansion coefficients are only slightly modified compared to Eq.5.25-Eq.5.28.

$$a_0^{s+} = \frac{\lambda \exp\left[-\frac{\omega}{c_e} x_e - \frac{\omega g^2}{c_e x_0}\right]}{4\pi\epsilon_0\omega} \quad (5.41)$$

$$a_n^{s+} = \frac{\lambda \exp\left[-\frac{\omega}{c_e} x_e - \frac{\omega g^2}{c_e x_0}\right]}{4\pi\epsilon_0\omega} \sum_{k=1}^n \frac{(n-1)!}{k!(k-1)!(n-k)!} \left(-\frac{\omega g^2}{c_e x_0}\right)^k \quad (5.42)$$

$$a_0^{s-} = \frac{\lambda \exp\left[-\frac{\omega}{c_e} x_e\right]}{4\pi\epsilon_0\omega} \quad (5.43)$$

$$a_n^{s-} = \frac{\lambda \exp\left[-\frac{\omega}{c_e} x_e\right]}{4\pi\epsilon_0\omega} \sum_{k=1}^n \frac{(n-1)!}{k!(k-1)!(n-k)!} \left(\frac{\omega g^2}{c_e x_0}\right)^n. \quad (5.44)$$

Note that the coefficients above are again purely real rather than complex. Their behaviour with respect to the parameter $\frac{\omega g^2}{c_e x_0}$ is shown in figure 5.5. Despite the reality of the coefficients in this case, their behaviour is more akin to the case of an electron moving along the top of the crescent. That is, they show no oscillatory behaviour, but monotonic decay with respect to frequency.

The results indicate that the response of the nanoparticle to the fields of the passing electron may be quite different depending on the direction of incidence. The behaviour for an electron passing on the right or along the top can be expected to be quite similar, as the expansion coefficients are monotonically decreasing with frequency, in both cases. An electron moving to the left of the non-concentric annulus may, however, lead to a qualitatively different response, as the expansion coefficients of the source show damped oscillatory behaviour, in this case.

5.3.3 Induced potentials and boundary conditions

In this subsection, we determine the induced and scattered electrostatic potential of the non-concentric annulus, albeit in the concentric annulus frame. This section closely follows the presentation in the supplementary material of [66].

5.3.3.1 Potentials and boundary condition at the interfaces

The source potential can be written in terms of the plasmon modes of the annulus system as

$$\phi^{sou} = \sum_{n=0}^{\infty} a_n^{s\pm} \left(\frac{r}{x_0} \right)^{\pm n} e^{\mp in\phi}, \quad (5.45)$$

with the expansion coefficients determined in the previous section. For a potential that is finite at the origin and at infinity, this indicates that the complete potential must be written as [66]

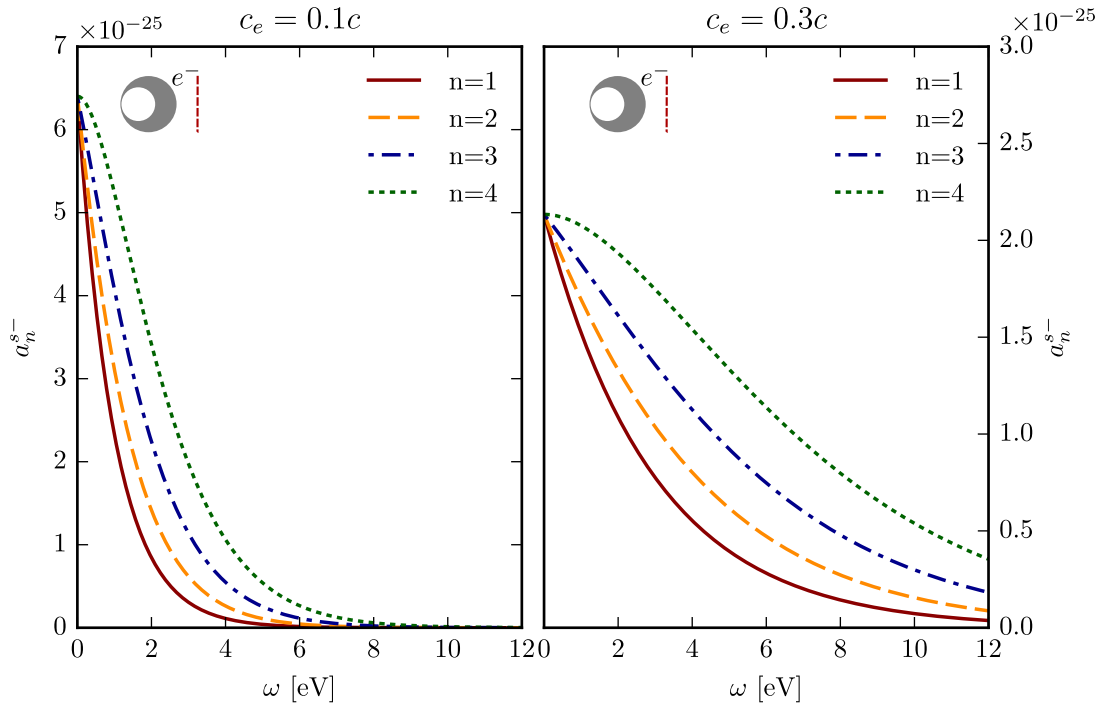


Figure 5.5: The value of the source expansion coefficients a_n^{s-} with $n = 1, 2, 3, 4$ for an electron passing to the right of the nanoparticle (see figure 5.2 (d), blue line). The parameters are $\lambda = 1.602 \times 10^{-19}$, $g^2 = 2 \times 10^{-8}$, $x_0 = 1.5$, $x'_e = -0.4g^2$, $c_e = 0.1c$ on the left and $c_e = 0.3c$ on the right.

$$\phi_I = \sum_{n=0}^{\infty} \left[a_n^{s+} e^{-in\phi} + (b_n + a_n^{rad+}) e^{in\phi} \right] \left(\frac{r}{x_0} \right)^n \quad \text{for } r < x_0 \quad (5.46)$$

$$\phi_{II} = \sum_{n=0}^{\infty} \left[(a_n^{s-} + a_n^{rad}) \left(\frac{x_0}{r} \right)^n e^{in\phi} + b_n \left(\frac{r}{x_0} \right)^n e^{in\phi} \right] \quad \text{for } R_0 > r > x_0 \quad (5.47)$$

$$\phi_{III} = \sum_{n=0}^{\infty} \left[c_n \left(\frac{x_0}{r} \right)^n e^{in\phi} + d_n e^{in\phi} \left(\frac{r}{x_0} \right)^n \right] \quad \text{for } R_1 > r > R_0 \quad (5.48)$$

$$\phi_{IV} = \sum_{n=0}^{\infty} e_n e^{in\phi} \left(\frac{x_0}{r} \right)^n \quad \text{for } R_1 > r > R_0 \quad (5.49)$$

where R_0 and R_1 are the inner and outer radius of the annulus as shown in figure 5.2. Three classes of expansion coefficients need to be distinguished here. First, the source coefficients $a_n^{s\pm}$, which are already known. Second, the electrostatic scattering coefficients b_n, c_n, d_n and e_n . These can be determined from the boundary conditions at the interfaces [66]. In a purely electrostatic calculation this would be the whole story; we would like to include the radiative reaction of the nanoparticle, however. This effect is modeled by the expansion coefficients a_n^{rad} [66]. Their form is determined in section 5.3.3.2 and their role is akin to the coefficients E^{tra} and E^{ref} introduced to model the radiative reaction of the plasmonic grating in chapter 4.

Treating a_n^{rad} as known, the electrostatic expansion coefficients are easily determined from the boundary conditions imposed on the electric and electric displacement field at the interfaces [20, 66], i.e.

$$\partial_r \phi_I \Big|_{r=R_0} = \epsilon_m \partial_r \phi_{II} \Big|_{r=R_0} \quad (5.50)$$

$$\frac{1}{r} \partial_\phi \phi_I \Big|_{r=R_0} = \frac{1}{r} \partial_\phi \phi_{II} \Big|_{r=R_0} \quad (5.51)$$

and

$$\partial_r \phi_{III} \Big|_{r=R_1} = \epsilon_m \partial_r \phi_{II} \Big|_{r=R_1} \quad (5.52)$$

$$\frac{1}{r} \partial_\phi \phi_{III} \Big|_{r=R_1} = \frac{1}{r} \partial_\phi \phi_{II} \Big|_{r=R_1}. \quad (5.53)$$

From this we obtain a set of linear equations in terms a_n^{s-} and a_n^{rad-} [66]. These have a unique solution give by [66]

$$\begin{pmatrix} b_n \\ c_n \\ d_n \\ e_n \end{pmatrix} = \begin{pmatrix} \frac{\left(\frac{R_0}{x_0}\right)^{-2n} (\epsilon_d - \epsilon_m)(\epsilon_d + \epsilon_m) \left[\left(\frac{R_0}{x_0}\right)^{2n} - \left(\frac{R_1}{x_0}\right)^{2n} \right]}{(\epsilon_d - \epsilon_m)^2 \left(\frac{R_0}{x_0}\right)^{2n} - (\epsilon_d + \epsilon_m)^2 \left(\frac{R_1}{x_0}\right)^{2n}} \\ \frac{-2\epsilon_d(\epsilon_d + \epsilon_m) \left(\frac{R_1}{x_0}\right)^{2n}}{(\epsilon_d - \epsilon_m)^2 \left(\frac{R_0}{x_0}\right)^{2n} - (\epsilon_d + \epsilon_m)^2 \left(\frac{R_1}{x_0}\right)^{2n}} \\ \frac{2\epsilon_d(\epsilon_d - \epsilon_m)}{(\epsilon_d - \epsilon_m)^2 \left(\frac{R_0}{x_0}\right)^{2n} - (\epsilon_d + \epsilon_m)^2 \left(\frac{R_1}{x_0}\right)^{2n}} \\ \frac{-4\epsilon_d\epsilon_m \left(\frac{R_1}{x_0}\right)^{2n}}{(\epsilon_d - \epsilon_m)^2 \left(\frac{R_0}{x_0}\right)^{2n} - (\epsilon_d + \epsilon_m)^2 \left(\frac{R_1}{x_0}\right)^{2n}} \end{pmatrix} [a_n^{s-} + a_n^{rad-}]. \quad (5.54)$$

5.3.3.2 Radiative reaction boundary condition

We showed in previous chapters that the fields induced in a nanoparticle lead to a radiative reaction of the particle. That is, the particle itself will radiate into the far field. In the present case, all the information about this effect is contained in the hitherto undetermined expansion coefficients a_n^{rad-} . Their precise form is derived in the following; the argument follows the one in [53] and is reproduced in the supplementary of [66]. More details can be found in appendix C.

As a first step, we need to calculate the energy scattered into the far field by the non-concentric annulus. Suppose we surround the non-concentric annulus with a fictive absorbing material, with its circular boundary ‘far away’ from the non-concentric annulus (see appendix C for details on our definition of ‘far away’) [66]. Then we can imagine that the power radiated into the far field by the non-concentric annulus is equivalent to the power absorbed by this fictive material [53, 66]. The power absorbed by the fictive absorber is easily calculated in the concentric annulus frame. Here, the fictive absorber transforms to a ‘small’ circular particle inside the annulus at $x = x_0, y = 0$, with finite polarisability [53, 66] (see appendix C.2 for details). If the polarisability is known, the power absorbed by such a particle is readily calculated. Thus far, all the arguments presented hold in a purely electrostatic framework and make no reference to any radiative reaction. It must be realised, though, that a particle with finite polarisability in a non-zero electric field will also give rise to a scattered field. There will thus be multiple scattering events between the fictive absorber and the inner interface of the concentric annulus [53, 66]. It is this multiple scattering that represents the radiative reaction of the nanoparticle [53, 66].

In the following, we will derive a relation between the radiative reaction coefficients a_n^{rad-} and the electrostatic scattering coefficients b_n , as defined in Eq.5.46. This relation constitutes an additional ‘radiative’ boundary condition akin to the one presented in Eq.4.44 and enables us to unambiguously determine all the expansion coefficients in Eq.5.46-Eq.5.49. The calculation below has also been reproduced in the supplementary of [66], so we omit further reference to it.

It has been shown in [53] and, using a slightly different approach, the appendix C.2 that the polarisability of the fictive absorber in the annulus frame is given by

$$\gamma_{abs} = \frac{i\pi^2 \epsilon_0 k_0^2 g^4}{2}. \quad (5.55)$$

This leads to an induced dipole moment given by [52]

$$\mathbf{P}_{abs} = \gamma_{abs} \mathbf{E}_{sca}(r = x_0, \phi = 0). \quad (5.56)$$

The scattered field can be obtained from the scattered potential inside the annulus, which is (see Eq.5.46)

$$\phi^{sca} = \sum_n e^{in\phi} b_n \left(\frac{r}{x_0}\right)^n. \quad (5.57)$$

Hence, the fields are obtained from $\mathbf{E} = -\nabla\phi$ [20],

$$E_{sca}^r = -\sum_n \frac{n}{x_0} b_n e^{in\phi} \left(\frac{r}{x_0}\right)^{n-1} \quad (5.58)$$

$$E_{sca}^\phi = -\sum_n \frac{in}{x_0} b_n e^{in\phi} \left(\frac{r}{x_0}\right)^{n-1}. \quad (5.59)$$

At $r = x_0$, $\phi = 0$, the relations $\hat{x} = \hat{r}$ and $\hat{\phi} = \hat{y}$ hold. Thus

$$E_{sca}^x = -\sum_n \frac{n}{x_0} b_n \quad (5.60)$$

$$E_{sca}^y = -\sum_n \frac{n}{x_0} b_n i. \quad (5.61)$$

Substituting into Eq.5.56 yields the components of the dipole moment vector of the fictive absorber as,

$$p_{abs}^x = -\frac{i\pi^2\epsilon_0 k_0^2 g^4}{2x_0} \sum_n n b_n \quad (5.62)$$

$$p_{abs}^y = +\frac{\pi^2\epsilon_0 k_0^2 g^4}{2x_0} \sum_n n b_n. \quad (5.63)$$

A particle with finite dipole moment at position $x = x_0, y = 0$ leads to a potential

$$\begin{aligned} \phi^{rad} &= \frac{1}{2\pi\epsilon_0} \frac{\mathbf{p}_{abs} \cdot (\mathbf{r} - x_0 \hat{x})}{r^2 + x_0^2 - 2x_0 r \cos(\phi)} \quad (5.64) \\ &= \frac{p_{abs}^x}{2\pi\epsilon_0 x_0} \sum_n \left(\frac{x_0}{r}\right)^n \cos(n\phi) + \frac{p_{abs}^y}{2\pi\epsilon_0 x_0} \sum_n \left(\frac{x_0}{r}\right)^n \sin(n\phi) \quad \text{for } r > x_0. \end{aligned}$$

The potential above is the one generated by the scattering from the fictive absorber. By construction, this has been introduced using the expansion coefficients a_n^{rad} in the definition of the total potential (Eq.5.46). This means the radiative reaction part of the potential in Eq.5.46,

$$\phi^{rad} = \sum_n \left(\frac{x_0}{r}\right)^n (a_n^{rad-} \cos(n\phi) + a_n^{rad-} i \sin(n\phi)),$$

must be equal to the expression in Eq.5.64, i.e.

$$\frac{p_{abs}^x}{2\pi\epsilon_0 x_0} \sum_n \left(\frac{x_0}{r}\right)^n \cos(n\phi) + \frac{p_{abs}^y}{2\pi\epsilon_0 x_0} \sum_n \left(\frac{x_0}{r}\right)^n \sin(n\phi) \quad (5.65)$$

$$= \sum_n \left(\frac{x_0}{r}\right)^n (a_n^{rad-} \cos(n\phi) + a_n^{rad-} i \sin(n\phi)). \quad (5.66)$$

Substituting from Eq.5.62 and Eq.5.63 yields a relationship between a_m^{rad} and b_n ,

$$a_m^{rad} = -\frac{i\pi k_0^2 g^4}{4x_0^2} \sum_n n b_n. \quad (5.67)$$

This constitutes the missing ‘radiative’ boundary condition. Substituting for b_n from Eq.5.54 gives

$$\begin{aligned}
 a_m^{rad-} &= -\frac{i\pi k_0^2 g^4}{4x_0^2} \sum_n \left(\frac{\left(\frac{R_0}{x_0}\right)^{-2n} (\epsilon_d - \epsilon_m)(\epsilon_d + \epsilon_m) \left[\left(\frac{R_0}{x_0}\right)^{2n} - \left(\frac{R_1}{x_0}\right)^{2n}\right]}{(\epsilon_d - \epsilon_m)^2 \left(\frac{R_0}{x_0}\right)^{2n} - (\epsilon_d + \epsilon_m)^2 \left(\frac{R_1}{x_0}\right)^{2n}} \right) \\
 &\times n [a_n^{s-} + a_n^{rad-}] \\
 &= -\frac{i\pi k_0^2 g^4}{4x_0^2} \sum_n b_{2,n} n [a_n^{s-} + a_n^{rad-}], \tag{5.68}
 \end{aligned}$$

with

$$b_{2,n} = \left(\frac{\left(\frac{R_0}{x_0}\right)^{-2n} (\epsilon_d - \epsilon_m)(\epsilon_d + \epsilon_m) \left[\left(\frac{R_0}{x_0}\right)^{2n} - \left(\frac{R_1}{x_0}\right)^{2n}\right]}{(\epsilon_d - \epsilon_m)^2 \left(\frac{R_0}{x_0}\right)^{2n} - (\epsilon_d + \epsilon_m)^2 \left(\frac{R_1}{x_0}\right)^{2n}} \right). \tag{5.69}$$

The additional boundary condition can be written more concisely using matrix notation

$$(\mathbb{I} - \mathbf{B})\mathbf{a}^{rad} = \mathbf{B}\mathbf{a}^s, \tag{5.70}$$

with

$$B_{jn} = -\frac{i\pi k_0^2 g^4}{4x_0^2} b_{2,n} n \quad \forall j. \tag{5.71}$$

The vector modeling the radiative reaction, \mathbf{a}^{rad} , is thus found by inverting $(\mathbb{I} - \mathbf{B})$. In the present case, this can be done analytically by noting that the matrix \mathbf{B} can be written as

$$\mathbf{u}\mathbf{b}^T, \tag{5.72}$$

where \mathbf{u} is the eigenvector of \mathbf{B} simply consisting of a column of ones and the components of \mathbf{b} are given by $b_n = -\frac{i\pi k_0^2 g^4}{4x_0^2} b_{2,n} n$. Hence,

$$(\mathbb{I} - \mathbf{B}) = (\mathbb{I} - \mathbf{u}\mathbf{b}^T). \tag{5.73}$$

The matrix $(\mathbb{I} - \mathbf{u}\mathbf{b}^T)$ is considered a rank-one perturbation to the identity, since $\mathbf{u}\mathbf{b}^T$ has rank one. Its inverse is given by the Sherman-Morrison formula [150],

$$(\mathbb{I} - \mathbf{u}\mathbf{b}^T)^{-1} = \mathbb{I} + \frac{\mathbf{u}\mathbf{b}^T}{1 - \mathbf{b}^T\mathbf{u}}. \tag{5.74}$$

Left multiplying Eq.5.70 with the expression above gives,

$$\mathbf{a}^{\text{rad}} = \left[\left(\mathbb{I} + \frac{\mathbf{u}\mathbf{b}^{\text{T}}}{1 - \mathbf{b}^{\text{T}}\mathbf{u}} \right) \mathbf{u}\mathbf{b}^{\text{T}} \right] \mathbf{a}^{\text{s}} \quad (5.75)$$

$$= \left[\frac{\mathbf{u}}{1 - \mathbf{b}^{\text{T}}\mathbf{u}} \right] \mathbf{b}^{\text{T}} \mathbf{a}^{\text{s}}. \quad (5.76)$$

Since \mathbf{u} is a column of ones each element in \mathbf{a}^{rad} is given by

$$\begin{aligned} a_m^{\text{rad}} &= \frac{\mathbf{b}^{\text{T}}\mathbf{a}^{\text{s}}}{1 - \mathbf{b}^{\text{T}}\mathbf{u}} \quad \forall m \\ &= \frac{\sum_n -\frac{i\pi k_0^2 g^4}{4x_0^2} b_{2,n} n a_n^{\text{s}-}}{1 + \sum_n \frac{i\pi k_0^2 g^4}{4x_0^2} b_{2,n} n}. \end{aligned} \quad (5.77)$$

Note that Eq.5.77 above consists of a sum over all source coefficients. Since the expansion coefficients b_n, c_n, d_n and e_n all have contributions from a_n^{rad} , this means the radiative reaction does not only affect the magnitude b_n, c_n, d_n and e_n , but also leads to a coupling to all modes of the source a_n^{s} . For example b_1 , now contains contributions from all coefficients a_n^{s} . Again, the results of this section have been reproduced in [66].

This concludes the derivation of the induced and scattered potential of the annulus, as all expansion coefficients in Eq.5.46-Eq.5.49 have now been determined unambiguously.

5.3.4 Power scattered

The power scattered by the non-concentric annulus is now easy to calculate, as it is equal in magnitude to the power absorbed by the fictive absorber in the annulus frame, but of opposite sign. Thus [52]

$$P_{\text{sca}}(\omega) = -\frac{\omega}{2} \text{Im}(\mathbf{p} *_{\text{abs}} \cdot \mathbf{E}^{\text{sca}}(x_0, 0)).$$

Substituting the dipole moment from Eq.5.56 and the scattered field from Eq.5.58 gives [66],

$$\begin{aligned} P_{\text{sca}}(\omega) &= \frac{\pi^2 \epsilon_0 k_0^2 g^4 \omega}{4} |\mathbf{E}^{\text{sca}}(x_0, 0)|^2 \\ &= \frac{\pi^2 \epsilon_0 k_0^2 g^4 \omega}{2} \left| \sum_n \frac{n b_n}{x_0} \right|^2. \end{aligned} \quad (5.78)$$

Figure 5.6 shows a few realisations of this for a non-concentric annulus of diameter $\approx 21\text{nm}$. Here we assumed a low loss Drude model for the permittivity of the nanoparticle,

$$\epsilon_m = 1 - \frac{\omega_p^2}{\omega(\omega + i\gamma)}, \quad (5.79)$$

with $\omega_p = 8\text{eV}$ and $\gamma = 0.032\text{eV}$, as this leads to a set of well separated plasmon modes with sharp resonances. Comparisons with numerical simulations for realistic values of the permittivity are presented in a later section.

Figure 5.6 (a) compares the analytical results for the scattered power (in arbitrary units) in a purely electrostatic calculation ($a_n^{rad} = 0 \forall n$) with the scattered power including the radiative correction (a_n^{rad} defined in Eq.5.77). The results indicate that the radiative correction for the geometrical parameters chosen is small, yet it is bound to become more significant for larger nanoparticles. Figure 5.6 (b)-(d) give the power scattered for an electron passing the nanoparticle on its left (b), on its right (c) and along the top (d). Different curves correspond to different electron velocities. All three spectra show resonances at the same frequencies, but their shapes are different indicating that the response of the non-concentric annulus is very sensitive to the position and direction of motion of the injected electron. Another feature shared by the spectra is the large dip in scattering at the surface plasma frequency ($\omega_{sp} \approx 5.67$). This means the modes of high order n contribute only weakly to the scattering, which can be understood, since those modes are highly confined near thinnest part of the non-concentric annulus.

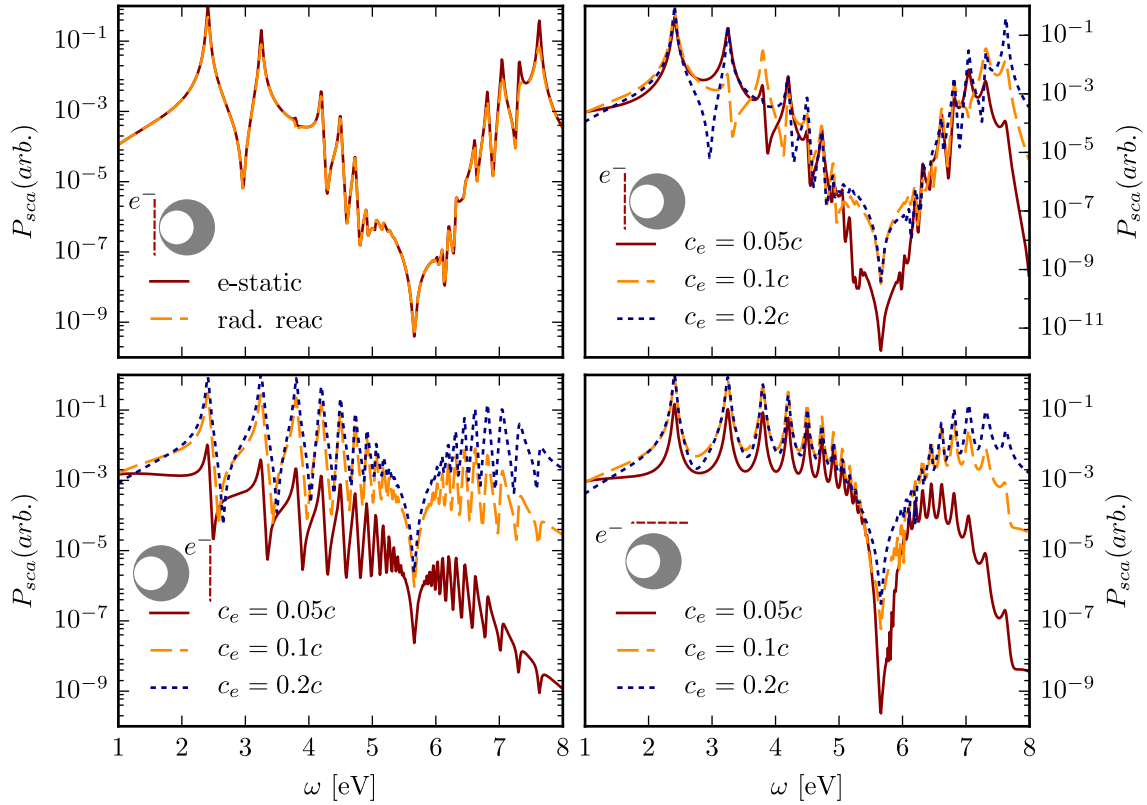


Figure 5.6: The power scattered by the non-concentric annulus. Figure (a) compares the electrostatic results with the result containing the radiative reaction for an electron passing on the crescent's left with $c_e = 0.2c$. Figure (b)-(d) all compare the scattered power for different electron velocities, as indicated in the legend. Figure (b) is for an electron passing on the left side, figure (c) for an electron passing on the right side and in figure (d) the electron passes along the top in the horizontal direction. The geometrical parameters were set to $g^2 = 2 \times 10^{-8}$, $x_0 = 1.5$, $R_0 = \exp(1)$ and $R_1 = \exp(1.2)$. The distance of the electron to the nanoparticle was $\approx 3.3\text{nm}$ for figure (a,b), $\approx 3.6\text{nm}$ for figure (c) and $\approx 2.4\text{nm}$ for figure (d). The permittivity of the nanoparticle is defined in Eq.5.79, the surrounding medium has $\epsilon_d = 1$. The power scattered is given in arbitrary units.

5.3.5 Power absorption

The power absorbed by the non-concentric annulus can be obtained from the resistive losses in it [52], i.e. from

$$Q = \frac{1}{2} \int_S dS \operatorname{Re}(\mathbf{j}^* \cdot \mathbf{E}). \quad (5.80)$$

Due to energy conservation, this must be the same as the power absorbed in the concentric annulus, which means the integration can be carried out over a rotationally symmetric domain and with the fields defined by the potential in Eq.5.46-Eq.5.49. Hence [66],

$$\begin{aligned} E_r &= -\partial_r \phi \\ &= -\sum_{n=0}^{\infty} \left[-nc_n \left(\frac{x_0^n}{r^{n+1}} \right) + nd_n \left(\frac{r^{n-1}}{x_0^n} \right) \right] e^{i\phi n} \end{aligned} \quad (5.81)$$

$$\begin{aligned} E_\phi &= -\frac{1}{r} \partial_\phi \phi \\ &= -\frac{1}{r} \sum_{n=0}^{\infty} in \left[c_n \left(\frac{x_0^n}{r^n} \right) + d_n \left(\frac{r^n}{x_0^n} \right) \right] e^{i\phi n}. \end{aligned} \quad (5.82)$$

The current is related to the electric field via [20, 66],

$$\mathbf{j} = -i\omega\epsilon_0(\epsilon_m - 1)\mathbf{E}. \quad (5.83)$$

Therefore, the power absorbed is given by the integral

$$Q = \frac{1}{2} \operatorname{Re} \int_{R_0}^{R_1} r dr \int_0^{2\pi} d\phi (j_r^* E_r + j_\phi^* E_\phi), \quad (5.84)$$

where R_0 and R_1 are the inner and outer boundary of the annulus, as defined in section 5.3.1. We start by evaluating the contribution from $j_r^* E_r$. The integrand of this integral reads [66],

$$\begin{aligned} j_r^* E_r &= i\omega\epsilon_0(\epsilon_m^* - 1) \sum_{n=0}^{\infty} \sum_{k=0}^{\infty} \left[-nc_n \left(\frac{x_0^n}{r^{n+1}} \right) + nd_n \left(\frac{r^{n-1}}{x_0^n} \right) \right] \\ &\times \left[-k(c_k)^* \left(\frac{x_0^k}{r^{k+1}} \right) + k(d_k)^* \left(\frac{r^{k-1}}{x_0^k} \right) \right] e^{i\phi(n-k)}. \end{aligned} \quad (5.85)$$

Evaluating the angular integral gives [66]

$$\int_0^{2\pi} d\phi j_r^* E_r = 2\pi i \omega \epsilon_0 (\epsilon_m^* - \epsilon_d) \times \sum_{n=0}^{\infty} \left[n^2 |c_n|^2 \left(\frac{x_0^{2n}}{r^{2n+2}} \right) - 2n^2 \text{Re}(d_n(c_n)^*) \frac{1}{r^2} + n^2 |d_n|^2 \left(\frac{r^{2n-2}}{x_0^{2n}} \right) \right]. \quad (5.86)$$

Finally, the radial integration leads to [66],

$$\int_0^{2\pi} d\phi \int r dr j_r^* E_r = 2\pi i \omega \epsilon_0 (\epsilon_m^* - 1) \sum_{n=0}^{\infty} \left[\frac{n}{2} |c_n|^2 x_0^{2n} (R_0^{-2n} - R_1^{-2n}) - 2n^2 \text{Re}(d_n(c_n)^*) \log(R_1/R_0) + \frac{n}{2} |d_n|^2 x_0^{-2n} (R_1^{2n} - R_0^{2n}) \right]. \quad (5.87)$$

The contribution from the term $j_\phi^* E_\phi$ can be calculated similarly and gives

$$\int_0^{2\pi} d\phi \int r dr j_\phi^* E_\phi = 2\pi i \omega \epsilon_0 (\epsilon_m^* - \epsilon_d) \sum_{n=0}^{\infty} \left[\frac{n}{2} |c_n^c|^2 x_0^{2n} (R_0^{-2n} - R_1^{-2n}) + 2n^2 \text{Re}(d_n^c(c_n^c)^*) \log(R_1/R_0) + \frac{n}{2} |d_n^c|^2 x_0^{-2n} (R_1^{2n} - R_0^{2n}) \right]. \quad (5.88)$$

Upon adding the two, the cross terms $\propto 2n^2 \text{Re}(d_n(c_n)^*)$ cancel and the final result is given by [66]

$$Q = \frac{1}{2} \int_S dS \text{Re}(\mathbf{j}^* \cdot \mathbf{E}) = \pi \omega \epsilon_0 \text{Im}(\epsilon_m) \sum_{n=0}^{\infty} \left[n |c_n|^2 x_0^{2n} (R_0^{-2n} - R_1^{-2n}) + n |d_n|^2 x_0^{-2n} (R_1^{2n} - R_0^{2n}) \right]. \quad (5.89)$$

Eq.5.89 determines the power absorbed by the non-concentric annulus when an electron moves past it in a straight line and at constant velocity.

Figure 5.7 gives the power absorption defined above for the same geometrical and with the same material parameters (see Eq.5.79), as the power scattered in figure 5.6. As before, the effect of the radiative correction shown in figure 5.7 (a) is quite small. The positions of the resonances are also unchanged compared to the scattering spectra, however, figure 5.7 (a)-(d) warrant some discussion. First, there is a qualitative difference between the spectrum in figure 5.7 (b) and figure 5.7 (c)-(d). In figure 5.7 (b), where the electron passes to the left of the crescent, higher order modes with $n > 6$ (counting from the left/right to $\omega_{sp} \approx 5.67 \text{eV}$) are barely visible. This is not the case for the electron

passing to the right and along the top. Here, a large number of high order modes is excited up to right below/above ω_{sp} . The similarity between figure 5.7 (c)-(d) and their contrast to figure 5.7 (a), does not come as a surprise. For we have shown previously that the source expansion coefficients for an electron passing to the right and along the top of the non-concentric annulus are in qualitative agreement, but that there is a

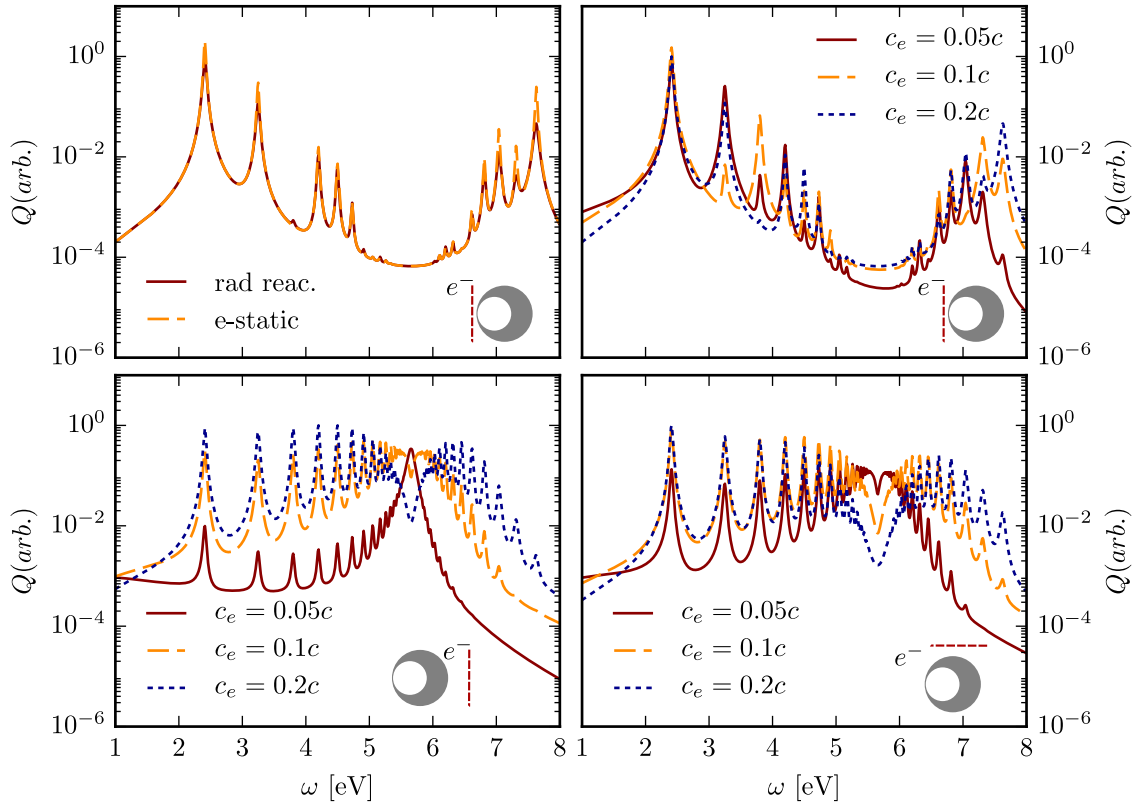


Figure 5.7: The power absorbed by the non-concentric annulus. Figure (a) compares the electrostatic results with the result containing the radiative reaction for an electron passing on the non-concentric annulus' left with $c_e = 0.2c$. Figure (b)-(d) all compare the scattered power for different electron velocities, as indicated in the legend. Figure (b) is for an electron passing on the left side, figure (c) for an electron passing on the right side and in figure (d) the electron passes along the top in the horizontal direction. The geometrical parameters were set to $g^2 = 2 \times 10^{-8}$, $x_0 = 1.5$, $R_0 = \exp(1)$ and $R_1 = \exp(1.2)$. The distance of the electron to the nanoparticle was $\approx 3.3nm$ for figure (a,b), $\approx 3.6nm$ for figure (c) and $\approx 2.4nm$ for figure (d). The permittivity of the nanoparticle is defined in Eq.5.79, the surrounding medium has $\epsilon_d = 1$. The power absorption is given in arbitrary units.

qualitative difference to an electron passing to the left of the non-concentric annulus (see section 5.3.2). Second, in figure 5.7 (a) the dependence of the spectra on the electron's velocity is distinctly different from the other two cases. In figure 5.7 (b) and (c) the change in the spectrum is fairly regular, with excitations away from the surface plasma frequency increasing in strength for increasing velocity, whereas excitations close to ω_{sp} are easier to excite with lower velocities. Figure 5.7 (a) shows no such regularity. Taking the resonance at $\approx 3.2eV$, we can see that the electrons with velocities $0.05c$ and $0.2c$ lead to similar absorption, however, the resonance is reduced by almost two orders of magnitude for an electron with velocity $0.1c$. Further, the next resonance at $\approx 3.9eV$ shows a distinctively different behaviour. Here, the electron with $c_e = 0.1c$ leads to the strongest excitation, whereas the one for $c_e = 0.05c$ is an order of magnitude smaller and the one for $c_e = 0.2c$ is barely visible. Clearly, there is no monotonic relation between the absorption peaks and the electron velocity. This too, can be explained examining the expansion coefficients of the electron's source potential. Recall that the expansion coefficients for an electron passing to the left of the non-concentric annulus showed damped oscillatory behaviour (see figure 5.3) [66]. It so happens that for the $n = 2$ resonance at $\approx 3.2eV$ the expansion coefficient for $c_e = 0.1c$ is close to a zero (see figure 5.3), so the strength of the resonance is strongly reduced. The same happens with the $n = 3$ resonance at $\approx 3.9eV$ for $c_e = 0.2c$, as the source expansion coefficient is close to zero at that frequency. The oscillatory behaviour of the source expansion coefficients thus opens up the possibility of 'accidental' degeneracies, where a zero of the n -th order expansion coefficients coincides with the resonance frequency of the n -th mode [66]. This also explains why this behaviour is not observed in figure 5.7 (b) and (c), as the expansion coefficients are monotonically decreasing functions of frequency for these cases (see figure 5.4 and 5.5).

5.3.6 Comparison with COMSOL

In this section, we compare our analytical theory with numerical simulations using COMSOL Multiphysics. Rather than comparing the power absorbed and power scattered, we compare experimentally accessible quantities [126]. Namely, the electron energy loss probability and the photon emission probability.

The electron energy loss probability can be obtained by first calculating the total energy loss as a function of frequency

$$e_{loss}^-(\omega) = P_{sca}(\omega) + Q(\omega), \quad (5.90)$$

then calculating $\int e_{loss}^-(\omega)d\omega$ and defining the electron energy loss probability density as

$$p(e_{loss}^-(\omega)) = \frac{e_{loss}^-(\omega)}{\int e_{loss}^-(\omega)d\omega}. \quad (5.91)$$

To obtain the particular probability of a specific electron losing energy at a specific frequency one would have to normalise by the energy of the incident electron, i.e. multiply the above probability by $\int e_{loss}^-(\omega)d\omega/E(e^-)$, where $E(e^-)$ is the energy of the incident electron.

To obtain the photon emission probability we first convert the scattered power into a photon number by dividing through $\hbar\omega$ and then calculate the total number of photons emitted. The photon emission probability density is thus

$$p(\gamma_{emis}(\omega)) = \frac{P_{sca}(\omega)/(\hbar\omega)}{\int [P_{sca}(\omega)/(\hbar\omega)] d\omega}. \quad (5.92)$$

It is important to point out again that all the calculations presented in this chapter have been done in two dimensions. This means that all the quantities given here are in units of ‘electron per unit length’ (see section 5.1 for details).

A note on numerical simulations. Our simulations are based on the RF-module of the COMSOL Multiphysics software package, which has been used to compare EELS simulations with experiments before [125]. COMSOL uses a finite element method (FEM) to model fully electrodynamic solutions to Maxwell’s equations in the frequency domain. While there is no predefined function to model the electric field generated by a moving line electron, it can be introduced as a surface current at the position of the line electron. For this, it is sufficient to note that the current associated with a line charge at position $x = x_e$, moving with velocity c_e in the y -direction is given by

$$\mathbf{j} = \frac{\lambda}{2\pi} \delta(x - x_e) e^{i\frac{\omega}{c_e}y} \hat{y}, \quad (5.93)$$

where λ is the charge per unit length and δ is the Dirac Delta function, see [149] for details. In the electrostatic and non-relativistic limit, this current leads to the exact same potential as given in 5.15 [149]. Note that the simulations, too, are carried out in two dimensions. COMSOL has a predefined function to calculate the resistive losses in a metallic particle using the same definition as we used in our theory. The power scattered by the nanoparticle can be obtained by drawing a box around the nanoparticle and comparing the power flow out of that box for the whole system, that is moving line electron and nanoparticle, with the power flow out of the box for the moving line electron,

only. Note, the box must be in the far field. Convergence of the numerical simulations with respect to mesh size and simulation domain has been ensured.

5.3.6.1 Vertically moving electron

Figure 5.8 gives the first comparison between COMSOL and our theory. To be as close to experiment as possible, we used experimental data for the permittivity of the nanoparticle. We chose Johnson and Christy's data for silver [65], with a surface plasma frequency $\omega_{sp} \approx 3.65eV$. The surrounding medium is still assumed to have $\epsilon_d = 1$. Figure 5.8 compares analytical and numerical results for the electron energy loss probability density (Eq.5.91) and photon emission probability density (Eq.5.92), for a line electron moving vertically on the left side of the non-concentric annulus [66]. The different results correspond to different line electron velocities $c_e = 0.05c$, $0.1c$ and $0.3c$ with corresponding kinetic energies $0.64keVm^{-1}$, $2.58keVm^{-1}$ and $24.7keVm^{-1}$, respectively [66].

	Analytics		COMSOL	
	$e_{loss}^- [eVm^{-1}]$	$N(\gamma)$	$e_{loss}^- [eVm^{-1}]$	$N(\gamma)$
$c_e = 0.05c$	6.04×10^{-11}	3.76×10^{-12}	6.11×10^{-11}	3.91×10^{-12}
$c_e = 0.1c$	8.62×10^{-11}	5.69×10^{-12}	8.78×10^{-11}	6.01×10^{-12}
$c_e = 0.3c$	4.65×10^{-11}	2.78×10^{-12}	4.74×10^{-11}	2.92×10^{-12}

Table 5.1: Table giving the total energy loss defined by $\int e_{loss}^-(\omega)d\omega$ in units of [eV per unit length] and the total number of photons emitted. Results for analytical calculations for a line electron passing to the left of the particle are compared with COMSOL simulations.

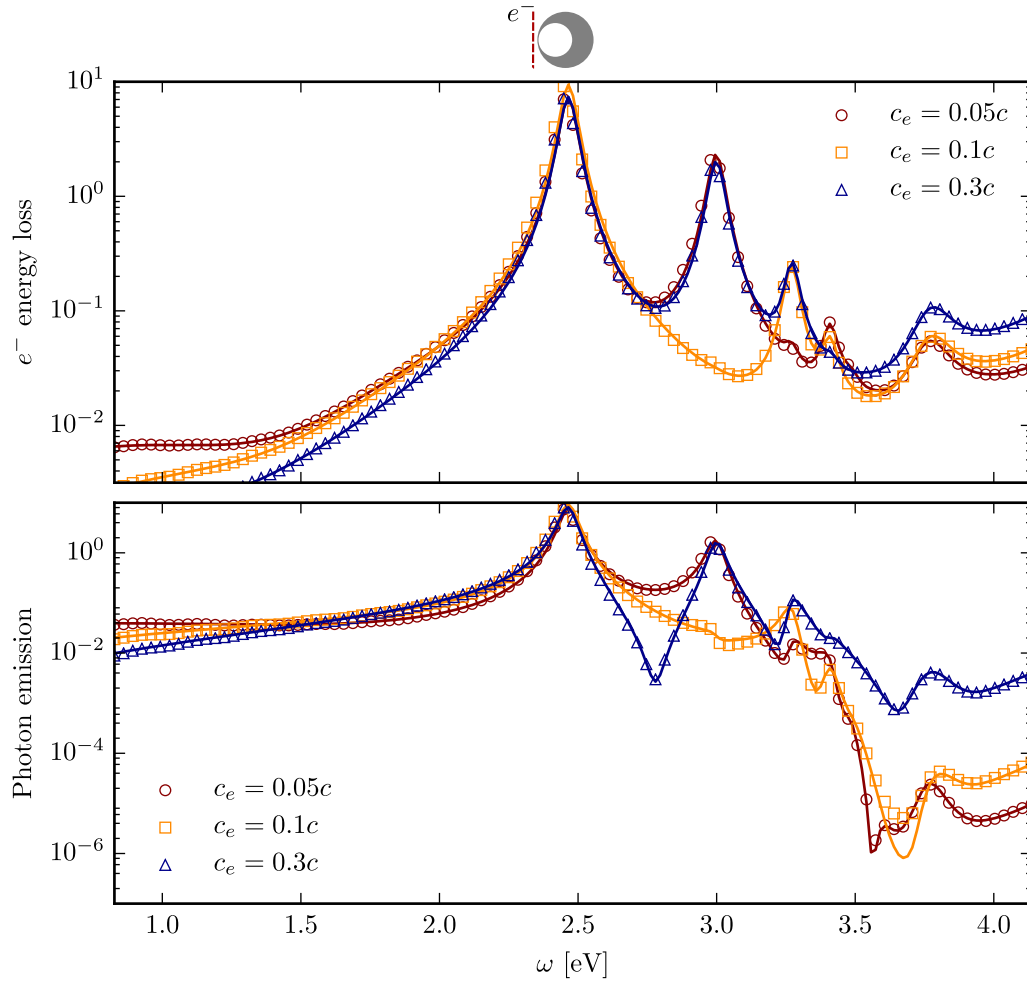


Figure 5.8: The electron energy loss (top) and photon emission (bottom) probability density for a (line) electron passing to the left of the non-concentric annulus. The electron energy loss probability density is in units of $[eV^{-1}$ per electron per unit length]. Similarly the photon emission probability density is in terms of the number of photons emitted in units of $[eV^{-1}$ per electron per unit length]. The area under each of the curves is unity. The solid lines correspond to analytical results, with the accompanying markers corresponding to COMSOL simulations. The geometrical parameters were set to $g^2 = 2 \times 10^{-8}$, $x_0 = 1.5$, $R_0 = \exp(1)$ and $R_1 = \exp(1.2)$, the distance to the particle was $\approx 3.3nm$ and the constant λ defined in Eq.5.15 was set to $1.602 \times 10^{-19} Cm^{-1}$. The data for $c_e = 0.05$ and $c_e = 0.1c$ is also published in [66].

Agreement between analytics and numerical simulations is very good for all three velocities. This is also reflected in table 5.1, which gives the total energy lost by the electron and total number of photons emitted for each of the three cases. There, too,

agreement between analytics and numerical simulations is very good. Examining the spectra in more detail, we note that it features an ‘accidental’ degeneracy, too. The $n = 2$ mode at $\approx 3eV$ is absent for the electron moving at $c_e = 0.1c$, whereas it is strongly excited for the electrons moving at $c_e = 0.05c$ and $c_e = 0.3c$ [66]. This is visible in both the electron loss and photon emission spectra. The same thing happens for the $n = 3$ mode and the electron of velocity $c_e = 0.05c$. The results indicate that it might not be universally true that an electron with fixed velocity can probe any mode of the system, as accidental degeneracies may occur [66]. However, this must not be a nuisance, as it opens up the possibility of switching a particular ‘unwanted’ mode off by tuning the electron’s velocity and direction of motion [66].

Figure 5.9 shows the electron loss and photon emission spectra for an electron passing to the right of the non-concentric annulus. The agreement between theory and simulations is excellent in this case as well. This is consolidated by the data for the total energy loss and the total number of electrons presented in table 5.2. There are two major differences between the spectra for the electron passing to the left and the right of the nanoparticle. First, figure 5.9 does not show any accidental degeneracies for any of the velocities shown here. This is understood, since the source expansion coefficients for this case are monotonically decaying functions of frequency and do not vanish in the frequency range of interest. Second, an electron passing to the right seems to be much better suited to excite the higher order modes around the surface plasma frequency ($\approx 3.65eV$). In particular, slow electrons seem to be more efficient in exciting these modes than faster ones. This is in agreement with our observations in section 5.3.5.

	Analytics		COMSOL	
	$e_{loss}^- [eVm^{-1}]$	$N(\gamma)$	$e_{loss}^- [eVm^{-1}]$	$N(\gamma)$
$c_e = 0.05c$	8.03×10^{-12}	1.45×10^{-13}	8.15×10^{-11}	1.49×10^{-12}
$c_e = 0.1c$	3.29×10^{-11}	9.19×10^{-13}	3.45×10^{-11}	9.48×10^{-12}
$c_e = 0.3c$	4.17×10^{-11}	1.65×10^{-12}	4.24×10^{-11}	1.64×10^{-12}

Table 5.2: Table giving the total energy loss defined by $\int e_{loss}^-(\omega)d\omega$ in units of [eV per unit length] and the total number of photons emitted. Results for analytical calculations for a line electron passing to the right of the particle are compared with COMSOL simulations.

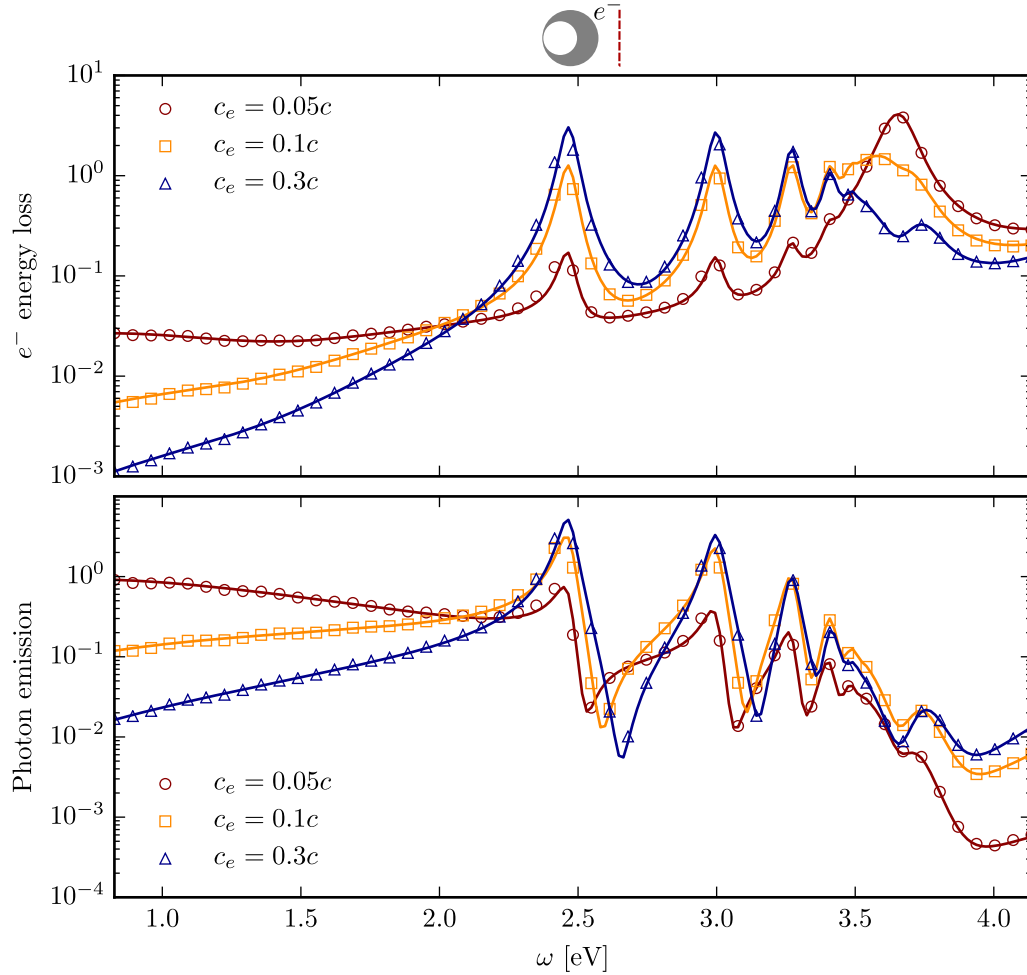


Figure 5.9: The electron energy loss (top) and photon emission (bottom) probability density for a (line) electron passing to the right of the non-concentric annulus. The electron energy loss probability density is in units of $[eV^{-1}$ per electron per unit length]. Similarly the photon emission probability density is in terms of the number of photons emitted in units of $[eV^{-1}$ per electron per unit length]. The area under each of the curves is unity. The solid lines correspond to analytical results, with the accompanying markers corresponding to COMSOL simulations. The geometrical parameters were set to $g^2 = 2 \times 10^{-8}$, $x_0 = 1.5$, $R_0 = \exp(1)$ and $R_1 = \exp(1.2)$, the distance to the particle was $\approx 3.3nm$ and the constant λ defined in Eq.5.15 was set to $1.602 \times 10^{-19}Cm^{-1}$.

5.3.6.2 Horizontally moving electron

Finally, we check the validity of our theory for an electron moving horizontally along the top of the non-concentric annulus. The results are shown in figure 5.10 (see also [66]). The data resembles the one for the electron passing to the right of the particle. This is to be expected since the source expansion coefficients for these two cases showed qualitatively similar behaviour. Agreement between analytics and COMSOL simulations is very good too, demonstrating the robustness of our approach. Data for the total energy lost by the electron and the total number of photons scattered is given in table 5.3 and consolidates the results.

	Analytics		COMSOL	
	$e_{loss}^- [eVm^{-1}]$	$N(\gamma)$	$e_{loss}^- [eVm^{-1}]$	$N(\gamma)$
$c_e = 0.05c$	3.05×10^{-11}	8.71×10^{-13}	3.15×10^{-11}	9.98×10^{-13}
$c_e = 0.1c$	7.55×10^{-11}	3.63×10^{-12}	8.07×10^{-11}	4.00×10^{-12}
$c_e = 0.3c$	5.01×10^{-11}	2.60×10^{-12}	5.34×10^{-11}	2.82×10^{-12}

Table 5.3: Table giving the total energy loss defined by $\int e_{loss}^-(\omega)d\omega$ in units of [eV per unit length] and the total number of photons emitted. Results for analytical calculations for a line electron passing along the top of the particle are compared with COMSOL simulations.

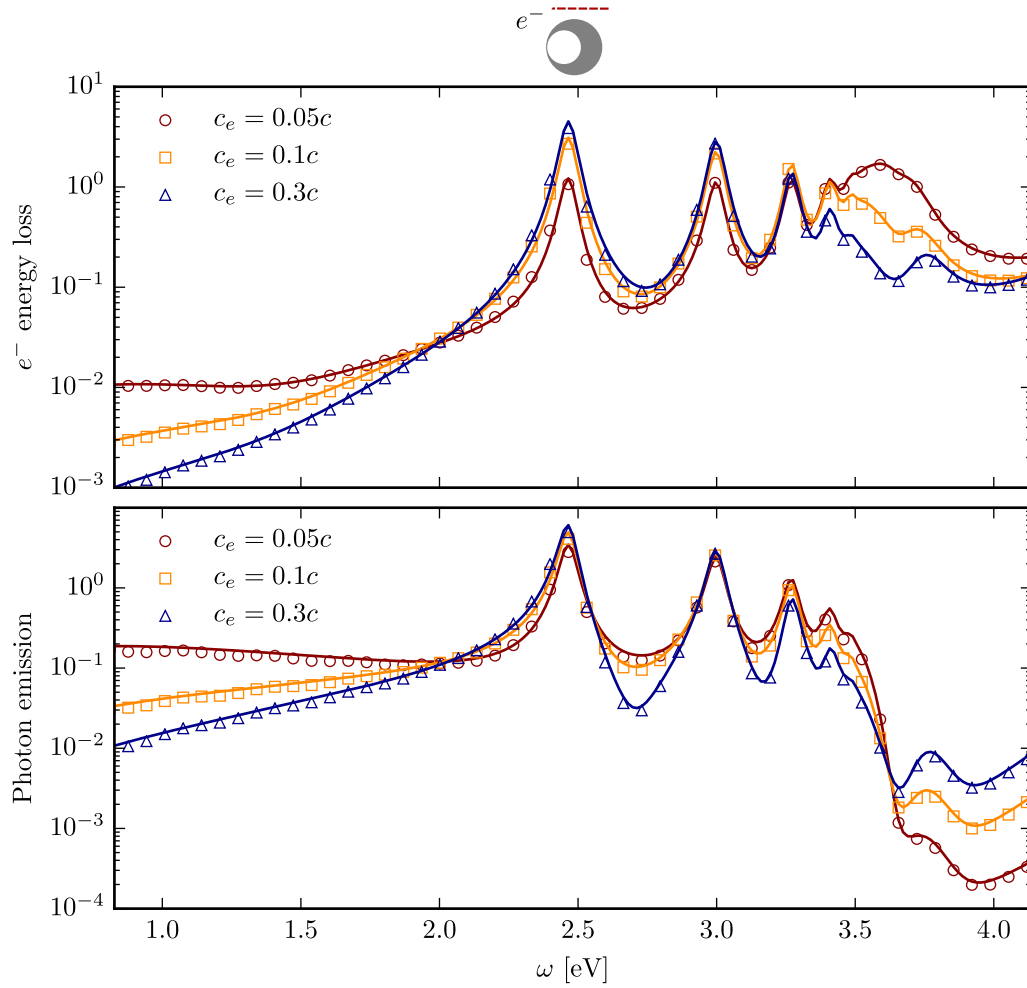


Figure 5.10: The electron energy loss (top) and photon emission (bottom) probability density for a (line) electron passing along the top of the non-concentric annulus. The electron energy loss probability density is in units of $[eV^{-1}$ per electron per unit length]. Similarly the photon emission probability density is in terms of the number of photons emitted in units of $[eV^{-1}$ per electron per unit length]. The area under each of the curves is unity. The solid lines correspond to analytical results, with the accompanying markers corresponding to COMSOL simulations. The geometrical parameters were set to $g^2 = 2 \times 10^{-8}$, $x_0 = 1.5$, $R_0 = \exp(1)$ and $R_1 = \exp(1.2)$, the distance to the particle was $\approx 3.3nm$ and the constant λ defined in Eq.5.15 was set to $1.602 \times 10^{-19} Cm^{-1}$. This data is also published in [66].

5.3.6.3 Breakdown of the theory

In the previous sections, we compared our analytical theory with fully electrodynamic simulations using the COMSOL Multiphysics package. The agreement between analytics

and simulations is very good. Here, we want to test the limits of our theory to gauge when it breaks down. There are two mechanisms that can lead to a breakdown of our theory. First, if the non-concentric annulus is taken to be larger we expect retardation effects to set in that are not included in our theory. Previously, we took the non-concentric annulus to be $\approx 21nm$, which is much smaller than the free space wavelength in the frequency region of interest. Here, we will increase its size. Second, if the electrons are very fast we expect relativistic effects to set in, the result being that the source field cannot be approximated by an electrostatic potential as in Eq.5.15. We expect relativistic effects to become important when the kinetic energy of the exciting electrons becomes comparable to their rest mass ($m_0 = 511keV$).

Figure 5.11 indicates the limitations of our theory. First, we compare analytics and simulations for non-concentric annulus of diameter $\approx 84nm$ (yellow squares). Agreement between analytics and simulations is still reasonable, however the numerical results are red shifted with respect to the analytical ones. This means retardation effects start to matter at this size. We expect the shifts to become stronger and the agreement worse for even larger nanoparticles. Second, we analyse the effect of increasing the (line) electron's velocity. The agreement for an electron moving at $c_e = 0.5c$ (nanoparticle diameter $21nm$) is still excellent, indicating that the non-relativistic approximation on the source goes quite a long way. These results are also reflected in the total electron energy loss and number of photons scattered, see table 5.4

We can thus conclude that our theory provides good results for particles of size less than $\approx 80nm$ and electron velocities at least up to $0.5c$.

	Analytics		COMSOL	
	$e_{loss}^- [eVm^{-1}]$	$N(\gamma)$	$e_{loss}^- [eVm^{-1}]$	$N(\gamma)$
$c_e = 0.5c$	2.57×10^{-11}	1.42×10^{-12}	2.59×10^{-11}	1.46×10^{-12}
$c_e = 0.1c$	1.02×10^{-10}	2.05×10^{-11}	1.05×10^{-10}	2.13×10^{-11}

Table 5.4: Table giving the total energy loss defined by $\int e_{loss}^-(\omega)d\omega$ in units of [eV per unit length] and the total number of photons emitted. Results for analytical calculations for a line electron passing along the top of the particle are compared with COMSOL simulations.

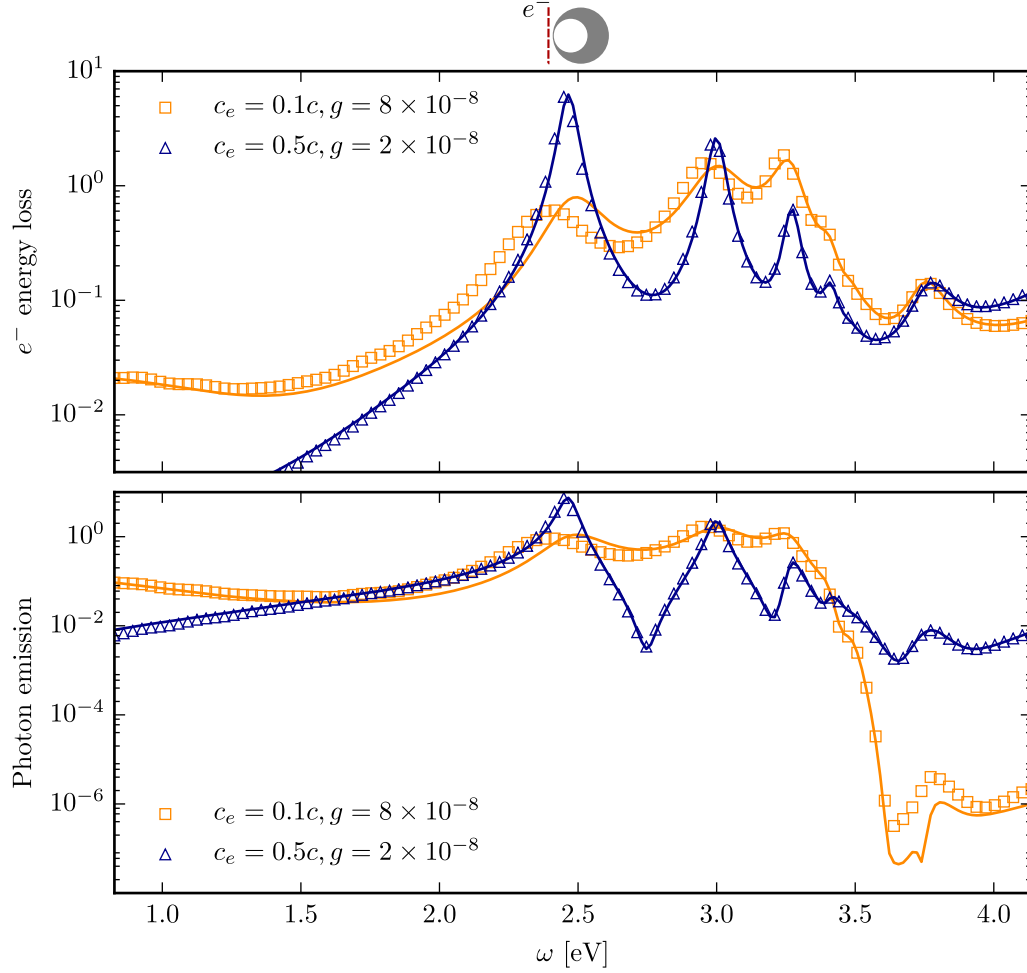


Figure 5.11: The electron energy loss (top) and photon emission (bottom) probability density for a (line) electron passing to the left of the non-concentric annulus. The electron energy loss probability density is in units of $[eV^{-1}$ per electron per unit length]. Similarly the photon emission probability density is in terms of the number of photons emitted in units of $[eV^{-1}$ per electron per unit length]. The area under each of the curves is unity. The solid lines correspond to analytical results, with the accompanying markers corresponding to COMSOL simulations. The geometrical parameters were set to $x_0 = 1.5$, $R_0 = \exp(1)$ and $R_1 = \exp(1.2)$, with g^2 as indicated. The distance to the particle was $\approx 3.3nm$ for the data with $c_e = 0.5c$, but was $\approx 5nm$ for the data with $c_e = 0.1c$. The constant λ defined in Eq.5.15 was set to $1.602 \times 10^{-19} Cm^{-1}$.

5.3.7 Time-response of the non-concentric annulus

In this section, we study the time-response of the non-concentric annulus when a line electron moves past it at high velocity. The section is based on results from [66]. The analytical treatment presented in the previous section lead to a fully analytical description of the system's response in the frequency domain, all under the electrostatic approximation. The time-response can thus be obtained by 'Fourier transforming' the frequency domain solutions. That is, by evaluating the integral [66]

$$\hat{\phi}(x', y', t) = \int_{-\infty}^{\infty} d\omega \phi(x', y', \omega) e^{-i\omega t} \quad (5.94)$$

$$= 2\text{Re} \left[\int_0^{\infty} d\omega \phi(x', y', \omega) e^{-i\omega t} \right], \quad (5.95)$$

where we used the reality condition on the potential, i.e. $\phi(-\omega) = \phi^*(\omega)$. Since $\phi(x', y', \omega)$ is known, this integral can be evaluated numerically in a very time efficient manner by using a 'Fast Fourier transform' algorithm [150]. Note that the integration runs from $\omega = 0$ to ∞ . This can of course be truncated at some finite frequency, but the experimental permittivity data available does not provide a sufficient frequency range. We thus resort to the simple Drude model defined in Eq.5.79, but increase the losses to a more realistic value of $\gamma = 0.32eV$.

The electron loss and photon emission spectra seen in figures 5.8, 5.9 and 5.10 already give some indication on the nature of the system's time response. In essence, a fast moving electron transfers some of its energy to the nanoparticle in a short 'pulse', containing a range of frequencies, which, for a pulse of a few femtoseconds is of the order of a few eV, due to Heisenberg's uncertainty principle [66, 151]. That means that there is a range of modes that are excited at the same time; they all influence the system's response [66]. The spectra in figures 5.8, 5.9 and 5.10 then tell us which modes dominate the time response. We thus expect the time response for an electron passing to the left of the non-concentric annulus to be dominated by the first two or maybe three plasmon modes (see figure 5.8). In contrast, the response of the other two cases can be expected to contain strong contributions from the higher order modes nearer the surface plasma frequency ($\omega_{sp} \approx 3.65eV$), as well (see figures 5.9 and 5.10). The time-simulation videos for the non-concentric annulus provided as supplementary (see appendix D), confirm exactly that [66]. Each video shows the time evolution for a non-concentric annulus with the geometric parameters set equal to the ones in figures 5.8 and 5.10, for each case there is a video showing the vertical and horizontal component of the electric field. As mentioned, the electron moves rapidly past the nanoparticle and excites a range of

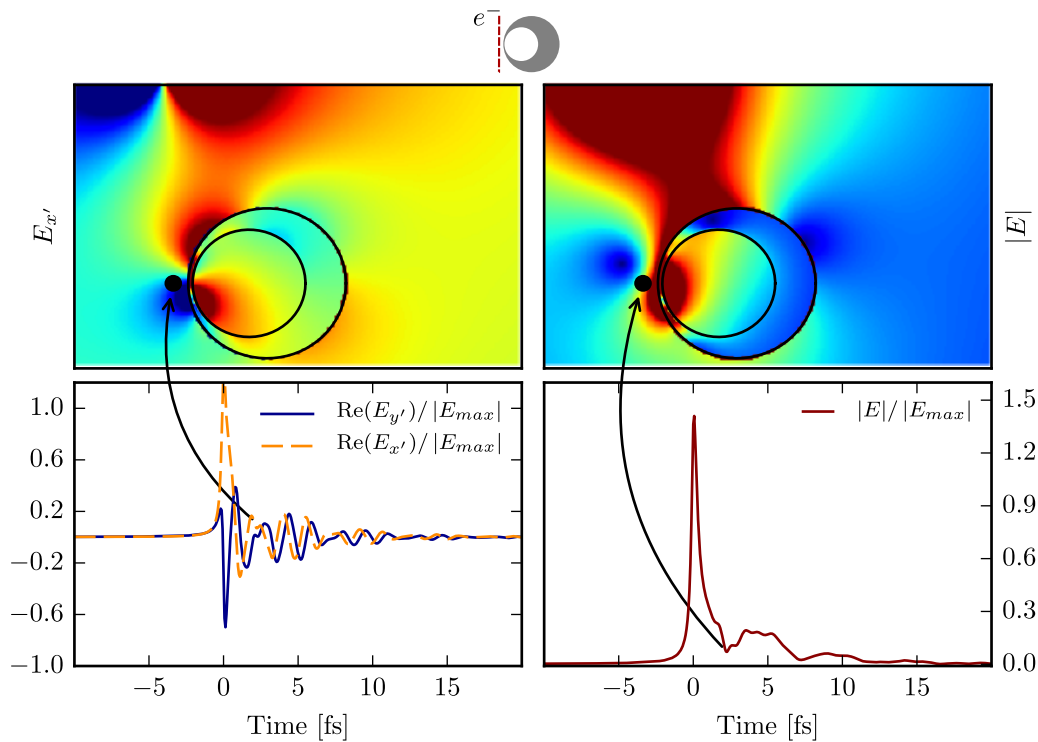


Figure 5.12: The top panel shows the electric field distribution at a specific time point (indicated by the arrow). E_v on the left and $|E|$ on the right. The bottom panel shows the time response of the crescent at a particular point (marked by the black dot in the top panel). In this case the electron moves vertically to the left of the nanoparticle. The plots in the bottom panel have been normalised by the maximum source field at the particular point. Modified with permission from [66]. Copyright 2016 American Chemical Society.

plasmon modes in the nanoparticle. In the case of the electron passing on the left side of the non-concentric annulus, these plasmons only exhibit one or two oscillations as one traces the inner surface of the particle in the angular direction. This indicates that the time signal is dominated by the two lowest order plasmon modes [66], as expected. On the contrary, the electric field pattern for the horizontally moving electron contains more oscillations along the angular direction and generally exhibits a richer and more complex time response [66]. This supports our belief that there are many modes contributing to the time response, in this case [66].

Earlier work on plasmonic nanoparticles with singular (i.e. very sharp) features demonstrated their light harvesting capabilities [27]. A singular crescent, for example, has been shown to harvest light over a broad range of frequencies and concentrate it at the touching point [27]. The non-concentric annulus can be considered the non-singular version of the crescent. While the light harvested in the singular crescent can

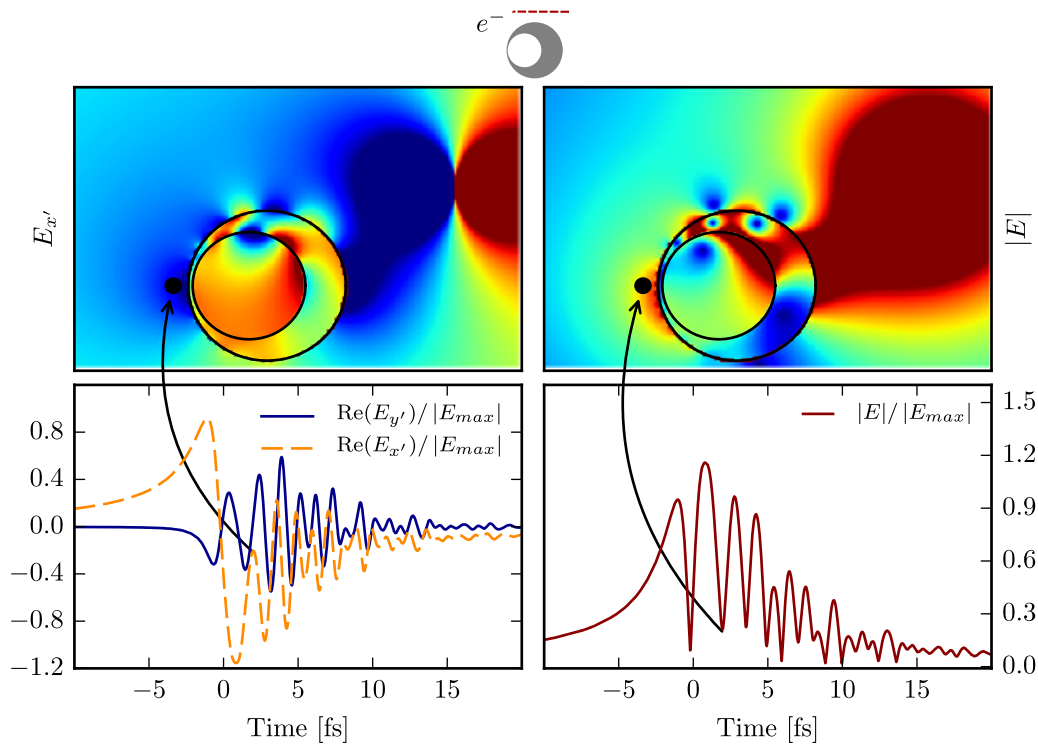


Figure 5.13: The top panel shows the electric field distribution at a specific time point (indicated by the arrow). E_v on the left and $|E|$ on the right. The bottom panel shows the time response of the crescent at a particular point (marked by the black dot in the top panel). In this case the electron moves vertically to the left of the nanoparticle. The plots in the bottom panel have been normalised by the maximum source field at the particular point. Modified with permission from [66]. Copyright 2016 American Chemical Society.

never reach its singular point [103], the missing of the singularity in the non-concentric annulus means that the plasmons can propagate around the nanoparticle along the angular direction [27]. This behaviour is visualised in the videos for the electron passing the nanoparticle in the horizontal direction. Plasmons are excited at the ‘fat’ end of the non-concentric annulus and can be seen to propagate towards its thin part in a clockwise direction [66]. Since the non-concentric annulus has a finite width at its thin end, the plasmons can propagate past it and loop around the nanoparticle until all their energy is converted to heat via resistive losses or emitted as photons [66].

Figures 5.12 and 5.13 provide time slices through the video simulation and time series data for a spatial point [66]. Here too, we note that the time response for the electron passing on the left is dominated by the low order plasmon modes, while many modes contribute in the horizontal case. This can be deduced from both the contour plot of $|E|$ (which shows more nodes and anti-nodes for the horizontal case) and the

time series data, which features much stronger oscillations and appears a lot richer for the horizontal case.

5.4 EELS for an ellipse using TO

In this section, we apply the TO approach to EELS to the case of an ellipse. We have already shown in chapter 3 that an ellipse can be mapped onto an annulus via a Joukowski transformation, which has been given in Eq.3.2 and is repeated here,

$$\zeta' = \frac{c'}{2} \left(\zeta + \frac{1}{\zeta} \right), \quad c' \in \mathbb{R}^+$$

Here, the primed coordinates refer to the ellipse's frame with $\zeta' = x' + iy'$ and the unprimed coordinates represent the annulus' frame $\zeta = x + iy$. As shown in chapter 3, an ellipse with semi-major axis $a' = c' \cosh(u_0)$ and semi-minor axis $b' = c' \sinh(u_0)$ transforms to an annulus with inner and outer radius $R_0 = e^{-u_0}$ and $R_1 = e^{u_0}$, respectively. The transformation of the geometry and the trajectory of the moving electron is shown schematically in figure 5.14. Note that the mapping from annulus to ellipse is two-to-one and that there is a branch cut at $r = 1$ (see chapter 3), leading to a charge trajectory both inside and outside the annulus.

Parts of the results in this section have been presented in the supplementary material of [66].

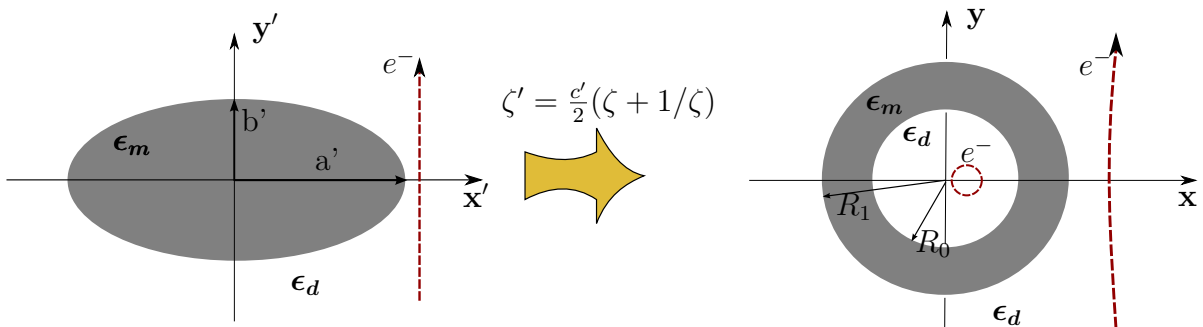


Figure 5.14: The transformation of the geometry and the (line) electron's trajectory from the ellipse's frame to the annulus' frame. Modified with permission from the supplementary material of [66]. Copyright 2016 American Chemical Society.

5.4.1 Transformation of the source potential

Here, we will derive the form of the source in the annulus frame. We know from Eq.5.15 that the potential of a charge moving in the vertical direction in the ellipse's frame is given by

$$\phi' = -\frac{\lambda}{4\pi\epsilon_0\omega} e^{-i\frac{\omega}{c_e}y'} e^{-|x'-x'_e|\frac{\omega}{c_e}}. \quad (5.96)$$

This means the potential incident on the ellipse, where $x' < x'_e$, is given by [66]

$$\phi^{sou} = \frac{\lambda}{4\pi\epsilon_0\omega} \exp\left[\frac{\omega}{c_e}(iy' + x' - x'_e)\right] \quad (5.97)$$

$$= \frac{\lambda \exp\left[-\frac{\omega}{c_e}x'_e\right]}{4\pi\epsilon_0\omega} \exp\left[\frac{\omega}{c_e}\zeta'\right]. \quad (5.98)$$

Substituting for ζ' from the Joukowski transformation in Eq.3.2 yields the potential in the annulus frame [66]

$$\phi^{sou} = \frac{\lambda \exp\left[-\frac{\omega}{c_e}x'_e\right]}{4\pi\epsilon_0\omega} \exp\left[\frac{\omega c'}{2c_e}\left(\zeta + \frac{1}{\zeta}\right)\right] \quad (5.99)$$

$$= \frac{\lambda \exp\left[-\frac{\omega}{c_e}x'_e\right]}{4\pi\epsilon_0\omega} \exp\left[\frac{\omega c}{2c_e}\left(re^{i\varphi} + \frac{1}{re^{i\varphi}}\right)\right]. \quad (5.100)$$

Similar to the non-concentric annulus case, we want to expand the above source potential in terms of the eigenfunctions of the annulus. That is, we want to write [66]

$$\phi^{sou} = \sum_{n=-\infty}^{n=\infty} a_n^s r^n e^{in\varphi}. \quad (5.101)$$

The expansion coefficients are determined in appendix A.2 and can be written as [66]

$$\begin{aligned} a_n^s &= \frac{\lambda \exp\left[-\frac{\omega}{c_e}u_0\right]}{4\pi\epsilon_0\omega} \sum_{k=0}^{\infty} \left(\frac{\omega c}{2c_e}\right)^{2k+|n|} \frac{1}{k!(k+|n|)!} \\ &= \frac{\lambda \exp\left[-\frac{\omega}{c_e}u_0\right]}{4\pi\epsilon_0\omega} I_{|n|}\left(\frac{\omega c}{c_e}\right), \end{aligned} \quad (5.102)$$

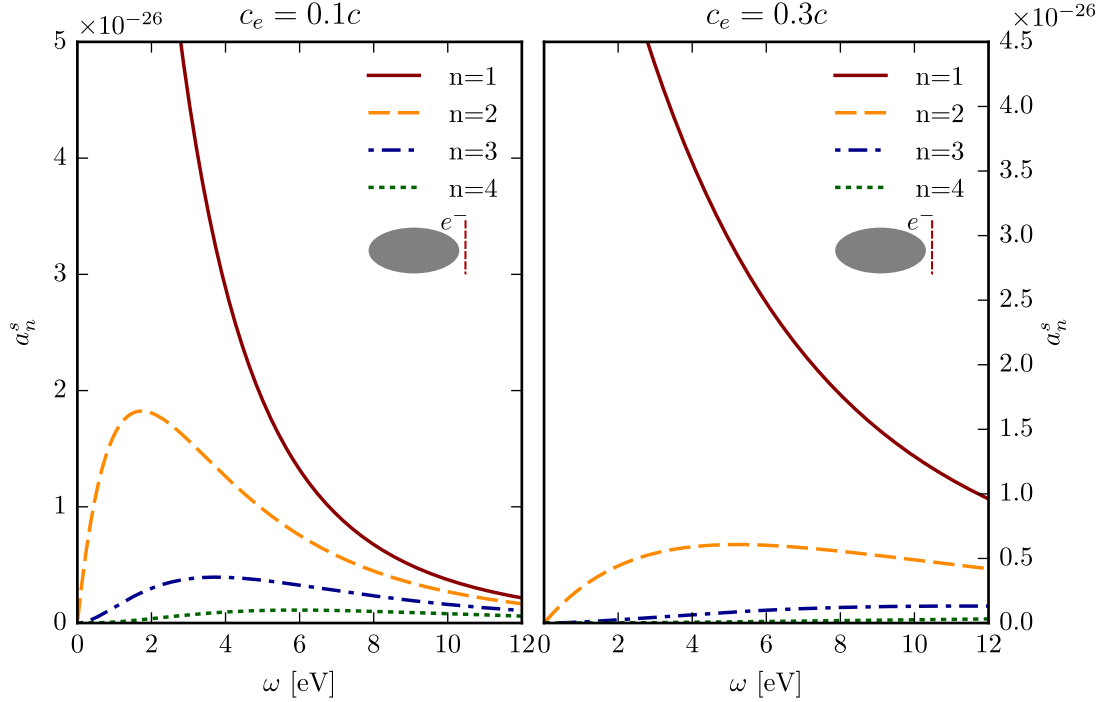


Figure 5.15: The value of the source expansion coefficients a_n^{s-} with $n = 1, 2, 3, 4$ for an electron passing vertically to the right of the ellipse (see figure 5.14). The parameters are $\lambda = 1.602 \times 10^{-19}$, $c' = 10^{-8}$, $u_0 = 0.4$, $x'_e = c' \cosh(u_0) + 2 \times 10^{-9}$, $c_e = 0.1$ on the left and $c_e = 0.3c$ on the right.

where we used the definition of the modified Bessel function of the first kind [152],

$$I_{|n|}\left(\frac{\omega c}{c_e}\right) = \sum_{k=0}^{\infty} \left(\frac{\omega c}{2c_e}\right)^{2k+|n|} \frac{1}{k!(k+|n|)!}. \quad (5.103)$$

The dependence of a_n^s on ω is shown for two different electron velocities in figure 5.15. Note that $I_{|n|}$, and thus a_n^s , is purely real and positive in the frequency range of interest ($\approx 0eV \dots 8eV$). Since no source coefficient passes through zero we do not expect any ‘accidental’ degeneracies, contrary to what has been observed for the non-concentric annulus.

5.4.2 Induced potentials and boundary conditions

In the following, we will determine the induced and scattered potentials in the annulus frame. We start by noting that $a_g^s = a_{-g}^s$, which means the source potential can be

rewritten as [66]

$$\phi_I^{sou} = \frac{a_0^s}{2} + \sum_{l=1}^{\infty} a_l^s r^{-l} e^{-il\varphi} + \sum_{l=1}^{\infty} a_l^s r^l e^{il\varphi} \varphi. \quad (5.104)$$

The form of the source potential indicates that the total potential in each region of the annulus geometry can be written as [66],

$$\begin{aligned} \phi_I &= \frac{a_0^s}{2} + \sum_{l=1}^{\infty} a_l^s r^{-l} (\cos(l\varphi) - i \sin(l\varphi)) + \sum_{l=1}^{\infty} a_l^s r^l (\cos(l\varphi) + i \sin(l\varphi)) \\ &\quad + \sum_{l=1}^{\infty} r^l (b_l^c \cos(l\varphi) + b_l^s i \sin(l\varphi)) \quad \text{for } r < R_0 \end{aligned} \quad (5.105)$$

$$\begin{aligned} \phi_{II} &= \frac{a_0^s}{2} + \sum_{l=1}^{\infty} r^{-l} (c_l^{c-} \cos(l\varphi) + c_l^{s-} i \sin(l\varphi)) \\ &\quad + \sum_{l=1}^{\infty} r^l (c_l^{c+} \cos(l\varphi) + c_l^{s+} i \sin(l\varphi)) \quad \text{for } R_0 < r < R_1 \end{aligned} \quad (5.106)$$

$$\begin{aligned} \phi_{III} &= \frac{a_0^s}{2} + \sum_{l=1}^{\infty} a_l^s r^l (\cos(l\varphi) + i \sin(l\varphi)) + \sum_{l=1}^{\infty} a_l^s r^{-l} (\cos(l\varphi) - i \sin(l\varphi)) \\ &\quad + \sum_{l=1}^{\infty} r^{-l} (d_l^c \cos(l\varphi) + d_l^s i \sin(l\varphi)) \quad \text{for } R_1 < r. \end{aligned} \quad (5.107)$$

There is an important difference here compared to the non-concentric annulus case. Namely that the potentials above are purely electrostatic and do not contain any terms modeling the radiative reaction of this system. This will be included separately in a later section. The electrostatic expansion coefficients $b_l^{c/s}$, $c_l^{c/s-}$, $c_l^{c/s+}$ and $d_l^{c/s}$ are determined from the boundary conditions in Eq.5.50-Eq.5.53, as before. We consider an ellipse with permittivity ϵ_m surrounded by a dielectric of unit permittivity. Under these conditions, the cosine coefficients are determined to be [66]

$$b_l^c = \left[\frac{((\epsilon_m^2 - 1)(R_1^{2l} - R_0^{2l}) - 4\epsilon_m R_1^{2l} R_0^{2l})}{(\epsilon_m - 1)^2 R_0^{2l} - (\epsilon_m + 1)^2 R_1^{2l}} R_0^{-2l} - 1 \right] a_l^s \quad (5.108)$$

$$c_l^{c-} = -2 \frac{(\epsilon_m - 1) R_0^{2l} R_1^{2l} + (\epsilon_m + 1) R_1^{2l}}{(\epsilon_m - 1)^2 R_0^{2l} - (\epsilon_m + 1)^2 R_1^{2l}} a_l^s \quad (5.109)$$

$$c_l^{c+} = -2 \frac{(\epsilon_m - 1) + (\epsilon_m + 1) R_1^{2l}}{(\epsilon_m - 1)^2 R_0^{2l} - (\epsilon_m + 1)^2 R_1^{2l}} a_l^s \quad (5.110)$$

$$d_l^c = \left[\frac{(\epsilon_m^2 - 1)(R_1^{2l} - R_0^{2l}) - 4\epsilon_m R_1^{2l} R_0^{2l}}{(\epsilon_m - 1)^2 R_0^{2l} - (\epsilon_m + 1)^2 R_1^{2l}} R_1^{2l} - 1 \right] a_l^s, \quad (5.111)$$

and the sine coefficients as [66],

$$b_l^s = \left[\frac{-(\epsilon_m^2 - 1)(R_1^{2l} - R_0^{2l}) - 4\epsilon_m R_1^{2l} R_0^{2l}}{(\epsilon_m - 1)^2 R_0^{2l} - (\epsilon_m + 1)^2 R_1^{2l}} R_0^{-2l} - 1 \right] a_l^s \quad (5.112)$$

$$c_l^{s-} = -2 \frac{(\epsilon_m - 1) R_0^{2l} R_1^{2l} - (\epsilon_m + 1) R_1^{2l}}{(\epsilon_m - 1)^2 R_0^{2l} - (\epsilon_m + 1)^2 R_1^{2l}} a_l^s \quad (5.113)$$

$$c_l^{s+} = -2 \frac{-(\epsilon_m - 1) + (\epsilon_m + 1) R_1^{2l}}{(\epsilon_m - 1)^2 R_0^{2l} - (\epsilon_m + 1)^2 R_1^{2l}} a_l^s \quad (5.114)$$

$$d_l^s = \left[\frac{(\epsilon_m^2 - 1)(R_1^{2l} - R_0^{2l}) + 4\epsilon_m R_1^{2l}}{(\epsilon_m - 1)^2 R_0^{2l} - (\epsilon_m + 1)^2 R_1^{2l}} R_1^{2l} + 1 \right] a_l^s. \quad (5.115)$$

5.4.3 Power absorbed by the ellipse

Knowledge of the electrostatic potential inside the annulus makes it possible to calculate the power absorbed by it in the same way as in section 5.3.5. That is, we calculate the resistive losses in the annulus via

$$Q(\omega) = -\frac{1}{2} \text{Re} \left(\int_S \mathbf{j}^* \cdot \mathbf{E} dS \right), \quad (5.116)$$

and deduce from energy conservation that the energy absorbed by the ellipse is the same. The steps to derive $Q(\omega)$ are outlined below and reproduced in the supplementary of [66]. The electric field inside the annulus is obtained from the electrostatic potential defined in Eq.5.106 as

$$E_r = \sum_{l=1}^{\infty} l r^{-l-1} (c_l^{c-} \cos(l\varphi) + c_l^{s-} i \sin(l\varphi)) - \sum_{l=1}^{\infty} l r^{l-1} (c_l^{c+} \cos(l\varphi) + c_l^{s+} i \sin(l\varphi)) \quad (5.117)$$

$$E_\phi = \sum_{l=1}^{\infty} l r^{-l-1} (c_l^{c-} \sin(l\varphi) - c_l^{s-} i \cos(l\varphi)) + \sum_{l=1}^{\infty} l r^{l-1} (c_l^{c+} \sin(l\varphi) - c_l^{s+} i \cos(l\varphi)). \quad (5.118)$$

The currents are obtained via Ohm's law $\mathbf{j} = -i\omega(\epsilon_m - 1)\epsilon_0\mathbf{E}$ [4]. Hence,

$$j_r^* = i\omega(\epsilon_m^* - 1)\epsilon_0 \sum_{l=1}^{\infty} \left[lr^{-l-1}((c_l^{c-})^* \cos(l\varphi) - (c_l^{s-})^* i \sin(l\varphi)) \right. \\ \left. - lr^{l-1}((c_l^{c+})^* \cos(l\varphi) - (c_l^{s+})^* i \sin(l\varphi)) \right], \quad (5.119)$$

$$j_\phi^* = i\omega(\epsilon_m^* - 1)\epsilon_0 \sum_{l=1}^{\infty} \left[lr^{-l-1}((c_l^{c-})^* \sin(l\varphi) + (c_l^{s-})^* i \cos(l\varphi)) \right. \\ \left. + lr^{l-1}((c_l^{c+})^* \sin(l\varphi) + (c_l^{s+})^* i \cos(l\varphi)) \right]. \quad (5.120)$$

The integral for $Q(\omega)$ has two contributions, the first from $j_r^* E_r$ the second from $j_\phi^* E_\phi$. The integrand of the first of these is given by,

$$j_r^* E_r = i\omega(\epsilon^* - 1)\epsilon_0 \sum_{l,g=1}^{\infty} gl \left(\left[r^{-l-1}((c_l^{c-})^* \cos(l\varphi) - (c_l^{s-})^* i \sin(l\varphi)) \right. \right. \\ \left. \left. - r^{l-1}((c_l^{c+})^* \cos(l\varphi) - (c_l^{s+})^* i \sin(l\varphi)) \right] \right. \\ \left. \times \left[r^{-g-1}(c_g^{c-} \cos(g\varphi) + c_g^{s-} i \sin(g\varphi)) - r^{g-1}(c_g^{c+} \cos(g\varphi) + c_g^{s+} i \sin(g\varphi)) \right] \right). \quad (5.121)$$

While this is a long expression, the integral of it is straightforward to evaluate by noting that $\sin(g\varphi)/\cos(g\varphi)$ are orthogonal and using the standard integral $\int_{R_0}^{R_1} dr r^{\pm 2l-1} = \frac{1}{\pm 2l-1} (R_1^{\pm 2l} - R_0^{\pm 2l})$. Similar considerations apply for $j_\phi^* E_\phi$. Here we simply quote the final result for the resistive losses in the annulus[66],

$$Q = -\frac{\omega}{2}\pi\epsilon_0\text{Im}(\epsilon_m) \sum_{l=1}^{\infty} \left[\frac{l^2}{2l-1} (|c_l^{s+}|^2 + |c_l^{c+}|^2) (R_1^{2l} - R_0^{2l}) \right. \\ \left. - \frac{l^2}{2l+1} (|c_l^{s-}|^2 + |c_l^{c-}|^2) (R_1^{-2l} - R_0^{-2l}) \right]. \quad (5.122)$$

5.4.4 Power scattered

The power scattered by the non-concentric annulus has been obtained by surrounding it with a fictive absorber and calculating the power absorbed by this fictive material. Due to energy conservation, the power scattered by the nanoparticle and the power absorbed by the fictive absorber are equal. In the annulus frame this fictive absorber transformed to a small particle with finite polarisability. The same method can be applied to find

the power scattered by the ellipse [66]. In this case, the fictive absorber surrounding the ellipse transforms to a small particle at the origin with finite polarisability.

Taking the polarisability of this fictive absorber to be γ_{abs} , the power absorbed by it or equivalently the power scattered by the ellipse can be determined from the induced dipole moment of the fictive absorber. We know dipole moment and incident electric field of a particle at the origin are related via [52]

$$\mathbf{p}_{abs} = \gamma_{abs} \mathbf{E}_{inc}(x = 0, y = 0). \quad (5.123)$$

The incident field is equal to the field scattered by the annulus, i.e. it can be obtained from the potential [66] as

$$\phi_I^{sca} = \sum_{l=1}^{\infty} r^l (b_l^c \cos(l\varphi) + b_l^s i \sin(l\varphi)) \quad (5.124)$$

$$\mathbf{E}(x = 0, y = 0) = -b_1^c \hat{x} - ib_1^s \hat{y}. \quad (5.125)$$

Substituting into the formula for the dipole moment gives,

$$\mathbf{p}_{abs} = \gamma_{abs} (-b_1^c \hat{x} - ib_1^s \hat{y}). \quad (5.126)$$

As previously, the power absorbed by such a particle is [52, 66]

$$P_{abs} = \frac{\omega}{2} \text{Im}(\mathbf{p}^*_{abs} \cdot \mathbf{E}^{sca}(0, 0)) \quad (5.127)$$

$$= \frac{\omega}{2} \text{Im}(\gamma_{abs}^* (|b_1^c|^2 + |b_1^s|^2)), \quad (5.128)$$

which is identical to the power scattered by the ellipse. Of course, we have not said anything about γ_{abs} yet, this will be determined in the next section.

Before moving on, it is worth to pausing and examining the implications of Eq.5.128. In contrast to the power scattered by the non-concentric annulus, the formula in Eq.5.128 only contains contributions from the first order modes, meaning that the radiative reaction of the nanoparticle will only affect these two modes [66]. Further, the scattering spectrum will only have contributions from the first order modes. Of course, this should not come as a surprise, as it simply restates the dipole selection rule discussed in chapter 3.

5.4.5 Radiative reaction

In the previous section, we calculated the power scattered by the ellipse by introducing a fictive absorber surrounding the ellipse. This absorber transformed to a small absorbing particle at the origin of the annulus. It has previously been shown in [53] and in section 5.3.3.2 that the multiple scattering between this fictive absorber and the annulus can be used to model the radiative reaction of the system. However, in the case of the ellipse a complication arises. Since the Joukowski transformation (Eq.3.2) is a two-to-one mapping from the annulus to the ellipse, the fictive absorber in the ellipse frame transforms to two fictive absorbers in the annulus frame. One is the small absorbing particle at the origin and the other is a fictive absorber surrounding the whole structure. This is shown schematically in figure 5.16. In the following two sections, we determine the influence of these two fictive absorbers on the plasmon excitations of the ellipse. The presentation follows the supplementary material of [66].

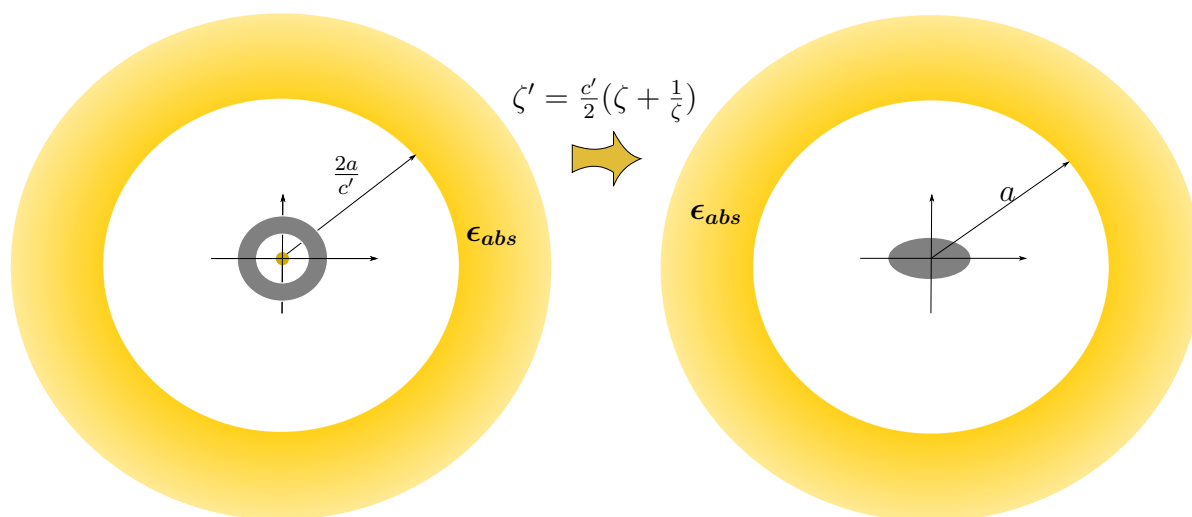


Figure 5.16: Transformation of the fictive absorber surrounding the elliptical particle. An absorber with a circular boundary at $r' = a$ and extending to infinity transforms to a small absorber at the origin with radius $r = c'/(2a)$ and an absorber surrounding the annulus with its boundary at $r = 2a/c'$. Both absorbers lead to multiple scattering with the annulus. Modified with permission from the supplementary material of [66]. Copyright 2016 American Chemical Society.

5.4.5.1 Fictive absorber at the origin

To model the multiple scattering between the fictive absorber at the origin and the inner surface of the annulus, it is paramount to relate the field scattered by the annulus to the field scattered back by the fictive absorber. For this, the dipole moment and hence the polarisability of the absorber have to be determined. It can be shown (see appendix C.1) that the permittivity of the fictive absorber surrounding the ellipse at position $r' = a$ has to be

$$\epsilon_{abs} = 1 + 2i\pi\left(\frac{k_0}{2}a\right)^2, \quad (5.129)$$

which is conserved under a conformal map to the annulus frame [42]. Next, we determine the shape and size of the fictive absorber at the origin in the annulus frame. The Joukowski transformation reads

$$\zeta' = \frac{c'}{2}\left(\zeta + \frac{1}{\zeta}\right). \quad (5.130)$$

Thus, for a particle near the origin, $\zeta \approx 0$, the second term in the transformation formula dominates and it reduces to

$$\zeta' = \frac{c'}{2\zeta}. \quad (5.131)$$

Hence a circle of radius $r' = a$ in the ellipse's frame transforms to a circle of radius

$$r = \frac{c'}{2a} \quad (5.132)$$

in the annulus frame. To conclude, the fictive absorber at the origin in the annulus frame is a cylindrical particle with radius $r = \frac{c'}{2a}$ and permittivity $\epsilon_{abs} = 1 + 2i\pi\left(\frac{k_0}{2}a\right)^2$ [66]. A cylindrical particle at the origin with this radius and permittivity acquires a dipole moment given by [66],

$$\mathbf{p}_{\text{abs}} = 2\pi\epsilon_0 \frac{(c')^2}{4a^2} \left(\frac{\epsilon_{\text{abs}} - 1}{\epsilon_{\text{abs}} + 1} \right) \mathbf{E}(\boldsymbol{\zeta} = \mathbf{0}) \quad (5.133)$$

$$\approx 2\pi\epsilon_0 \frac{(c')^2}{4a^2} i\pi \left(\frac{k_0}{2} a \right)^2 \mathbf{E}(\boldsymbol{\zeta} = \mathbf{0}) \quad (5.134)$$

$$= i\pi^2 \epsilon_0 \frac{(c')^2}{8} k_0^2 \mathbf{E}(\boldsymbol{\zeta} = \mathbf{0}) \quad (5.135)$$

$$= \gamma_{\text{abs}} \mathbf{E}(\boldsymbol{\zeta} = \mathbf{0}), \quad (5.136)$$

when an electric field is incident on it [52]. Here we defined the particles polarisability as [66],

$$\gamma_{\text{abs}} = i\pi^2 \epsilon_0 \frac{(c')^2}{8} k_0^2 \quad (5.137)$$

and the results are accurate to order $\mathcal{O}((\frac{k_0}{2}a)^2)$. Eq.5.126 then gives us the dipole moment of the fictive absorber as [66]

$$\mathbf{p}_{\text{abs}} = \begin{pmatrix} -\gamma_{\text{abs}} b_1^c \\ -i\gamma_{\text{abs}} b_1^s \end{pmatrix}. \quad (5.138)$$

Finally, the potential scattered/radiated by the dipole absorber at the origin is given by

$$\Phi_{I,\text{rad}} = \frac{1}{2\pi\epsilon_0} \frac{p_{\text{abs},x} \cos(\varphi) + p_{\text{abs},y} \sin(\varphi)}{r}. \quad (5.139)$$

Of course, this contribution has to be added to the total potential in that region. Which means the potential in Eq.5.105 has to be changed to

$$\begin{aligned} \Phi_I &= \frac{a_0^s}{2} + \sum_{l=1}^{\infty} a_l^s r^{-l} (\cos(l\varphi) - i \sin(l\varphi)) + \sum_{l=1}^{\infty} r^l (b_l^c \cos(l\varphi) + b_l^s i \sin(l\varphi)) \\ &+ \frac{1}{2\pi\epsilon_0} \frac{p_{\text{abs},x} \cos(\varphi) + p_{\text{abs},y} \sin(\varphi)}{r} \quad \text{for } r < R_0. \end{aligned} \quad (5.140)$$

This will alter the boundary condition for the $l = 1$ term, but higher order modes remain unaffected [66].

5.4.5.2 Fictive absorber surrounding the annulus

As aforementioned and shown in figure 5.16, there is also a fictive absorber surrounding the annulus. If the fictive absorber is far away from the surface of the annulus, the term

$$\zeta' = \frac{c'}{2}\zeta, \quad (5.141)$$

dominates the Joukowski transformation $\zeta' = \frac{c'}{2}(\zeta + \frac{1}{\zeta})$; a circle of radius $r' = a$ transforms to a circle of radius $r = 2a/c'$ in the annulus frame [66]. This circle forms the inner boundary of the fictive absorber. Details on how to choose a are given in appendix C.1, it essentially must be large enough such that all but the $l = 1$ modes have decayed to zero when reaching the surface of the fictive absorber.

Of course, the absorber surrounding the annulus also gives rise to a reflected field [66]. The field incident on the fictive absorber is equal to the field scattered by the annulus and its potential is given by [66]

$$\Phi_{II,sca}(r \longrightarrow 2a/c) = \frac{1}{r}d_1^c \cos(\varphi) + \frac{1}{r}id_1^s \sin(\varphi). \quad (5.142)$$

There will thus be a reflected and transmitted potential given by [66]

$$\phi_{II,rad} = rR_{rad}^c \cos(\varphi) + riR_{rad}^s \sin(\varphi) \quad \text{for } r < \frac{2a}{c'} \quad (5.143)$$

$$\phi_{II,tra} = \frac{1}{r}T_{rad}^c \cos(\varphi) + \frac{1}{r}iT_{rad}^s \sin(\varphi) \quad \text{for } r > \frac{2a}{c'}. \quad (5.144)$$

Matching $\phi_{II,rad} + \phi_{II,sca}$ and $\phi_{II,tra}$ at $r = 2a/c'$ yields [66]

$$R_{rad}^c - \left(\frac{2a}{c'}\right)^{-2} d_1^c = -\epsilon_{abs} \left(\frac{2a}{c'}\right)^{-2} T_{rad}^c \quad (5.145)$$

$$R_{rad}^c + \left(\frac{2a}{c'}\right)^{-2} d_1^c = \left(\frac{2a}{c'}\right)^{-2} T_{rad}^c, \quad (5.146)$$

which can be solved to give

$$R_{rad}^c = \left(\frac{2a}{c'}\right)^{-2} \frac{1 - \epsilon_{abs}}{1 + \epsilon_{abs}} d_1^c \quad (5.147)$$

and equivalently for the sine reflection coefficient

$$R_{rad}^s = \left(\frac{2a}{c'}\right)^{-2} \frac{1 - \epsilon_{abs}}{1 + \epsilon_{abs}} d_1^s. \quad (5.148)$$

Using $\epsilon_{abs} = 1 + 2i\pi(\frac{k_0}{2}a)^2$ and expanding to first order, the coefficients reduce to [66]

$$R_{rad}^{c/s} = - \left(\frac{2a}{c'}\right)^{-2} i\pi\left(\frac{k_0}{2}a\right)^2 d_1^{c/s} \quad (5.149)$$

$$= \frac{-i\pi(c')^2 k_0^2}{16} d_1^{c/s}. \quad (5.150)$$

As was the case for the fictive absorber at the origin, the field reflected by the fictive absorber has to be added to the total potential in that region. That is, the potential in Eq.5.107 has to be modified to [66]

$$\begin{aligned} \Phi_{III} = & \frac{a_0^s}{2} + \sum_{l=1}^{\infty} a_l^s r^l (\cos(l\varphi) + i \sin(l\varphi)) + \sum_{l=1}^{\infty} r^{-l} (d_l^c \cos(l\varphi) + d_l^s i \sin(l\varphi)) \\ & + r R_{rad}^c \cos(\varphi) + r i R_{rad}^s \sin(\varphi) \quad \text{for } R_1 < r < \frac{2a}{c}. \end{aligned} \quad (5.151)$$

Again, this only alters the $l = 1$ coefficients and leaves higher order modes unchanged.

5.4.5.3 Modified expression for the $l = 1$ scattering coefficients

The presence of the fictive absorber modifies the boundary conditions of the $l = 1$ mode. Hence, we must re-derive expressions for the expansion coefficients $b_1^{c/s}$, $c_1^{c/s-}$, $c_1^{c/s+}$ and $d_1^{c/s}$, but can use the formulae we derived earlier for any $l \neq 1$. The modified potential for the $l = 1$ term in each region reads[66]

$$\begin{aligned} \phi_I^1 = & a_1^s r^{-1} (\cos(\varphi) - i \sin(\varphi)) + r^1 (b_1^c \cos(\varphi) + b_1^s i \sin(\varphi)) \\ & + \frac{1}{2\pi\epsilon_0} \frac{p_{abs,x} \cos(\varphi) + p_{abs,y} \sin(\varphi)}{r} \quad \text{for } r < R_0 \end{aligned} \quad (5.152)$$

$$\phi_{II}^1 = r^{-1} (c_1^{c-} \cos(\varphi) + c_1^{s-} i \sin(\varphi)) + r^1 (c_1^{c+} \cos(\varphi) + c_1^{s+} i \sin(\varphi)) \quad \text{for } R_0 < r < R_1 \quad (5.153)$$

$$\begin{aligned} \phi_{III}^1 = & a_1^s r^1 (\cos(\varphi) + i \sin(\varphi)) + r^{-1} (d_1^c \cos(\varphi) + d_1^s i \sin(\varphi)) \\ & + r R_{rad}^c \cos(\varphi) + r i R_{rad}^s \sin(\varphi) \quad \text{for } R_1 < r < \frac{2a}{c}. \end{aligned} \quad (5.154)$$

The usual boundary conditions at the interface (Eq.5.50-Eq.5.53) yield a set of linear equations that can be solved to give [66]

$$b_1^c = -a_1^s \left(\left[C_0(\epsilon + 1)^2 R_0^2 R_1^{-2} - C_0(\epsilon - 1)^2 - (\epsilon^2 - 1)(R_0^2 R_1^{-2} - 1)R_1^{-2} \right] - 4\epsilon R_0^2 R_1^{-2} \right) / C \quad (5.155)$$

$$c_1^{c-} = 2a_1^s R_0^2 \left(\left[C_0(1 - \epsilon_0) + (1 + \epsilon)R_1^{-2} \right] - \left[R_1^{-2}(C_0(1 + \epsilon) + R_0^2(1 - \epsilon)) \right] \right) / C \quad (5.156)$$

$$c_1^{c+} = 2R_1^{-2} a_1^s \left(\left[(\epsilon - 1)R_0^2 R_1^{-2} - C_0(\epsilon + 1)R_0^2 \right] + \left[(\epsilon + 1)R_0^2 - (\epsilon - 1)C_0 \right] \right) / C \quad (5.157)$$

$$d_1^c = -a_1^s \left(C_0 \left[(\epsilon + 1)^2 R_0^2 R_1^{-2} - (\epsilon - 1)^2 \right] - R_0^2 \left[(\epsilon^2 - 1)(R_0^2 R_1^{-2} - 1) \right] - 4\epsilon R_0^2 R_1^{-2} \right) / C \quad (5.158)$$

with the denominator

$$C = R_0^2 R_1^{-2} \left[(\epsilon + 1)^2 - (\epsilon - 1)^2 R_0^2 R_1^{-2} \right] + C_0 \left[(\epsilon^2 - 1)(R_0^2 R_1^{-2} - 1)(R_0^2 + R_1^{-2}) \right] + C_0^2 \left[(1 + \epsilon)^2 R_0^2 R_1^{-2} - (\epsilon - 1)^2 \right] \quad (5.159)$$

and

$$C_0 = \frac{i\pi(c')^2 k_0^2}{16}. \quad (5.160)$$

And similarly for the sine coefficients [66]

$$b_1^s = -a_1^s \left(- \left[C_0(\epsilon + 1)^2 R_0^2 R_1^{-2} - C_0(\epsilon - 1)^2 - (\epsilon^2 - 1)(R_0^2 R_1^{-2} - 1)R_1^{-2} \right] - 4\epsilon R_0^2 R_1^{-2} \right) / C \quad (5.161)$$

$$c_1^{s-} = 2a_1^s R_0^2 \left(- \left[C_0(1 - \epsilon) + (1 + \epsilon)R_1^{-2} \right] - \left[R_1^{-2}(C_0(1 + \epsilon) + R_0^2(1 - \epsilon)) \right] \right) / C \quad (5.162)$$

$$c_1^{s+} = 2R_1^{-2} a_1^s \left(- \left[(\epsilon - 1)R_0^2 R_1^{-2} - C_0(\epsilon + 1)R_0^2 \right] + \left[(\epsilon + 1)R_0^2 - (\epsilon - 1)C_0 \right] \right) / C \quad (5.163)$$

$$d_1^s = -a_1^s \left(C_0 \left[(\epsilon + 1)^2 R_0^2 R_1^{-2} - (\epsilon - 1)^2 \right] - R_0^2 \left[(\epsilon^2 - 1)(R_0^2 R_1^{-2} - 1) \right] + 4\epsilon R_0^2 R_1^{-2} \right) / C \quad (5.164)$$

with C from Eq.5.159.

This completes the section on the radiative correction, as it is now included in the expressions for the expansion coefficients. As aforementioned, only the dipole $l = 1$ modes are affected, since only those couple to plane waves transporting energy to infinity. A

behaviour which does not come unexpected in light of the dipole selection rule discussed in chapter 3.

5.4.6 Comparison with COMSOL

Here, we compare our analytical results for the electron energy loss and photon emission spectra with fully electrodynamic solutions using COMSOL Multiphysics. The simulations have been set up in the same way as described in 5.3.6, but using an elliptical nanoparticle. Figure 5.17 shows results using a Drude model permittivity in Eq.5.79 for the nanoparticle, with $\gamma = 0.32eV$, $\omega_p = 8eV$ and $\omega_{sp} \approx 5.67eV$. Whereas in figure 5.18 experimental data has been used [65]. In both cases, the surrounding medium has $\epsilon_d = 1$. The electron energy loss probability and photon emission probability have been obtained from Eq.5.91 and Eq.5.92, respectively.

Figure 5.17 (left) shows the effect of the radiative reaction on the electron energy loss and photon emission spectrum. The effect of the radiative reaction is much more prominent than for a non-concentric annulus of similar dimensions, see figure 5.7 for comparison. On the right of the same figure, we compare the electron energy loss probability and photon emission probability with COMSOL simulations for different electron velocities. Agreement between analytics and simulations is very good. While the electron is able to excited higher order plasmon modes, as visible in the electron loss spectrum, the dipole selection rule holds in the photon emission spectrum to good accuracy. There are only slight discrepancies for the case of an electron moving with velocity $c_e = 0.05c$. There we can see a small peak at $\approx 6eV$, which indicates coupling between the quadrupole ($l = 2$) mode of the ellipse and the quadrupole mode of an electromagnetic wave (see also chapter 3). This peak is likely to become stronger for

	Analytics		COMSOL	
	$e_{loss}^- [eVm^{-1}]$	$N(\gamma)$	$e_{loss}^- [eVm^{-1}]$	$N(\gamma)$
$c_e = 0.05c$	8.91×10^{-12}	3.89×10^{-13}	1.23×10^{-11}	4.54×10^{-13}
$c_e = 0.1c$	1.80×10^{-11}	1.14×10^{-12}	2.26×10^{-11}	1.31×10^{-12}
$c_e = 0.3c$	1.65×10^{-11}	1.18×10^{-12}	1.87×10^{-11}	1.40×10^{-12}

Table 5.5: Table giving the total energy loss defined by $\int e_{loss}^-(\omega)d\omega$ in units of [eV per unit length] and the total number of photons emitted. Results for analytical calculations for a line electron passing to the right of the ellipse are compared with COMSOL simulations. This data is for a nanoparticle with experimental permittivity data of silver [65].

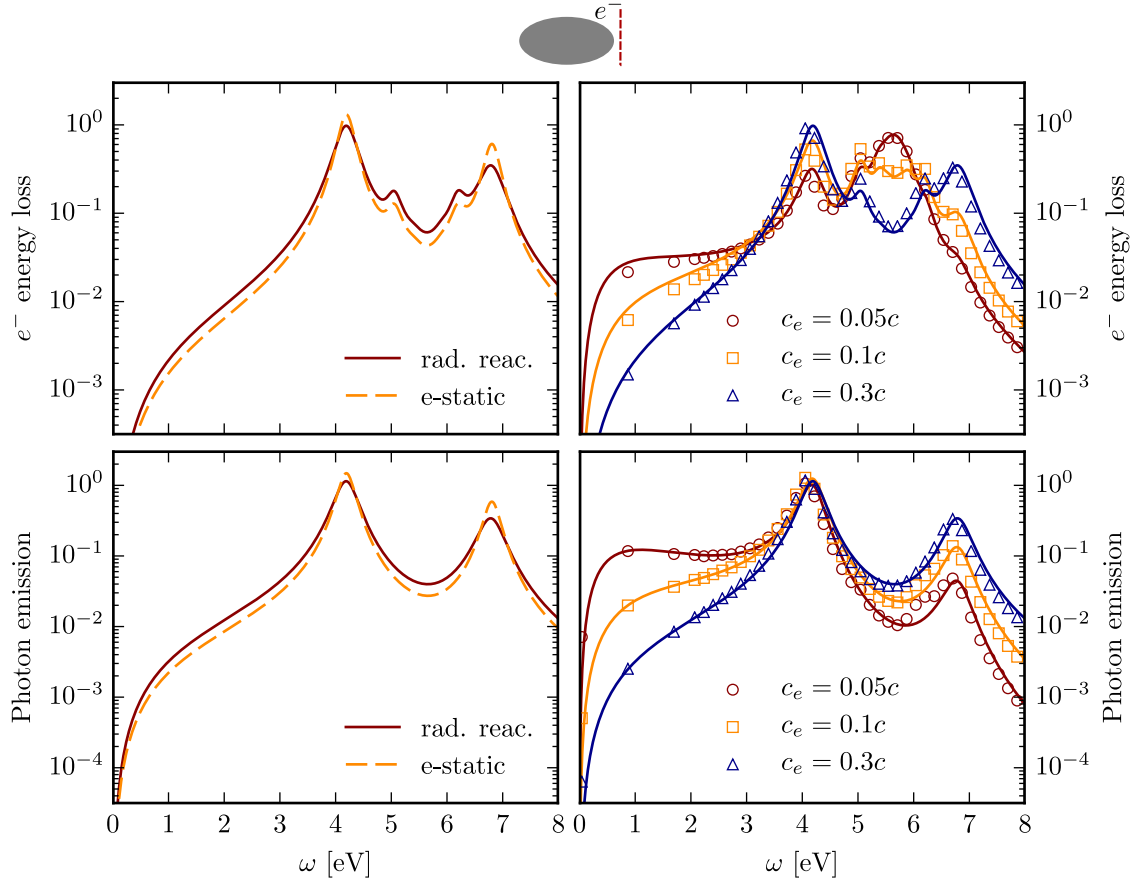


Figure 5.17: The electron energy loss (top) and photon emission (bottom) probability density for a (line) electron passing to the right of the ellipse. The electron energy loss probability density is in units of $[eV^{-1}$ per electron per unit length]. Similarly the photon emission probability density is in terms of the number of photons emitted in units of $[eV^{-1}$ per electron per unit length]. The area under each of the curves is unity. The solid lines correspond to analytical results, with the accompanying markers corresponding to COMSOL simulations. On the left, we compare the electrostatic solution to the one including the radiative reaction of the ellipse for $c_e = 0.3c$. The geometrical parameters were set to $u_0 = 0.4$, $c' = 10^{-8}$ giving an ellipse of width $\approx 22nm$ and height $\approx 8nm$. The distance of the electron to the particle was $2nm$. The constant λ defined in Eq.5.15 was set to $1.602 \times 10^{-19} Cm^{-1}$.

lower losses or larger nanoparticles. To conclude, the dipole selection rule also holds for a moving electron as a source, but only approximately.

Figure 5.17 compares analytics and simulations for experimental values of the permittivity of silver [65]. Agreement is good in this case too, though it is not as good as it was for the non-concentric annulus. This is also reflected in the total energy lost

by the (line) electron and total number of photons emitted as tabulated in table 5.5. The discrepancies seem strongest for the lowest electron velocities. However, both the resonance frequencies and their peak heights are predicted to very good accuracy.

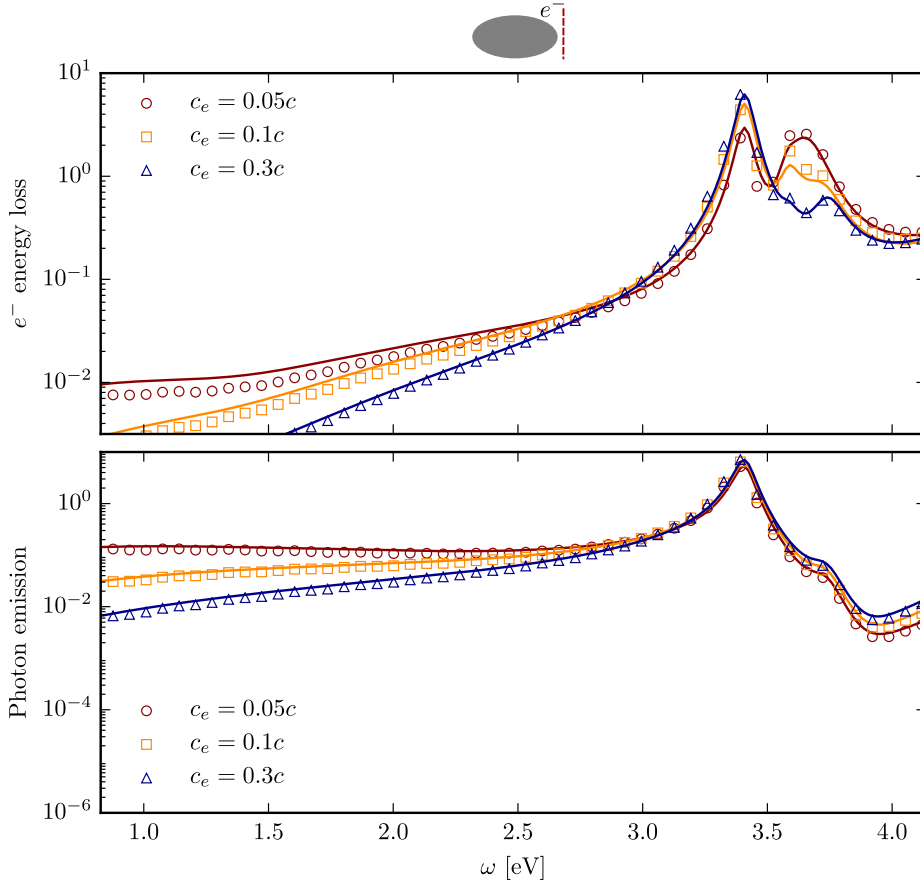


Figure 5.18: The electron energy loss (top) and photon emission (bottom) probability density for a (line) electron passing to the right of the ellipse. The electron energy loss probability density is in units of $[eV^{-1}$ per electron per unit length]. Similarly the photon emission probability density is in terms of the number of photons emitted in units of $[eV^{-1}$ per electron per unit length]. The area under each of the curves is unity. The solid lines correspond to analytical results, with the accompanying markers corresponding to COMSOL simulations. We used permittivity data from [65] for the nanoparticle. All other parameters are the same as in figure 5.17. This data has also been published in the supplementary material of [66].

5.4.7 Time response of the ellipse

In the previous few sections, we solved for the electromagnetic response of an elliptical nanoparticle when a fast (line) electron moves past it. All the calculations have been done in frequency space, but have been fully analytical. This allows us to obtain the time response of the system in the same way as for the non-concentric annulus, i.e. by implementing a ‘Fast Fourier transform’ of the frequency space solution, see Eq.5.95.

Please see the supplementary media files (appendix D) for a video simulation showing the electric field distribution in and around the nanoparticle when the line electron moves past it. As was the case for the non-concentric annulus, plasmons are strongly excited as soon as the electron is in the vicinity of the particle. However, since the non-concentric annulus possesses a ‘special’ point (where it is thinnest), plasmons could be seen to propagate towards that point. Such a behaviour is not observed for the ellipse, as it

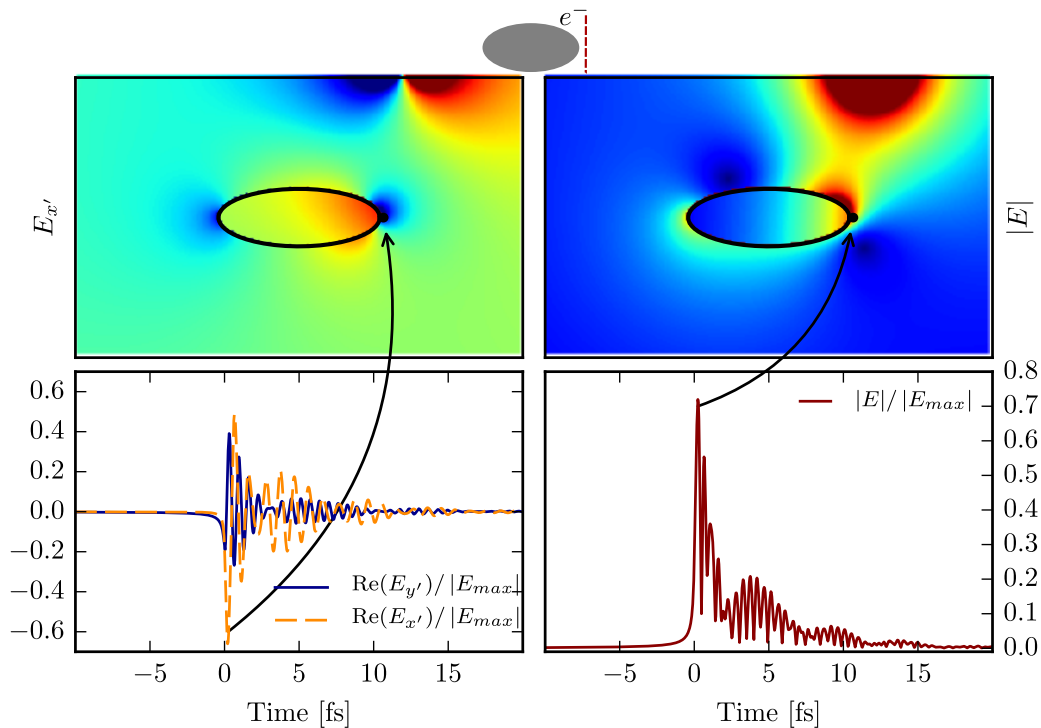


Figure 5.19: The top panel shows the electric field distribution at a specific time point (indicated by the arrow). E_u on the left and $|E|$ on the right. The bottom panel shows the time response of the crescent at a particular point (marked by the black dot in the top panel). In this case, the electron moves vertically to the left of the nanoparticle. The plots in the bottom panel have been normalised by the maximum source field at that particular point.

does not possess a unique sharp feature at which the plasmons are concentrated (at least not for a sufficiently ‘round’ ellipse).

Figure 5.19 shows a snapshot of the time response (top panels), together with a time series at a particular point in space (bottom panels). The strong fields at the top of the top two panels stem from the electron, which has just moved out of the frame. Near the ellipse, the emergence of plasmons can be observed. The time series for the electric field components and its magnitude show rapid oscillations modulated by a longer wavelength envelope function, i.e. the characteristic field pattern for the interference of two waves of different frequency. From the spectrum in figure 5.17 we deduce that this interference pattern is generated by the two dipole resonances at $\approx 4.2eV$ and $\approx 6.7eV$, as the two other peaks are considerably smaller. As for the non-concentric annulus, these oscillations are prominent on a time scale of about ten femtoseconds. At longer times most of the energy has been absorbed via resistive losses or emitted as photons.

5.5 Summary

To summarise, we have shown that the TO approach to solve problems in plasmonics can be adapted to treat electron energy loss calculations. We compared our theoretical results with fully electrodynamic simulations and found excellent agreement for structures much smaller than the wavelength. Interestingly, despite the non-relativistic approximations applied in the theory, the results compared well with numerical simulations even for rather large velocities $\approx 0.5c$. The major advantage of the TO approach to electron energy loss calculations is that it is fully analytic. This does not only lead to deeper physical insight, but also allows us to study the time evolution of these systems in a time efficient manner, by ‘Fourier transforming’ the frequency space solutions.

Chapter 6

Conclusion

At the beginning of this thesis we set out to answer, among others, two questions: firstly, “Can Transformation optics be used to study plasmonic systems of extent greater than the wavelength of light, such that currents can flow on a scale larger than the wavelength?” and secondly, “Can Transformation optics be used to reveal, study and make use of symmetries in plasmonic systems?”. The answer to both is yes.

The crux of the first question is the current flowing on a scale larger or comparable to the wavelength. This meant that magnetic effects could not be ignored. Indeed the study of the plasmonic grating showed, that it is of paramount importance to treat the strong currents induced in such systems for an accurate description of their optical response. While several technical issues had to be overcome, TO has been successfully applied to predict the spectral properties and calculate the optical response of a thin plasmonic grating in the electrostatic limit, though incorporating magnetic effects in the form of a radiative reaction is possible as well. This was achieved by transforming the grating to a much simpler system. Although the plasmonic grating was the system studied in detail in chapter 4, it is not the only one that can be analysed using this approach. Indeed we showed that a chain of particles on top of a flat surface could be analysed using very similar methods and so could half-spaces with a periodically modulated interface and nanoparticle chains inside a dielectric. Moreover, all these systems were related in some sense, which brings us to the second question.

While extending the TO approach to semi-infinite periodic structures was mainly about tackling some technical challenges, using TO to study symmetries is more subtle. Symmetries often provide a means of classification and so they did here. Albeit, it was not the geometrical symmetries of the nanoparticle that provided classification of the plasmon modes, but the symmetries of the underlying ‘mother’ structure. This already was apparent in the first chapter, where a hidden rotational symmetry in the

ellipse and spheroid could be revealed by transforming them to a symmetric annulus and spherical shell, respectively. This rotational symmetry enabled us to classify the plasmon modes of the angular momentum numbers in the transformed ‘mother’ frame. Not only did this allow us to solve the system analytically, but it also showed a connection between symmetry breaking in the ellipse/spheroid frame and plasmon hybridisation in the annulus/shell frame. Yet it was for the plasmonic grating that the usefulness of TO to reveal hidden symmetries really showed its hand. Here, we were able to relate not a single grating, but a whole *class* of gratings to a single underlying semi-infinite slab. Since the slab was translationally invariant, this had profound consequences on the spectra of the gratings. Translational invariance leads to a gapless excitation spectrum, while one expects energy bands and gaps for a periodically modulated plasmonic grating. Yet, the underlying symmetry of the ‘mother’ structure forbids this, leading to ‘degeneracy’ points where two bands cross. Though this result only holds strictly at the centre of the Brillouin zone, it is an intriguing feature that is most easily explained using the TO framework. Moreover, the same transformation could be used to map a chain of nanoparticles on a surface into the same translationally invariant slab. A modified version of the transformation could similarly be used to map two half-spaces with modulated interface and an isolated chain of nanoparticles onto two half-spaces with planar interface. In each case, it wasn’t a single structure that could be transformed, but a whole ‘equivalence’ class, so to speak. This did not only confirm that TO can be used to study underlying symmetries in plasmonic systems, but also that there are good reasons for doing so. Namely, they classify both the eigenmodes and the spectral properties of the system, they allow for analytical solutions, they provide unique physical insight and TO provides the ideal tool to uncover them.

The last section of the thesis was less concerned with the concept of symmetries, though they certainly played a large role in the analytical solution to the problem at hand. There, we extended the TO approach to analytically calculate the electron energy loss (EELS) and cathodoluminescence (CL) spectra for a two-dimensional ellipse and non-concentric annulus. Again, this was made possible and largely simplified by transforming the ellipse and the non-concentric annulus to a more symmetrical ‘mother’ structure. Analytical solutions to EELS and CL problems are rare [132], but TO has been shown previously to be a great tool to study the plasmonic properties of nanoparticles with complex shapes and here we extended its range of applicability to EELS and CL studies. Most importantly, these are not restricted to the frequency domain. Since all calculations are done analytically and the resulting computations are very fast, it is possible to conduct a time-domain analysis by a simple ‘Fast Fourier Transform’ of

the analytical solutions. This makes it possible to create video simulations of ‘EELS experiments’ and some examples are given in the supplementary, together with a simple GUI program that implements the TO solutions to EELS and CL problems for a few geometries.

Of course, no thesis is ever complete and this one is no exception to the rule. There are a number of shortcomings that we would like to discuss here, as well as avenues of future studies that became apparent during the research.

First, some technical issues. In the study of the plasmonic grating in chapter 4 the calculation of the band structure was only accurate near the centre of the Brillouin zone, but could not match numerical simulations at the zone edge. This also meant that the calculation of the optical response was limited to normal incidence. Problems arose due to the analytical structure of the conformal transformation, which features many branch cuts that lead to unphysical discontinuities in the potential, for \mathbf{k} -vectors away from the zone centre. The solution to this problem has proven elusive to the author for quite some time. Fortunately, John Pendry succeeded in extending the approach presented in this thesis to calculate the band structure near the zone edge. This is not included in this thesis, but we want to stress here that it is possible.

Second, this thesis mainly focussed on method development and as such, applications played only a minor part in it. Naturally, methods are only really useful if, some day, they can be applied to solve some interesting problems. In our case, the methods developed to treat the plasmonic grating have been successfully applied by Huidobro et. al [153] to study graphene sheets with inhomogeneous doping on both flat and corrugated substrates. Here, too, TO could be used to calculate the optical response of the system. Additionally, the analytical nature of the solution allowed to efficiently optimise the system parameters to maximise absorption. It is our hope, that this does not remain the only instance where our approach proved valuable in the physical interpretation and accurate description of periodic plasmonic systems.

Third, interaction with experiments was minimal. This is the case for both the first two sections and the section on TO for EELS. In the case of the plasmonic grating, a particularly interesting route for further investigation is the bi-anisotropy. Experiments are currently under way to design plasmonic gratings, which maximise this effect and lead to a strong electro-magnetic coupling. The last chapter extended TO to treat EELS and CL studies. Here, we were mainly concerned to develop the formalism and treat two toy systems: the ellipse and the non-concentric annulus. We do expect, however, to be able to treat more complicated and interesting systems and hope that we can

provide some physical insight into EELS and CL experiments. We feel quite positive that this is possible, as Luo et. al [149] have already considered two, closely spaced, three-dimensional spheres.

To sum up, we believe that the techniques developed in this thesis are powerful enough to have an impact on future theoretical investigations of plasmonic systems and to possibly provide some insight into applications and experimental results. Some promising routes of further research include: the extension of the TO approach for plasmonic gratings to non-normal incidence, further investigations into the bi-anisotropy of these gratings, the extension of the TO for EELS approach to other structures (e.g. 2-D knife edge, 2-D blunt knife edge, 2-D bow-tie antennas, 3-D spheroids, 3-D hyperboloids, etc.), application of these techniques to interpret experimental data and to use the analytical properties of the solutions to optimise systems for a particular application.

Appendix A

Supporting analytical calculations for a two-dimensional ellipse

A.1 Resonance condition for an ellipse

Here, we'll derive the resonance condition for an ellipse. The ellipse with semi-major axis $a' = c' \cosh(u_0)$ and semi-minor axis $b' = c' \sinh(u_0)$ can be transformed to an annulus with inner radius $R_0 = e^{-u_0}$ and outer radius $R_1 = e^{u_0}$, as has been shown in section 3.1. The potential in the annulus region must satisfy Laplace's equation in polar coordinates [52]. This means the electrostatic potential can be written as

$$\phi_I = \sum_n r^{-n} (a_n^{sou} \cos(n\phi) + A_n^{sou} \sin(n\phi)) + r^n ((a_n^{sca} \cos(n\phi) + A_n^{sca} \sin(n\phi))) \quad (\text{A.1})$$

$$\phi_{II} = \sum_n r^{-n} (b_n^{in} \cos(n\phi) + B_n^{in} \sin(n\phi)) + r^n ((c_n^{in} \cos(n\phi) + C_n^{in} \sin(n\phi))) \quad (\text{A.2})$$

$$\phi_{III} = \sum_n r^{-n} (d_n^{sca} \cos(n\phi) + D_n^{sca} \sin(n\phi)) + r^n ((d_n^{sou} \cos(n\phi) + D_n^{sou} \sin(n\phi))), \quad (\text{A.3})$$

where ϕ_I holds for $r < R_0$, ϕ_{II} holds for $R_0 < r < R_1$ and ϕ_{III} for $r > R_1$. Here, a_n^{sou}/A_n^{sou} and d_n^{sou}/D_n^{sou} are the source coefficients of the dipole inside and the constant electric field outside the annulus. The other coefficients give the scattered and induced fields and are to be determined from the boundary conditions [20]. Demanding continuity of the tangential component of the electric field and the normal component of the electric displacement field yields the following set of boundary equations for each n for the cosine

coefficients

$$\begin{pmatrix} \epsilon_d R_0^{2n} & \epsilon_m & -\epsilon_m R_0^{2n} & 0 \\ R_0^{2n} & -1 & -R_0^{2n} & 0 \\ 0 & -\epsilon_m & \epsilon_m R_1^{2n} & \epsilon_d \\ 0 & 1 & R_1^{2n} & -1 \end{pmatrix} \begin{pmatrix} a_n^{sca} \\ b_n^{in} \\ c_n^{in} \\ d_n^{sca} \end{pmatrix} = \begin{pmatrix} \epsilon_d a_n^{sou} \\ -a_n^{sou} \\ \epsilon_d R_1^{2n} d_n^{sou} \\ R_1^{2n} d_n^{sou} \end{pmatrix}. \quad (\text{A.4})$$

These can be solved to give

$$a_n^{sca} = \frac{a_n^{sou}(\epsilon_d^2 - \epsilon_m^2)(R_0^{2n} - R_1^{2n}) - 4d_n^{sou}\epsilon_d\epsilon_m R_0^{2n} R_1^{2n}}{R_0^{2n}[(\epsilon_d - \epsilon_m)^2 R_0^{2n} - (\epsilon_d + \epsilon_m)^2 R_1^{2n}]} \quad (\text{A.5})$$

$$b_n^{in} = -\frac{2a_n^{sou}(\epsilon_d + \epsilon_m)\epsilon_d R_1^{2n} + 2d_n^{sou}\epsilon_d(\epsilon_m - \epsilon_d)R_0^{2n} R_1^{2n}}{[(\epsilon_d - \epsilon_m)^2 R_0^{2n} - (\epsilon_d + \epsilon_m)^2 R_1^{2n}]} \quad (\text{A.6})$$

$$c_n^{in} = \frac{2\epsilon_d(\epsilon_d - \epsilon_m)a_n^{sou} - 2\epsilon_d(\epsilon_d + \epsilon_m)R_1^{2n}d_n^{sou}}{[(\epsilon_d - \epsilon_m)^2 R_0^{2n} - (\epsilon_d + \epsilon_m)^2 R_1^{2n}]} \quad (\text{A.7})$$

$$d_n^{sca} = \frac{-4\epsilon_d\epsilon_m a_n^{sou} R_1^{2n} + (\epsilon_d^2 - \epsilon_m^2)(r_-^{2n} - r_+^{2n})R_1^{2n}d_n^{sou}}{[(\epsilon_d - \epsilon_m)^2 R_0^{2n} - (\epsilon_d + \epsilon_m)^2 R_1^{2n}]} \quad (\text{A.8})$$

The coefficients for the sine terms are similar. The plasmon resonance condition is obtained from the zeros of the denominator [52], i.e. from

$$[(\epsilon_d - \epsilon_m)^2 R_0^{2n} - (\epsilon_d + \epsilon_m)^2 R_1^{2n}] = 0 \quad (\text{A.9})$$

$$[(\epsilon_d - \epsilon_m)R_0^n - (\epsilon_d + \epsilon_m)R_1^n][(\epsilon_d - \epsilon_m)R_0^n + (\epsilon_d + \epsilon_m)R_1^n] = 0. \quad (\text{A.10})$$

There are thus two types of modes corresponding to the zero of either factor, substituting $R_0 = e^{-u_0}$ and $R_1 = e^{u_0}$, and rearranging gives the two resonance condition for even

$$\tanh(nu_0) = -\frac{\epsilon_d}{\epsilon_m},$$

and odd modes

$$\tanh(nu_0) = -\frac{\epsilon_m}{\epsilon_d},$$

as given in section 3.1.

A.2 Expansion coefficients: EELS for the ellipse

In this section, we derive the expansion coefficients given in Eq.5.102. We aimed for an expansion of the source potential of an electron in the annulus frame in Eq.5.100

$$\phi^{sou} = \frac{\lambda \exp\left[-\frac{\omega}{c_e} x'_e\right]}{4\pi\epsilon_0\omega} \exp\left[\frac{\omega c}{2c_e} \left(re^{i\varphi} + \frac{1}{re^{i\varphi}}\right)\right], \quad (\text{A.11})$$

as an infinite series of the form

$$\phi^{sou} = \sum_{n=-\infty}^{n=\infty} a_n^s r^n e^{in\varphi}. \quad (\text{A.12})$$

We start by writing

$$\exp\left[\frac{\omega c}{2c_e} \left(re^{i\varphi} + \frac{1}{r}e^{-i\varphi}\right)\right] = \exp\left[\frac{\omega c}{2c_e} re^{i\varphi}\right] \exp\left[\frac{\omega c}{2c_e} \frac{1}{re^{i\varphi}}\right] \quad (\text{A.13})$$

$$= \sum_{n=0}^{\infty} \left(\frac{\omega c}{2c_e}\right)^n \frac{r^n e^{in\varphi}}{n!} \sum_{k=0}^{\infty} \left(\frac{\omega c}{2c_e}\right)^k \frac{r^{-k} e^{-ik\varphi}}{k!} \quad (\text{A.14})$$

$$= \sum_{n=0}^{\infty} \sum_{k=0}^{\infty} \left(\frac{\omega c}{2c_e}\right)^{n+k} \frac{r^{n-k} e^{i(n-k)\varphi}}{n!k!}. \quad (\text{A.15})$$

We now assume that the double sum in the equation above can be written as a single sum, such that

$$\sum_{n=0}^{\infty} \sum_{k=0}^{\infty} \left(\frac{\omega c}{2c_e}\right)^{n+k} \frac{r^{n-k} e^{i(n-k)\varphi}}{n!k!} = \sum_{l=-\infty}^{l=\infty} s_l r^l e^{il\varphi}. \quad (\text{A.16})$$

Multiplying both sides of the above equation by $e^{-il|y|}$ and integrating y over a full period gives

$$\sum_{n=0}^{\infty} \sum_{k=0}^{\infty} \left(\frac{\omega c}{2c_e}\right)^{n+k} \frac{r^{n-k}}{n!k!} 2\pi \delta_{|g|,n-k} = \sum_{l=-\infty}^{l=\infty} s_l r^l \delta_{|g|,l} 2\pi \quad (\text{A.17})$$

$$\sum_{k=0}^{\infty} \left(\frac{\omega c}{2c_e}\right)^{2k+|g|} \frac{r^{|g|}}{k!(k+|g|)!} 2\pi = s_{|g|} r^{|g|} 2\pi \quad (\text{A.18})$$

$$\sum_{k=0}^{\infty} \left(\frac{\omega c}{2c_e}\right)^{2k+|g|} \frac{1}{k!(k+g)!} = s_{|g|}. \quad (\text{A.19})$$

This determines the coefficients s_l with $l > 0$. Now let us evaluate the coefficients for $l < 0$, we multiply by $e^{il|y|}$ and integrate y over a full period to get,

$$\sum_{n=0}^{\infty} \sum_{k=0}^{\infty} \left(\frac{\omega c}{2c_e} \right)^{n+k} \frac{r^{n-k}}{n!k!} 2\pi \delta_{|g|, k-n} = \sum_{l=-\infty}^{l=\infty} s_l r^l \delta_{|g|, -l} 2\pi. \quad (\text{A.20})$$

Note that if we now substitute for $n = k - |g|$, we need to remember that the range of n is restricted, since $n > 0$. This means that the sum over k can only run over the terms where $k - |g| \geq 0$. Thus we get

$$\sum_{k \geq |g|}^{\infty} \left(\frac{\omega c}{2c_e} \right)^{2k-|g|} \frac{r^{-|g|}}{k!(k-|g|)!} 2\pi = s_{-|g|} r^{-|g|} 2\pi. \quad (\text{A.21})$$

A simple change of variable from $k \rightarrow k' + |g|$ brings this into the form

$$\sum_{k'=0}^{\infty} \left(\frac{\omega c}{2c_e} \right)^{2k'+|g|} \frac{r^{-|g|}}{k!(k+|g|)!} 2\pi = s_{-|g|} r^{-|g|} 2\pi \quad (\text{A.22})$$

$$\sum_{k'=0}^{\infty} \left(\frac{\omega c}{2c_e} \right)^{2k'+|g|} \frac{1}{k!(k+|g|)!} = s_{-|g|}, \quad (\text{A.23})$$

which is identical to the coefficient $s_{|g|}$. We can thus conclude that

$$a_n^s = \frac{\lambda \exp \left[-\frac{\omega}{c_e} u_0 \right]}{4\pi \epsilon_0 \omega} s_n \quad (\text{A.24})$$

$$= \frac{\lambda \exp \left[-\frac{\omega}{c_e} u_0 \right]}{4\pi \epsilon_0 \omega} \sum_{k=0}^{\infty} \left(\frac{\omega c}{2c_e} \right)^{2k+|n|} \frac{1}{k!(k+|n|)!}, \quad (\text{A.25})$$

which is the equation given in Eq.5.102.

Appendix B

Supporting analytical calculations for the grating

B.1 The conformal transformation as a Fourier series

Here we expand the conformal transformation generating a grating from a thin slab given in Eq.4.3 as a Fourier series. We start from

$$w = \gamma \log\left(\frac{1}{e^\zeta - iw_0} + iy_0\right), \quad (\text{B.1})$$

which we can rewrite as

$$w = \gamma \log\left(\frac{1}{e^\zeta - e^{w_1}} + e^{y_1}\right), \quad (\text{B.2})$$

with $e^{w_1} = iw_0$ and $e^{y_1} = iy_0$. We now try to rewrite this expression in a more amenable form.

$$\begin{aligned} \log\left(\frac{1}{e^\zeta - e^{w_1}} + e^{y_1}\right) &= \log\left(\frac{1}{e^\zeta(1 - e^{w_1-\zeta})} + e^{y_1}\right) \\ &= \log\left(\frac{1}{e^\zeta(1 - e^{w_1-\zeta})}(1 + e^{y_1}e^\zeta(1 - e^{w_1-\zeta}))\right) \\ &= -\log\left(e^\zeta(1 - e^{w_1-\zeta})\right) + \log\left(1 + e^{y_1}e^\zeta(1 - e^{w_1-\zeta})\right) \\ &= -\zeta - \log(1 - e^{w_1-\zeta}) + \log\left(1 + e^{y_1}e^\zeta(1 - e^{w_1-\zeta})\right). \end{aligned} \quad (\text{B.3})$$

The second term in this equation can be expanded as a power series such that

$$\log(1 - e^{w_1 - \zeta}) = \sum_{g=1}^{\infty} \frac{-1}{g} e^{g(w_1 - \zeta)}. \quad (\text{B.4})$$

This series converges if

$$|e^{(w_1 - \zeta)}| < 1 \quad (\text{B.5})$$

$$|w_0| < e^x \quad (\text{B.6})$$

$$\log(|w_0|) < x, \quad (\text{B.7})$$

i.e. as long as x is right of the left Branch point this is a convergent series. The third term of the coordinate transformation

$$\log(1 + e^{y_1} e^{\zeta} - e^{w_1 + y_1}) \quad (\text{B.8})$$

can be expanded around $\zeta_0 = -e^{w_1 + y_1}$, since

$$\log(1 + x) = \log(1 + x_0) + \sum_{g=1}^{\infty} \frac{(-1)^{g+1}}{g} \frac{1}{(1 + x_0)^n} (x - x_0)^n. \quad (\text{B.9})$$

In our case this gives

$$\begin{aligned} \log(1 + e^{y_1} e^{\zeta} - e^{w_1 + y_1}) &= \log(1 - e^{w_1 + y_1}) + \sum_{g=1}^{\infty} \frac{(-1)^{g+1}}{g} \frac{1}{(1 - e^{w_1 + y_1})^g} \\ &\quad \times (e^{y_1} e^{\zeta} - e^{w_1 + y_1} + e^{w_1 + y_1})^g \\ &= \log(1 - e^{w_1 + y_1}) + \sum_{g=1}^{\infty} \frac{(-1)^{g+1}}{g} \frac{1}{(1 - e^{w_1 + y_1})^g} e^{g(\zeta + y_1)}. \end{aligned} \quad (\text{B.10})$$

According to the ratio test [39] this series converges if

$$\lim_{g \rightarrow \infty} \left| \frac{e^{(g+1)(\zeta + y_1)} (1 - e^{w_1 + y_1})^g g + 1}{(1 - e^{w_1 + y_1})^{g+1} e^{g(\zeta + y_1)} g} \right| < 1 \quad (\text{B.11})$$

$$\left| \frac{e^{(\zeta + y_1)}}{(1 - e^{w_1 + y_1})} \right| < 1 \quad (\text{B.12})$$

$$y_0 e^x < |1 + w_0 y_0| \quad (\text{B.13})$$

$$e^x < |w_0 + 1/y_0| \quad (\text{B.14})$$

$$x < \log(|w_0 + 1/y_0|), \quad (\text{B.15})$$

which means x has to be to the left of the right branch point. That means in the region $\log(|w_0|) < x < \log(|w_0 + 1/y_0|)$ we can write the coordinate transformation as follows

$$\begin{aligned} w/\gamma &= \log(1 - e^{w_1+y_1}) - \zeta + \sum_{g=1}^{\infty} \frac{1}{g} e^{g(w_1-\zeta)} + \sum_{g=1}^{\infty} \frac{(-1)^{g+1}}{g} \frac{1}{(1 - e^{w_1+y_1})^g} e^{g(\zeta+y_1)} \\ &= \log(1 + y_0 w_0) - \zeta + \sum_{g=1}^{\infty} \frac{i^g}{g} \left[\frac{(-1)^{g+1}}{(w_0 + 1/y_0)^g} e^{g\zeta} + w_0^g e^{-g\zeta} \right]. \end{aligned} \quad (\text{B.16})$$

Let us rewrite this in terms of the real and imaginary part. The third term (hereafter called Γ) can be rewritten as

$$\begin{aligned} \Gamma &= \sum_{g=1}^{\infty} \frac{i^g}{g} \left[\frac{(-1)^{g+1}}{(w_0 + 1/y_0)^g} e^{g\zeta} + w_0^g e^{-g\zeta} \right] \\ &= \sum_{g=1}^{\infty} \frac{i^{2g}}{2g} \left[\frac{(-1)^{2g}(-1)}{(w_0 + 1/y_0)^{2g}} e^{2g\zeta} + w_0^{2g} e^{-2g\zeta} \right] \\ &\quad + \sum_{g=1}^{\infty} \frac{i^{2g-1}}{2g-1} \left[\frac{(-1)^{2g-1+1}}{(w_0 + 1/y_0)^{2g-1}} e^{(2g-1)\zeta} + w_0^{2g-1} e^{-(2g-1)\zeta} \right]. \end{aligned} \quad (\text{B.17})$$

B.1.1 Real part of Γ

That means the real part of Γ is given by

$$\text{Re}(\Gamma) = \sum_{g=1}^{\infty} \frac{\cos(2gy) i^{2g}}{2g} \left[\frac{(-1)^{2g}(-1) e^{2gx}}{(w_0 + 1/y_0)^{2g}} + w_0^{2g} e^{-2gx} \right] \quad (\text{B.18})$$

$$+ \sum_{g=1}^{\infty} \frac{i^{2g-1} i \sin((2g-1)y)}{2g-1} \left[\frac{(-1)^{2g-1+1} e^{(2g-1)x}}{(w_0 + 1/y_0)^{2g-1}} - w_0^{2g-1} e^{-(2g-1)x} \right] \quad (\text{B.19})$$

Eventually, we would like to rewrite our plane wave in terms of functions $e^{|g|x+igy}$, which can be done by noting that

$$\begin{aligned} &\sum_{g=1}^{\infty} i^{2g} \frac{\cos(2gy)}{2g} \left[\frac{(-1)^{2g}(-1) e^{2gx}}{(w_0 + 1/y_0)^{2g}} + w_0^{2g} e^{-2gx} \right] = \\ &\sum_{g=1}^{\infty} \frac{i^{2g}}{2g} \frac{e^{i2gy} + e^{-i2gy}}{2} \left[\frac{(-1)^{2g}(-1) e^{2gx}}{(w_0 + 1/y_0)^{2g}} + w_0^{2g} e^{-2gx} \right] = \\ &\sum_{\substack{g=-\infty \\ g \neq 0}}^{\infty} \frac{i^{2|g|}}{2} \frac{e^{i2gy}}{2|g|} \left[\frac{(-1)^{2|g|}(-1) e^{2|g|x}}{(w_0 + 1/y_0)^{2|g|}} + w_0^{2|g|} e^{-2|g|x} \right]. \end{aligned}$$

Likewise we can rewrite the sin part as

$$\begin{aligned}
& \sum_{g=1}^{\infty} \frac{i^{2g-1} i \sin((2g-1)y)}{2g-1} \left[\frac{(-1)^{2g-1+1} e^{(2g-1)x}}{(w_0 + 1/y_0)^{2g-1}} - w_0^{2g-1} e^{-(2g-1)x} \right] = \\
& \sum_{g=1}^{\infty} \frac{i^{|2g-1|}}{|2g-1|} \frac{\text{sign}(2g-1) e^{i(2g-1)y}}{2} \left[\frac{(-1)^{2g-1+1} e^{(2g-1)|x}}{(w_0 + 1/y_0)^{|2g-1|}} - w_0^{|2g-1|} e^{-|(2g-1)|x} \right] + \\
& \sum_{g=-\infty}^0 \frac{i^{|2g-1|}}{|2g-1|} \frac{\text{sign}(2g-1) e^{i(2g-1)y}}{2} \left[\frac{(-1)^{2g-1+1} e^{(2g-1)|x}}{(w_0 + 1/y_0)^{|2g-1|}} - w_0^{|2g-1|} e^{-|(2g-1)|x} \right] = \\
& \sum_{g=-\infty}^{\infty} \frac{i^{|2g-1|}}{|2g-1|} \frac{\text{sign}(2g-1) e^{i(2g-1)y}}{2} \left[\frac{(-1)^{2g-1+1} e^{(2g-1)|x}}{(w_0 + 1/y_0)^{|2g-1|}} - w_0^{|2g-1|} e^{-|(2g-1)|x} \right] \quad (\text{B.20})
\end{aligned}$$

Now we can combine these two terms, but we do it stepwise. First we combine the terms in the sum running from $g = 1$ to infinity

$$\begin{aligned}
& \sum_{g=1}^{\infty} \frac{i^{2|g|}}{2} \frac{e^{i2gy}}{2|g|} \left[\frac{(-1)^{2|g|} (-1) e^{2|g|x}}{(w_0 + 1/y_0)^{2|g|}} + w_0^{2|g|} e^{-2|g|x} \right] + \\
& \sum_{g=1}^{\infty} \frac{i^{|2g-1|}}{|2g-1|} \frac{e^{i(2g-1)y}}{2} \left[\frac{(-1)^{2g-1+1} e^{(2g-1)|x}}{(w_0 + 1/y_0)^{|2g-1|}} - w_0^{|2g-1|} e^{-|(2g-1)|x} \right] = \\
& \sum_{g=1}^{\infty} \frac{i^{|g|}}{2} \frac{e^{igy}}{|g|} \left[\frac{(-1)^{|g|+1} e^{|g|x}}{(w_0 + 1/y_0)^{|g|}} + (-1)^{|g|} w_0^{|g|} e^{-|g|x} \right] = \\
& \sum_{g=1}^{\infty} \frac{(-i)^{|g|}}{2} \frac{e^{igy}}{|g|} \left[\frac{-e^{|g|x}}{(w_0 + 1/y_0)^{|g|}} + w_0^{|g|} e^{-|g|x} \right] = \quad (\text{B.21})
\end{aligned}$$

The terms for negative g can be written as

$$\begin{aligned}
& \sum_{g=-\infty}^{-1} \frac{i^{2|g|}}{2} \frac{e^{i2gy}}{2|g|} \left[\frac{(-1)^{2|g|} (-1) e^{2|g|x}}{(w_0 + 1/y_0)^{2|g|}} + w_0^{2|g|} e^{-2|g|x} \right] + \\
& \sum_{g=-\infty}^0 \frac{i^{|2g-1|}}{|2g-1|} \frac{e^{i(2g-1)y}}{2} \left[\frac{(-1)^{2g-1} e^{(2g-1)|x}}{(w_0 + 1/y_0)^{|2g-1|}} + w_0^{|2g-1|} e^{-|(2g-1)|x} \right] = \\
& \sum_{g=-\infty}^{-1} \frac{i^{|g|}}{|g|} \frac{e^{igy}}{2} \left[\frac{-e^{|g|x}}{(w_0 + 1/y_0)^{|g|}} + w_0^{|g|} e^{-|g|x} \right]. \quad (\text{B.22})
\end{aligned}$$

So finally we can write the real part of Γ as

$$\operatorname{Re}(\Gamma) = \sum_{\substack{g=-\infty \\ g \neq 0}}^{\infty} \left(d_g^+ e^{|g|x} + d_g^- e^{-|g|x} \right) e^{igy}, \quad (\text{B.23})$$

where we defined

$$\begin{aligned} d_g^+ &= \frac{(-i)^{|g|}}{2|g|} \frac{-1}{(w_0 + 1/y_0)^{|g|}} \quad \text{for } g > 0 \\ &= \frac{e^{-i\frac{\pi}{2}g}}{2|g|} \frac{-1}{(w_0 + 1/y_0)^{|g|}} \quad \forall g \end{aligned} \quad (\text{B.24})$$

$$\begin{aligned} d_g^- &= \frac{(-i)^{|g|}}{2|g|} w_0^{|g|} \quad \text{for } g > 0 \\ &= \frac{e^{-i\frac{\pi}{2}g}}{2|g|} w_0^{|g|} \quad \forall g \end{aligned} \quad (\text{B.25})$$

as given in Eq.4.7 the supplementary material of [102]. Note that the reality conditions $(d_g^+)^* = d_{-g}^+$, $(d_g^-)^* = d_{-g}^-$ hold.

B.1.2 Imaginary part of Γ

Similarly to the calculation above, we can also rewrite the imaginary part of Γ (as defined in Eq.B.17) as a Fourier series. The imaginary part of gamma is given by

$$\begin{aligned} i\operatorname{Im}(\Gamma) &= \sum_{g=1}^{\infty} \frac{i^{2g}}{2g} i \sin(2gy) \left[\frac{(-1)^{2g}(-1)}{(w_0 + 1/y_0)^{2g}} e^{2gx} - w_0^{2g} e^{-2gx} \right] \\ &+ \sum_{g=1}^{\infty} \frac{i^{2g-1}}{2g-1} \cos((2g-1)y) \left[\frac{(-1)^{2g-1+1}}{(w_0 + 1/y_0)^{2g-1}} e^{(2g-1)x} + w_0^{2g-1} e^{-(2g-1)x} \right] \end{aligned} \quad (\text{B.26})$$

$$\begin{aligned} \operatorname{Im}(\Gamma) &= \sum_{g=1}^{\infty} \frac{i^{2g}}{2g} \sin(2gy) \left[\frac{(-1)^{2g}(-1)}{(w_0 + 1/y_0)^{2g}} e^{2gx} - w_0^{2g} e^{-2gx} \right] \\ &+ \sum_{g=1}^{\infty} \frac{i^{2g-1}}{2g-1} i \cos((2g-1)y) \left[\frac{(-1)^{2g-1}}{(w_0 + 1/y_0)^{2g-1}} e^{(2g-1)x} - w_0^{2g-1} e^{-(2g-1)x} \right]. \end{aligned} \quad (\text{B.27})$$

As for the real part we write,

$$\begin{aligned}
& \sum_{g=1}^{\infty} \frac{i^{2g-1}}{2g-1} i \cos((2g-1)y) \left[\frac{(-1)^{2g-1}}{(w_0 + 1/y_0)^{2g-1}} e^{(2g-1)x} - w_0^{2g-1} e^{-(2g-1)x} \right] = \\
& \sum_{g=1}^{\infty} \frac{i^{2g-1}}{2g-1} i \frac{e^{i(2g-1)y} + e^{-i(2g-1)y}}{2} \left[\frac{(-1)^{2g-1}}{(w_0 + 1/y_0)^{2g-1}} e^{(2g-1)x} - w_0^{2g-1} e^{-(2g-1)x} \right] = \\
& \sum_{g=-\infty}^{\infty} \frac{i^{|2g-1|}}{|2g-1|} i \frac{e^{i(2g-1)y}}{2} \left[\frac{(-1)^{|2g-1|}}{(w_0 + 1/y_0)^{|2g-1|}} e^{|(2g-1)x} - w_0^{|2g-1|} e^{-|(2g-1)x} \right] = \quad (B.28)
\end{aligned}$$

and

$$\begin{aligned}
& \sum_{g=1}^{\infty} \frac{i^{2g}}{2g} \sin(2gy) \left[\frac{(-1)^{2g}(-1)}{(w_0 + 1/y_0)^{2g}} e^{2gx} - w_0^{2g} e^{-2gx} \right] = \\
& \sum_{g=1}^{\infty} \frac{i^{2g}}{2g} (-i) \text{sign}(2g) \frac{e^{i2gy}}{2} \left[\frac{(-1)^{2g}(-1)}{(w_0 + 1/y_0)^{2g}} e^{2gx} - w_0^{2g} e^{-2gx} \right] + \\
& \sum_{g=-\infty}^{-1} \frac{i^{2g}}{2g} (-i) \text{sign}(2g) \frac{e^{i2gy}}{2} \left[\frac{(-1)^{2g}(-1)}{(w_0 + 1/y_0)^{2g}} e^{2gx} - w_0^{2g} e^{-2gx} \right] = \\
& \sum_{\substack{g=-\infty \\ g \neq 0}}^{\infty} \frac{i^{2g}}{2g} (-i) \text{sign}(2g) \frac{e^{i2gy}}{2} \left[\frac{(-1)^{2g}(-1)}{(w_0 + 1/y_0)^{2g}} e^{2gx} - w_0^{2g} e^{-2gx} \right]. \quad (B.29)
\end{aligned}$$

Let us combine the terms running over positive values of g again,

$$\begin{aligned}
& \sum_{g=1}^{\infty} \frac{i^{2g}}{2g} (-i) \frac{e^{i2gy}}{2} \left[\frac{-1}{(w_0 + 1/y_0)^{2g}} e^{2gx} - w_0^{2g} e^{-2gx} \right] + \\
& \sum_{g=1}^{\infty} \frac{i^{2g-1}}{2g-1} i \frac{e^{i(2g-1)y}}{2} \left[\frac{-1}{(w_0 + 1/y_0)^{2g-1}} e^{(2g-1)x} - w_0^{2g-1} e^{-(2g-1)x} \right] \\
& \sum_{g=1}^{\infty} \frac{(-i)^{|g|+1}}{|g|} \frac{e^{igy}}{2} \left[\frac{-1}{(w_0 + 1/y_0)^{|g|}} e^{|g|x} - w_0^{|g|} e^{-|g|x} \right]. \quad (B.30)
\end{aligned}$$

Combining the terms running over negative g gives

$$\begin{aligned}
& \sum_{g=-\infty}^0 \frac{i^{|2g-1|}}{|2g-1|} i \frac{e^{i(2g-1)y}}{2} \left[\frac{-1}{(w_0 + 1/y_0)^{|2g-1|}} e^{|(2g-1)x} - w_0^{|2g-1|} e^{-|(2g-1)x} \right] + \\
& \sum_{g=-\infty}^{-1} \frac{i^{2|g|}}{2|g|} i \frac{e^{i2gy}}{2} \left[\frac{-1}{(w_0 + 1/y_0)^{2|g|}} e^{2|g|x} - w_0^{2|g|} e^{-2|g|x} \right] = \\
& \sum_{g=-\infty}^{-1} \frac{i^{|g|+1}}{|g|} \frac{e^{igy}}{2} \left[\frac{-1}{(w_0 + 1/y_0)^{|g|}} e^{|g|x} - w_0^{|g|} e^{-|g|x} \right]. \quad (B.31)
\end{aligned}$$

Finally we can write this as a single Fourier series

$$\text{Im}(\Gamma) = \sum_{\substack{g=-\infty \\ g \neq 0}}^{\infty} \left(h_g^+ e^{|g|x} + h_g^- e^{-|g|x} \right) e^{igy}, \quad (\text{B.32})$$

with

$$\begin{aligned} h_g^+ &= \frac{(-i)^{|g|}}{2|g|} \frac{i}{(w_0 + 1/y_0)^{|g|}} \quad \text{for } g > 0 \\ &= \frac{e^{-i\frac{\pi}{2}g}}{2|g|} \frac{\text{sign}(g)i}{(w_0 + 1/y_0)^{|g|}} \quad \forall g \end{aligned} \quad (\text{B.33})$$

$$\begin{aligned} h_g^- &= \frac{i(-i)^{|g|}}{2|g|} w_0^{|g|} \quad \text{for } g > 0 \\ &= \frac{i \text{sign}(g) e^{-i\frac{\pi}{2}g}}{2|g|} w_0^{|g|} \quad \forall g \end{aligned} \quad (\text{B.34})$$

as given in Eq.4.7 the supplementary material of [102]. Note that the reality conditions $(h_g^+)^* = h_{-g}^+$, $(h_g^-)^* = h_{-g}^-$ hold.

B.1.3 Coordinate transformation as a Fourier series

With the results obtained in the two previous sections we are now in a position to write down explicit expressions for the real and imaginary part of our coordinate transformation. That is in the region $\log(|w_0|) < x < \log(|w_0 + 1/y_0|)$ the transformation

$$\begin{aligned} w &= \gamma \log \left(\frac{1}{e^z - e^{w_1}} + e^{y_1} \right) \\ &= \gamma [\log(1 + y_0 w_0) - z + \text{Re}(\Gamma) + i \text{Im}(\Gamma)]. \end{aligned} \quad (\text{B.35})$$

In terms of the real and imaginary part we have

$$\begin{aligned}
u &= \gamma [\log(1 + y_0 w_0) - x + \operatorname{Re}(\Gamma)] \\
&= \gamma \left[\log(1 + y_0 w_0) - x + \sum_{\substack{g=-\infty \\ g \neq 0}}^{\infty} (d_g^+ e^{|g|x} + d_g^- e^{-|g|x}) e^{igy} \right] \quad (\text{B.36})
\end{aligned}$$

$$\begin{aligned}
v &= \gamma [-y + \operatorname{Im}(\Gamma)] \\
&= \gamma \left[-y + \sum_{\substack{g=-\infty \\ g \neq 0}}^{\infty} (h_g^+ e^{|g|x} + h_g^- e^{-|g|x}) e^{igy} \right] \quad (\text{B.37})
\end{aligned}$$

as given in Eq.4.5 and the supplementary material of [66].

Appendix C

Modelling the radiative reaction

In this appendix, we derive an expression for permittivity of the fictive absorber that is used to model the radiative reaction of a nanoparticle in the TO framework. This section follows the presentation in [53] in spirit, but differs in the technical details. In particular, section C.1 is published verbatim in the supplementary material of [66] and is reprinted here with permission. Copyright 2016 American Chemical Society.

C.1 Permittivity of the fictive absorber

The problem that has to be addressed is the following. It is known that any nanoparticle that has an electric field incident on it will scatter parts of that field. The question is, how can the energy scattered to infinity by the particle be calculated within an electrostatic framework? To answer this question we first look at what happens electrostatically.

For 2-d nanoparticles smaller than the wavelength the fields scattered by them to infinity will be given by cylindrical waves to a very good approximation. A cylindrical wave with an electric field in the $x - y$ -plane has a magnetic component in the z -direction. That component only needs to fulfil the scalar wave equation in cylindrical coordinates and, for outgoing waves, can be written as [110]:

$$H_z = H_0 \mathcal{H}_m(k_0 r) e^{im\phi} e^{-i\omega t}, \quad (\text{C.1})$$

where \mathcal{H}_m is the Hankel function of the first kind [152]. In the following we will not write the time dependence explicitly. The electric field can be obtained from [20]

$$\nabla \times \mathbf{H} = -i\omega\epsilon_0\mathbf{E}, \quad (\text{C.2})$$

$$-i\omega\epsilon_0\mathbf{E} = \frac{1}{r}\partial_\phi H_z \hat{r} - \partial_r H_z \hat{\phi}. \quad (\text{C.3})$$

Before we evaluate the derivatives we will make the near field approximation $k_0r \ll 1$. In this case (for $m \geq 0$)

$$\mathcal{H}_m(k_0r) = \begin{cases} 1 + i\frac{2}{\pi}(\log(k_0r/2) + \gamma) & \text{for } m = 0 \\ \frac{1}{m!}\left(\frac{k_0r}{2}\right)^m - i\frac{(m-1)!}{\pi}\left(\frac{2}{k_0r}\right)^m & \text{for } m > 0. \end{cases} \quad (\text{C.4})$$

The derivatives of this asymptotic form are straight forward to evaluate

$$\partial_r \mathcal{H}_m(k_0r) = \begin{cases} i\frac{2}{\pi}\frac{2}{k_0r} & \text{for } m = 0 \\ \frac{1}{(m-1)!}\left(\frac{k_0}{2}\right)^m r^{m-1} + i\frac{m!}{\pi}\left(\frac{2}{k_0}\right)^m r^{-m-1} & \text{for } m > 0. \end{cases} \quad (\text{C.5})$$

So we obtain for the angular component of the electric field

$$E_\phi = \frac{H_0}{i\omega\epsilon_0} e^{im\phi} \times \left[\begin{cases} \frac{2}{\pi}\frac{2}{k_0r} & \text{for } m = 0 \\ \frac{1}{(m-1)!}\left(\frac{k_0}{2}\right)^m r^{m-1} + i\frac{m!}{\pi}\left(\frac{2}{k_0}\right)^m r^{-m-1} & \text{for } m > 0. \end{cases} \right] \quad (\text{C.6})$$

and for the radial component

$$E_r = -\frac{H_0}{\omega\epsilon_0} e^{im\phi} \left[\frac{1}{(m-1)!}\left(\frac{k_0}{2}\right)^m r^{m-1} - i\frac{m!}{\pi}\left(\frac{2}{k_0}\right)^m r^{-m-1} \right] \quad \text{for } m > 0, \quad (\text{C.7})$$

since the ϕ -derivative of the $m = 0$ component is zero.

To model these fields in an electrostatic framework we are going to assume that the above fields are created by a radiating nanoparticle, which acts as a source and the reflection of the source fields from an absorber. Our task is to find the permittivity of the absorber which gives rise to a reflection matching the above solutions. That is we assume our total field is given by

$$E^{tot} = E^{sou} + E^{sca}, \quad (\text{C.8})$$

where E^{sou} is the field generated by the nanoparticle and E^{sca} corresponds to the field reflected from by the absorber. But before we can do that we have to solve the electrostatic problem first. So we assume that there is a source at the origin leading to fields of the form r^{-m} . These fields are then reflected by the absorber, which we place at $r = a$,

such that $ak_0 \ll 1$. The reflected fields have the form r^m . Inside the fictive absorber we can only have fields decaying with increasing radius. Therefore we can write the electrostatic potential in the two regions

$$\Phi_I^m = (r^{-m} + Rr^m)e^{im\phi} + \Phi_0 \quad \text{for } m > 0, r < a \quad (\text{C.9})$$

$$\Phi_{II}^m = Tr^{-m}e^{im\phi} \quad \text{for } m > 0, r > a \quad (\text{C.10})$$

$$\Phi_I^0 = A + D \log(r) \quad \text{for } m = 0, r < a \quad (\text{C.11})$$

$$\Phi_{II}^0 = T_0 \log(r) \quad \text{for } m = 0, r > a \quad (\text{C.12})$$

This leads to the fields

$$E_I^\phi = -im(r^{-m-1} + Rr^{m-1})e^{im\phi} \quad \text{for } m > 0, r < a \quad (\text{C.13})$$

$$E_I^r = m(r^{-m-1} - Rr^{m-1})e^{im\phi} \quad \text{for } m > 0, r < a$$

$$E_{II}^\phi = -imTr^{-m-1}e^{im\phi} \quad \text{for } m > 0, r > a$$

$$E_I^r = Tmr^{-m-1}e^{im\phi} \quad \text{for } m > 0, r > a$$

$$E_I^{0,r} = Dr^{-1} \quad \text{for } m = 0, r < a$$

$$E_I^{0,r} = T_0r^{-1} \quad \text{for } m = 0, r > a.$$

At the boundary between the two media ($r = a$) the tangential component of the electric and the normal component of the displacement field have to be continuous [20]. This gives

$$(a^{-m-1} + Ra^{m-1}) = Ta^{-m-1} \quad (\text{C.14})$$

$$(a^{-m-1} - Ra^{m-1}) = \epsilon_{abs}Ta^{-m-1} \quad (\text{C.15})$$

or

$$1 + Ra^{2m} = \frac{1}{\epsilon_{abs}}(1 - Ra^{2m}) \quad (\text{C.16})$$

$$\epsilon_{abs} = \frac{(1 - Ra^{2m})}{(Ra^{2m} + 1)} \quad (\text{C.17})$$

$$R = a^{-2m} \frac{1 - \epsilon_{abs}}{1 + \epsilon_{abs}}. \quad (\text{C.18})$$

For the zero order mode we only have one equation and thus cannot determine D unambiguously, here we have

$$D = T_0 \epsilon_{abs}. \quad (\text{C.19})$$

The task is now to match the electrostatic solution to the electrodynamic one. This will yield a condition on the permittivity of the absorber ϵ_{abs} . We can see that we cannot match the $m = 0$ mode to the electrodynamic solution because there $E_\phi^{dynamic} \neq 0$, whereas $E_\phi^{static} = 0$. The other modes can be matched, however. The resulting reflection coefficient will depend on m . So the permittivity of the absorber would also have to depend on m . To match the coefficients in front of r^{-m-1} between the electrostatic and electrodynamic case we set H_0 to be

$$H_0^m = -i\omega\epsilon_0 m \frac{\pi}{m!} \left(\frac{2}{k_0}\right)^{-m}. \quad (\text{C.20})$$

Then equating the electrodynamic (Eq.C.6) and electrostatic E_ϕ (Eq.C.13) gives the value for R (we could equally well match E_r)

$$-ime^{im\phi} \left[\frac{-i\pi}{m!(m-1)!} \left(\frac{k_0}{2}\right)^{2m} r^{m-1} + r^{-m-1} \right] = -im(r^{-m-1} + Rr^{m-1})e^{im\phi} \quad (\text{C.21})$$

$$R = \frac{-i\pi}{m!(m-1)!} \left(\frac{k_0}{2}\right)^{2m}. \quad (\text{C.22})$$

This can now be used to determine the permittivity of the fictive absorber from Eq.C.18

$$\epsilon_{abs}^m = \frac{1 - \frac{-i\pi}{m!(m-1)!} \left(\frac{k_0}{2}a\right)^{2m}}{1 + \frac{-i\pi}{m!(m-1)!} \left(\frac{k_0}{2}a\right)^{2m}}. \quad (\text{C.23})$$

For the first order mode $m = 1$, this becomes

$$\epsilon_{abs}^1 = \frac{1 + i\pi\left(\frac{k_0}{2}a\right)^2}{1 - i\pi\left(\frac{k_0}{2}a\right)^2} \quad (\text{C.24})$$

$$\approx 1 + 2i\pi\left(\frac{k_0}{2}a\right)^2 - 2\pi^2\left(\frac{k_0}{2}a\right)^4 + O\left(\left(\frac{k_0}{2}a\right)^6\right). \quad (\text{C.25})$$

This means we can model scattered light propagating to infinity by placing a fictive absorber around the scatterer that has a permittivity given by Eq.C.25. There are however constraints on where to place that fictive absorber. On the one hand it has to be in the near field such that $k_0a \ll 1$ holds. On the other hand it has to be far enough

from the surface of the particle such that only the first order mode is present in the fields that reach the absorber. The energy absorbed by the fictive absorber is then identical to the energy scattered to infinity by the nanoparticle. This approach also allows to take radiation damping into account. This can be done by solving the multiple scattering problem between the nanoparticle and the fictive absorber, as has been shown above [66].

C.2 Polarisability of the fictive absorber

Here, we deduce the polarisability of the fictive absorber used in our calculation of the EELS spectra of a non-concentric annulus. As above, assume the non-concentric annulus is surrounded by a fictive absorber with circular boundary at $r' = a$. The transformation to the concentric annulus,

$$\zeta' = \frac{g^2}{\zeta - x_0}, \quad (\text{C.26})$$

transforms this fictive absorber into a small cylindrical particle of radius $r = \frac{g^2}{a}$, at position $(x = x'_0, y = 0)$. Here the primed coordinates refer to the non-concentric annulus frame. Such a particle, placed in a constant electric field \mathbf{E}_0 and surrounded by vacuum, will acquire a dipole moment given by

$$\mathbf{p}_{abs} = 2\pi\epsilon_0 \frac{g^4}{a^2} \left(\frac{\epsilon_{abs} - 1}{\epsilon_{abs} + 1} \right) \mathbf{E}_0 \quad (\text{C.27})$$

$$= \gamma_{abs} \mathbf{E}_0. \quad (\text{C.28})$$

Using the expression for the permittivity of the fictive in Eq.C.25 to second order in k_0a , allows us to write

$$\left(\frac{\epsilon_{abs} - 1}{\epsilon_{abs} + 1} \right) \approx \left(\frac{i\pi(\frac{k_0}{2}a)^2 - \pi^2(\frac{k_0}{2}a)^4}{i\pi(\frac{k_0}{2}a)^2 - \pi^2(\frac{k_0}{2}a)^4 + 1} \right) \quad (\text{C.29})$$

$$\approx \left(i\pi(\frac{k_0}{2}a)^2 - \pi^2(\frac{k_0}{2}a)^4 \right) \times \left(1 - i\pi(\frac{k_0}{2}a)^2 + \pi^2(\frac{k_0}{2}a)^4 \right) \quad (\text{C.30})$$

$$= i\pi(\frac{k_0}{2}a)^2 + O((\frac{k_0}{2}a)^6). \quad (\text{C.31})$$

Substituting this back into the equation for the dipole moment of the fictive absorber gives

$$\mathbf{p}_{abs} = i \frac{\pi^2}{2} \epsilon_0 g^4 k_0^2 \mathbf{E}_0, \quad (\text{C.32})$$

which indicates that the polarisability of the fictive absorber is given by

$$\gamma_{abs} = i \frac{\pi^2}{2} \epsilon_0 g^4 k_0^2, \quad (\text{C.33})$$

as given in Chapter 5 and [53].

Appendix D

Supplementary material: time-domain simulation files

Video files showing the time-domain solution of the EELS calculations discussed in chapter 5 are provided as supplementary material. They can be found on the supplied USB-drive or are available from the author. The following files are included:

- **Horizontal_E_field_electron_passes_horizontally_annulus.mp4**
Shows the time evolution of the horizontal component of the electric field as a line electron moves past a non-concentric annulus horizontally along the top.
- **Vertical_E_field_electron_passes_horizontally_annulus.mp4**
Shows the time evolution of the vertical component of the electric field as a line electron moves past a non-concentric annulus horizontally along the top.
- **Horizontal_E_field_electron_passes_vertically_annulus.mp4**
Shows the time evolution of the horizontal component of the electric field as a line electron moves past a non-concentric annulus vertically to the left of the particle.
- **Vertical_E_field_electron_passes_vertically_annulus.mp4**
Shows the time evolution of the vertical component of the electric field as a line electron moves past a non-concentric annulus vertically to the left of the particle.
- **Horizontal_E_field_ellipse.mp4**
Shows the time evolution of the horizontal component of the electric field as a line electron moves past an ellipse vertically to the right.

- **Vertical_E_field_component_ellipse.mp4**

Shows the time evolution of the vertical component of the electric field as a line electron moves past an ellipse vertically to the right.

Appendix E

Copyright permissions for references
[62] and [102]

7/12/2016

RightsLink Printable License

**AMERICAN PHYSICAL SOCIETY LICENSE
TERMS AND CONDITIONS**

Jul 12, 2016

This Agreement between Matthias Kraft ("You") and American Physical Society ("American Physical Society") consists of your license details and the terms and conditions provided by American Physical Society and Copyright Clearance Center.

License Number	3906501511610
License date	Jul 12, 2016
Licensed Content Publisher	American Physical Society
Licensed Content Publication	Physical Review B
Licensed Content Title	Transformation optics and hidden symmetries
Licensed Content Author	Matthias Kraft et al.
Licensed Content Date	Jun 20, 2014
Licensed Content Volume Number	89
Type of Use	Thesis/Dissertation
Requestor type	Student
Format	Print, Electronic
Portion	chart/graph/table/figure
Number of charts/graphs/tables/figures	4
Portion description	Figure 3, Figure 4, Figure 6, Figure 9
Rights for	Main product
Duration of use	Life of Current Edition
Creation of copies for the disabled	no
With minor editing privileges	no
For distribution to	Worldwide
In the following language(s)	Original language of publication
With incidental promotional use	no
The lifetime unit quantity of new product	100000 or more
The requesting person/organization is:	Matthias Kraft, Imperial College London
Order reference number	
Title of your thesis / dissertation	Transformation optics: a tool to reveal and make use of symmetries in plasmonics
Expected completion date	Aug 2016
Expected size (number of pages)	200
Requestor Location	Matthias Kraft Imperial College London Accounts Payable Lvl 3 Sherfield Building London, SW7 2AZ United Kingdom

7/12/2016

RightsLink Printable License

	Attn: Matthias Kraft
Customer VAT ID	GB649926678
Billing Type	Invoice
Billing Address	Matthias Kraft Imperial College London Accounts Payable Lvl 3 Sherfield Building London, United Kingdom SW7 2AZ Attn: Matthias Kraft
Total	0.00 USD
Terms and Conditions	

Terms and Conditions

The American Physical Society (APS) is pleased to grant the Requestor of this license a non-exclusive, non-transferable permission, limited to [**print** and/or **electronic** format, depending on what they chose], provided all criteria outlined below are followed.

1. You must also obtain permission from at least one of the lead authors for each separate work, if you haven't done so already. The author's name and affiliation can be found on the first page of the published Article.
2. For electronic format permissions, Requestor agrees to provide a hyperlink from the reprinted APS material using the source material's DOI on the web page where the work appears. The hyperlink should use the standard DOI resolution URL, <http://dx.doi.org/{DOI}>. The hyperlink may be embedded in the copyright credit line.
3. For print format permissions, Requestor agrees to print the required copyright credit line on the first page where the material appears: "Reprinted (abstract/excerpt/figure) with permission from [(FULL REFERENCE CITATION) as follows: Author's Names, APS Journal Title, Volume Number, Page Number and Year of Publication.] Copyright (YEAR) by the American Physical Society."
4. Permission granted in this license is for a one-time use and does not include permission for any future editions, updates, databases, formats or other matters. Permission must be sought for any additional use.
5. Use of the material does not and must not imply any endorsement by APS.
6. Under no circumstance does APS purport or intend to grant permission to reuse materials to which it does not hold copyright. It is the requestors sole responsibility to ensure the licensed material is original to APS and does not contain the copyright of another entity, and that the copyright notice of the figure, photograph, cover or table does not indicate that it was reprinted by APS, with permission from another source.
7. The permission granted herein is personal to the Requestor for the use specified and is not transferable or assignable without express written permission of APS. This license may not be amended except in writing by APS.
8. You may not alter, edit or modify the material in any manner.
9. You may translate the materials only when translation rights have been granted.
10. You may not use the material for promotional, sales, advertising or marketing purposes.
11. The foregoing license shall not take effect unless and until APS or its agent, Copyright Clearance Center (CCC), receives payment in full in accordance with CCC Billing and Payment Terms and Conditions, which are incorporated herein by reference.
12. Should the terms of this license be violated at any time, APS or CCC may revoke the license with no refund to you and seek relief to the fullest extent of the laws of the USA. Official written notice will be made using the contact information provided with the permission request. Failure to receive such notice will not nullify revocation of the permission.
13. APS reserves all rights not specifically granted herein.
14. This document, including the CCC Billing and Payment Terms and Conditions, shall be the entire agreement between the parties relating to the subject matter hereof.

Other Terms and Conditions

Version 1.1

7/12/2016

RightsLink Printable License

Questions? customercare@copyright.com or +1-855-239-3415 (toll free in the US) or +1-978-646-2777.



7/12/2016

Rightslink® by Copyright Clearance Center



RightsLink®

Home

Create Account

Help

ACS Publications
Most Trusted. Most Cited. Most Read.

Title: Transformation Optics: A Time- and Frequency-Domain Analysis of Electron-Energy Loss Spectroscopy

Author: Matthias Kraft, Yu Luo, J. B. Pendry

Publication: Nano Letters

Publisher: American Chemical Society

Date: Jul 1, 2016

Copyright © 2016, American Chemical Society

LOGIN

If you're a **copyright.com user**, you can login to RightsLink using your copyright.com credentials. Already a **RightsLink user** or want to [learn more?](#)

PERMISSION/LICENSE IS GRANTED FOR YOUR ORDER AT NO CHARGE

This type of permission/license, instead of the standard Terms & Conditions, is sent to you because no fee is being charged for your order. Please note the following:

- Permission is granted for your request in both print and electronic formats, and translations.
- If figures and/or tables were requested, they may be adapted or used in part.
- Please print this page for your records and send a copy of it to your publisher/graduate school.
- Appropriate credit for the requested material should be given as follows: "Reprinted (adapted) with permission from (COMPLETE REFERENCE CITATION). Copyright (YEAR) American Chemical Society." Insert appropriate information in place of the capitalized words.
- One-time permission is granted only for the use specified in your request. No additional uses are granted (such as derivative works or other editions). For any other uses, please submit a new request.

BACK

CLOSE WINDOW

Copyright © 2016 [Copyright Clearance Center, Inc.](#) All Rights Reserved. [Privacy statement.](#) [Terms and Conditions.](#)
Comments? We would like to hear from you. E-mail us at customercare@copyright.com

Bibliography

- [1] D. Neuschwander, *Emmy Noether's wonderful theorem* (Johns Hopkins University Press, Baltimore, MD, 2011).
- [2] L. D. Landau and E. M. Lifshitz, *Mechanics*, 3rd ed. (Butterworth-Heinemann [Imprint], San Diego, 1976).
- [3] N. Ashcroft and N. Mermin, *Solid State Physics* (Holt, Rinehart and Winston, New York, 1976).
- [4] S. A. Maier, *Plasmonics: Fundamentals and Applications* (Springer, New York, 2010).
- [5] D. Bohm and D. Pines, "A Collective Description of Electron Interactions: III. Coulomb Interactions in a Degenerate Electron Gas," *Phys. Rev.* **92**, 609–625 (1953).
- [6] A. Sommerfeld, "Über die Fortpflanzung elektrodynamischer Wellen längs eines Drahtes," *Ann. Phys.* **303**, 233–290 (1899).
- [7] J. Zenneck, "Über die Fortpflanzung ebener elektromagnetischer Wellen längs einer ebenen Leiterfläche und ihre Beziehung zur drahtlosen Telegraphie," *Ann. Phys.* **328**, 846–866 (1907).
- [8] I. V. Zabkov, V. V. Klimov, I. V. Treshin, and O. A. Glazov, "Plasmon oscillations in a linear cluster of spherical nanoparticles," *Quant. Electron.* **41**, 742–747 (2011).
- [9] J. Kottmann, O. Martin, D. Smith, and S. Schultz, "Spectral response of plasmon resonant nanoparticles with a non-regular shape," *Opt. Express* **6**, 213–219 (2000).
- [10] A. Dhawan, S. J. Norton, M. D. Gerhold, and T. Vo-Dinh, "Comparison of FDTD numerical computations and analytical multipole expansion method for plasmonics-active nanosphere dimers." *Opt. Express* **17**, 9688–9703 (2009).

-
- [11] E. Prodan, C. Radloff, N. J. Halas, and P. Nordlander, “A Hybridization Model for the Plasmon Response of Complex Nanostructures,” *Science* **302**, 419–422 (2003).
- [12] P. Nordlander and E. Prodan, “Plasmon Hybridization in Nanoparticles near Metallic Surfaces,” *Nano Lett.* **4**, 2209–2213 (2004).
- [13] E. Prodan and P. Nordlander, “Structural Tunability of the Plasmon Resonances in Metallic Nanoshells,” *Nano Lett.* **3**, 543–547 (2003).
- [14] H. Ditlbacher, J. R. Krenn, G. Schider, A. Leitner, and F. R. Aussenegg, “Two-dimensional optics with surface plasmon polaritons,” *Appl. Phys. Lett.* **81**, 1762 (2002).
- [15] S. A. Maier, P. G. Kik, H. A. Atwater, S. Meltzer, E. Harel, B. E. Koel, and A. Requicha, “Local detection of electromagnetic energy transport below the diffraction limit in metal nanoparticle plasmon waveguides.” *Nat. Mater.* **2**, 229–32 (2003).
- [16] A. Aubry, D. Y. Lei, A. I. Fernández-Domínguez, Y. Sonnefraud, S. A. Maier, and J. B. Pendry, “Plasmonic Light-Harvesting Devices over the Whole Visible Spectrum,” *Nano Lett.* **10**, 2574–2579 (2010).
- [17] L. R. Hirsch, R. J. Stafford, J. A. Bankson, S. R. Sershen, B. Rivera, R. E. Price, J. D. Hazle, N. J. Halas, and J. L. West, “Nanoshell-mediated near-infrared thermal therapy of tumors under magnetic resonance guidance.” *P. Natl. Acad. Sci. USA* **100**, 13549–54 (2003).
- [18] C. E. Talley, J. B. Jackson, C. Oubre, N. K. Grady, C. W. Hollars, S. M. Lane, T. R. Huser, P. Nordlander, and N. J. Halas, “Surface-enhanced Raman scattering from individual Au nanoparticles and nanoparticle dimer substrates.” *Nano Lett.* **5**, 1569–74 (2005).
- [19] J. N. Anker, W. P. Hall, O. Lyandres, N. C. Shah, J. Zhao, and R. P. Van Duyne, “Biosensing with plasmonic nanosensors.” *Nat. Mater.* **7**, 442–53 (2008).
- [20] J. D. Jackson, *Classical Electrodynamics*, 3rd ed. (Wiley, New York, 1999).
- [21] N. Kundtz, D. Smith, and J. Pendry, “Electromagnetic Design With Transformation Optics,” *P. IEEE* **99**, 1622–1633 (2011).
- [22] Y. Luo, *Transformation optics applied to plasmonics*, Dissertation for the degree of Doctor of Philosophy (PhD), Imperial College London, London (2012).

- [23] E. Post, *Formal Structure of Electromagnetics*, 1st ed. (Dover Publications, Inc, Amsterdam, (reprint Mineola, NY), 1997).
- [24] A. J. Ward and J. B. Pendry, “Refraction and geometry in Maxwell’s equations,” *J. Mod. Opt.* **43**, 773–793 (1996).
- [25] D. Shyrokı, “Note on transformation to general curvilinear coordinates for Maxwell’s curl equations,” arXiv.org eprint [arXiv:physics/0307029](https://arxiv.org/abs/physics/0307029) [[physics.optics](https://arxiv.org/abs/physics/0307029)] (2003).
- [26] U. Leonhardt, “Optical Conformal Mapping,” *Science* **312**, 1777–1780 (2006).
- [27] A. Aubry and J. B. Pendry, “Transformation Optics for Plasmonics,” in *Active Plasmonics and Tuneable Plasmonic Metamaterials*, edited by A. V. Zayats and S. A. Maier (Wiley, Hoboken, N.J., 2013) Chap. 4, pp. 105–152, 1st ed.
- [28] J. B. Pendry, D. Schurig, and D. R. Smith, “Controlling electromagnetic fields,” *Science* **312**, 1780–2 (2006).
- [29] D. Schurig, J. J. Mock, B. J. Justice, S. A. Cummer, J. B. Pendry, A. F. Starr, and D. R. Smith, “Metamaterial electromagnetic cloak at microwave frequencies,” *Science* **314**, 977–80 (2006).
- [30] T. Ergin, N. Stenger, P. Brenner, J. B. Pendry, and M. Wegener, “Three-dimensional invisibility cloak at optical wavelengths,” *Science* **328**, 337–9 (2010).
- [31] M. W. McCall, A. Favaro, P. Kinsler, and A. Boardman, “A spacetime cloak, or a history editor,” *J. Opt.* **13**, 029501–029501 (2011).
- [32] M. Fridman, A. Farsi, Y. Okawachi, and A. L. Gaeta, “Demonstration of temporal cloaking,” *Nature* **481**, 62–5 (2012).
- [33] S. A. Cummer and D. Schurig, “One path to acoustic cloaking,” *New J. Phys.* **9**, 45–45 (2007).
- [34] M. Farhat, S. Enoch, S. Guenneau, and A. Movchan, “Broadband Cylindrical Acoustic Cloak for Linear Surface Waves in a Fluid,” *Phys. Rev. Lett.* **101**, 134501 (2008).
- [35] B. Popa, L. Zigoneanu, and S. Cummer, “Experimental Acoustic Ground Cloak in Air,” *Phys. Rev. Lett.* **106**, 253901 (2011).

-
- [36] P. A. Huidobro, M. L. Nesterov, L. Martín-Moreno, and F. J. García-Vidal, “Transformation optics for plasmonics,” *Nano Lett.* **10**, 1985–90 (2010).
- [37] Y. Liu, T. Zentgraf, G. Bartal, and X. Zhang, “Transformational plasmon optics,” *Nano Lett.* **10**, 1991–7 (2010).
- [38] T. Zentgraf, Y. Liu, M. H. Mikkelsen, J. Valentine, and X. Zhang, “Plasmonic Luneburg and Eaton lenses,” *Nature Nanotechnol.* **6**, 151–5 (2011).
- [39] K. F. Riley, S. J. Bence, and M. P. Hobson, *Mathematical methods for Physics and Engineering: A Comprehensive Guide*, 3rd ed. (Cambridge University Press, Cambridge, 2002).
- [40] U. Leonhardt and T. G. Philbin, “Transformation Optics and the Geometry of Light,” *Prog. Optics* **53**, 69–152 (2009).
- [41] M. J. Ablowitz and A. S. Fokas, *Complex Variables: Introduction and Applications*, 2nd ed. (Cambridge University Press, Cambridge, 2003).
- [42] J. B. Pendry and S. A. Ramakrishna, “Near-field lenses in two dimensions,” *J. Phys. Condens. Matter* **14**, 8463–8479 (2002).
- [43] R. Schinzinger and P. A. A. Laura, *Conformal Mapping - Methods and Applications* (Dover Publications, Inc, Minealo, N.Y., 2003).
- [44] A. V. Radchik, G. B. Smith, and A. J. Reuben, “Quasistatic optical response of separate, touching, and intersecting cylinder pairs,” *Phys. Rev. B* **46**, 6115–6125 (1992).
- [45] R. McPhedran and D. McKenzie, “Electrostatic and optical resonances of arrays of cylinders,” *Appl. Phys.* **23**, 223–235 (1980).
- [46] R. C. McPhedran and G. W. Milton, “Transport Properties of Touching Cylinder Pairs and of the Square Array of Touching Cylinders,” *Proc. Roy. Soc. A* **411**, 313–326 (1987).
- [47] A. Aubry, D. Y. Lei, S. A. Maier, and J. B. Pendry, “Interaction between Plasmonic Nanoparticles Revisited with Transformation Optics,” *Phys. Rev. Lett.* **105**, 233901 (2010).

- [48] A. Aubry, D. Y. Lei, S. A. Maier, and J. B. Pendry, “Interaction between Plasmonic Nanoparticles Revisited with Transformation Optics,” *Phys. Rev. Lett.* **105**, 233901 (2010).
- [49] D. Y. Lei, A. Aubry, Y. Luo, S. A. Maier, and J. B. Pendry, “Plasmonic interaction between overlapping nanowires.” *ACS Nano* **5**, 597–607 (2011).
- [50] Y. Luo, J. B. Pendry, and A. Aubry, “Surface plasmons and singularities.” *Nano Lett.* **10**, 4186–91 (2010).
- [51] Y. Luo, D. Y. Lei, S. A. Maier, and J. B. Pendry, “Broadband Light Harvesting Nanostructures Robust to Edge Bluntness,” *Phys. Rev. Lett.* **108**, 023901 (2012).
- [52] L. Novotny and B. Hecht, *Principles of Nano-Optics*, 2nd ed. (Cambridge University Press, Cambridge, 2006).
- [53] A. Aubry, D. Y. Lei, S. A. Maier, and J. B. Pendry, “Conformal transformation applied to plasmonics beyond the quasistatic limit,” *Phys. Rev. B* **82**, 205109 (2010).
- [54] Y. Luo, A. Aubry, and J. B. Pendry, “Electromagnetic contribution to surface-enhanced Raman scattering from rough metal surfaces: A transformation optics approach,” *Phys. Rev. B* **83**, 155422 (2011).
- [55] J. Zhang and A. V. Zayats, “Multiple Fano resonances in single-layer nonconcentric core-shell nanostructures,” *Opt. Express* **21**, 8426–8436 (2013).
- [56] A. I. Fernández-Domínguez, S. A. Maier, and J. B. Pendry, “Collection and Concentration of Light by Touching Spheres: A Transformation Optics Approach,” *Phys. Rev. Lett.* **105**, 266807 (2010).
- [57] J. B. Pendry, A. I. Fernández-Domínguez, Y. Luo, and R. Zhao, “Capturing photons with transformation optics,” *Nat. Phys.* **9**, 518–522 (2013).
- [58] A. I. Fernández-Domínguez, A. Wiener, F. J. García-Vidal, S. A. Maier, and J. B. Pendry, “Transformation-Optics Description of Nonlocal Effects in Plasmonic Nanostructures,” *Phys. Rev. Lett.* **108**, 106802 (2012).
- [59] Y. Luo, A. I. Fernández-Domínguez, A. Wiener, S. A. Maier, and J. B. Pendry, “Surface Plasmons and Nonlocality: A Simple Model,” *Phys. Rev. Lett.* **111**, 093901 (2013).

- [60] J. B. Pendry, A. Aubry, D. R. Smith, and S. A. Maier, “Transformation Optics and Subwavelength Control of Light,” *Science* **337**, 549–552 (2012).
- [61] J. B. Pendry, Y. Luo, and R. Zhao, “Transforming the optical landscape,” *Science* **348**, 521–524 (2015).
- [62] M. Kraft, J. B. Pendry, S. A. Maier, and Y. Luo, “Transformation optics and hidden symmetries,” *Phys. Rev. B* **89**, 245125 (2014).
- [63] P. M. Morse and H. Feshbach, *Methods of Theoretical Physics, Part II* (McGraw-Hill Book Company, INC., New York, 1953).
- [64] C. F. Bohren and D. R. Huffman, *Absorption and Scattering of Light by Small Particles* (Wiley-VCH, Weinheim, 1998).
- [65] P. B. Johnson and R. W. Christy, “Optical Constants of the Noble Metals,” *Phys. Rev. B* **6**, 4370–4379 (1972).
- [66] M. Kraft, Y. Luo, and J. B. Pendry, “Transformation Optics: A Time- and Frequency-Domain Analysis of Electron-Energy Loss Spectroscopy,” *Nano Lett.* **16**, 5156–5162 (2016).
- [67] S. J. Norton and T. Vo-Dinh, “Plasmon Resonances of Nanoshells of Spheroidal Shape,” *IEEE T. Nanotechnol.* **6**, 627–638 (2007).
- [68] N. I. Grigorochuk, “Plasmon resonant light scattering on spheroidal metallic nanoparticle embedded in a dielectric matrix,” *EPL* **97**, 45001 (2012).
- [69] J. J. Penninkhof, A. Moroz, A. van Blaaderen, and A. Polman, “Optical Properties of Spherical and Oblate Spheroidal Gold Shell Colloids,” *J. Phys. Chem. C* **112**, 4146–4150 (2008).
- [70] S. Oldenburg, R. Averitt, S. Westcott, and N. Halas, “Nanoengineering of optical resonances,” *Chem. Phys. Lett.* **288**, 243 – 247 (1998).
- [71] R. W. Wood, “On a Remarkable Case of Uneven Distribution of Light in a Diffraction Grating Spectrum,” *Philos. Mag. Series 6* **4**, 396–402 (1902).
- [72] A. Hessel and A. A. Oliner, “A New Theory of Wood’s Anomalies on Optical Gratings,” *Appl. Opt.* **4**, 1275–1297 (1965).
- [73] Lord Rayleigh, “On the Dynamical Theory of Gratings,” *Proc. R. Soc. Lond. A* **79**, 399–416 (1907).

- [74] U. Fano, “Zur Theorie der Intensitätsanomalien der Beugung,” *Ann. Phys.* **424**, 393–443 (1938).
- [75] U. Fano, “The Theory of Anomalous Diffraction Gratings and of Quasi-Stationary Waves on Metallic Surfaces (Sommerfeld’s Waves),” *J. Opt. Soc. Am.* **31**, 213–222 (1941).
- [76] M. Sarrazin, J.-P. Vigneron, and J.-M. Vigoureux, “Role of Wood anomalies in optical properties of thin metallic films with a bidimensional array of subwavelength holes,” *Phys. Rev. B* **67**, 085415 (2003).
- [77] Y. Francescato, V. Giannini, and S. A. Maier, “Plasmonic Systems Unveiled by Fano Resonances,” *ACS Nano* **6**, 1830–1838 (2012).
- [78] A. E. Miroshnichenko, S. Flach, and Y. S. Kivshar, “Fano resonances in nanoscale structures,” *Rev. Mod. Phys.* **82**, 2257–2298 (2010).
- [79] B. Luk’yanchuk, N. Zheludev, S. Maier, N. Halas, P. Nordlander, H. Giessen, and C. Chong, “The Fano resonance in plasmonic nanostructures and metamaterials,” *Nat. Mater.* **9**, 707–715 (2010).
- [80] S. R. K. Rodriguez, A. Abass, B. Maes, O. T. A. Janssen, G. Vecchi, and J. Gómez Rivas, “Coupling Bright and Dark Plasmonic Lattice Resonances,” *Phys. Rev. X* **1**, 021019 (2011).
- [81] C. Genet, M. P. van Exter, and J. Woerdman, “Fano-type interpretation of red shifts and red tails in hole array transmission spectra,” *Opt. Commun.* **225**, 331–336 (2003).
- [82] T. Ebbesen, H. Lezec, H. Ghaemi, T. Thio, and P. Wolff, “Extraordinary Optical Transmission Through Sub-Wavelength Hole Arrays,” *Nature* **391**, 667–669 (1998).
- [83] L. Martín-Moreno, F. García-Vidal, H. Lezec, K. Pellerin, T. Thio, J. Pendry, and T. Ebbesen, “Theory of Extraordinary Optical Transmission through Sub-wavelength Hole Arrays,” *Phys. Rev. Lett.* **86**, 1114–1117 (2001).
- [84] J. L. West and N. J. Halas, “Engineered nanomaterials for biophotonics applications: improving sensing, imaging, and therapeutics.” *Annu. Rev. Biomed. Eng.* **5**, 285–92 (2003).

- [85] K. M. Byun, S. M. Jang, S. J. Kim, and D. Kim, “Effect of target localization on the sensitivity of a localized surface plasmon resonance biosensor based on subwavelength metallic nanostructures.” *J. Opt. Soc. Am. A* **26**, 1027–34 (2009).
- [86] M. Grande, R. Marani, F. Portincasa, G. Morea, V. Petruzzelli, A. D’Orazio, V. Marrocco, D. de Ceglia, and M. Vincenti, “Asymmetric plasmonic grating for optical sensing of thin layers of organic materials,” *Sensor. Actuat. B-Chem.* **160**, 1056–1062 (2011).
- [87] W.-K. Kuo, C.-H. Chang, C.-J. Wu, and H.-H. Yu, “Phase-detection-sensitivity enhancement of grating-coupled surface plasmon resonance sensor with light incident at nonzero azimuth angle,” *J. Nanophotonics* **6**, 063524 (2012).
- [88] A. Campion and P. Kambhampati, “Surface-enhanced Raman scattering,” *Chem. Soc. Rev.* **27**, 241–250 (1998).
- [89] X. Deng, G. B. Braun, S. Liu, P. F. Sciortino, B. Koefer, T. Tomblor, and M. Moskovits, “Single-order, subwavelength resonant nanograting as a uniformly hot substrate for surface-enhanced Raman spectroscopy.” *Nano Lett.* **10**, 1780–6 (2010).
- [90] N. Mattiucci, G. D’Aguanno, H. O. Everitt, J. V. Foreman, J. M. Callahan, M. C. Buncick, and M. J. Bloemer, “Ultraviolet surface-enhanced Raman scattering at the plasmonic band edge of a metallic grating,” *Opt. Express* **20**, 1868–1877 (2012).
- [91] H. A. Atwater and A. Polman, “Plasmonics for improved photovoltaic devices.” *Nat. Mater.* **9**, 205–13 (2010).
- [92] H. Shen and B. Maes, “Combined plasmonic gratings in organic solar cells,” *Opt. Express* **19**, 144–150.
- [93] K. Tvingstedt, N.-K. Persson, O. Inganäs, A. Rahachou, and I. V. Zozoulenko, “Surface plasmon increase absorption in polymer photovoltaic cells,” *Appl. Phys. Lett.* **91**, 113514 (2007).
- [94] R. A. Pala, J. White, E. Barnard, J. Liu, and M. L. Brongersma, “Design of Plasmonic Thin-Film Solar Cells with Broadband Absorption Enhancements,” *Adv. Mater.* **21**, 3504–3509 (2009).

- [95] C. Min, J. Li, G. Veronis, J.-Y. Lee, S. Fan, and P. Peumans, “Enhancement of optical absorption in thin-film organic solar cells through the excitation of plasmonic modes in metallic gratings,” *Appl. Phys. Lett.* **96**, 133302 (2010).
- [96] A. Baba, N. Aoki, K. Shinbo, K. Kato, and F. Kaneko, “Grating-Coupled Surface Plasmon Enhanced Short-Circuit Current in Organic Thin-Film Photovoltaic Cells,” *ACS Appl. Mater. Interfaces* **3**, 2080–2084 (2011).
- [97] A. P. Kulkarni, K. M. Noone, K. Munechika, S. R. Guyer, and D. S. Ginger, “Plasmon-enhanced charge carrier generation in organic photovoltaic films using silver nanoprisms,” *Nano Lett.* **10**, 1501–5 (2010).
- [98] V. E. Ferry, L. A. Sweatlock, D. Pacifici, and H. A. Atwater, “Plasmonic nanostructure design for efficient light coupling into solar cells,” *Nano Lett.* **8**, 4391–7 (2008).
- [99] L. Wen, F. Sun, and Q. Chen, “Cascading metallic gratings for broadband absorption enhancement in ultrathin plasmonic solar cells,” *Appl. Phys. Lett.* **104**, 151106 (2014).
- [100] J. N. Munday and H. A. Atwater, “Large Integrated Absorption Enhancement in Plasmonic Solar Cells by Combining Metallic Gratings and Antireflection Coatings,” *Nano Lett.* **11**, 2195–2201 (2011).
- [101] W. L. Barnes, T. W. Preist, S. C. Kitson, and J. R. Sambles, “Physical origin of photonic energy gaps in the propagation of surface plasmons on gratings,” *Phys. Rev. B* **54**, 6227–6244 (1996).
- [102] M. Kraft, Y. Luo, S. A. Maier, and J. B. Pendry, “Designing Plasmonic Gratings with Transformation Optics,” *Phys. Rev. X* **5**, 031029 (2015).
- [103] A. Aubry, D. Y. Lei, S. A. Maier, and J. B. Pendry, “Broadband plasmonic device concentrating the energy at the nanoscale: The crescent-shaped cylinder,” *Phys. Rev. B* **82**, 125430 (2010).
- [104] G. W. Semenoff, “Condensed-Matter Simulation of a Three-Dimensional Anomaly,” *Phys. Rev. Lett.* **53**, 2449–2452.
- [105] X. Huang, Y. Lai, Z. H. Hang, H. Zheng, and C. T. Chan, “Dirac cones induced by accidental degeneracy in photonic crystals and zero-refractive-index materials,” *Nat. Mater.* **10**, 582–586 (2011).

- [106] G. Weick, C. Woollacott, W. Barnes, O. Hess, and E. Mariani, “Dirac-like Plasmons in Honeycomb Lattices of Metallic Nanoparticles,” *Phys. Rev. Lett.* **110**, 106801 (2013).
- [107] R. Feynman, R. Leighton, and M. Sands, *The Feynman Lectures on Physics*, 2nd ed., Vol. 2 (Addison-Wesley, Boston, 1963).
- [108] P. Tassin, T. Koschny, and C. M. Soukoulis, “Effective material parameter retrieval for thin sheets: Theory and application to graphene, thin silver films, and single-layer metamaterials,” *Physica B* **407**, 4062 – 4065 (2012).
- [109] M. Sarrazin, J.-P. Vigneron, and J.-M. Vigoureux, “Role of Wood anomalies in optical properties of thin metallic films with a bidimensional array of subwavelength holes,” *Phys. Rev. B* **67**, 085415 (2003).
- [110] J. A. Kong, *Electromagnetic Wave Theory*, 6th ed. (EMW Publishing, Cambridge, MA, 2005).
- [111] Z. Li, K. Aydin, and E. Ozbay, “Determination of the effective constitutive parameters of bianisotropic metamaterials from reflection and transmission coefficients,” *Phys. Rev. E* **79**, 026610 (2009).
- [112] M. Kraft, A. Braun, Y. Luo, S. A. Maier, and J. B. Pendry, “Bianisotropy and Magnetism in Plasmonic Gratings,” *ACS Photonics* **3**, 764–769 (2016).
- [113] R. H. Ritchie, “Plasma Losses by Fast Electrons in Thin Films,” *Phys. Rev.* **106**, 874–881 (1957).
- [114] H. Watanabe, “Experimental evidence for the collective nature of the characteristic energy loss of electrons in solids - Studies on the dispersion relation of plasma frequency,” *J. Phys. Soc. Jpn.* **11**, 112–119 (1956).
- [115] C. J. Powell and J. B. Swan, “Origin of the characteristic electron energy losses in aluminum,” *Phys. Rev.* **115**, 869–875 (1959).
- [116] J. A. Scholl, A. García-Etxarri, A. L. Koh, and J. A. Dionne, “Observation of quantum tunneling between two plasmonic nanoparticles,” *Nano Lett.* **13**, 564–9 (2013).
- [117] J. A. Scholl, A. L. Koh, and J. A. Dionne, “Quantum plasmon resonances of individual metallic nanoparticles,” *Nature* **483**, 421–427 (2012).

- [118] H. Duan, A. I. Fernández-Domínguez, M. Bosman, S. A. Maier, and J. K. W. Yang, “Nanoplasmonics: Classical down to the Nanometer Scale,” *Nano Letters* **12**, 1683–1689 (2012).
- [119] T. Coenen, *Angle-resolved cathodoluminescence nanoscopy*, Dissertation for the degree of Doctor of Philosophy (PhD), University of Amsterdam, Amsterdam (2014).
- [120] A. L. Koh, K. Bao, I. Khan, W. E. Smith, G. Kothleitner, P. Nordlander, S. A. Maier, and D. W. McComb, “Electron energy-loss spectroscopy (EELS) of surface plasmons in single silver nanoparticles and dimers: Influence of beam damage and mapping of dark modes,” *ACS Nano* **3**, 3015–3022 (2009).
- [121] J. Nelayah, M. Kociak, O. Stéphan, F. J. García de Abajo, M. Tencé, L. Henrard, D. Taverna, I. Pastoriza-Santos, L. M. Liz-Marzán, and C. Colliex, “Mapping surface plasmons on a single metallic nanoparticle,” *Nat. Phys.* **3**, 348–353 (2007).
- [122] O. Nicoletti, M. Wubs, N. A. Mortensen, W. Sigle, P. A. van Aken, and P. A. Midgley, “Surface plasmon modes of a single silver nanorod: an electron energy loss study,” *Opt. Express* **19**, 15371–15379 (2011).
- [123] R. Gómez-Medina, N. Yamamoto, M. Nakano, and F. J. García De Abajo, “Mapping plasmons in nanoantennas via cathodoluminescence,” *New J. Phys.* **10**, 105009 (2008).
- [124] P. Chaturvedi, K. H. Hsu, A. Kumar, K. H. Fung, J. C. Mabon, and N. X. Fang, “Imaging of Plasmonic Modes of Silver Nanoparticles Using High-Resolution,” *ACS Nano* **3**, 2965–2974 (2009).
- [125] A. Koh, A. I. Fernández-Domínguez, S. A. Maier, J. Yang, and D. McComb, “Mapping of Electron-Beam-Excited Plasmon Modes in Lithographically-Defined Gold Nanostructures,” *Nano Lett.* **11**, 1323–1330 (2011).
- [126] F. J. García De Abajo and M. Kociak, “Probing the photonic local density of states with electron energy loss spectroscopy,” *Phys. Rev. Lett.* **100**, 1–4 (2008).
- [127] U. Hohenester, H. Ditlbacher, and J. R. Krenn, “Electron-energy-loss spectra of plasmonic nanoparticles,” *Phys. Rev. Lett.* **103**, 1–4 (2009).
- [128] K. J. Savage, M. M. Hawkeye, R. Esteban, A. G. Borisov, J. Aizpurua, and J. J. Baumberg, “Revealing the quantum regime in tunnelling plasmonics.” *Nature* **491**, 574–7 (2012).

-
- [129] M. Kuttge, E. J. R. Vesseur, and A. Polman, “Fabry-Perot resonators for surface plasmon polaritons probed by cathodoluminescence,” *Appl. Phys. Lett.* **94**, 29–32 (2009).
- [130] A. C. Atre, B. J. M. Brenny, T. Coenen, A. García-Etxarri, A. Polman, and J. A. Dionne, “Nanoscale optical tomography with cathodoluminescence spectroscopy,” *Nat. Nanotechnol.* **10**, 429–436 (2015).
- [131] R. Egerton, *Electron Energy-Loss Spectroscopy in the Electron Microscope*, 3rd ed. (Springer, New York, USA, 2011).
- [132] F. J. García De Abajo, “Optical excitations in electron microscopy,” *Rev. Mod. Phys.* **82**, 209–275 (2010).
- [133] Y. Cao, A. Manjavacas, N. Large, and P. Nordlander, “Electron Energy-Loss Spectroscopy Calculation in Finite-Difference Time-Domain Package,” *ACS Photonics* **2**, 369–375 (2015).
- [134] F. J. García de Abajo and A. Howie, “Retarded field calculation of electron energy loss in inhomogeneous dielectrics,” *Phys. Rev. B* **65**, 115418 (2002).
- [135] U. Hohenester, “Simulating electron energy loss spectroscopy with the MNPBEM toolbox,” *Comput. Phys. Commun.* **185**, 1177 – 1187 (2014).
- [136] N. Geuquet and L. Henrard, “EELS and optical response of a noble metal nanoparticle in the frame of a discrete dipole approximation,” *Ultramicroscopy* **110**, 1075 – 1080 (2010).
- [137] N. W. Bigelow, A. Vaschillo, V. Iberi, J. P. Camden, and D. J. Masiello, “Characterization of the electron- and photon-driven plasmonic excitations of metal nanorods,” *ACS Nano* **6**, 7497–7504 (2012).
- [138] N. W. Bigelow, A. Vaschillo, J. P. Camden, and D. J. Masiello, “Signatures of Fano Interferences in the Electron Energy Loss Spectroscopy and Cathodoluminescence of Symmetry-Broken Nanorod Dimers,” *ACS Nano* **7**, 4511–4519 (2013).
- [139] B. W. Reed, J. M. Chen, N. C. MacDonald, J. Silcox, and G. F. Bertsch, “Fabrication and STEM/EELS measurements of nanometer-scale silicon tips and filaments,” *Phys. Rev. B* **60**, 5641–5652 (1999).

- [140] N. Talebi, W. Sigle, R. Vogelgesang, and P. van Aken, “Numerical simulations of interference effects in photon-assisted electron energy-loss spectroscopy,” *New J. Phys.* **15**, 053013 (2013).
- [141] C. Matyssek, J. Niegemann, W. Hergert, and K. Busch, “Computing electron energy loss spectra with the Discontinuous Galerkin Time-Domain method,” *Photonic Nanostruct.* **9**, 367–373 (2011).
- [142] P. M. Echenique and J. B. Pendry, “Absorption profile at surfaces,” *J. Phys. C* **8**, 2936 (1975).
- [143] R. Garcia-Molina, A. Gras-Marti, A. Howie, and R. H. Ritchie, “Retardation effects in the interaction of charged particle beams with bounded condensed media,” *J. Phys. C* **18**, 5335 (1985).
- [144] J. Crowell and R. H. Ritchie, “Radiative Decay of Coulomb-Stimulated Plasmons in Spheres,” *Phys. Rev.* **172**, 436–440 (1968).
- [145] T. L. Ferrell and P. M. Echenique, “Generation of Surface Excitations on Dielectric Spheres by an External Electron Beam,” *Phys. Rev. Lett.* **55**, 1526–1529 (1985).
- [146] N. Zabala, A. Rivacoba, and P. Echenique, “Coupling effects in the excitations by an external electron beam near close particles,” *Phys. Rev. B* **56**, 7623–7635 (1997).
- [147] M. Schmeits, “Surface-plasmon coupling in cylindrical pores,” *Phys. Rev. B* **39**, 7567–7577 (1989).
- [148] B. Illman, V. Anderson, R. Warmack, and T. Ferrell, “Spectrum of surface-mode contributions to the differential energy-loss probability for electrons passing by a spheroid,” *Phys. Rev. B* **38**, 3045–3049 (1989).
- [149] Y. Luo, M. Kraft, and J. B. Pendry, “Harnessing transformation optics for understanding electron energy loss and cathodoluminescence,” [arXiv.org preprint arXiv:1605.09319](https://arxiv.org/abs/1605.09319) [cond-mat.mes-hall] (2016).
- [150] W. H. Press, S. A. Teukolsky, W. T. Vetterling, and B. P. Flannery, *Numerical Recipes 3rd Edition: The Art of Scientific Computing*, 3rd ed. (Cambridge University Press, 2007).
- [151] J. J. Sakurai, *Modern Quantum Mechanics (Revised Edition)*, revised ed. (Addison Wesley, Reading, MA, 1993).

-
- [152] DLMF, “NIST Digital Library of Mathematical Functions,” <http://dlmf.nist.gov/>, Release 1.0.10 of 2015-08-07, online companion to [154].
- [153] P. A. Huidobro, M. Kraft, R. Kun, S. A. Maier, and J. B. Pendry, “Graphene, plasmons and transformation optics,” *Journal of Optics* **18**, 044024 (2016).
- [154] F. W. J. Olver, D. W. Lozier, R. F. Boisvert, and C. W. Clark, eds., *NIST Handbook of Mathematical Functions*, 1st ed. (Cambridge University Press, New York, 2010.) Print companion to [152].